INVESTIGATING THE ROLES OF MATRIX NANOTOPOGRAPHY AND ELASTICITY IN THE OSTEOGENIC DIFFERENTIATION OF MESENCHYMAL STEM CELLS

by

Isaac A. Janson

**A dissertation submitted in partial fulfillment
of the requirements for the degree of
Doctor of Philosophy
(Materials Science and Engineering)
in the University of Michigan
2014**

Doctoral Committee:

Professor Brian J. Love, Chair
Professor Joerg Lahann
Professor Peter X. Ma
Associate Professor Andrew J. Putnam

The footsteps of Nature are to be trac'd, not only in her ordinary course, but when she seems to be put to her shifts, to make many doublings and turnings, and to use some kind of art in endeavoring to avoid our discovery.

-Robert Hooke

DEDICATION

to

those whose aim is to advance science to help others;

more importantly

to

those who support, unwaveringly, the tinkerers, engineers,

and scientists through the struggles and the triumphs.

ACKNOWLEDGEMENTS

Each and every one of us does not get to where we are today, both personally and professionally, without an enormous amount of help and guidance. Therefore, I would be remiss if I did not take significant time and care to acknowledge the contributions that so many have made in helping me get to this point. The list of people to thank is… thankfully long.

First, I would like to thank my advisor Professor Andrew Putnam. You have helped me understand the dedication, drive, and persistence that Ph.D. level science requires. Along the way you have challenged me both personally and professionally. I thank you for your patience during the many challenges that we stumbled through.

I would like to thank the other committee members, Professor Joerg Lahann, Professor Brian Love, and Professor Peter Ma. Thank you for your insights and guidance to improve my thesis. Your input was invaluable.

To Professor Albert Yee, I appreciate your steadfast resolve to do great science and commitment to high standards. Thank you for your guidance and support, especially during the early years at Irvine.

I need to acknowledge funding sources that were critical to my success. NIH R01-HL085339 and R21-DE021537, the NSF Integrative Graduate Education and Research Traineeship (IGERT) LifeChips fellowship, the GAANN fellowship, as well as the Rackham Graduate School travel award aided me during my graduate studies.

To the members, past and present of CSET lab (and honorary member-Dr. Ram Rao), thank you to all of you. Thank you to Peter Kim. Peter was instrumental in welcoming me as a friend and colleague. He helped me learn cell culture and helped me grow in so many other aspects of research. Peter was (and still is) a phenomenal

mentor and role-model. Thank you to Dr. Suraj Kachgal. He helped me try to better understand the why of everything rather than simply following along because that is how it had always been done. Thank you to Dr. Bita Carrion. Working with Bita was always a delight because of her quiet resolve and openness to collaboration. Dr. Yen Peng Kong deserves many, many thanks as well. Yen spent a great deal of time teaching me many new processing techniques in Irvine and helping me with troubleshooting here in Ann Arbor. He is an incredibly patient and gifted teacher too. Thank you to Dr. Jake Ceccarelli for your help through the trials and tribulations. Your keen eye for the important issues was helpful. To the current CSET graduate crew, Ana, Marina, and Rahul. All of you helped me stay sane, especially over the last two years. Marina, thanks for your upbeat personality and listening ear. Rahul, thanks for challenging the status quo and helping out with so many of my questions. To the future members of CSET, or whatever the name becomes, good luck and be curious. Do not forget to question established methods and dogma, they are often wrong or not well understood.

I need to take a moment to thank Mark Vander Roest. He is an exceptional undergraduate (soon to be graduate) student that has helped me complete this thesis much sooner than I could have without his help. You have also taught me that mentoring is much harder than it looks. Good luck in your next adventure!

The friends along the way, both here and those I met in Irvine, you made the experience incredibly rich. Thanks to Neha, Sibu, and Charlie for your love of techno. Thanks to David Lai for too many reasons too list. Thanks to Tapiwa for your love of soccer and entertaining my love for trivia night. Thanks to Brandon, Joe, and Jeremy for entertaining discussions about Purdue, the Big Ten, sports, and countless other random things. To the UC Irvine crowd, Matt Sullivan, Matt Weeks, Jungyun Kim, Himanshu (H-town) Sharma, Adam Gardner, Nick Bell and more, thanks for making California so enjoyable.

I need also remember the help and support my family (Erin and Kemp, Kirsten, Ethan, Christine, Amy and Scott, the Carmel sisters, Janet, Bob, Laura, The Wajdas, my Grandparents K and D!, and so many more) has given me, especially over the last few years. The trips to visit me in California helped make the transition to West Coast life so much easier. I have been incredibly blessed to have such unwavering support from my parents Mark and Rita Janson. Thank you for all your advice and guidance. My in-laws deserve great thanks too, Mary Rose and Harry McCullough and Meg and Jeff Frazer. They have always been warm, welcoming and supporting of this crazy Ph.D. process.

Finally, without question, I could not have come this far without my wife Michelle. Her patience knows no bounds as we have dealt with long-distance for far too long. I appreciate all your sacrifices as we have gone through this adventure together. I will never be able to thank you enough for all your encouraging words, your openness to change, and your endless commitment to us. Thank you and I love you! Now let's get onto the next adventure!!

TABLE OF CONTENTS

LIST OF TABLES

LIST OF FIGURES

LIST OF APPENDICES

LIST OF ABBREVIATIONS

AFM	atom force microscope
AGM	adipogenic growth media
AIM	adipogenic induction media
APMDS	(3-acryloxy propyl) methyl dichlororsilane
COL I	collagen type I
CSD	critical size defect
DAPI	4',6-diamidino-2-phenylindole dihydrochloride
ECM	extracellular matrix
EDS	(x-ray) energy dispersive spectroscopy
FN	fibronectin
FDTS	(heptadecafluoro-1,2,2,2-tetrahydrodecyl) trichlorosilane
MC3T3-E1	mouse calvarial pre-osteoblast cell
MMA	methyl methacrylate
MSC	mesenchymal stem cell
OGM	osteogenic growth media
OBM	osteogenic base media
PEGDA	(poly) ethylene glycol diacrylate
PMMA	(poly) methyl methacrylate
PUA	(poly) urethane vinyl acrylate
SEM	scanning electron microscope
SFE	surface free energy
Sulfo-SANPAH	sulfosuccinimidyl 6-(4'-azido-2'-nitrophenylamino)hexanoate
UV	ultra-violet

ABSTRACT

The chemical, mechanical, and topographical features of the extracellular matrix (ECM) have all been documented to influence osteogenic differentiation. Furthermore, topography and matrix elasticity play key roles in the architecture and functionality of various tissues *in vivo*, raising the possibility that these cues can be instructive when incorporated into biomaterials for regenerative applications.

We used thin film substrates of poly(methyl methacrylate) (PMMA) with nanoscale gratings to investigate the influence of controlled nanotopography (compared to a 'smooth' uncontrolled topographic surface) mimicking the size and architecture of collagen fibrils in bone on the osteogenic phenotype of mesenchymal stem cells (MSCs), focusing in particular on their ability to produce mineral similar to native bone. Analysis revealed controlled grating topography ranging from ~415 nm to 140 in width and 200 to 110 nm in depth. Topography induced anisotropy in both contact angles and surface free energy (SFE). Smooth PMMA had an SFE of 40 mN/m. Topographic surfaces had elevated and reduced SFEs when measuring parallel to (up to ~45 mN/m) or perpendicular to the gratings (as low as ~31 mN/m) respectively. Topography influenced alignment, and enhanced

MSC proliferation after 14 days of culture. Focal adhesion size was influenced after 7 days though the osteogenic phenotype was minimally influenced by topography as calcium deposition was not increased after 21 days in culture. Ca: P ratios were similar to native mouse bone on films with gratings of 415 nm width and 200 nm depth (G415) and 303 nm width and 190 nm depth (G303). Notably, all surfaces had Ca:P ratios significantly lower than G415 films (less than 1.39).

We also used thin films of poly(ethylene glycol diacrylate) (PEGDA) with nanoscale gratings (as previously described with PMMA) and tunable elasticity to investigate their potential synergistic effect on the osteogenic phenotype of MSCs. Three distinct moduli were used having a shear storage modulus of ~64, 300, and 530 kPa respectively. Topography did not influence cell alignment nor did the combination of matrix topography and elasticity enhance the calcium deposition compared to smooth controls. Ca:P ratios (ranging from 1.3 to 1.4) were similar on nanoPEGDA compared to smooth controls. Collagen I density (5 or 50 μg/mL) did not significantly influence calcium deposition.

These data demonstrate that nanotopographic PMMA films, mimicking the architecture of bone, do not enhance calcium levels in mineral deposited by hMSCs. We showed that increased focal adhesion size on PMMA nanotopography is insufficient by itself to drive increased calcium deposition. Reports in literature rarely quantify changes in focal adhesions with changes in mineral quantity and composition and instead focus on other markers of osteogenesis that have minor roles in mineral

formation. Our results mirror an *in vivo* report suggesting that topography does not enhance osteogenesis. Additionally, in the first known attempt to combine adhesion ligand concentration (Col I) to nanogratings on surfaces with varied mechanical properties, these inputs were insufficient to synergistically enhance an osteogenic phenotype in MSCs. Collectively, these results highlight the importance of studying cell functional output rather than minor markers of cell behavior exclusively as cell function is a greater indicator of differentiation. Potentially, the matrix adhesion, topographic, and mechanical cues we altered, did not modulate the ability of a cell to adhere significantly enough to influence their osteogenic differentiation.

CHAPTER 1

Introduction

1.1 Motivation and Tissue Engineering Background

The human body is composed of thousands of interworking parts. From small molecules, to large proteins, to individual cells, to complete organ-tissue systems; each part is integral to the body. Typically, all these parts work in concert extraordinarily well. In a few circumstances—injury, cancer, disease—these parts may not be able to repair the malady back to proper functionality leading to reduced performance, increased chronic pain and mental distress, and diminished quality of life. Cases when the body has difficulty with self-repair are the motivation for the field of tissue engineering and regenerative medicine.

The history of tissue engineering and regenerative medicine goes back to ancient Greece mythology. Tissue engineering may have been first mentioned during the days of Greek poet Aeschylus and the story of Prometheus. Prometheus was cruelly punished by Zeus for misdeeds. As punishment, Zeus allows an eagle to feast daily on Prometheus' continually regenerating liver[1]. Around the same time of the Prometheus storyline, Etruscans substituted missing teeth with bridges fashioned

from oxen bone[2]. This might have been the first (non-fictional) record to restore lost function using tissue engineering methods. More recently, developments during the 20th century lead to hip and knee replacements, pacemakers, and artificial heart valves[2]. Regeneration of liver, skin, bone, and other tissues has been a focus since the late '80s and early '90s, now considered to be the birth of the modern era of tissue engineering[2-4]. Tissue engineering involves applying engineering and life science principles to the generation of biological substitutes with the goal of creating, restoring, or preserving lost organ functions[5]. Restoration and regeneration is a multimodal process involving cell proliferation, differentiation and plasticity. Controlling the multimodal processes through a thorough understanding of the biological regulators of regeneration has the potential for wide-ranging impact. Most current pharmaceutical therapies could be replaced by tissue regenerative therapies[1]. Thus, studying and understanding the key biological processes for regeneration is necessary to achieve these possibilities.

Regeneration is largely limited in the human body; only the liver and bone are capable of scarless self-renewal (in contrast to other species that have greater regeneration capacity)[1]. Even with this capability, bone injuries or defects above a critical size can limit the body's innate capacity for repair and may result in a non-union[6-8]. Large defects and injuries include cortical defects, infection, tumor resection, and implant loosening[9]. Most times these maladies are termed a critical size defect (CSD): defects larger than this cannot be spontaneously regenerated. CSDs are

usually 1.5 to 2 times greater than the diameter of the long bone diaphysis but vary depending on the host and the bone[10]. These factors highlight the need to develop therapies for bone regeneration. First, a discussion of the physiological role of bone will help highlight the importance of bone to a healthy functioning person.

1.2 Bone function and physiology

Bone serves both a biological and mechanical purpose[11-13]. Biologically, bone is a reservoir for minerals and the site of leukocyte (and other blood cell) production[14]. Specifically, bone contains essential minerals including calcium and phosphate that serve vital roles in many metabolic biological processes[12,13]. Other chemical messengers like parathyroid hormone and calcitonin regulate the concentration of calcium in serum[15]. Blood cell formation in the bone marrow helps supply a fresh and sufficient source of platelets and red blood cells and helps maintain our innate and adaptive immunities[14,16]. Additionally, bone serves to support the tissues of the body and provides protection to vital organs (lungs, heart, brain etc.). Mechanically, bone must function well under tensile and compressive stresses, but must also withstand impact and bending stresses[13]. For perspective, the tensile strength of bone is nearly equal that of cast iron, yet bone is three times lighter and ten times more flexible[17]. Therefore, bone is a versatile and critical tissue.

'Bone' and 'bone tissue' describe a family of materials of varied structure that share a common building block: the mineralized collagen fibril[12]. This family includes dentin (the inner layers of teeth), cementum (the thin layer of material that binds teeth's roots to the jaw), mineralized tendons, long bones and more. The fibrous protein collagen backbone of bone constitutes the main component of the 3D matrix on which mineral forms. The proportions of mineral and collagen vary greatly across the bone family[12]. Additionally, the manner in which these mineralized fibrils are arranged into higher ordered structures also varies; this is the basis for the different members of the bone family. These differences will now be discussed in greater detail to highlight the formation and hierarchical structure of bone.

1.3 Bone formation, hierarchy, and structure

At a macroscopic level, bone formation typically occurs through two mechanisms: intramembranous (direct or primary) osteogenesis or endochondral (secondary) ossification[1,18,19]. Intramembranous ossification results from the differentiation of osteoprogenitor cells into bone producing cells known as osteoblasts[20]. Angiogenesis is required for effective bone formation via intramembranous ossification. In contrast, endochondral ossification does not require a pre-established blood supply for the transition of cartilage to bone as the angiogenic signals are regulated temporally as the process evolves[18]. Endochondral

ossification is preceded first by collagen expression during the inflammatory and reparative stages. During the inflammatory stage, nutrient vessels are disrupted and hematoma formation occurs leading to cell death and infiltration of inflammatory cells[21]. The reparative phase follows inflammation and occurs 7-14 days following fracture. Being that this inflammation site is relatively hypoxic, chondrocytic cells deposit type II collagen in a cartilaginous matrix and promote growth of new woven bone. Ossification of the cartilaginous matrix occurs simultaneously with revascularization[15]. The final ossification step involves remodeling of the newly deposited woven bone to the original lamellar structure and outer bone diameter[1,17]. Endochondral ossification is favored for bone regeneration of the shaft (diaphysis) region of long bones and other similar sites[18].

To truly understand bone formation from a microscopic level we need to investigate the components of bone and their size. Bone is a hierarchically structured composite material consisting almost exclusively of type I collagen, hydroxyapatite (HA) ($(Ca_{10}(PO_4)_6(OH)_2$), and water. Type I collagen fibrils are typically 80-100 nm in diameter and unknown length due to the fact the fibrils merge with their neighbors (Figure 1.1). Each fibril is made up of three polypeptide chains that are wound together in a triple helix giving the resulting structure a cylindrical shape. Triple helices are approximately 300 nm long and have a 1.5 nm diameter[12]. The fibrils associate with each other to form filamentous web-like networks. Bone extracellular matrix (ECM) is more than 90% collagen I (col I). Collagen I, incidentally, is required for

HA growth[15,22]. Calcium, is a key component of HA, however, mineral precipitation is primarily dependent upon extracellular phosphate concentration[23]. After initial nucleation in matrix vesicles[15], nanoscale HA particles grow at interfragmental gap sites in the collagen fibrils that are approximately 40 nm wide[24] to form a composite fibril.

Fibril arrays form macroscopic structures at larger length scales and form different types of bone dependent on their arrangement and alignment. The degree of alignment varies dependent on the maturity of the bone. Immature (woven) bone differs from mature (lamellar) bone in composition, organization, and mechanical properties[17]. Woven bone has an irregular, nearly random arrangement of collagen fibrils. Lamellar bone, in contrast, has an aligned collagen network. Collagen fiber and HA alignment are critical to the mechanical integrity of bone[12]. Thus alignment (topography) is essential to proper bone function.

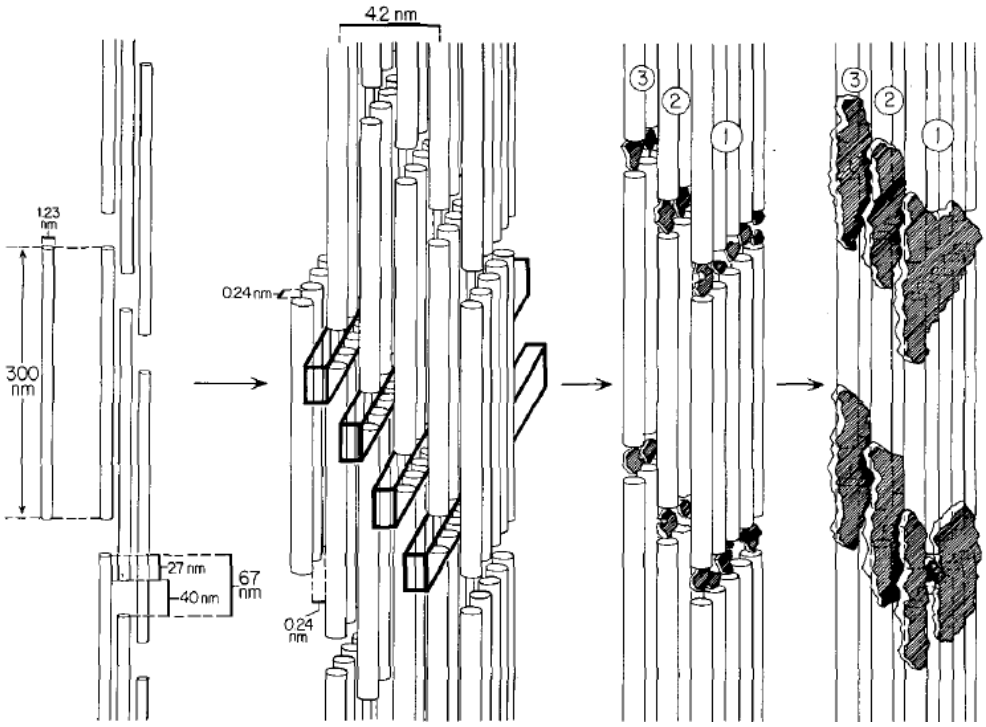

Figure 1.1. **The nanoscale and structure of collagen fibrils.** Schematic illustrating the structure and scale of the collagen I network that supports hydroxyapatite formation- the basic building blocks of bone[24].

The alignment of the fibrils is important to topography and important to the hierarchical structure. In, general the hierarchical structure of bone is composed of the following seven levels: 1.) major components (HA, Col I, water), 2.) mineralized collagen fibrils, 3.) fibril arrays, 4.) fibril array patterns, 5.) cylindrical motifs-osteons, 6.) spongy or compact bone, and 7.) whole bone (as depicted in Figure 1.2)[12]. Each of these levels is important to the various tissue functions mentioned earlier, from providing mechanical support for the body to providing space for production of platelets and other blood cells. In other words, bone structure and function are intimately related.

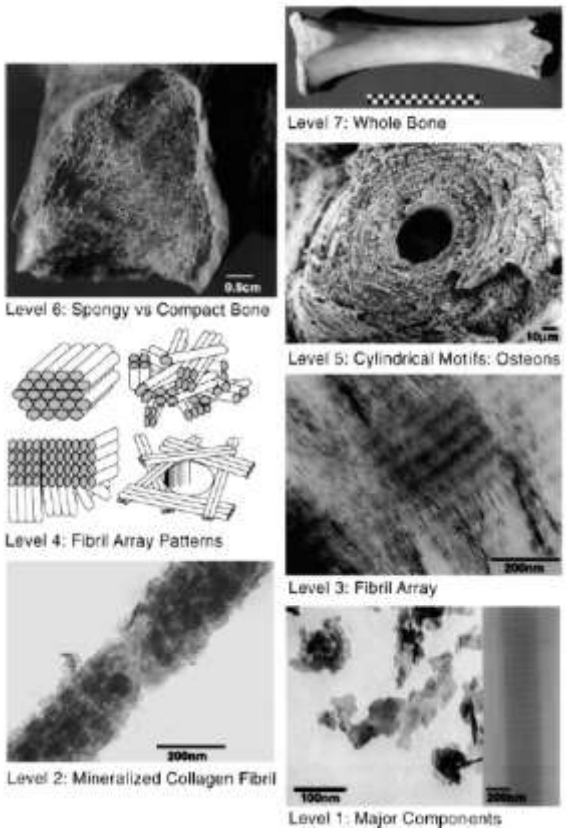

Figure 1.2. Bone has a hierarchial structure. Schematic illustrating the seven hierarchical structural levels of bone-ranging from the nanoscale components to macro level of whole bone[12].

1.4 Cellular aspects of bone and MSCs differentiation potential

All the processes described above (as well as bone resorption) are tightly regulated by cells embedded in the bone: osteoblasts, osteocytes, and osteoclasts[11,15,19,25,26]. Various biochemical, mechanical, cell-cell signals etc., are integrated by these cells to control the movement of calcium, phosphate, and other ions, as well as production of inhibitors (such as pyrophosphate) and nucleators of mineral formation into or out of the ECM[15,19]. Cell orientation and cell density vary depending on bone type. Osteocytes in woven bone are oriented in a seemingly random way but are oriented parallel to the highly aligned collagen fibrils in lamellar

bone. Another difference is the cell density; woven bone has higher cell density relative to lamellar bone[17]. As a result woven bone is rapidly deposited and rapidly turned over. Lamellar bone has a much slower rate of turnover. Thus, bone formation is continually changing and highly dynamic.

The cells that regulate this highly dynamic process evolved developmentally from pluripotent cells known as mesenchymal stem cells (MSCs). MSCs are characterized by their high self-renewal activity, multi-lineage differentiation potential, and anti-inflammatory characteristics making them ideal for cellular therapy and regenerative medicine applications[27,28]. MSCs can be isolated from bone marrow, adipose tissue, dental pulp, and elsewhere. Isolated MSCs can differentiate into fibroblasts, adipocytes, osteoblasts, chondrocytes, and skeletal muscle[29,30]. (Differentiation is the process of cell maturation from a progenitor to a fully functioning adult cell that that expresses specific markers and proteins and performs specific biochemical, structural, and biological functions[2].) Controlling and directing differentiation through various environmental cues is currently an of significant research interest.

MSCs are known to be influenced by environmental cues including biochemical and matrix signals. Biochemical cues can be autocrine, endocrine, or paracrine signals[22,28,31]. Matrix 'inputs' (cues) can include elasticity, topography, or surface chemistry (ligand identity and concentration). Typically, these matrix cues are coupled as cell adhesion to surfaces depends on ligand availability. Cell adhesion enables

probing of the surrounding matrix stiffness. All of these 'inputs' have been shown to influence cell behaviors such as proliferation, migration, and differentiation[32-37]. Specifically, when investigating MSC differentiation on surfaces of varied stiffness, surfaces that had the highest stiffness were the best promoters of osteogenesis[38]. Similarly, topography has been suggested to drive osteogenic differentiation[39]. Osteogenic differentiation is also driven by ligand identity and concentration[40]. Typically, these 'inputs' activate intracellular signalling pathways, including the MAPK cascade, which is a known driver of osteogenesis[33,41]. Collectively, manipulating these 'inputs' may allow for greater control of MSC differentiation.

1.5 Overarching hypothesis

Generally, we hypothesize that nanotopography and matrix stiffness will influence MSC behavior. We have detailed this general hypothesis in three parts as follows.

Part 1: **Model nanotopographic surfaces mimic an environment similar to that seen in native bone and will enhance osteogenic differentiation compared to smooth surfaces.**

Part 2: **We hypothesize that topography induces changes in protein adsorption in comparison to smooth surfaces; specifically, changes in protein**

identity, quantity, and conformation/structure underlie the observed changes in cellular behavior imparted by the topography.

Part 3: **Finally, we hypothesize that topography acts in a similar fashion to matrix compliance (potentially via activation of the MAPK cascade through involvement of RhoA and ROCK); suggesting a synergistic effect of topography and matrix compliance on osteogenesis.**

This hypothesis will be tested using two platforms for cell culture: 1. nanofilms of poly(methyl methacrylate) (PMMA) using a polymerization technique previously developed to produce films with nanotopography[42] and 2. poly(ethylene glycol diacrylate) (PEGDA), a material previously established to have tunable mechanical properties. Both of these materials are well-established biomaterials used clinically for various purposes[43-46].

1.6 Specific Aims

Specific Aim 1: Develop and characterize model nanotopographic surfaces that mimic the native architecture of bone. Characterization will verify the surface feature size and shape.

Specific Aim 2: Assess the impact of topographical cues on MSC osteogenic differentiation and cell phenotype using the model surfaces from

Aim 1. Potentially investigate changes in adsorbed protein identity, quantity, and conformation dependent on observed phenotypic changes.

Specific Aim 3: Investigate if nanotopography and matrix stiffness synergistically enhances osteogenic differentiation. Dependent on synergistic effects, determine if the biological mechanism is similar for matrix stiffness and nanotopography.

1.7 Translational Potential

Chronic disability in people over 50 years of age is strongly associated with disorders of the musculoskeletal system; osteoarthritis (OA) of the spine and diarthrodial joints (shoulder, hip, etc.) being the most common [31]. Current therapies, either pharmacological or biological, do not prevent the destruction of the OA joint and ultimately lead to total joint replacement (TJR). Medical expenses involving TJR (hip and knee replacement) were estimated to exceed $20 billion in 2003 and is expected to be more than $74 billion by 2015 [47]. This market continues to grow in part because of the increasing need for therapy in younger people. It is expected that patient age for TJR will skew younger. As of 2006, approximately 43% of patients under age 65 needed TJR, that number is projected to exceed 50% by 2030 [48]. Younger patients are at higher risk for revision surgery (due to implant failure,

loosening, instability, or infection) because of higher activity levels. Revision may be needed for other reasons such as stress shielding[2], meaning that the implant shields the stresses normally carried by healthy bone. Bone cells remodel bone dependent upon stress level, therefore, the perceived reduced stress load on healthy bone leads to subsequent bone resorption resulting in implant loosening[49]. Revisions are also necessary in tooth repair—between 5 and 18% of orthodontic implants require revision after 10 years[50]. Revisions in TJR or in dental applications are undesirable as they involve risk of infection, require time for recovery, and generate pain and discomfort.

Given that there will be a larger share of people needing TJR and revision surgery in the coming years, methods to improve and enhance implant effectiveness are needed. Currently, methods vary from scaffold based regeneration to surface roughness enhancements to improve tooth regeneration or increase bone-implant fixation[50,51]. Bone tissue engineering is a therapeutic target for improving implant lifetime in orthopedic and dental surgery; finding microenvironments that enhance growth and differentiation of MSCs into osteoblasts are potentially viable strategies[27]. Because an adequate supply of MSCs is needed for efficient bone regeneration, there remains a need for methods to control and enhance MSC proliferation[52]. Strategies that enhance osseointegration improve the mechanical stability of the implant leading to short and long term benefits. Short term, the patient will be able to rebound from surgery more quickly; long term the need for revision will be reduced. Addition of

topographic or biochemical cues to implants [53] to enhance MSC proliferation and drive osteogenic differentiation leading to *in situ* regeneration[54] of bone at the implant site may potentially improve long term implant viability and reduction of revision surgeries. These outcomes would improve the quality of life for a large number of people.

1.8 Overview

This dissertation is organized as follows. Chapter 2 is a review of the main concepts pertaining to this thesis, specifically a critical review of the topography literature and how it relates to cell behaviors such as migration, proliferation, and differentiation. The discussion includes possible mechanisms for enhanced differentiation, e.g. activation of the MAPK cascade. Also discussed is the relationship between these mechanisms and the influence matrix mechanics has on cell behavior. Relating topography and mechanics via a common mechanism is also detailed. Chapter 3 outlines a method to produce films with nanotopography. Characterization of the surface of these PMMA films using microscopy and surface energy techniques to analyze surface properties is also discussed. Chapter 4 elucidates the behavior of MSCs on the films produced in Chapter 4. Discussion of the importance of quantitative assessment of cell behaviors is highlighted focusing on the mineral quantity and quality. Chapter 5 describes methods to produce surfaces with varied

elasticity coupled with nanotopography to investigate the possible synergistic enhancement on osteogenic differentiation. Chapter 6 provides a summary of key findings and suggests potential future directions to further understand the role of topography and matrix stiffness on osteogenic differentiation. (The appendices describe work tangentially related to the main thesis subject matter.) Chapter 2 is to be published elsewhere (Wiley). Most of the material from Chapter 3 and 4 has been published (Public Library of Science). Material from Chapter 5 is to be published in the future. Appendix 1 has been published elsewhere (Liebert).

1.9 References

1 Schmidt-Bleek, K., Petersen, A., Dienelt, A., Schwarz, C. & Duda, G. N. Initiation and early control of tissue regeneration - bone healing as a model system for tissue regeneration. *Expert Opin Biol Th* **14**, 247-259, doi:Doi 10.1517/14712598.2014.857653 (2014).

2 Eisenbarth, E. Biomaterials for tissue engineering. *Adv Eng Mater* **9**, 1051-1060, doi:DOI 10.1002/adem.200700287 (2007).

3 Bell, E. Tissue Engineering - a Perspective. *J Cell Biochem* **45**, 239-241, doi:DOI 10.1002/jcb.240450302 (1991).

4 Fisher, M. B. & Mauck, R. L. Tissue Engineering and Regenerative Medicine: Recent Innovations and the Transition to Translation. *Tissue Eng Part B-Re* **19**, 1-13, doi:DOI 10.1089/ten.teb.2012.0723 (2013).

5 Langer, R. & Vacanti, J. P. Tissue Engineering. *Science* **260**, 920-926, doi:DOI 10.1126/science.8493529 (1993).

6 Kadiyala, S., Jaiswal, N. & Bruder, S. P. Culture-expanded, bone marrow-derived mesenchymal stem cells can regenerate a critical-sized segmental bone defect. *Tissue Eng* **3**, 173-185, doi:DOI 10.1089/ten.1997.3.173 (1997).

7 Zhang, Z. Y. *et al.* Neo-vascularization and bone formation mediated by fetal mesenchymal stem cell tissue-engineered bone grafts in critical-size femoral defects. *Biomaterials* **31**, 608-620, doi:DOI 10.1016/j.biomaterials.2009.09.078 (2010).

8 Glatt, V. *et al.* Improved Healing of Large Segmental Defects in the Rat Femur by Reverse Dynamization in the Presence of Bone Morphogenetic Protein-2. *J Bone Joint Surg Am* **94A**, 2063-2073, doi:Doi 10.2106/Jbjs.K.01604 (2012).

9 Dimitriou, R., Mataliotakis, G. I., Calori, G. M. & Giannoudis, P. V. The role of barrier membranes for guided bone regeneration and restoration of large bone defects: current experimental and clinical evidence. *Bmc Med* **10**, doi:Artn 81 Doi 10.1186/1741-7015-10-81 (2012).

10 Gugala, Z., Lindsey, R. W. & Gogolewski, S. New approaches in the treatment of critical-size segmental defects in long bones. *Macromol Symp* **253**, 147-161, doi:DOI 10.1002/masy.200750722 (2007).

11 Kerschnitzki, M. *et al.* The organization of the osteocyte network mirrors the extracellular matrix orientation in bone. *J Struct Biol* **173**, 303-311, doi:DOI 10.1016/j.jsb.2010.11.014 (2011).

12 Weiner, S. & Wagner, H. D. The material bone: Structure mechanical function relations. *Annual Review of Materials Science* **28**, 271-298, doi:DOI 10.1146/annurev.matsci.28.1.271 (1998).

13 Weiner, S., Traub, W. & Wagner, H. D. Lamellar bone: Structure-function relations. *J Struct Biol* **126**, 241-255, doi:DOI 10.1006/jsbi.1999.4107 (1999).

14 Ueda, Y., Kondo, M. & Kelsoe, G. Inflammation and the reciprocal production of granulocytes and lymphocytes in bone marrow. *J Exp Med* **201**, 1771-1780, doi:Doi 10.1084/Jem.20041419 (2005).

15 Allori, A. C., Sailon, A. M. & Warren, S. M. Biological basis of bone formation, remodeling, and repair - Part II: Extracellular matrix. *Tissue Eng Part B-Re* **14**, 275-283, doi:DOI 10.1089/ten.teb.2008.0083 (2008).

16 Travlos, G. S. Normal structure, function, and histology of the bone marrow. *Toxicol Pathol* **34**, 548-565, doi:Doi 10.1080/01926230600939856 (2006).

17 Buckwalter, J. A., Glimcher, M. J., Cooper, R. R. & Recker, R. Bone biology .1. Structure, blood supply, cells, matrix, and mineralization. *Aaos Instr Cours Lec* **45**, 371-386 (1996).

18 Evans, C. H. Advances in Regenerative Orthopedics. *Mayo Clin Proc* **88**, 1323-1339, doi:DOI 10.1016/j.mayocp.2013.04.027 (2013).

19 Kini, U. & Nandeesh, B. N. Physiology of Bone Formation, Remodeling, and Metabolism. 29-57, doi:10.1007/978-3-642-02400-9_2 (2012).

20 Maes, C. *et al.* Osteoblast Precursors, but Not Mature Osteoblasts, Move into Developing and Fractured Bones along with Invading Blood Vessels. *Dev Cell* **19**, 329-344, doi:DOI 10.1016/j.devcel.2010.07.010 (2010).

21 Lane, J. M., Suda, M., Vondermark, K. & Timpl, R. Immunofluorescent Localization of Structural Collagen Types in Endochondral Fracture Repair. *J Orthopaed Res* **4**, 318-329, doi:DOI 10.1002/jor.1100040308 (1986).

22 Allori, A. C., Sailon, A. M. & Warren, S. M. Biological basis of bone formation, remodeling, and repair - Part I: Biochemical signaling molecules. *Tissue Eng Part B-Re* **14**, 259-273, doi:DOI 10.1089/ten.teb.2008.0082 (2008).

23 Murshed, M., Harmey, D., Millan, J. L., McKee, M. D. & Karsenty, G. Unique coexpression in osteoblasts of broadly expressed genes accounts for the spatial restriction of ECM mineralization to bone. *Gene Dev* **19**, 1093-1104, doi:Doi 10.1101/Gad.1276205 (2005).

24 Landis, W. J., Song, M. J., Leith, A., Mcewen, L. & Mcewen, B. F. Mineral and Organic Matrix Interaction in Normally Calcifying Tendon Visualized in 3 Dimensions by High-Voltage Electron-Microscopic Tomography and Graphic Image-Reconstruction. *J Struct Biol* **110**, 39-54, doi:DOI 10.1006/jsbi.1993.1003 (1993).

25 Bueno, E. M. & Glowacki, J. Cell-free and cell-based approaches for bone regeneration. *Nat Rev Rheumatol* **5**, 685-697, doi:DOI 10.1038/nrrheum.2009.228 (2009).

26 Marquis, M. E. *et al.* Bone cells-biomaterials interactions. *Front Biosci-Landmrk* **14**, 1023-1067, doi:Doi 10.2741/3293 (2009).

27 Chatakun, P. *et al.* The effect of five proteins on stem cells used for osteoblast differentiation and proliferation: a current review of the literature. *Cell Mol Life Sci* **71**, 113-142, doi:DOI 10.1007/s00018-013-1326-0 (2014).

28 Murphy, M. B., Moncivais, K. & Caplan, A. I. Mesenchymal stem cells: environmentally responsive therapeutics for regenerative medicine. *Exp Mol Med* **45**, doi:ARTN e54DOI 10.1038/emm.2013.94 (2013).

29 Caplan, A. I. What's in a Name? *Tissue Eng Pt A* **16**, 2415-2417, doi:DOI 10.1089/ten.tea.2010.0216 (2010).

30 Prockop, D. J. Marrow stromal cells as steam cells for nonhematopoietic tissues. *Science* **276**, 71-74, doi:DOI 10.1126/science.276.5309.71 (1997).

31 Barry, F. & Murphy, M. Mesenchymal stem cells in joint disease and repair. *Nat Rev Rheumatol* **9**, 584-594, doi:DOI 10.1038/nrrheum.2013.109 (2013).

32 Doyle, A. D., Wang, F. W., Matsumoto, K. & Yamada, K. M. One-dimensional topography underlies three-dimensional fibrillar cell migration. *J Cell Biol* **184**, 481-490, doi:DOI 10.1083/jcb.200810041 (2009).

33 Khatiwala, C. B., Peyton, S. R., Metzke, M. & Putnam, A. J. The regulation of osteogenesis by ECM rigidity in MC3T3-E1 cells requires MAPK activation. *J Cell Physiol* **211**, 661-672, doi:Doi 10.1002/Jcp.20974 (2007).

34 Lim, J. Y. *et al.* The regulation of integrin-mediated osteoblast focal adhesion and focal adhesion kinase expression by nanoscale topography. *Biomaterials* **28**, 1787-1797, doi:DOI 10.1016/j.biomaterials.2006.12.020 (2007).

35 Wood, J. A. *et al.* The modulation of canine mesenchymal stem cells by nano-topographic cues. *Exp Cell Res* **318**, 2438-2445, doi:DOI 10.1016/j.yexcr.2012.06.022 (2012).

36 Khatiwala, C. B., Peyton, S. R. & Putnam, A. J. Intrinsic mechanical properties of the extracellular matrix affect the behavior of pre-osteoblastic MC3T3-E1 cells. *Am J Physiol-Cell Ph* **290**, C1640-C1650, doi:DOI 10.1152/ajpcell.00455.2005 (2006).

37 Kim, J. *et al.* Designing nanotopographical density of extracellular matrix for controlled morphology and function of human mesenchymal stem cells. *Sci Rep-Uk* **3**, doi:Artn 3552 Doi 10.1038/Srep03552 (2013).

38 Engler, A. J., Sen, S., Sweeney, H. L. & Discher, D. E. Matrix elasticity directs stem cell lineage specification. *Cell* **126**, 677-689, doi:DOI 10.1016/j.cell.2006.06.044 (2006).

39 Dalby, M. J. *et al.* The control of human mesenchymal cell differentiation using nanoscale symmetry and disorder. *Nat Mater* **6**, 997-1003, doi:Doi 10.1038/Nmat2013 (2007).

40 Kundu, A. K. & Putnam, A. J. Vitronectin and collagen I differentially regulate osteogenesis in mesenchymal stem cells. *Biochem Bioph Res Co* **347**, 347-357, doi:DOI 10.1016/j.bbrc.2006.06.110 (2006).

41 Khatiwala, C. B., Kim, P. D., Peyton, S. R. & Putnam, A. J. ECM Compliance Regulates Osteogenesis by Influencing MAPK Signaling Downstream of RhoA and ROCK. *J Bone Miner Res* **24**, 886-898, doi:Doi 10.1359/Jbmr.081240 (2009).

42 Suh, K. Y., Park, M. C. & Kim, P. Capillary Force Lithography: A Versatile Tool for Structured Biomaterials Interface Towards Cell and Tissue Engineering. *Advanced Functional Materials* **19**, 2699-2712, doi:DOI 10.1002/adfm.200900771 (2009).

43 Lewis, G. Viscoelastic properties of injectable bone cements for orthopaedic applications: State-of-the-art review. *J Biomed Mater Res B* **98B**, 171-191, doi:Doi 10.1002/Jbm.B.31835 (2011).

44 Jaberi, J., Gambrell, K., Tiwana, P., Madden, C. & Finn, R. Long-Term Clinical Outcome Analysis of Poly-Methyl-Methacrylate Cranioplasty for Large Skull Defects. *J Oral Maxil Surg* **71**, E81-E88, doi:DOI 10.1016/j.joms.2012.09.023 (2013).

45 Pasut, G. & Veronese, F. M. PEG conjugates in clinical development or use as anticancer agents: An overview. *Adv Drug Deliver Rev* **61**, 1177-1188, doi:DOI 10.1016/j.addr.2009.02.010 (2009).

46 Ghosh, K. *et al.* Cell adaptation to a physiologically relevant ECM mimic with different viscoelastic properties. *Biomaterials* **28**, 671-679, doi:DOI 10.1016/j.biomaterials.2006.09.038 (2007).

47 Velikonja, N., Stres, H., et al. in *Autologous Cell Therapies for Bone Tissue Regeneration* (ed H. Tal) 1-352 (InTech, Croatia, 2012).

48 Kurtz, S. M. *et al.* Future Young Patient Demand for Primary and Revision Joint Replacement: National Projections from 2010 to 2030. *Clin Orthop Relat R* **467**, 2606-2612, doi:DOI 10.1007/s11999-009-0834-6 (2009).

49 Ong, K. L., Day, J. S., Kurtz, S. M., Field, R. E. & Manley, M. T. Role of Surgical Position on Interface Stress and Initial Bone Remodeling Stimulus around Hip Resurfacing Arthroplasty. *J Arthroplasty* **24**, 1137-1142, doi:DOI 10.1016/j.arth.2008.08.005 (2009).

50 Hacking, S. A. & Khademhosseini, A. Applications of Microscale Technologies for Regenerative Dentistry. *J Dent Res* **88**, 409-421, doi:Doi 10.1177/0022034509334774 (2009).

51 Prodanov, L. *et al.* The effect of nanometric surface texture on bone contact to titanium implants in rabbit tibia. *Biomaterials* **34**, 2920-2927, doi:DOI 10.1016/j.biomaterials.2013.01.027 (2013).

52 Dimitriou, R., Jones, E., McGonagle, D. & Giannoudis, P. V. Bone regeneration: current concepts and future directions. *Bmc Med* **9**, doi:Artn 66 Doi 10.1186/1741-7015-9-66 (2011).

53 Bruinink, A. *et al.* Addition of nanoscaled bioinspired surface features: A revolution for bone-related implants and scaffolds? *J Biomed Mater Res A* **102**, 275-294, doi:Doi 10.1002/Jbm.A.34691 (2014).

54 Ko, I. K., Lee, S. J., Atala, A. & Yoo, J. J. In situ tissue regeneration through host stem cell recruitment. *Exp Mol Med* **45**, doi:ARTN e57 DOI 10.1038/emm.2013.118 (2013).

CHAPTER 2

Extracellular matrix elasticity and topography: material-based cues that affect cell function via similar mechanisms

2.1 Introduction

Adhesion to the extracellular matrix (ECM) is critical for cell differentiation, function, and tissue organization[1,2]. The primary mode of cell adhesion to the ECM is through integrins. Integrins associate with ECM proteins such as laminin, collagen, fibronectin (and others). When integrins and other structural components cluster together, a focal adhesion complex is formed. As this focal complex grows it matures into a focal adhesion (FA). Focal adhesions transform both chemical and mechanical information provided via the ECM into intracellular biochemical signals, which in turn alter cell migration, proliferation and differentiation[3].

The composition of the ECM not only dictates initial cell adhesive events but also influences cells' ability to manipulate adhesion sites. Cells manipulate the initial adhesion surface either through secretion of new ECM components[4], or through manipulation of the 'native' ECM[5] or serum proteins[6]. This manipulation may involve

cellular contractility that exposes otherwise hidden peptide sequences (indicating a dynamic adhesion environment)[7]. The simplest adhesion motif available to a cell is an amino acid sequence of arginine, glycine, and aspartic acid (RGD). The RGD sequence was first identified in fibronectin[8], but is also present in vitronectin, osteopontin, and laminin[9,10],and has been extensively used throughout the biomaterials literature to functionalize materials and facilitate cell adhesion. Other peptide sequences capable of mediating or influencing cell adhesion have also been identified in other ECM proteins, including GFOGER and DGEA from collagen[9,11], KQAGDV, REDV, and PHSRN from fibronectin[12], and YIGSR, IKVAV, and LRE from laminin[11,12], and are used to promote cell adhesion to materials. Functionalizing materials with short peptides provides a facile and relatively well-controlled means to dictate cell adhesion[13],but it is clear that such short peptide sequences do not completely recapitulate the biological activity of full length ECM proteins[14].

In addition to its chemical composition, the ECM's mechanical properties are also important regulators of cell behavior. The most often characterized and reported mechanical influence is the ECM's elasticity, best defined as the material's ability to undergo non-permanent deformation. 'Soft' materials are easily deformed at low stresses, whereas 'hard' materials require greater stresses to produce the same amount of deformation (strain)[15]. Matrix elasticity has been shown to influence cell migration, differentiation, gene expression[16-18], as well as FA and stress fiber assembly, cell

spreading, and adhesive forces[19]. A cell dynamically probes the elasticity of the ECM through the use of different integrins[20]. Matrix elasticity is known to influence a specific signaling pathway involving RhoA, mitogen activated protein kinase (MAPK), and extracellular signal-regulated kinase (ERK) and will be discussed in greater detail below[21].

In addition to stimulating cells mechanically, the ECM provides topographic stimuli. Hierarchical topographical structures provide guidance cues to resident cells in native tissues like myocardium and bone[22-25]. *In vitro* topographic cues (i.e., surfaces with features that include micro- and nano-scale ridges, gratings, holes, pillars etc.) have been shown to alter cell behavior in comparison to smooth surfaces[22,26-30]. Some of these surfaces mimic the native structure of various tissues[22,29]. Other surfaces probe the interactions of cells on topography to understand the role topography may play in altering cell behavior[27,29,30]. These surfaces provide an idealized template for answering fundamental questions regarding the signaling cascades and mechanism(s) that lead to altered cell behavior. The mechanism(s) that influence cell behavior on topography are generally poorly understood[25], compared to those for matrix elasticity; nonetheless, recent findings suggest that common mechanism(s) may link these two parameters.

2.2 Matrix elasticity and cellular behavior

A variety of material platforms and methods have been used to explore the influence of ECM elasticity on cell function. Most widely used include polymers such as poly(dimethylsiloxane) (PDMS) , poly (urethane acrylate) (PUA) , and hydrogels made from polyacrylamide (PAA) or poly (ethylene glycol) (PEG)[16,17,31-34].To alter elasticity in these materials, the amount of polymer, cross-linker, and in some cases the amount of photoinitiator, can be varied to produce substrates of desired elastic properties.

Cell adhesion and spreading were amongst the first cell functions shown to be influenced by ECM elasticity. Cells anchor to the surface via adhesion complexes composed of clustered integrins.[35] These complexes can trigger a cell response that depends on both the identity of the anchor site and the forces generated influencing spreading[36]. Smooth muscle cell (SMC) spreading has also been shown to increase quantitatively with substrate elasticity.[16,37]. The magnitude of spreading was also strongly dependent on ECM ligand density (fibronectin) for SMCs cultured on soft substrates (polyacrylamide)[16]. However, varying fibronectin density by an order of magnitude on a rigid control substrate (polystyrene) had no effect on SMC spreading, suggesting that matrix elasticity may override ligand density after some threshold is surpassed. Similar findings were reported for endothelial cells grown on substrates of varied elasticity[38]. Substrate elasticity strongly influenced cell adhesion (and subsequent differentiation) of neural stem cells[39]. By contrast, the spreading area of a

pre-osteoblastic cell line (MC3T3-E1) has been shown to be insensitive to changes in matrix elasticity for two different ligand densities (type I collagen)[40]. These results suggest that cell spreading's dependence on substrate elasticity surfaces varies with both cell type and ligand identity.

The ability of a cell to sense matrix elasticity is related to myosin-dependent effects on the actin cytoskeleton and focal adhesions[15,18,41]. Myosin-mediated maturation involves changes in adhesion composition that alter the structural properties of adhesions[15]. Focal adhesion composition in SMCs changed with increasing substrate elasticity as qualitative and quantitative increases in vinculin were reported[16]. A similar increase in vinculin expression was also observed in preosteoblasts[40]. The observed increase in vinculin did not depend on ligand density, indicating that matrix mechanics alters the recruitment of focal adhesion proteins. Being that focal adhesions are involved in cell migration it is not surprising that cell migration speed is also dependent on matrix elasticity[16,40]. Cell migration speeds were attenuated to speeds observed on soft substrates when RhoA, a critical mechanosensitive switch, was inhibited[16]. These results indicate that RhoA and other cytoskeletal machinery are involved in the cellular response to substrates of varied elasticity.

A recent study has also shown that matrix elasticity plays a role in matrix reorganization[6]. Specifically, human mesenchymal stem cells (MSCs) grown on

polyacrylamide substrates of varied stiffness covalently tethered with fibronectin or collagen were able to unfold plasma fibronectin to a greater extent on stiffer substrates after 24 hours. Unfolding of fibronectin, however, was not observed on PDMS surfaces (though the stiffest PDMS surfaces were ~7x stiffer than the stiffest polyacrylamide surfaces). These findings were attributed to the differences in material architecture: polyacrylamide has pores on the nanoscale that are absent in PDMS. Thus, the stiffness of the underlying substrate is not the only factor driving increased fibronectin unfolding; a substrate must have the architecture and stiffness to support the cell-generated forces that lead to unfolding. The degree of unfolding and magnitude of strain of single fibronectin fibers influenced MSC differentiation (Figure 2.1). Enhanced osteogenic differentiation resulted (assessed by alkaline phosphatase (ALP) staining) in pure osteogenic differentiation media or in mixtures of adipogenic and osteogenic differentiation media when greater strain of fibronectin occurred. The mechanism for differentiation was attributed to the adhesion integrins $\alpha_v\beta_3$. These adhesion integrins showed different susceptibility to fibronectin stretch ($\alpha_v\beta_3$ signaled preferentially over $\alpha_5\beta_1$ on relaxed fibers) suggesting that conformational change may regulate osteogenesis. These findings suggest that early events regarding matrix elasticity, matrix architecture, adhesion, and ECM remodeling are crucial to mechanotransduction and differentiation (Figure 2.2).

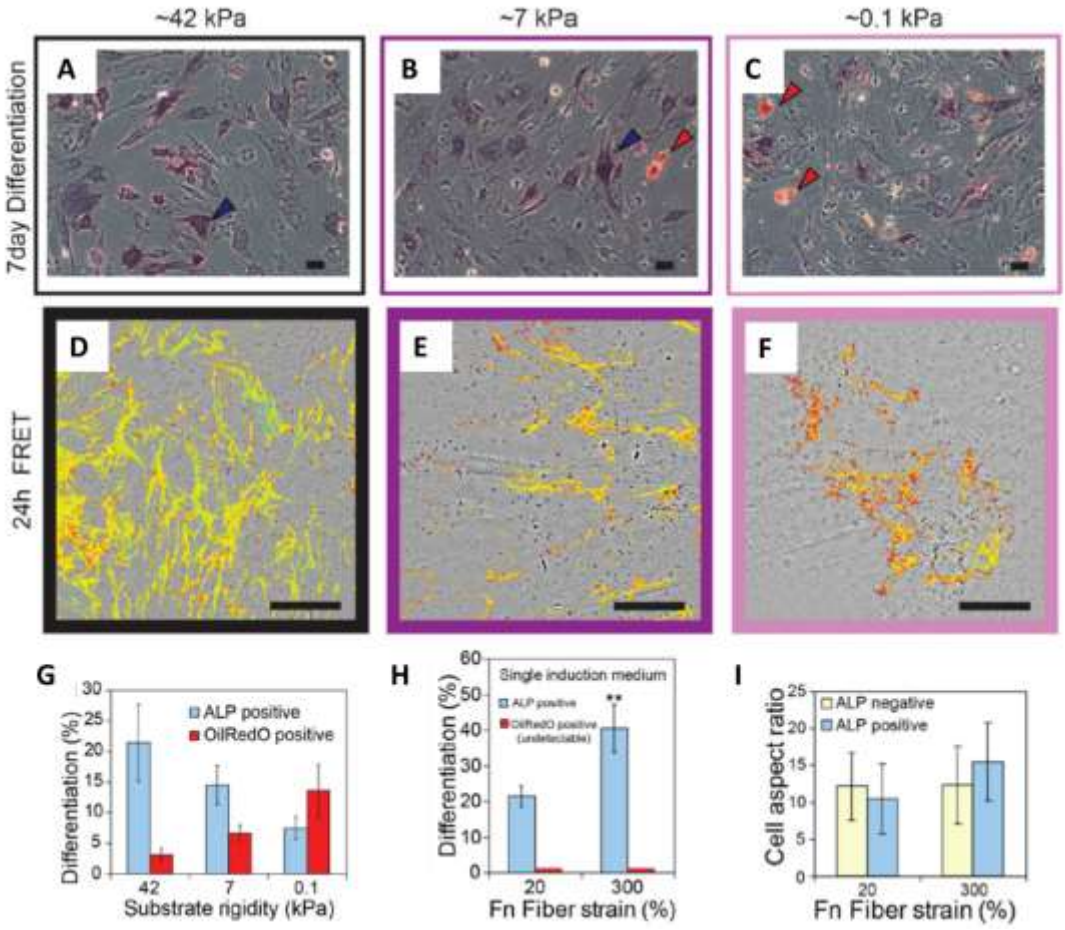

Figure 2.1 Substrate elasticity influences cell protein unfolding. A-C.) Brightfield micrographs of hMSCs cultured on fibronectin functionalized polyacrylamide gels of varying stiffness after 7 day differentiation in mixed (osteogenic and adipogenic) induction medium supplemented with trace amounts of FRET (Förster resonance energy transfer) fibronectin stained for alkaline phosphatase (ALP) (blue arrows) and Oil Red O (red arrows). Scale bars = 50 μm. D-F.) Ratiometric FRET-fibronectin I_A/I_D (acceptor intensity/donor intensity) ratios of hMSC assembled fibronectin ECM on fibronectin functionalized polyacrylamide gels of varying stiffness after 24 hours in mixed media (false colored). The false color scheme represents the relative stretching of fibronectin fibrils with red indicating folded and blue indicating complete unfolded fibronectin (yellow indicating partial unfolding). Scale bars = 50 μm. G.) Differentiation percentage of hMSCs (mean ± s.d.) after 7 days in mixed media on varied stiffness gels as determined by Oil Red O and ALP positive cells. H.) Differentiation percentage of hMSCs (mean ± s.d.) after 7 days in single induction media on single fibronectin fibers with varied strains as determined by Oil Red O and ALP positive cells. I.) Aspect ratio of ALP positive (blue) and ALP negative (yellow) hMSCs (mean ± s.d.) on single strained fibronectin fibers[6].

MSC differentiation has been shown to be dependent on matrix elasticity and ECM identity. On matrices mimicking elasticity of brain, MSCs showed characteristics of neuronal cells. On matrices that mimicked the elasticity of striated muscle, MSCs had similar shape to myoblasts. Stiffest substrates yielded cells similar to osteoblasts[18]. Surfaces with the increasing matrix elasticity were shown to modulate a key regulator of mechanotransduction- focal adhesion kinase (FAK)[41]. FAK[18] and phosphorylated FAK (pFAK)[38,40] levels were observed to increase with increasing matrix elasticity in MSCs[18] and ECs[38] and preosteoblasts[40] respectively. MSC osteogenic differentiation was shown to depend on FAK when grown on collagen I. FAK independence was observed for cells grown on vitronectin and fibronectin[42]. These reports suggest that mechanotransduction is dependent on both matrix elasticity and ECM protein identity.

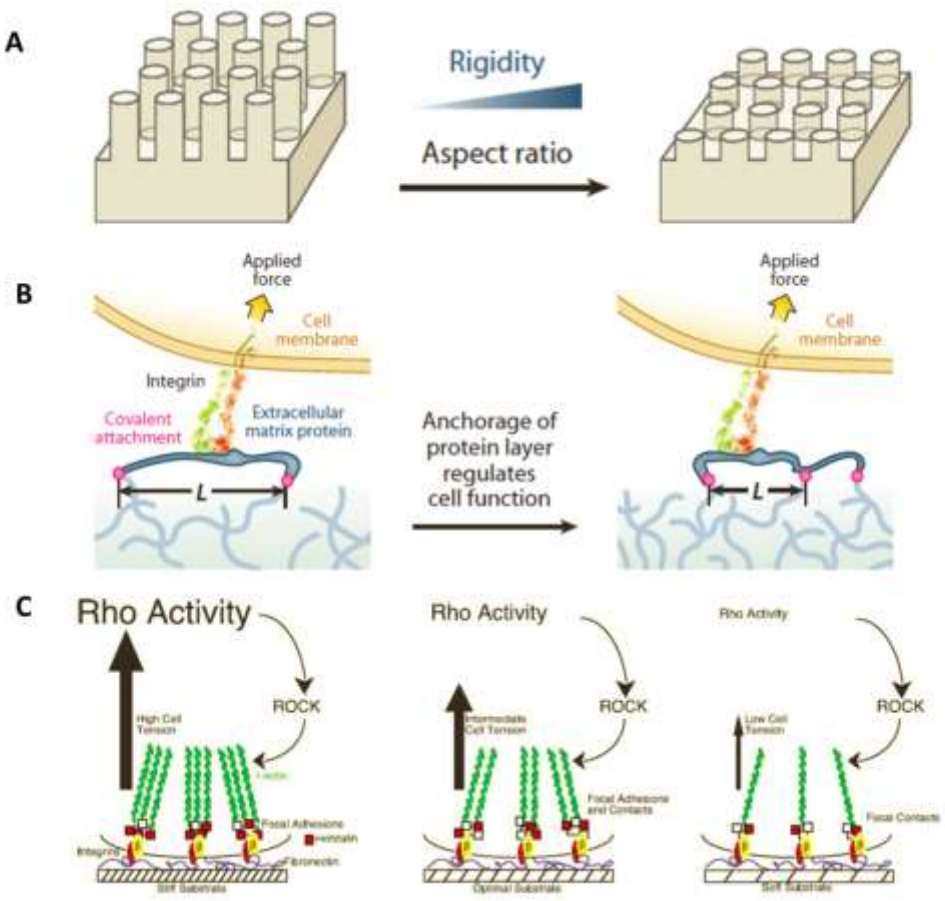

Figure 2.2 Substrate elasticity alters cell behavior. A.) Schematic illustrating that rigidity of posts (PDMS or other material) can be altered by changing their aspect ratio. B.) The rigidity of gels is oftentimes altered by varying the cross-linking density; this can also alter the architecture of the polymer network. Cells adhere to their underlying surface, either to adsorbed or covalently attached extracellular matrix (ECM) proteins via receptors known as integrins. Integrins are part of focal adhesions which can transduce mechanical inputs to cells[41]. C.) A schematic for a proposed model by which ECM elasticity regulates smooth muscle cell (SMC) migration: cells cultured on rigid substrates likely possess high RhoA activity, which promotes the formation of robust actin stress fibers and focal adhesions via ROCK. Very stiff surfaces promote cells with too much isometric tension which can inhibit migration. Cells on soft substrates have low RhoA activity which prevents maturation of focal adhesions and inhibits cell migration. Optimally stiff surfaces promote adhesion formation at the cell's leading edge and adhesion turnover at the trailing edge, supporting maximal migration[16].

Matrix elasticity and ECM protein identity activate FAK, which triggers downstream signaling of the mitogen-activated protein kinase (MAPK) cascade. The MAPK cascade conveys information about the extracellular environment to the cell nucleus and plays a role in skeletal development[21]. Evidence suggests that MAPK levels are dependent on matrix stiffness and is involved in regulation of osteogenesis as increases in ALP expression were observed to be dependent on matrix elasticity in mouse pre-osteoblasts[17]. Changes in substrate elasticity altered the RhoA-ROCK pathway inducing changes in the MAPK cascade[21]. The RhoA-Rho-kinase (ROCK) pathway was shown to influence the transcription factor RUNX2, important for osteoblast differentiation and bone formation, in a matrix elasticity dependent manner. Rho and ROCK are known to be important to the actin cytoskeleton network. Disruption of the actin network inhibits osteogenic differentitation and favors adipogenic differentiation. Furthermore, increased adipogenic differentiation potential is associated with RhoA and ROCK inhibition[28,43]. RhoA and ROCK have also been shown to play a role in chondrogenic differentation[44]. Collectively, these findings suggest that activation of the MAPK cascade via matrix mechanics can help drive osteogenic differentiation in certain cell types. Factors that promote osteogenic differentiation, include the type of substrate, amount and type of ligand, and matrix elasticity. Ultimately, these factors promote adhesion through integrins known to transduce mechanical signals in an osteospecific way.

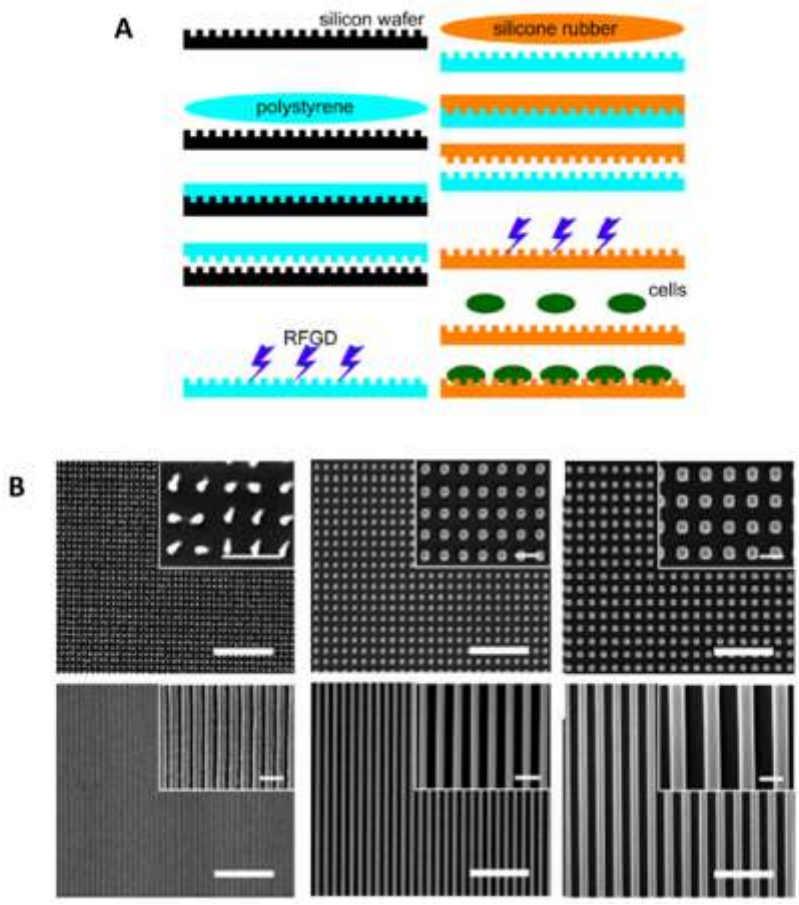

Figure 2.3 Various methods and nanopatterns for cell culture. A.) Illustration depicting methods to produce nanotopograhic surfaces of poly(dimethylsiloxane) PDMS from a polystyrene mold (created from a silicon master). Cells can then be seeded on these surfaces for experimentation[45]. B.) Scanning electron microscopy (SEM) micrographs of poly(urethane acrylate) (PUA) nanopatterns fabricated by UV-assisted capillary force lithography. Sizes range from 150 nm to 600 nm. Scale bar 5 μm and 1 μm (inset)[29].

2.3 Topography and cellular behavior

This section includes discussion regarding both physical topographical features (lines, gratings, holes, pillars, etc.) and 'tracks' or 'islands' of printed or adsorbed ECM

proteins, what we call 'chemical topography'. In some cases, both methods are coupled to investigate cell behavior.

Producing surfaces with defined topographical features can be achieved by a number of methods that are detailed elsewhere[46-49]. Here we briefly mention some of them. Techniques, including nanoimprint lithography[49], capillary force lithography[47], ultraviolet assisted lithography[48], embossing, photolithography, and micromachining[46] are typically used for polymeric substrates (Figure 2.3). Deep reactive ion-etching, acid etching, photolithography, sandblasting, and mechanical machining are some of the methods used to impart topography or enhance roughness on ceramic, semi-conductive, and metallic substrate surfaces[46]. These methods can produce micro or nano –sized features. Other methods such as self-assembled monolayers (SAMs) and micro-contact printing (μCP) direct or impart various proteins to defined areas on a substrate surface[50,51]. These can be coupled with topographic surfaces to have distinct control of surface features and adhesion islands[26].

Cell migration and shape has been shown to be modulated by topography[52,53]. Cell migration on micron-sized 'chemical' topography was investigated using multiple cell types seeded in 3-D matrices, on 2-D surfaces, and on '1-D' lines (1 to 10 micron width)[53]. The lines were coated with various ECM proteins (fibrinogen, vitronectin, and fibronectin). Fibroblasts adhered and spread on 1-D lines similar to spreading' behavior in 3-D matrices. Knockdown of the small GTPase Rac in 2D cells produced

an elongated cell morphology similar to cell morphology seen in 1-D. An elongated phenotype by itself is insufficient to promote rapid migration as migration speeds of Rac knockdown cells did not increase and vinculin staining of the Rac knockdown cells showed that adhesions on the 2D ECM proteins remained spatially separated. Thus, spatial distribution of cell adhesions and consequently cell migration is affected by ECM topography.

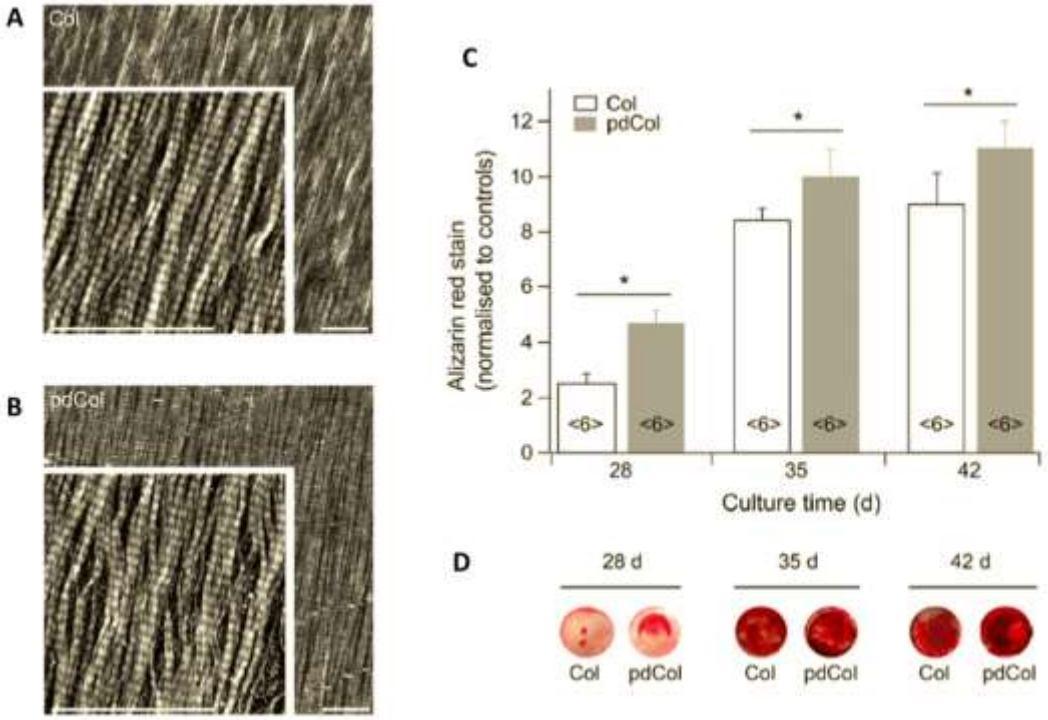

Figure 2.4 Protein conformation alters mineralization. A-B.) AFM micrographs of native (A) and partially-denatured (B) collagen I matrices. Scale =1 μm. C-D.) Alzarin red staining of mouse calvarial pre-osteoblasts deposited mineral after 28, 35, 42 days compared to controls (images, D). Cells cultured on partially denatured collagen deposited more calcium than cells on native collagen (C)[54].

Cell adhesion, as described previously, is critical to downstream cell behavior. Topographic surfaces present either physical features or areas of confined ECM proteins (chemical topography) that cells must navigate. One of the early studies investigating the role of nanotopography on adhesion found diminished adhesion on ordered arrays of pits or pillars[55]. Nanorough titanium enhanced adhesion of mouse MSCs compared to other surfaces after four hours. After 6 hours, hMSC adhesion was enhanced on titanium surfaces with roughness imparted by 150 and 450 nm features compared to 20 nm features[56]. Nanorough titanium had no modulatory effect on cell adhesion after one day for osteoblasts[57]; these reports indicate that cell type is an important factor when discussing the impact of topography.

Depending on the surface features and available ECM proteins, integrin expression and focal adhesion size is altered on various surface sizes and shapes[56,58, 59]. A critical focal adhesion size threshold of fibroblasts was investigated on 'nanoislands' of fibronectin (FN) showing that integrin clustering and adhesive force were influenced by ECM area[19]. Stable integrin-FN clusters did not form below an area threshold of 0.11 μm^2. In this study, the cell was confined to 10 μm in all cases, effectively decoupling the effect of cell spreading and integrin-FN cluster formation. Altering the size of the confined area could possibly alter the findings, though this was not investigated. Similar feature size inhibition was reported with human fibronectin coated nanopits in poly(lactic acid) (PLA)/ poly(styrene) (PS) demixed films.

Preosteoblasts reorganized adsorbed fibronectin on 29 nm and 45 nm pit surfaces but were unable to modify the matrix on pits 14 nm in size[35]. Interestingly, fibronectin stretch, exposes cryptic sites, yet diminishes affinity for cell binding sites[41], though it is unclear if fibronectin stretch had any impact on the preosteoblasts. The cells were, however, unable to form focal plaques large enough to generate enough force to reorganize the matrix[35]. Fibronectin adsorbed in greater quantities on the 14 nm surface and may have contributed to the results. A greater quantity of fibronectin implies a greater concentration of RGDs for cell adhesion. Thus, the limited area for integrin clustering likely prevented subsequent focal adhesion formation and matrix reorganization.

The type of adhesion motif available on surfaces is important for cell behavior as well. Preosteoblasts grown on denatured collagen are claimed to have enhanced osteogenic differentiation compared to native collagen (Figure 2.4)[54]. The adhesion to denatured collagen may be a result of exposure of cryptic binding sites for fibronectin[60]. Cells can bind to fibronectin via RGD sequences or the PHSRN binding site via the $\alpha_5\beta_1$ integrin[6]. Adhesion to collagen I typically, occurs in an RGD independent mechanism[54]. Further supporting the importance of adhesion motif was a study showing that vitronectin and collagen I support MSC osteogenesis through unique integrin-mediated signaling mechanisms[61]. Fibronectin coated PEG gels with nanotopography were suggested to have increased neonatal rat ventricular myocytes

(NRVM) adhesion though no explicit quantitative test confirmed this conjecture (Figure 2.5); this was inferred from cell penetration into nanogratings and lower longitudinal conduction velocity on the smallest nanogratings[22]. Differences in cell behavior results can be attributed to different surface chemistry, surface topographical features (size and shape), identity of matrix protein, and cell type.

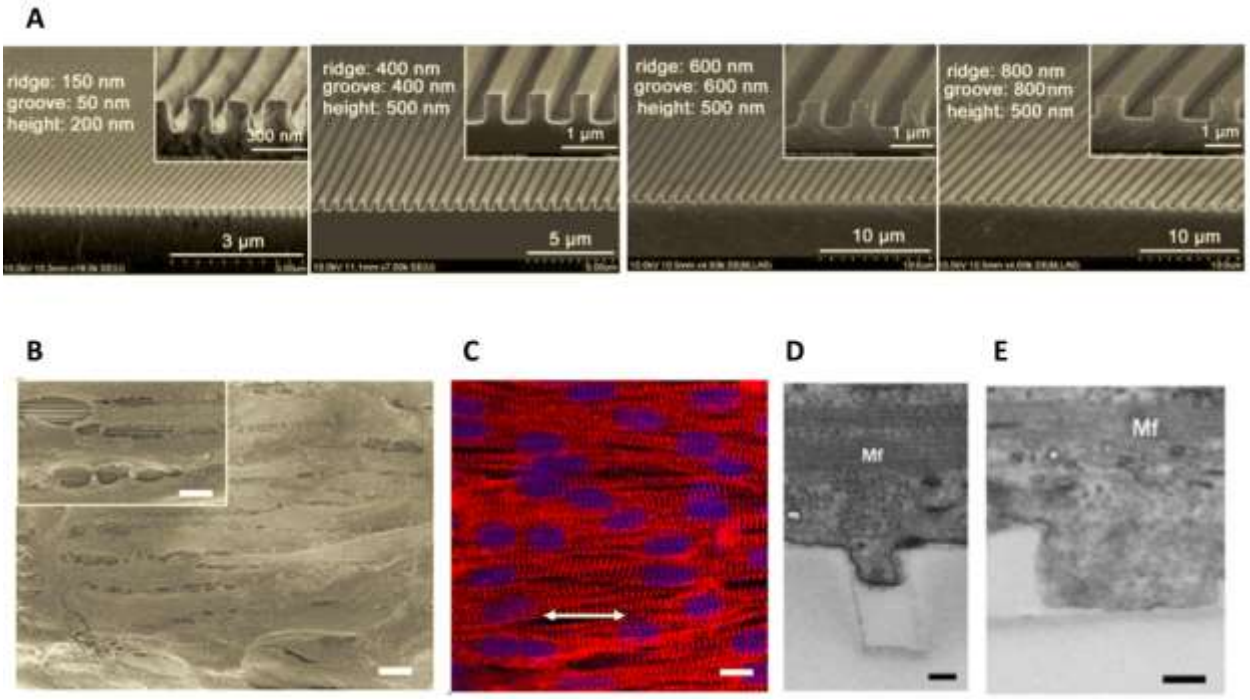

Figure 2.5 Nanotopography influences alignment of myocytes. A.) SEM micrographs of poly (ethylene glycol) (PEG) gels with nanotopgraphy ranging from 50 to 800 nm in size[22]. B). SEM image of neonatal rat ventricular myocytes (NRVM) grown on fibronectin coated PEG nanotopographic gels aligned with the underlying topography. Inset shows transverse intercellular connections (scale = 5 µm). C.) Immunofluorescent image of sarcomeric α-actinin (red) and nuclei (blue) observed in NRVMs grown on PEG nanotopography (scale =10 µm). D and E.) SEM micrographs illustrate that cells penetrate into nanometer grooves; 'Mf' depicts myofilaments (scale = 200 nm).

Topography, in addition to altering adhesion, can influence cell alignment. Recently, both physical and chemical topographic methods were employed to investigate pre-osteoblast alignment using a polymeric base surface coated with titanium and gold with micron sized gratings. μCP was utilized to imprint fibronectin lanes either parallel or perpendicular to the underlying physical surface. In spite of a perpendicular ECM cue, cells showed preferential alignment to the underlying physical topography (Figure 2.6)[26]. NRVMs, grown on fibronectin coated nanogratings, aligned parallel to the topography[22]. Alignment of hMSCs to the underlying nanotopography of both (collagen coated) PDMS and (uncoated) tissue culture polystyrene (TCPS) has been reported[58]. Similarly, rat bone marrow MSCs grown on PDMS substrates with nano and micro-sized feature also aligned parallel to the underlying gratings[45]. However, when these cells were mechanically loaded, cells reoriented perpendicular to both the topography and the loading axis when the magnitude of stretch exceeded 3%. These findings suggest physical topography can drive cell alignment even in the presence of chemical cues and mechanical stretch (3% or less). There is a critical size limit (75 nm width and 33 nm depth) for parallel alignment (at least in rat osteoblast-like cells).[62] This agrees with a previous report that groove depth plays a role in cells sensitivity to topographical cues[63].

Cell shape is influenced by alignment and recent studies have investigated cell shape exclusive of physical topography. One impactful study involved confined

hMSCs and their lineage commitment[28]. Interestingly, experiments with fibronectin coated nonpatterned substrates showed that cell seeding density alone can drive stem cell commitment. In other experiments, PDMS micro- islands coated with fibronectin were used to limit cell to cell contacts. hMSCs, when allowed to spread, differentiated along an osteogenic lineage (as determined by alkaline phosphatase and RT-PCR data). Kilian et al. explored the influence of cell shape independent of cell surface area[64]. MSCs were exposed to mixed osteogenic and adipogenic differentiation media and grown on fibronectin stamped islands of varied size and shape. Shapes that caused cell elongation (but of equal surface area), drove cells to differentiate along an osteoblastic lineage. Pharmacological factors were used to interrupt cytoskeletal tension (via inhibition of myosin II and ROCK). When cells grown on star-shaped islands (promoting an osteogenic phenotype in the absence of inhibitors) were inhibited, cells differentiated along an adipogenic lineage. Ultimately, the ability of cell to generate contractile forces was important for lineage commitment.

Cell traction force depends on adhesion size. Traction force has been shown to depend linearly on adhesion site size, with greater force per area applied to adhesions larger than 1 μm^2. Studies have also shown the opposite trend in adhesions smaller than 1 μm^2 at the leading edge of cell movement. Cells applied larger forces per area to the adhesions smaller than 1 μm^2 compared to larger adhesions[65]. During early FA maturation and growth a correlation exists between FA size and traction

force magnitude. This relationship is absent in mature adhesions, however, indicating that FA size alone is not a predictor of the local tension exerted at the adhesion[66]. Recently, it was found that the minimum area required for stable formation of nanoscale focal adhesions and force transduction has a dynamic threshold involving an equilibrium between adhesive force and cytoskeletal tension pathways, and the structural linkages involved in force transmission[19].

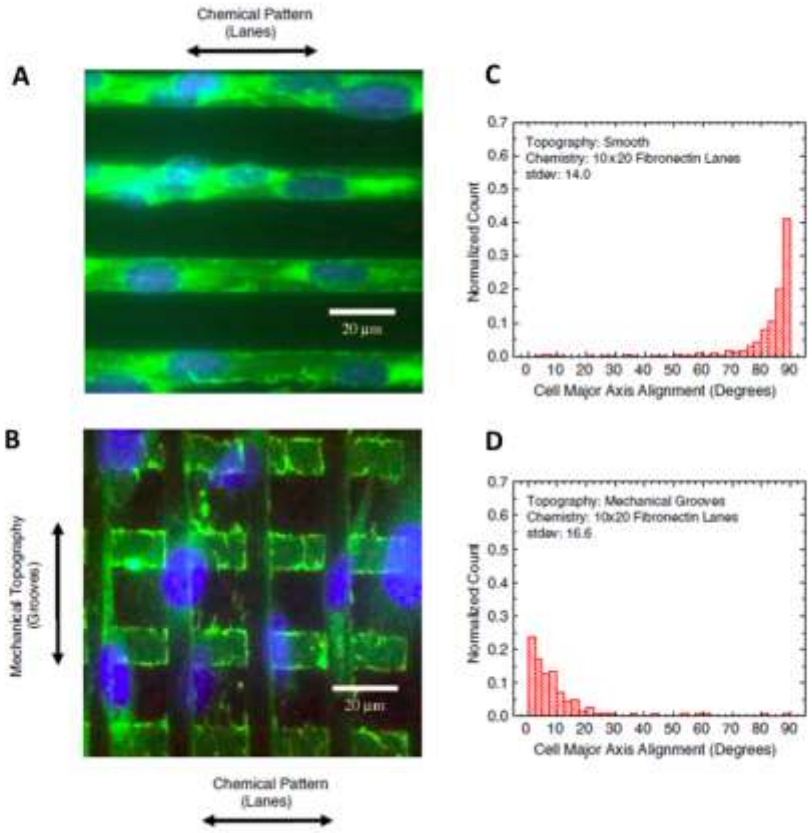

Figure 2.6 Physical topography can override chemical topography. A-B.) Immunofluorescence images of mouse calvarial pre-osteoblasts on patterned substrates with chemical topography (fibronectin lanes) (A) or chemical and physical topography (B). Physical topography is perpendicular to the chemical topography in (B). C-D.) Analysis of cell alignment on surfaces (A) and (B) shown in the cell distribution histograms (C) and (D) respectively. These data suggest that physical topography can be a greater driver of alignment than chemical topography[26].

Topography's influence on cell proliferation is mixed. Cell proliferation on nanorough Ti films was not influenced compared to smooth surfaces[57]. After 72 hours, another report suggested that nanotopographic Ti roughness size was influential on hMSC proliferation- the smallest features, ~20 nm, inhibited proliferation[56]. Polymeric surfaces with nanoridges and holes induced a greater proliferation rate in canine MSCs after five days[52]. Proliferation of hMSCs grown on polyurethane nanogratings was not affected by topography[67]. Our own work on nanotopographic poly(methyl methacrylate) (PMMA) has shown that hMSC proliferation is not altered at early time points but is enhanced at day 14 compared to smooth controls[68]. These results show that proliferation might be enhanced on topography, but is dependent upon cell type, surface chemistry, and surface feature.

Differentiation of cells (as determined by protein expression, gene expression, or functional assays) is also altered on topographic surfaces. Varied size and arrangement of nanopits either enhanced or inhibited deposition of osteospecific proteins[69]. Depending on the feature size and arrangement, the surface promoted MSC stemness[30]. hMSCs grown on gelatin coated poly (urethane acrylate) nanogratings showed upregulation of osteogenic genes in comparison to control surfaces[29]. Gene expression, however, does not prove functional commitment to an osteogenic lineage, yet gene expression is often used to show differentiation. Another study investigated both gene expression and the functional output of osteogenesis:

mineral formation. Lamers et al. found increases in some osteogenic specific markers on nanotopography relative to smooth controls[62]. Mineral formation showed the presence and alignment of CaP deposits on topographic surfaces. Alignment of CaP was observed on substrates with grooves 50 nm in width and 17 nm depth. No images or quantification of CaP was shown, so it is not clear how topography influences mineral deposition relative to smooth surfaces. After 16 days, however, cells were no longer in contact with underlying topography, potentially indicating a limiting time for the direct influence of the surface on cell behavior. The study involving MSCs on nanogratings of polyurethane saw enhanced osteogenic gene expression[67]. Calcium deposition was improved on 400 nm surfaces relative to smooth controls but only at day 7 and 14; this effect was not observed at day 21. Our own results indicate a similar response with some calcium deposition enhancement at day 14 but no increase observed at day 21[68]. These findings indicate that topography (*in vitro*) may be influential for osteoenic differentiation at early time points; later time points look less promising. Long term investigations *in vivo* need to be completed to fully understand the impact of topography on bone strength and growth. The greater surface area of nano- and microtopographic surfaces may promote greater contact with *in vivo* tissue enhancing implant-tissue strength independent of any cell based differentiation changes.

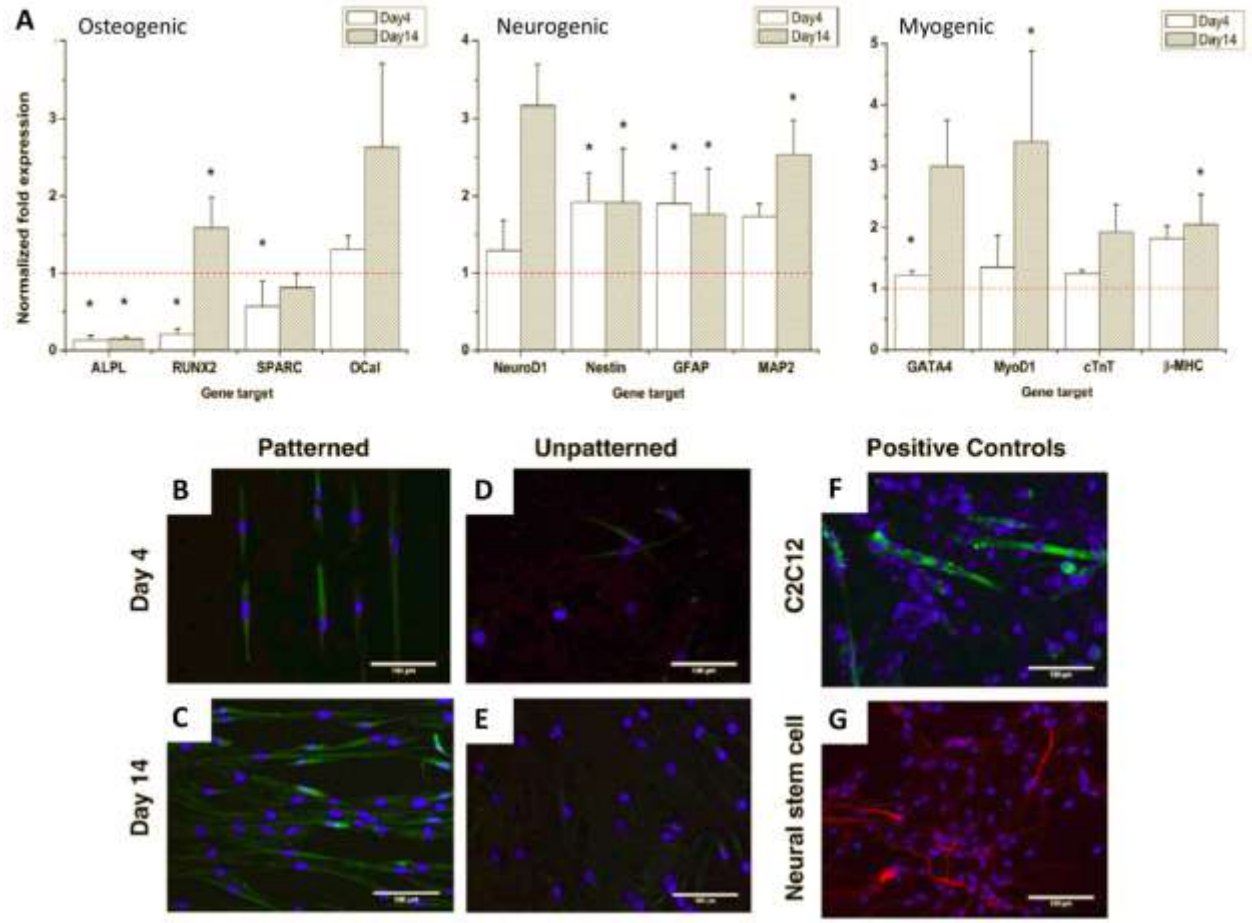

Figure 2.7 Patterned surfaces support myogenic differentiation. A.) Relative gene expression of osteogenic, neurogenic, and myogenic markers at day 4 (white) and day 14 (grey) on micropatterned PLGA coated with fibronectin. B-C.) Immunofluorescence images of staining for mature markers of neurogenic differentiation (heavy chain cardiac myosin, green) on micropatterned surfaces after day 4 (B) and day 14 (C). Similar images on smooth surfaces at day 4 (D) and day 14 (E). Positive control cells stained positive for heavy chain cardiac myosin (F). A neurogenic positive control stained positive for MAP2 (red) (G). (Scale bar = 100 μm)[70].

Despite a recent surge in reports of cell behavior and topography, the mechanisms remain incompletely understood. Topography's influence on cell behavior seems to lie with alterations to protein structure, distribution of adhesion motifs, and integrin activation[25]. Size of topography influenced integrin response on poly-L-lactide/polystyrene (PLLA/PS) demixed films as increased expression of

paxillin (an integrin binding protein) and pFAK were observed in human osteoblasts after growth for up to 24 hours on nano-PLLA/PS films (14 and 29 nm pits) compared to flat films[71] Altered integrin response is important, yet the type of integrins used are critical to mechanotransduction, as $\alpha_5\beta_1$ integrins determine adhesion force; $\alpha_v\beta_3$ is primarily involved in mechanotransduction of fibroblasts[20]. Both integrin clusters were reported to be important for osteogenic differentiation in hMSCs (ALP assay, no functional assays were performed)[6]. Thus, surfaces tailored to activate both integrin clusters types might be more effective at driving mechanotransduction pathways such as the MAPK cascade. Additionally, inhibition of fibroblast myosin contractility on nanoislands restored FN-integrin clustering below the critical area threshold mentioned earlier[19]. This further supports that availability of sufficient adhesion size is critical to integrin clustering and subsequent mechanotransduction.

RhoA GTPase is known to be involved in mechanotransduction. McBeath et al. showed that increased RhoA levels were due to cell shape as levels of the downstream Rho effector ROCK were also higher in spread subconfluent cells[28]. Utilizing various constitutively active or dominant-negative RhoA adenovirus constructs, they found that hMSCs grown on islands without supplements can induce differentiation. This indicated that RhoA can eliminate the need for differentiation inducing soluble factors. Additionally, results indicated that cell shape and active

RhoA are both necessary to drive hMSC differentiation. When ROCK was supplemented to cells on small islands they became osteogenic. Thus, RhoA is downstream of soluble differentiation factors and that cell shape mediated control of stem cell commitment is regulated by ROCK induced cytoskeletal tension. The implications are that ROCK is downstream of both RhoA and cell shape.

Topography, in driving RhoA and RhoGTPases, may also drive myogenesis. Rho GTPases mediate a switch between adipogenesis and myogenesis. Specifically, activation of Rho kinase by Rho is required for myogenesis[72]. A recent report suggested that hMSCs grown on fibronectin coated poly(lactic-co-glycolic acid) (PLGA) microchannels (not exposed to soluble induction factors) were driven toward a myogenic lineage, though in this specific study, Rho levels were not investigated, but other markers of myogenesis were (Figure 2.7)[70]. Key early regulators of cardiomyogenesis were upregulated on patterned surfaces. Neural markers were upregulated at day 4 and 14 as well. Surprisingly, osteogenic markers were not upregulated. Immunofluorescent staining proved the presence of the cardiac myosin heavy chain when cells were grown on patterned surfaces, especially after 14 days. MAP2 (an encoder essential for the formation and upkeep of neurites) was not detected on either smooth or patterned surfaces. The authors concluded that the micropatterns directed the cells toward a myogenic lineage. The micropatterns controlled the distribution of the adhesion motifs, influencing the spatial distribution

of focal adhesions. Focal adhesions help transduce force to the nucleus via the cytoskeleton. One mechanism of mechanotransduction proposed suggests that tugging on the nuclear membrane can affect gene activity by altering accessibility to transcription factors. RhoA-ROCK-tension signaling may influence stem cell fate via transduction at focal adhesions, though this was not investigated in this study.

The MAPK family, including RhoA,[73,74] is known to regulate proliferation and differentiation of osteoblasts and osteoprogenitor cells through adhesion mediated phosphorylation of FAK [59]. When FAK activity was inhibited in MSCs grown on laminin, osteogenic differentiation was attenuated[42]. Interestingly, down regulation of ERK/MAPK signaling molecules was observed in STRO-1+ skeletal stem cells grown on nanopits arranged in square and hexagonal lattices whereas gratings promoted up-regulation in ERK/MAPK signaling[59]. This points to the fact that protein adsorption on surfaces and the subsequent arrangement of adhesions dictates cell shape and downstream signaling. Functional assays of mineralization were not performed, making it hard to assess what impact topography has on actual cell function.

2.4 Protein adsorption

An additional aspect relevant to cell attachment and response to substrates of varied topography or elasticity is protein structure[75]. Notably, conformation changes to albumin on SAM surfaces allowed platelet adhesion; significant because albumin

was not previously known to have any platelet specific binding sites[75]. In contrast, films of poly(lactic-glycolic acid) with nanotopography promote the native structure of fibrinogen, leading to decreased platelet attachment compared to smooth surfaces[76,77]. Cell response to collagen I attached to PDMS was shown to be independent of elasticity; cell response was found to depend on elasticity for polyacrylamide gels[78]. Collagen I attachment is influenced by structural differences in the polymer network of the PDMS and polyacrylamide substrates respectively. These reports suggest that topography and elasticity are influential in protein structure as it relates to cell behavior.

In addition to surface factors, native protein structure is dependent on environmental factors (e.g. polarity, temperature, pH) and the amino acid sequences that compose the protein[79-81]. The internal energy that stabilizes the native state is rather large and ranges from 10^4-10^5 k_BT for a typical protein containing 300 amino acid groups[4]. Proteins differ from simple polymers in that they have low conformational freedom because they are low-entropy structures [80] yet the presence of polar, charged, or nonpolar side chains provides multiple modes of interaction with a biomaterial surface[82]. These interactions (involving electrostatic, dispersion and hydrophobic forces[80]) often lead to conformation changes as hydrophobic and hydrophilic domains rearrange to interact with a thermodynamically (thus energetically) favorable microenvironment be it the surface (of an implant, substrate,

etc.) or neighboring water molecules. (Energy differences between conformations usually varies from 1 to 10 k_BT, allowing for fast conformational transitions[4].) A decrease in ordered structure suggests higher conformational entropy, hence adsorption is favored. Yet this increased entropy must be balanced by the enthalpy term involving intramolecular interactions (notably hydrogen bonding); this balance dictates whether or not an increase or decrease in ordered protein structure is observed[4,80].

The kinetics of protein adsorption plays a role in the specific proteins initially available on a biomaterial surface. The speed of adsorption is often so rapid that measured adsorption rates are hindered by mass transport limitations [75]. Abundant proteins usually adsorb first[4]. Over time, higher affinity proteins displace first to adsorb but lower affinity proteins. [80] Fibrinogen initially adsorbs to surfaces from serum but is replaced by kininogen, Factor XII, and plasminogen[83]. Similarly, vitronectin adsorbs preferentially to hydroxyapatite surfaces compared to fibronectin because of its greater ability to adsorb over other adhesion-inhibiting proteins and because of its higher concentration in fetal bovine serum[5]. Total adsorbed adhesion protein quantity, however, is poorly correlated with cell adhesion; accessibility of adhesion motifs is typically more important[80]. Ultimately, the substrate surface chemistry and topography strongly influences the composition, structure, and biological activity (adhesion motif accessibility) of protein adsorption[9,80,84,85].

2.5 Matrix elasticity and topography: commonalities

Coupling matrix mechanics and topography is a relatively recent idea. Yim et al. postulated that topography has a greater influence on f-actin organization than matrix mechanics because they observed similar cytoskeletal arrangement of f-actin on nanotopographic surfaces of PDMS and TCPS in hMSCs[58]. Actin levels were quantitatively higher in cells grown on unpatterned TCPS and PDMS than nanopatterned surfaces. Mathieu et al. reported that cytoskeletal actin is responsible for most of a cell's stiffness[43] so Yim et al. investigated the hMSC elasticity via AFM indentation measurements. Cell elastic modulus was significantly reduced when plated on nanopatterned TCPS compared to smooth TCPS; cell modulus was significantly higher when grown on nanogratings of PDMS compared to smooth PDMS. The authors contend that it is easier for cells to develop higher cytoskeletal tension on stiffer substrates, thus, the reduced cell modulus observed on nanopatterned TCPS was likely influenced by the spatial organization of the actin network and the reduced cross-linking because of parallel network structure[58]. This theory might be true on TCPS but does not explain the opposite trend observed on PDMS. Potentially, the actin alignment and corresponding cell elastic modulus is influenced by both substrate elasticity and topography.

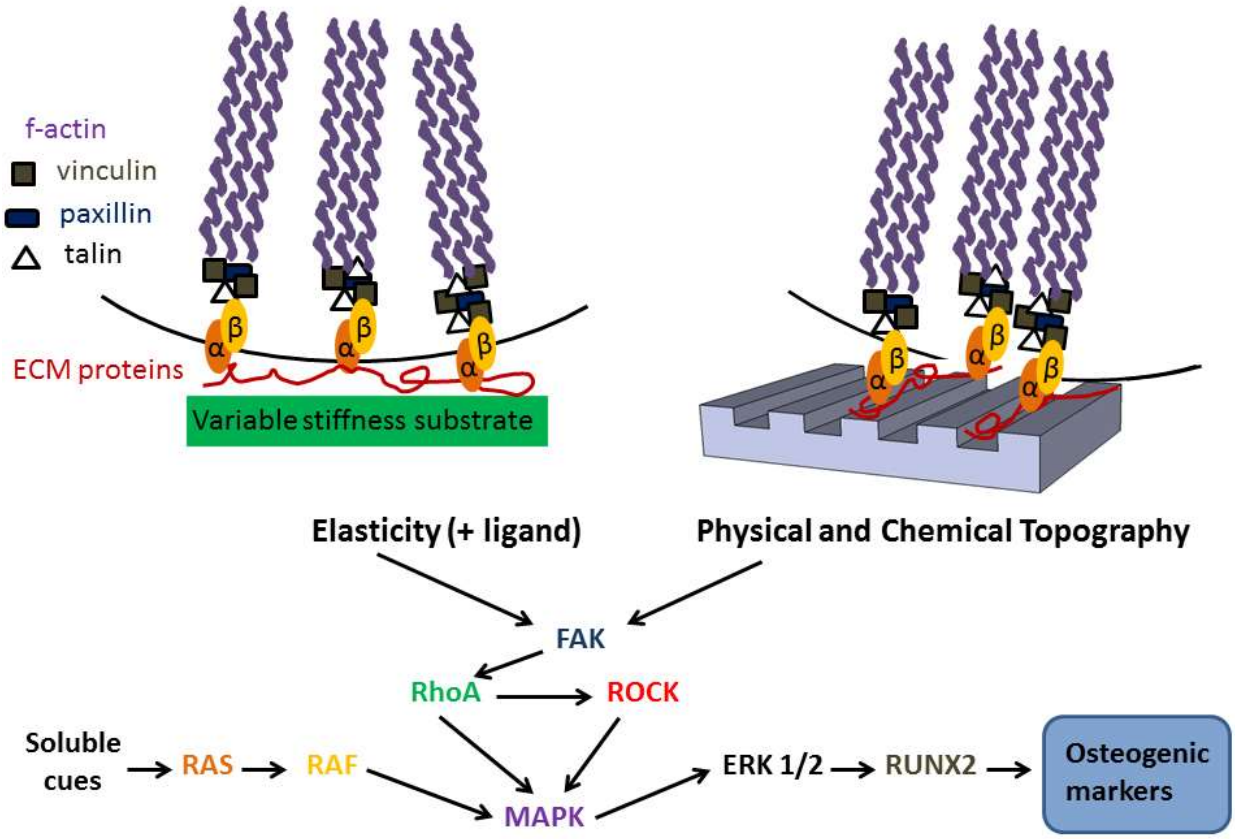

Figure 2.8 The link between matrix elasticity and substrate topography is the RhoA-ROCK pathway. This schematic illustrates a common mechanism shared between (physical and chemical) topography and matrix elasticity. This mechanism is activated when focal adhesions interact with various surface ligands that promote upregulation of FAK, MAPK, and downstream osteogenic markers such as ALP, bone sialoprotein, osteopointin, and matrix formation capable of mineralization. Not all surface topgraphies, elasticities, and ligands promote this mechanism, thus, the mechanism is not universal for all situations or cell types.

Elements involved in mechanotransduction were also investigated and shown to be influenced by elasticity and topography. The results showed slightly elevated pFAK levels on nanopatterns compared to smooth surfaces. Additionally, pFAK

levels were slightly higher on smooth TCPS compared to PDMS (PDMS- 2-4 MPa; PS- 2 GPa elastic modulus). These results agree with results using mouse pre-osteoblasts that showed stiffer substrates (Young's modulus) resulted in higher pFAK levels relative to softer substrates[40]. This suggests a possible link between topography and matrix mechanics as pFAK levels were elevated on topographic surfaces of PDMS and TCPS (compared to smooth controls). Nanopatterned PDMS had elevated levels of pFAK compared to nanoTCPS. This finding may suggest that topography when coupled with stiffness might indeed be more influential than matrix mechanics in driving osteogenic differentiation. It must be noted that in addition to differences in surface chemistry of the two substrates, PDMS was coated with collagen whereas TCPS was exposed to serum proteins. Therefore, observations and mechanistic hypotheses cannot be attributed solely to topography or elasticity. Overall, however, this work indicates that pFAK is, at least, part of a common mechanism linking topography and matrix elasticity (Figure 2.8).

As previously discussed, cell adhesion, spreading, and migration are dependent on the availability and accessibility of adhesion motifs. The magnitude of these behaviors depends on matrix elasticity and topography (both size and shape). On stiff surfaces, cells are able to generate forces that are greater than on soft surfaces, indicating that changes in unfolded serum proteins and the cytoskeletal network depend on substrate mechanics[6,38]. Topography too, can modulate the accessibility of

motifs, either the available size[19], or the spatial arrangement[15,27] potentially limiting the force a cell can generate. In addition, topography (via altered surface energy) can modulate protein adhesion, limiting the type of motif available or affecting structure. Collectively, integrin clustering is influenced by adhesion motif availability on topographic and varied elasticity substrates. Altered clustering and intergrin activation influences mechanotransduction and downstream cell signaling. Hence, topography and matrix elasticity can be combined to alter cell behaviors and mechanotransduction.

Other mechanisms might be influenced by substrates with topographic or varied elasticity. Calcium channels may be involved in sensing mechanical inputs, though this is believed to be transient[86]. Fluid flow and other inputs are transient, whereas matrix topography and elasticity are generally static[87]. Specific topography, and specific matrix elasticity allow for generation of force sufficient to activate pathways that have been implicated in driving osteogenesis.

2.6 Conclusion

It is clear from the findings discussed here that matrix elasticity and topography can influence cell behavior. The pertinent questions are: 1. Under what conditions? and 2. How long do we have control of cell behavior (when using topography and matrix elasticity)? These questions cannot be answered universally because of

inconsistent results. Inconsistent results are due to a lack of compete functional analysis of cell behavior and varied material characteristics. Functional analysis is often limited to a genotypic response or superficial markers of differentiation. Examples of true functional analysis are mineralization (in osteoblasts) or synchronous beating (in cardiomyocytes). Showing hallmark genes of differentiation without further evidence for phenotypic function is insufficient to prove full cell commitment. Other inconsistencies arise from materials related differences: surface chemistry, shape, size, matrix elasticity, and adsorbed ligand type that drive cellular changes. Cell response to these variables is not universal either. Thus, while certain topographies and substrate elasticities may drive cell differentiation of specific cell types via mechanotransduction it is extremely difficult to recommend any particular set of parameters for clinical therapies that require differentiation or maintenance of stemness. In order to better develop parameters for *in vivo* and clinical therapies, future studies need to investigate the MAPK and other pathways to confirm the initial reports that link topography and matrix elasticity. A robust cell response under a variety of conditions might be clinically useful to accelerate osteogenesis on implant surfaces[9,88] or promote cartilage formation *in vivo*[43,44]. At this time, however, the jury is still out.

2.7 References

1 Adams, J. C. & Watt, F. M. Regulation of Development and Differentiation by the Extracellular-Matrix. *Development* **117**, 1183-1198 (1993).

2 De Arcangelis, A. & Georges-Labouesse, E. Integrin and ECM functions - roles in vertebrate development. *Trends in Genetics* **16**, 389-395, doi:Doi 10.1016/S0168-9525(00)02074-6 (2000).

3 Geiger, B., Spatz, J. P. & Bershadsky, A. D. Environmental sensing through focal adhesions. *Nat Rev Mol Cell Bio* **10**, 21-33, doi:Doi 10.1038/Nrm2593 (2009).

4 Ballet, T., Boulange, L., Brechet, Y., Bruckert, F. & Weidenhaupt, M. Protein conformational changes induced by adsorption onto material surfaces: an important issue for biomedical applications of material science. *B Pol Acad Sci-Tech* **58**, 303-315, doi:DOI 10.2478/v10175-010-0028-0 (2010).

5 Wilson, C. J., Clegg, R. E., Leavesley, D. I. & Pearcy, M. J. Mediation of biomaterial-cell interactions by adsorbed proteins: A review. *Tissue Eng* **11**, 1-18, doi:DOI 10.1089/ten.2005.11.1 (2005).

6 Li, B. J., Moshfegh, C., Lin, Z., Albuschies, J. & Vogel, V. Mesenchymal Stem Cells Exploit Extracellular Matrix as Mechanotransducer. *Sci Rep-Uk* **3**, doi:Artn 2425 Doi 10.1038/Srep02425 (2013).

7 Vogel, V. & Sheetz, M. Local force and geometry sensing regulate cell functions. *Nat Rev Mol Cell Bio* **7**, 265-275, doi:Doi 10.1038/Nrm1890 (2006).

8 Ruoslahti, E. Fibronectin and Its Receptors. *Annu Rev Biochem* **57**, 375-413 (1988).

9 Garcia, A. J. & Keselowsky, B. G. Biomimetic surfaces for control of cell adhesion to facilitate bone formation. *Crit Rev Eukar Gene* **12**, 151-162, doi:DOI 10.1615/CritRevEukaryotGeneExpr.v12.i2.50 (2002).

10 Wheeldon, I., Farhadi, A., Bick, A. G., Jabbari, E. & Khademhosseini, A. Nanoscale tissue engineering: spatial control over cell-materials interactions. *Nanotechnology* **22**, doi:Artn 212001 Doi 10.1088/0957-4484/22/21/212001 (2011).

11 Gu, X. X. & Masters, K. S. Regulation of valvular interstitial cell calcification by adhesive peptide sequences. *J Biomed Mater Res A* **93A**, 1620-1630, doi:Doi 10.1002/Jbm.A.32660 (2010).

12 Zhu, J. M. & Marchant, R. E. Design properties of hydrogel tissue-engineering scaffolds. *Expert Rev Med Devic* **8**, 607-626, doi:Doi 10.1586/Erd.11.27 (2011).

13 Collier, J. H. & Segura, T. Evolving the use of peptides as components of biomaterials. *Biomaterials* **32**, 4198-4204, doi:DOI 10.1016/j.biomaterials.2011.02.030 (2011).

14 Barker, T. H. The role of ECM proteins and protein fragments in guiding cell behavior in regenerative medicine. *Biomaterials* **32**, 4211-4214, doi:DOI 10.1016/j.biomaterials.2011.02.027 (2011).

15 Schwarz, U. S. & Gardel, M. L. United we stand - integrating the actin cytoskeleton and cell-matrix adhesions in cellular mechanotransduction. *J Cell Sci* **125**, 3051-3060, doi:Doi 10.1242/Jcs.093716 (2012).

16 Peyton, S. R. & Putnam, A. J. Extracellular matrix rigidity governs smooth muscle cell motility in a biphasic fashion. *J Cell Physiol* **204**, 198-209, doi:Doi 10.1002/Jcp.20274 (2005).

17 Khatiwala, C. B., Peyton, S. R., Metzke, M. & Putnam, A. J. The regulation of osteogenesis by ECM rigidity in MC3T3-E1 cells requires MAPK activation. *J Cell Physiol* **211**, 661-672, doi:Doi 10.1002/Jcp.20974 (2007).

18 Engler, A. J., Sen, S., Sweeney, H. L. & Discher, D. E. Matrix elasticity directs stem cell lineage specification. *Cell* **126**, 677-689, doi:DOI 10.1016/j.cell.2006.06.044 (2006).

19 Coyer, S. R. *et al.* Nanopatterning reveals an ECM area threshold for focal adhesion assembly and force transmission that is regulated by integrin activation and cytoskeleton tension. *J Cell Sci* **125**, 5110-5123, doi:Doi 10.1242/Jcs.108035 (2012).

20 Roca-Cusachs, P., Gauthier, N. C., del Rio, A. & Sheetz, M. P. Clustering of alpha(5)beta(1) integrins determines adhesion strength whereas alpha(v)beta(3) and talin enable mechanotransduction. *P Natl Acad Sci USA* **106**, 16245-16250, doi:DOI 10.1073/pnas.0902818106 (2009).

21 Khatiwala, C. B., Kim, P. D., Peyton, S. R. & Putnam, A. J. ECM Compliance Regulates Osteogenesis by Influencing MAPK Signaling Downstream of RhoA and ROCK. *J Bone Miner Res* **24**, 886-898, doi:Doi 10.1359/Jbmr.081240 (2009).

22 Kim, D. H. *et al.* Nanoscale cues regulate the structure and function of macroscopic cardiac tissue constructs. *P Natl Acad Sci USA* **107**, 565-570, doi:DOI 10.1073/pnas.0906504107 (2010).

23 Weiner, S. & Wagner, H. D. The material bone: Structure mechanical function relations. *Annual Review of Materials Science* **28**, 271-298, doi:DOI 10.1146/annurev.matsci.28.1.271 (1998).

24 Kerschnitzki, M. *et al.* The organization of the osteocyte network mirrors the extracellular matrix orientation in bone. *J Struct Biol* **173**, 303-311, doi:DOI 10.1016/j.jsb.2010.11.014 (2011).

25 Kim, D. H., Provenzano, P. P., Smith, C. L. & Levchenko, A. Matrix nanotopography as a regulator of cell function. *J Cell Biol* **197**, 351-360, doi:DOI 10.1083/jcb.201108062 (2012).

26 Charest, J. L., Eliason, M. T., Garcia, A. J. & King, W. P. Combined microscale mechanical topography and chemical patterns on polymer cell culture substrates. *Biomaterials* **27**, 2487-2494, doi:DOI 10.1016/j.biomaterials.2005.11.022 (2006).

27 Kong, Y. P., Tu, C. H., Donovan, P. J. & Yee, A. F. Expression of Oct4 in human embryonic stem cells is dependent on nanotopographical configuration. *Acta Biomater* **9**, 6369-6380, doi:DOI 10.1016/j.actbio.2013.01.036 (2013).

28 McBeath, R., Pirone, D. M., Nelson, C. M., Bhadriraju, K. & Chen, C. S. Cell shape, cytoskeletal tension, and RhoA regulate stem cell lineage commitment. *Dev Cell* **6**, 483-495, doi:Doi 10.1016/S1534-5807(04)00075-9 (2004).

29 You, M. H. *et al.* Synergistically Enhanced Osteogenic Differentiation of Human Mesenchymal Stem Cells by Culture on Nanostructured Surfaces with Induction Media. *Biomacromolecules* **11**, 1856-1862, doi:Doi 10.1021/Bm100374n (2010).

30 McMurray, R. J. *et al.* Nanoscale surfaces for the long-term maintenance of mesenchymal stem cell phenotype and multipotency. *Nat Mater* **10**, 637-644, doi:Doi 10.1038/Nmat3058 (2011).

31 Trappmann, B. *et al.* Extracellular-matrix tethering regulates stem-cell fate. *Nat Mater* **11**, 642-649, doi:Doi 10.1038/Nmat3339 (2012).

32 Choi, S. J., Kim, H. N., Bae, W. G. & Suh, K. Y. Modulus- and surface energy-tunable ultraviolet-curable polyurethane acrylate: properties and applications. *J Mater Chem* **21**, 14325-14335, doi:Doi 10.1039/C1jm12201k (2011).

33 Peyton, S. R., Raub, C. B., Keschrumrus, V. P. & Putnam, A. J. The use of poly(ethylene glycol) hydrogels to investigate the impact of ECM chemistry and mechanics on smooth muscle cells. *Biomaterials* **27**, 4881-4893, doi:DOI 10.1016/j.biomaterials.2006.05.012 (2006).

34 Kim, J. *et al.* Synergistic effects of nanotopography and co-culture with endothelial cells on osteogenesis of mesenchymal stem cells. *Biomaterials* **34**, 7257-7268, doi:DOI 10.1016/j.biomaterials.2013.06.029 (2013).

35 Gonzalez-Garcia, C., Sousa, S. R., Moratal, D., Rico, P. & Salmeron-Sanchez, M. Effect of nanoscale topography on fibronectin adsorption, focal adhesion size and matrix organisation. *Colloid Surface B* **77**, 181-190, doi:DOI 10.1016/j.colsurfb.2010.01.021 (2010).

36 Pelham, R. J. & Wang, Y. L. Cell locomotion and focal adhesions are regulated by substrate flexibility. *P Natl Acad Sci USA* **94**, 13661-13665, doi:DOI 10.1073/pnas.94.25.13661 (1997).

37 Engler, A. J. *et al.* Myotubes differentiate optimally on substrates with tissue-like stiffness: pathological implications for soft or stiff microenvironments. *J Cell Biol* **166**, 877-887, doi:DOI 10.1083/jcb.200405004 (2004).

38 Pompe, T. *et al.* Dissecting the Impact of Matrix Anchorage and Elasticity in Cell Adhesion. *Biophys J* **97**, 2154-2163, doi:DOI 10.1016/j.bpj.2009.07.047 (2009).

39 Saha, K. *et al.* Substrate Modulus Directs Neural Stem Cell Behavior. *Biophys J* **95**, 4426-4438, doi:DOI 10.1529/biophysj.108.132217 (2008).

40 Khatiwala, C. B., Peyton, S. R. & Putnam, A. J. Intrinsic mechanical properties of the extracellular matrix affect the behavior of pre-osteoblastic MC3T3-E1 cells. *Am J Physiol-Cell Ph* **290**, C1640-C1650, doi:DOI 10.1152/ajpcell.00455.2005 (2006).

41 Schoen, I., Pruitt, B. L. & Vogel, V. The Yin-Yang of Rigidity Sensing: How Forces and Mechanical Properties Regulate the Cellular Response to Materials.

Annual Review of Materials Research **43**, 589-618, doi:10.1146/annurev-matsci-062910-100407 (2013).

42 Salasznyk, R. M., Klees, R. F., Williams, W. A., Boskey, A. & Plopper, G. E. Focal adhesion kinase signaling pathways regulate the osteogenic differentiation of human mesenchymal stem cells. *Exp Cell Res* **313**, 22-37, doi:DOI 10.1016/j.yexcr.2006.09.013 (2007).

43 Mathieu, P. S. & Loboa, E. G. Cytoskeletal and Focal Adhesion Influences on Mesenchymal Stem Cell Shape, Mechanical Properties, and Differentiation Down Osteogenic, Adipogenic, and Chondrogenic Pathways. *Tissue Eng Part B-Re* **18**, 436-444, doi:DOI 10.1089/ten.teb.2012.0014 (2012).

44 Woods, A. & Beier, F. RhoA/ROCK signaling regulates chondrogenesis in a context-dependent manner. *J Biol Chem* **281**, 13134-13140, doi:DOI 10.1074/jbc.M509433200 (2006).

45 Prodanov, L. *et al.* The interaction between nanoscale surface features and mechanical loading and its effect on osteoblast-like cells behavior. *Biomaterials* **31**, 7758-7765, doi:DOI 10.1016/j.biomaterials.2010.06.050 (2010).

46 Ross, A. M., Jiang, Z. X., Bastmeyer, M. & Lahann, J. Physical Aspects of Cell Culture Substrates: Topography, Roughness, and Elasticity. *Small* **8**, 336-355, doi:DOI 10.1002/smll.201100934 (2012).

47 Suh, K. Y., Park, M. C. & Kim, P. Capillary Force Lithography: A Versatile Tool for Structured Biomaterials Interface Towards Cell and Tissue Engineering. *Advanced Functional Materials* **19**, 2699-2712, doi:DOI 10.1002/adfm.200900771 (2009).

48 Choi, S. J., Yoo, P. J., Baek, S. J., Kim, T. W. & Lee, H. H. An ultraviolet-curable mold for sub-100-nm lithography. *J Am Chem Soc* **126**, 7744-7745, doi:Doi 10.1021/Ja048972k (2004).

49 Huang, X. D. *et al.* Reversal imprinting by transferring polymer from mold to substrate. *J Vac Sci Technol B* **20**, 2872-2876, doi:Doi 10.1116/1.1523404 (2002).

50 Mrksich, M. *et al.* Controlling cell attachment on contoured surfaces with self-assembled monolayers of alkanethiolates on gold. *P Natl Acad Sci USA* **93**, 10775-10778, doi:DOI 10.1073/pnas.93.20.10775 (1996).

51 Bernard, A. *et al.* Printing patterns of proteins. *Langmuir* **14**, 2225-2229, doi:Doi 10.1021/La9800371 (1998).

52 Wood, J. A. *et al.* The modulation of canine mesenchymal stem cells by nano-topographic cues. *Exp Cell Res* **318**, 2438-2445, doi:DOI 10.1016/j.yexcr.2012.06.022 (2012).

53 Doyle, A. D., Wang, F. W., Matsumoto, K. & Yamada, K. M. One-dimensional topography underlies three-dimensional fibrillar cell migration. *J Cell Biol* **184**, 481-490, doi:DOI 10.1083/jcb.200810041 (2009).

54 Taubenberger, A. V., Woodruff, M. A., Bai, H. F., Muller, D. J. & Hutmacher, D. W. The effect of unlocking RGD-motifs in collagen I on pre-osteoblast adhesion and differentiation. *Biomaterials* **31**, 2827-2835, doi:DOI 10.1016/j.biomaterials.2009.12.051 (2010).

55 Curtis, A. S. G. *et al.* Substratum nanotopography and the adhesion of biological cells. Are symmetry or regularity of nanotopography important? *Biophys Chem* **94**, 275-283, doi:Doi 10.1016/S0301-4622(01)00247-2 (2001).

56 Khang, D. *et al.* Role of subnano-, nano- and submicron-surface features on osteoblast differentiation of bone marrow mesenchymal stem cells. *Biomaterials* **33**, 5997-6007, doi:DOI 10.1016/j.biomaterials.2012.05.005 (2012).

57 Cai, K. Y., Bossert, J. & Jandt, K. D. Does the nanometre scale topography of titanium influence protein adsorption and cell proliferation? *Colloid Surface B* **49**, 136-144, doi:DOI 10.1016/j.colsurfb.2006.02.016 (2006).

58 Yim, E. K. F., Darling, E. M., Kulangara, K., Guilak, F. & Leong, K. W. Nanotopography-induced changes in focal adhesions, cytoskeletal organization, and mechanical properties of human mesenchymal stem cells. *Biomaterials* **31**, 1299-1306, doi:DOI 10.1016/j.biomaterials.2009.10.037 (2010).

59 Biggs, M. J. P. *et al.* The use of nanoscale topography to modulate the dynamics of adhesion formation in primary osteoblasts and ERK/MAPK signalling in STRO-1+enriched skeletal stem cells. *Biomaterials* **30**, 5094-5103, doi:DOI 10.1016/j.biomaterials.2009.05.049 (2009).

60 Mauney, J. R. *et al.* Matrix-mediated retention of in vitro osteogenic differentiation potential and in vivo bone-forming capacity by human adult

bone marrow-derived mesenchymal stem cells during ex vivo expansion. *J Biomed Mater Res A* **79A**, 464-475, doi:Doi 10.1002/Jbm.A.30876 (2006).

61 Kundu, A. K. & Putnam, A. J. Vitronectin and collagen I differentially regulate osteogenesis in mesenchymal stem cells. *Biochem Bioph Res Co* **347**, 347-357, doi:DOI 10.1016/j.bbrc.2006.06.110 (2006).

62 Lamers, E. *et al.* The influence of nanoscale grooved substrates on osteoblast behavior and extracellular matrix deposition. *Biomaterials* **31**, 3307-3316, doi:DOI 10.1016/j.biomaterials.2010.01.034 (2010).

63 Teixeira, A. I., Abrams, G. A., Bertics, P. J., Murphy, C. J. & Nealey, P. F. Epithelial contact guidance on well-defined micro- and nanostructured substrates. *J Cell Sci* **116**, 1881-1892, doi:Doi 10.1242/Jcs.00383 (2003).

64 Kilian, K. A., Bugarija, B., Lahn, B. T. & Mrksich, M. Geometric cues for directing the differentiation of mesenchymal stem cells. *P Natl Acad Sci USA* **107**, 4872-4877, doi:DOI 10.1073/pnas.0903269107 (2010).

65 Slater, J. H. & Frey, W. Nanopatterning of fibronectin and the influence of integrin clustering on endothelial cell spreading and proliferation. *J Biomed Mater Res A* **87A**, 176-195, doi:Doi 10.1002/Jbm.A.31725 (2008).

66 Stricker, J., Aratyn-Schaus, Y., Oakes, P. W. & Gardel, M. L. Spatiotemporal Constraints on the Force-Dependent Growth of Focal Adhesions. *Biophys J* **100**, 2883-2893, doi:DOI 10.1016/j.bpj.2011.05.023 (2011).

67 Watari, S. *et al.* Modulation of osteogenic differentiation in hMSCs cells by submicron topographically-patterned ridges and grooves. *Biomaterials* **33**, 128-136, doi:DOI 10.1016/j.biomaterials.2011.09.058 (2012).

68 Janson, I. A., Kong, Y. P. & Putnam, A. J. Nanotopographic Substrates of Poly (Methyl Methacrylate) Do Not Strongly Influence the Osteogenic Phenotype of Mesenchymal Stem Cells In Vitro. *Plos One* **9**, e90719, doi:10.1371/journal.pone.0090719 (2014).

69 Dalby, M. J. *et al.* The control of human mesenchymal cell differentiation using nanoscale symmetry and disorder. *Nat Mater* **6**, 997-1003, doi:Doi 10.1038/Nmat2013 (2007).

70 Tay, C. Y. *et al.* Micropatterned matrix directs differentiation of human mesenchymal stem cells towards myocardial lineage. *Exp Cell Res* **316**, 1159-1168, doi:DOI 10.1016/j.yexcr.2010.02.010 (2010).

71 Lim, J. Y. *et al.* The regulation of integrin-mediated osteoblast focal adhesion and focal adhesion kinase expression by nanoscale topography. *Biomaterials* **28**, 1787-1797, doi:DOI 10.1016/j.biomaterials.2006.12.020 (2007).

72 Sordella, R., Jiang, W., Chen, G. C., Curto, M. & Settleman, J. Modulation of rho GTPase signaling regulates a switch between adipogenesis and myogenesis. *Cell* **113**, 147-158, doi:Doi 10.1016/S0092-8674(03)00271-X (2003).

73 Putnam, A. J., Khatiwala, C. B., Kim, P. D. & Peyton, S. R. ECM Compliance Regulates Osteogenesis by Influencing MAPK Signaling Downstream of RhoA and ROCK. *J Bone Miner Res* **24**, 886-898, doi:10.1359/Jbmr.081240 (2009).

74 Biggs, M. J. P. & Dalby, M. J. Focal adhesions in osteoneogenesis. *P I Mech Eng H* **224**, 1441-1453, doi:Doi 10.1243/09544119jeim775 (2010).

75 Szott, L. M. & Horbett, T. A. Protein interactions with surfaces: cellular responses, complement activation, and newer methods. *Curr Opin Chem Biol* **15**, 677-682, doi:DOI 10.1016/j.cbpa.2011.04.021 (2011).

76 Koh, L. B., Rodriguez, I. & Venkatraman, S. S. Conformational behavior of fibrinogen on topographically modified polymer surfaces. *Phys Chem Chem Phys* **12**, 10301-10308, doi:Doi 10.1039/C001747g (2010).

77 Koh, L. B., Rodriguez, I. & Venkatraman, S. S. The effect of topography of polymer surfaces on platelet adhesion. *Biomaterials* **31**, 1533-1545, doi:DOI 10.1016/j.biomaterials.2009.11.022 (2010).

78 Trappmann, B. *et al.* Extracellular-matrix tethering regulates stem-cell fate. *Nat Mater* **11**, 642-649, doi:10.1038/nmat3339 (2012).

79 Gao, J. M., Bosco, D. A., Powers, E. T. & Kelly, J. W. Localized thermodynamic coupling between hydrogen bonding and microenvironment polarity substantially stabilizes proteins. *Nat Struct Mol Biol* **16**, 684-U681, doi:Doi 10.1038/Nsmb.1610 (2009).

80 Norde, W., Horbett, T. A. & Brash, J. L. Proteins at Interfaces III: Introductory Overview. *Acs Sym Ser* **1120**, 1-34 (2012).

81 Rabe, M., Verdes, D. & Seeger, S. Understanding protein adsorption phenomena at solid surfaces. *Adv Colloid Interfac* **162**, 87-106, doi:DOI 10.1016/j.cis.2010.12.007 (2011).

82 Horbett, T. A. Protein Adsorption on Biomaterials. *Adv Chem Ser*, 233-244 (1982).

83 Brash, J. L., Scott, C. F., Tenhove, P., Wojciechowski, P. & Colman, R. W. Mechanism of Transient Adsorption of Fibrinogen from Plasma to Solid-Surfaces - Role of the Contact and Fibrinolytic Systems. *Blood* **71**, 932-939 (1988).

84 Li, D. & Chen, H. Regulation of Protein/Surface Interactions by Surface Chemical Modification and Topographic Design. *Acs Sym Ser* **1120**, 301-319 (2012).

85 Denis, F. A., Pallandre, A., Nysten, B., Jonas, A. M. & Dupont-Gillain, C. C. Alignment and assembly of adsorbed collagen molecules induced by anisotropic chemical nanopatterns. *Small* **1**, 984-991, doi:DOI 10.1002/smll.200500116 (2005).

86 Sachs, F. Stretch-Activated Ion Channels: What Are They? *Physiology* **25**, 50-56, doi:DOI 10.1152/physiol.00042.2009 (2010).

87 Kshitiz *et al.* Control of stem cell fate and function by engineering physical microenvironments. *Integr Biol-Uk* **4**, 1008-1018, doi:Doi 10.1039/C2ib20080e (2012).

88 Prodanov, L. *et al.* The effect of nanometric surface texture on bone contact to titanium implants in rabbit tibia. *Biomaterials* **34**, 2920-2927, doi:DOI 10.1016/j.biomaterials.2013.01.027 (2013).

CHAPTER 3

Synthesis and Characterization of a Material that Mimics Native Bone: Nanotopographic PMMA

3.1 Introduction

As mentioned in Chapter 1 and alluded to in Chapter 2, an aging population and the continued prevalence of bone defects worldwide drives the need for increased orthopedic procedures each year[1,2] . Revision surgeries continue to rise as well[1]. The cost of orthopedic injuries is estimated to be $17-20 billion annually in the United States[3]. Thus, strategies which enhance knowledge of bone formation or enhance current clinical practices are desirable. Improvements may prolong implant lifetime, reduce the need for revisions, and drive down the economic impact.

A cell's environment is critical to its function and behavior, and an important feature of the cellular microenvironment is the extracellular matrix (ECM). Cells sense and respond to both chemical and physical cues within the ECM, including adhesive ligands, mechanical properties, and topography[4,5]. Cells adhere to the ECM's various adhesion motifs through transmembrane integrin receptors, which are capable of transducing adhesive signals into biochemical signals and which physically connect the

ECM to the cell's underlying cytoskeleton. Different ECM ligands may engage different integrin receptors, and specific integrins are known to regulate osteogenic differentiation[6]. Matrix mechanical properties have also been shown to influence osteogenic differentiation, with more rigid substrates driving osteogenic differentiation in 2D cell cultures[7-9]. Other studies have shown micro- and nanotopography of varied surface chemistries to influence osteogenic differentiation as well[2,3,6,10-17]. Differentiation along an osteogenic lineage may be useful for bone tissue engineering strategies when combined with scaffolds to produce functional bone for various orthopedic therapies[2].

Bone is a hierarchical tissue that is mainly composed of type I collagen, hydroxyapatite (HA), and water. Human bone structure ranges many orders of magnitude in size: from whole bones nearly one meter in length to the individual collagen triple helices that are approximately 300 nm long and have a diameter of 1.5 nm[18]. Collagen is essential for HA formation[19]; together HA and collagen form a highly aligned composite matrix that gives bone its toughness and strength[18,20]. Thus, attempts to reproduce *in vivo* mineral *in vitro* may be enhanced by mimicking the structure of native bone. Ultimately, control of osteogenic differentiation via topography may be desirable for bone and orthopedic implant applications if indeed mineral production can be enhanced or if the mineral produced is similar to native bone.

We developed an approximate replica of the nanotopographic structure of bone using an idealized surface of poly(methyl methacrylate) (PMMA) to investigate the role of surface nanotopography in driving the osteogenic differentiation of MSCs. Clinically, PMMA is used as a bone cement in orthopedic applications[21,22]. We were motivated by the potential to enhance osteointegration and bone healing via imprinted nanotopographic cues on an FDA-approved orthopedic material. We hypothesized that our nanoPMMA surfaces with aligned features on the order of collagen fibrils would mimic the structure of native bone would enhance mineral quantity. To test this hypothesis, we used PMMA films manufactured via capillary assisted ultra-violet (UV) lithography and characterized with atomic force microscopy (AFM) and scanning electron microscopy (SEM) to validate their submicron dimensions. In addition, we measured contact angles via the sessile drop method to determine differences in surface free energy. Assessment of cell behavior and phenotype will be discussed in detail in Chapter 4.

3.2 Materials and Methods

3.2.1 Manufacturing of PMMA films

Films were made using a precursor solution of (poly) methyl methacrylate (PMMA)[generation 1 (Gen1-M_w: 15,000 g/mol); generation 2 (Gen2-M_w: 120,000 g/mol)] dissolved in methyl methacrylate (MMA) (8% wt./wt.) (all chemicals are from

Sigma, Saint Louis, MO, unless otherwise specified). A photoinitiatior, 2,2-dimethoxy-2-phenylacetophenone (DMPA) (Acros Organics) (2% wt/wt), was added to the solution prior to polymerization. The PMMA precursor solution was deposited on (heptadecafluoro-1,2,2,2-tetrahydrodecyl) trichlorosilane (FTDS) (Gelest, Morrisville, PA) coated silicon molds (LightSmyth Technologies, Eugene OR). The silicon (Si) molds were patterned with square wave gratings of different depths and widths in order to create PMMA films with varied nanotopography (Table 3.1). No. 1 coverglass slides (Fisher Scientific, Pittsburgh, PA) were coated with ~1 mM (3-acryloxy propyl) methyl dichlorosilane (APMDS) (Gelest) under vacuum overnight in a solution of dimethyl formamide (Fisher Scientific) and 1, 4- benzoquinone (9.25 mM). APMDS coated slides were rinsed in n-heptane and then dried with nitrogen gas. The pre-cursor solution was placed on top of the silicon molds and coated glass slides were placed on-top of the pre-cursor solution and subjected to UV-light ~365 nm (3.1 mW/cm^2) for an hour (Figure 3.1). Smooth PMMA films absent of controlled topography were also manufactured. PMMA films will be designated by the following names for simplicity and clarity: smooth, G415, G303, and G140.

Table 3.1 Nomenclature for PMMA films with nanotopographic features.

Name	Period (nm)	Groove depth (nm)	Duty cycle (%)	Line width (nm)
G415	833	200	50	416
G303	606	190	50	303
G140	278	110	50	139

3.2.2 Characterization of PMMA films with atomic force microscopy

To assess the topographic surface features of nanoPMMA films, a Dimension Icon scanning probe microscope (Bruker, Camarillo, CA) was used for imaging. Specifically, NCH-10 silicon probes (NanoAndMore USA, Lady's Island, SC) were used to scan the PMMA substrates. A sampling rate of 384 lines and a scan rate of 0.5 Hz were used.

3.2.3 Characterization of PMMA films with scanning electron microscopy

To use another complementary method to assess nanofeatures PMMA films were scanned using electron microscopy. The substrates were sputter-coated with gold and examined with a Phillips XL30FEG SEM at working distance of 5 mm, an accelerating voltage of 5 kV, and a spot size of 3.

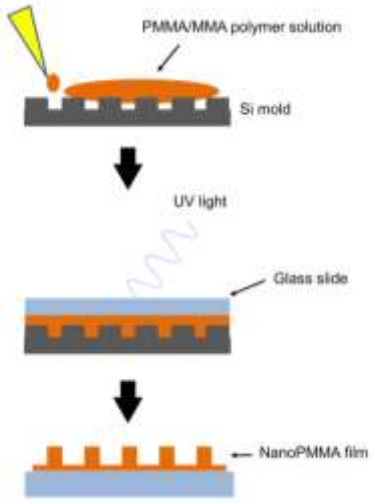

Figure 3.1. Capillary assisted UV lithography polymerization method was used to produce PMMA films with nanotopography. A precursor solution of PMMA and MMA was placed on a Si mold containing nanoscale gratings. A glass slide was placed on top of the precursor solution, which was then exposed to UV light for one hour. After polymerization the mold was removed. The final product was a PMMA film with nanoscale gratings of varied width and depth. See Table 3.1 for dimensions.

3.2.4 Determination of contact angles

A Ramé-Hart standard contact angle goniometer (model 200-F1; Succusunna, NJ) with Drop Image Advanced software was used to measure contact angles on PMMA films. Data were acquired as volume was added or retracted from the surface to determine the advancing and receding contact angles. A minimum of three independent measurements were made on each surface using deionized water and diiodomethane (DIM).

3.2.5 Wenzel to Cassie wetting transition calculations

Roughness plays a part in the wettability of a surface. The Wenzel model was derived using surface force balance and empirical considerations and relates the contact angle upon a rough solid surface, Θ, to the contact angle on a smooth surface Θ_0 [23]. This relation is described by:

$$\cos\Theta = R_f \cos\Theta_0 \qquad (1).$$

R_f is a nondimensional surface roughness factor that is equal to the ratio of the surface area to its flat projected area $R_f = A_{SL}/A_F$. R_f can be determined for the nanoPMMA surfaces as described below (modified from the approach for rectangular asperities[23].) The area of each rectangular asperity on nanoPMMA, A_{asp}= 2rl + 2hl where 2r = width of each grating, l is the length of each grating (using 1000 nm) and h is the height of each grating. Thus, A_{SL}= A_F + A_F η(2rl + 2hl)- $A_F\eta$2rl where η is the

density of asperities per unit area (1000 nm x 1000nm). Simplifying this yields $A_{SL} = A_F (2hl\eta + 1)$. Thus, $R_f = 2hl\eta + 1$. Cassie wetting, in contrast, involves surfaces of two fractions, one with fractional area f_1 and contact angle Θ_1 and the other fractional area f_2 and contact angle Θ_2 so that $f_1 + f_2 = 1$. The contact angle for the Cassie equation is given by:

$$\cos\ \Theta\ = f_1 \cos\Theta_1 + f_2 \cos\Theta_2 \quad (2).$$

For the special case of a composite interface consisting of the solid-liquid fraction ($f_1 = f_{SL}$, $\Theta_1 = \Theta_0$) and liquid-air fraction ($f_2 = f_{LA} = 1 - f_{SL}$, $\cos\Theta_2 = -1$) and combining R_f and equation 2 yields the Cassie-Baxter equation:

$$\cos\Theta = R_f f_{SL} \cos\Theta_0 - 1 + f_{SL} \quad (3).$$

Using values of 0.5 for f_{SL} and 1.48, 1.63, and 1.79 for R_f for G415, G303, and G140 surfaces respectively, the Wenzel and Cassie-Baxter equations were graphed to determine where the transition occurs between the Wenzel and Cassie wetting regimes.

3.2.6 Surface free energy calculations

We used equations first presented by Owens and Wendt [24] and used recently for nanoPMMA films to determine surface free energy[25]. Briefly, the relation between contact angle and surface free energy (SFE) is:

$$1+\cos\theta = 2\sqrt{\gamma_s^d}\left(\frac{\sqrt{\gamma_l^d}}{\gamma_l}\right)+2\sqrt{\gamma_s^h}\left(\frac{\sqrt{\gamma_l^h}}{\gamma_l}\right) \qquad (4)$$

where $\gamma_l = \gamma_l^d + \gamma_l^h$ and $\gamma_s = \gamma_s^d + \gamma_s^h$ are the surface free energies of a given liquid and solid. The contributions from different intermolecular forces are denoted by the superscripts: h and d refer to the hydrogen bonding and dispersion force components, respectively. Thus, using contact angles from two different liquids (water and DIM; see above), two equations can be solved simultaneously for γ_s^d and γ_s^h, to obtain γ_s, in this case the SFE of PMMA. We used the average advancing angles to compute a SFE value. Additionally, we used γ_l^h = 49.5 mN/m, γ_l^d = 1.3 mN/m and γ_l^h = 51 mN/m, γ_l^d = 21.8 mN/m for the respective DIM and water surface free energy components.

3. 2.7 Statistical Analysis

Statistical analyses were carried out using GraphPad Prism software. All data were assessed for normality (where appropriate) using the D'Agostino-Pearson normality test. When appropriate, one-way ANOVA or the Kruskal-Wallis analysis with the respective post-hoc (Tukey or Dunn's) test was performed. Data are reported as means ± standard deviations. Significance was set at $p < 0.05$.

3.3 Results

3.3.1 Nanotopography on PMMA films is confirmed by AFM.

PMMA films with nanotopographic features were fabricated using UV-assisted capillary force lithography (Figure 3.1). The topographic dimensions of the films were confirmed using AFM (Figure 3.3C). As expected, the films had similar dimensions to the Si master molds that were used for polymerization, and the substrates were designated G415, G303, and G140 based on these dimensions (Table 3.1; Figure 3.3).

3.3.2 Nanotopography on PMMA films is confirmed by SEM.

SEM micrographs (Figure 3.3A) of the PMMA nanotopographic films confirmed the AFM measurements- nanotopographic dimensions were imparted when these substrates were fabricated with capillary-assisted UV- lithography.

3.3.3 Contact angle measurements illustrate anisotropic wettability.

Measurements of contact angle using water and diiodomethane revealed contact angle anisotropy (Figure 3.4). Our results are in agreement with reports that suggested that as groove depth increases the contact angle decreases [26] and anistropic wetting increases as groove depth increases [27] as observed in our contact angle measurements on nanoPMMA parallel to the gratings (Figure 3.4B). Additionally, measurements of contact angles orthogonal to the gratings showed an increase. This increase is due to pinning at the grating wall as additional energy is needed for the drop to continue spreading orthogonal to the gratings. Thus, spreading is preferential

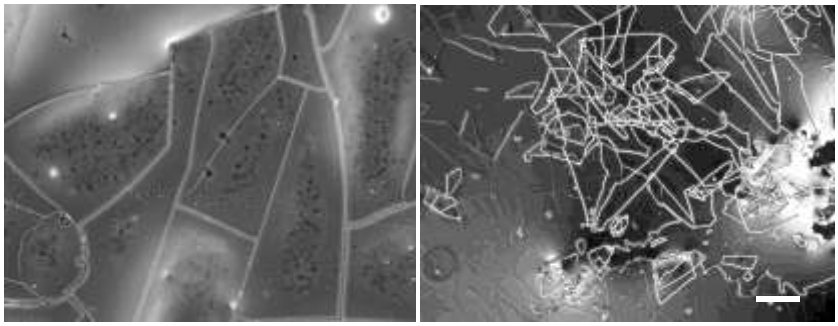

Figure 3.2. First generation nanoPMMA films produced via capillary assisted UV lithography were prone to cracking. As evident by these micrographs, exposure to ethanol or a few days in PBS solution (day 1 left micrograph, day 14 right micrograph) lead to significant instability and degradation of nanoPMMA films. This behavior was observed on all nanoPMMA film sizes. Processing parameters were changed to overcome this problem. (Scale 200 microns.)

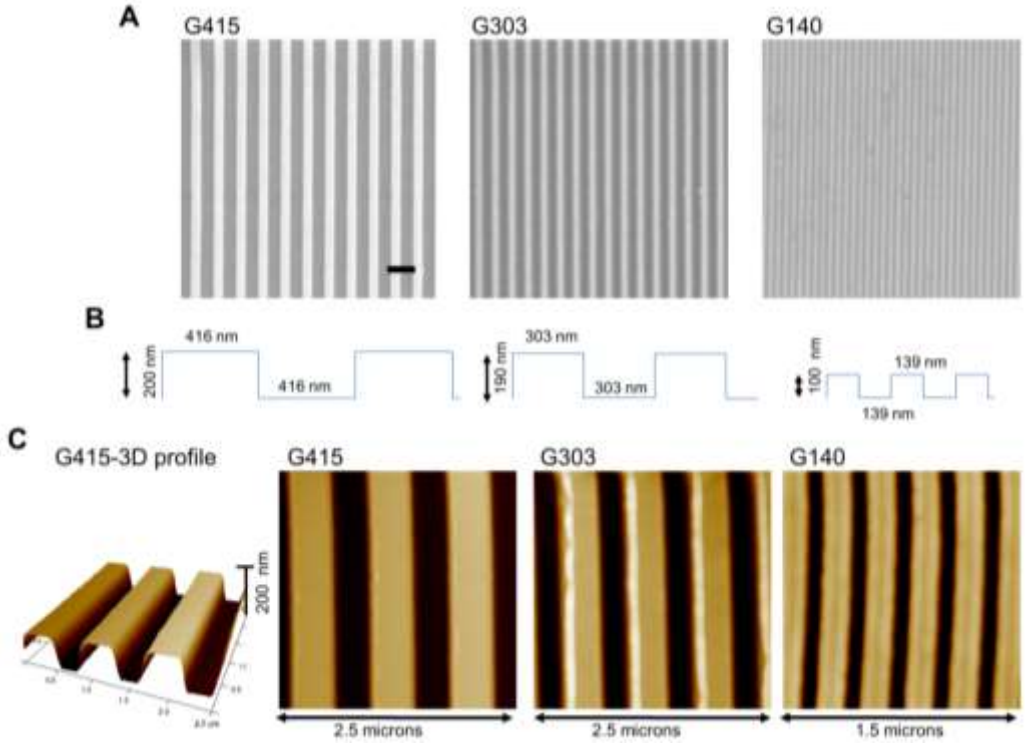

Figure 3.3. Capillary assisted UV lithography produced thin film substrates with nanotopography (2nd generation). (A) Scanning electron microscopy (SEM) was utilized to image nanoPMMA films. Micrographs confirm the presence of nanoscale dimensions in all three of the different film types utilized in this study: G415, G303, and G140 (scale bar = 1 micron). (B) Illustrations show the approximate dimensions (height and width) of the PMMA films. (C) Atomic force microscopy was used to confirm that PMMA films had the expected nanotopographic features (see Table 3.1 for dimensions).

along the grooves rather than perpendicular to the grooves as the energy cost is lower[28].

3.3.4 The Wenzel to Cassie transition is influenced by nanotopography.

The transition between Wenzel and Cassie wetting is illustrated in Figure 3.5. The Wenzel regime dominates all the surfaces from 0 to ~120° and then the transition to the Cassie regime begins. The transition angle is 132.5, 127.9, and 123.9° for G415, G303, and G140 surfaces respectively.

3.3.5 Surface free energy calculations illustrate slight differences and anisotropy.

Using the contact angle measurements, we then calculated the surface free energy of each surface using the approximation from Owens and Wendt for polymers[24]. While this approximation may not fully model the physical situation, however, most theoretical thermodynamic approximations for microscale and nanoscale gratings have yet to be verified experimentally[29-31]. Experimental validation is important as the Wenzel and Cassie theories do not always hold up in practice; three phase contact line approaches seem to be more valid.[32]. One report validated contact angle measurements parallel to micro and nanogratings (in agreement with Wenzel) but did not discuss SFE estimations different than Owens and Wendt[33]. The surface free energy of smooth PMMA was calculated to be 40.0 mN/m, very similar to the 40.2 mN/m value reported by Owens and Wendt. Our SFE calculations for nanoPMMA revealed changes in values depending on the direction of measurement (Table 3.2).

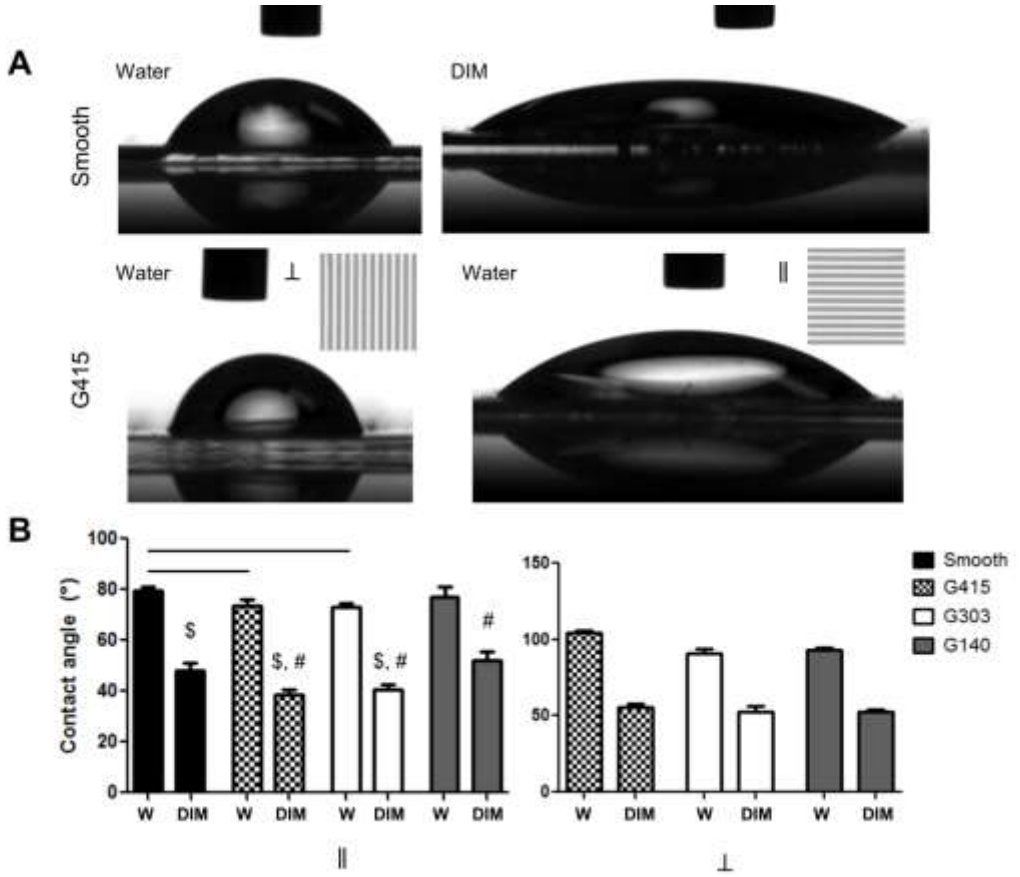

Figure 3.4. Contact angle measurements show anisotropy dependent on surface orientation. (A) Images illustrating wettability of water or diiodomethane on smooth or G415 PMMA films. Insets on G415 images show the direction of the underlying topography (⊥ indicates a drop perpendicular to the long axis of the topography; ‖ indicates a drop parallel to the long axis of the topography). Contact angle anisotropy can be observed on the G415 surfaces and also occurred on other nanoPMMA films (data not shown). (B) Graphs illustrate the quantification of the contact angles both parallel and perpendicular to the grating direction. Significant differences were seen between smooth PMMA and G415 and G303 (parallel) for water and DIM ($) contact angles ($). All surfaces, when perpendicular contact angles for nanoPMMA were compared to smooth PMMA for both liquids, were significant. W indicates contact angle measurement of water; DIM indicates indicates contact angle measurement of diiodomethane. All significance was $p<0.05$ (or smaller), $n \geq 3$.

SFE parallel to the gratings was higher for G415 and G303 surfaces and slightly lower but similar for G140 surfaces compared to smooth PMMA SFE. Perpendicular SFE values were slightly lower than smooth PMMA SFE and lower than SFE for

nanofilms parallel to nanogratings. These values are similar to those reported previously[25]. Our calculations confirm nanoPMMA film anisotropy.

Table 3.2 Calculated surface free energy values for PMMA films.

	(mN/m)	Smooth	G415 ‖	G303 ‖	G140 ‖	G415 ⊥	G303 ⊥	G140 ⊥
	γ_s^d	35.4	40.2	39.4	33.1	31.0	32.6	32.8
	γ_s^h	4.6	5.7	6.0	6.1	0.1	1.6	1.2
Total	$\gamma_{s,\,PMMA}$	40.0	45.9	45.5	39.2	31.1	34.2	34.0

3.4 Discussion

The ECM of bone is composed of mineral and collagen I fibrils. These Col I fibrils are arranged in an highly organized and structured way giving rise to mechanical strength and toughness. Mechanical toughness is reportedly due to the composite mineral and collagen structure[18,20]. Critical to mineral formation are the 10 to 100 nm gaps between fibrils that support aggregation and growth of amorphous hydroxyapatite particles[34,35]. Thus, being that the ECM is an instructive material that plays an important role in both normal and pathologic development and that recent studies have emphasized that the ECM's physical features induce a cellular response we created surfaces that mimic the nanoscale architecture of collagen fibrils. We manufactured PMMA substrates with nanoscale gratings via capillary assisted UV lithography and used them to assess the potential functional influence of ECM topography on the osteogenic phenotype of MSCs (see Chapter 4 for cell discussion

on modulated cell behavior.) We show that using this UV lithographic technique we are able to produce surfaces that mimic the size and structure of collagen fibrils in native bone.

To manufacture these substrates we employed a method that utilizes the capillarity of small channels to draw the precursor of MMA and PMMA into the nanogrooves. The capillary action is prominent in nanochannels because of the high surface to volume ratio[36]. A number of challenges arose in processing PMMA films

A

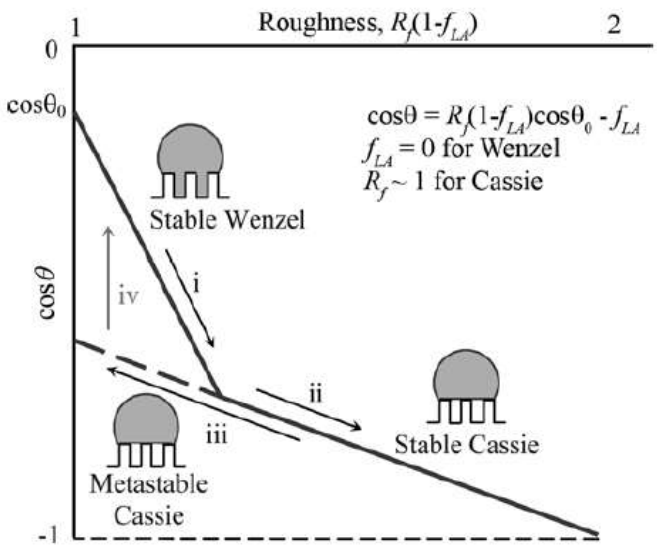
1
Roughness, $R_f(1-f_{LA})$
2
0
$\cos\theta_0$
$\cos\theta = R_f(1-f_{LA})\cos\theta_0 - f_{LA}$
$f_{LA} = 0$ for Wenzel
$R_f \sim 1$ for Cassie
Stable Wenzel
$\cos\theta$
iv
i
ii
iii
Stable Cassie
Metastable Cassie
-1

B

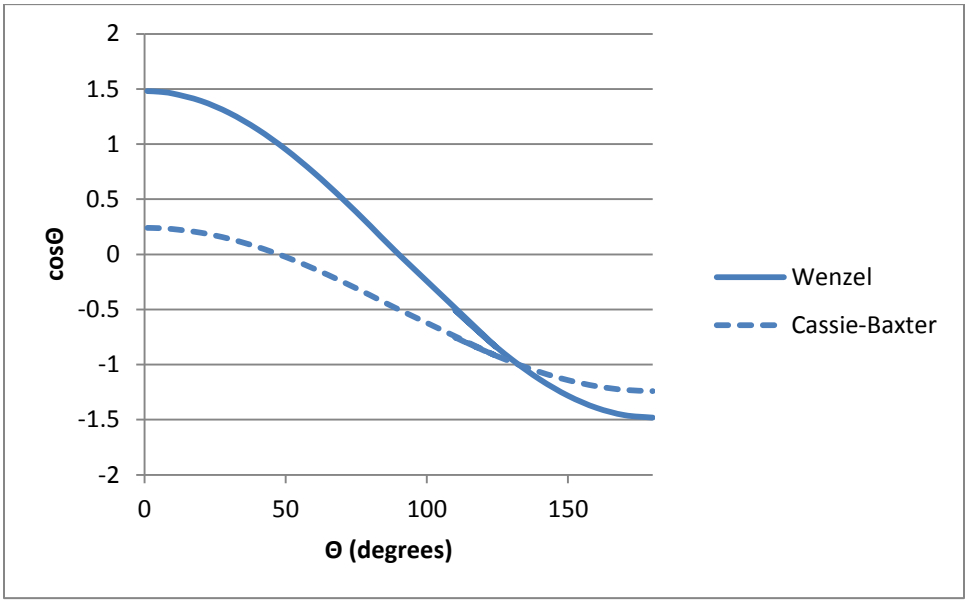
2
1.5
1
0.5
0
-0.5
-1
-1.5
-2
cosΘ
0
50
100
150
Θ (degrees)
Wenzel
Cassie-Baxter

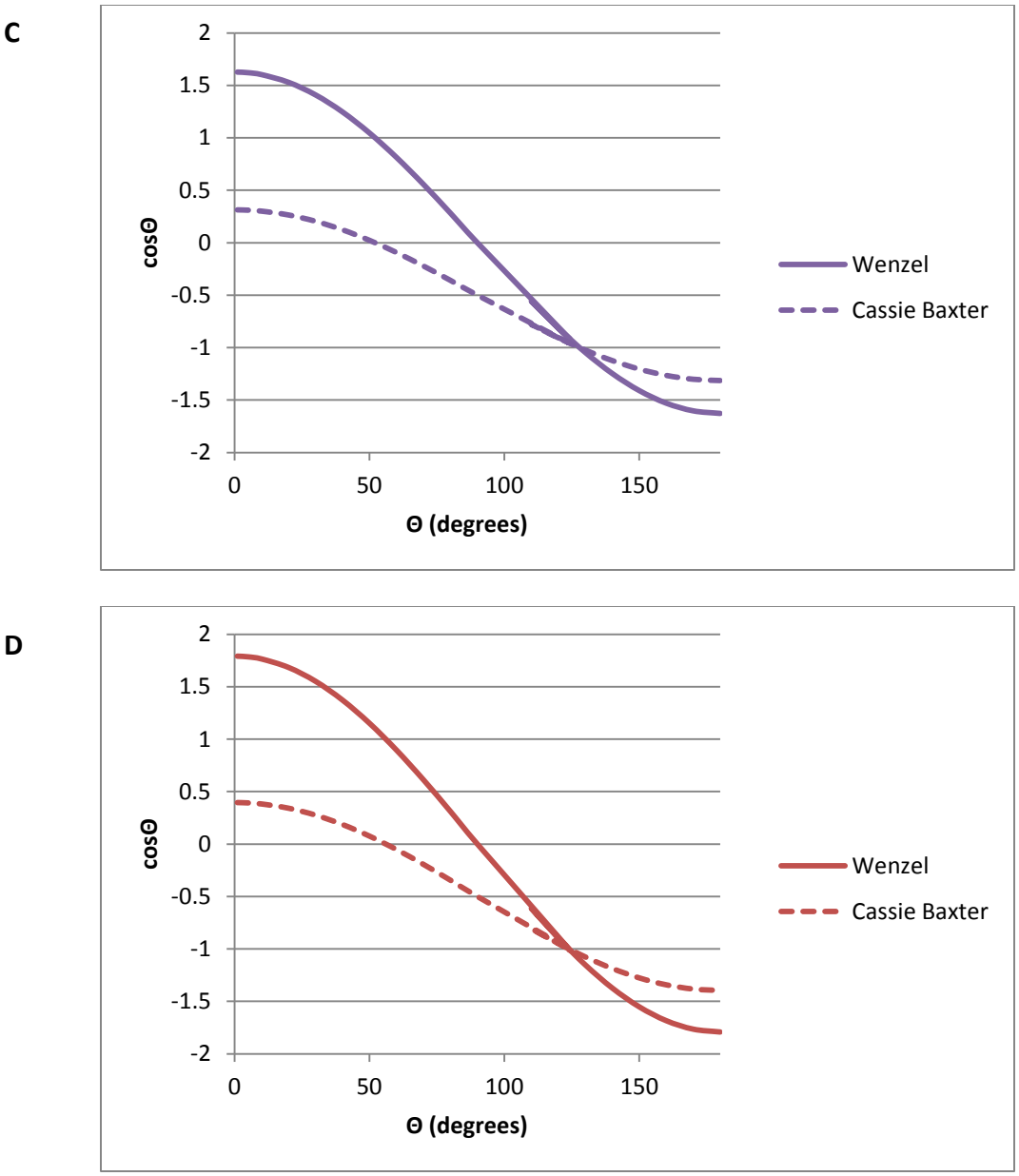

Figure 3.5 The transition between Wenzel and Cassie –Baxter wetting is impacted by the feature size on nanoPMMA. A general schematic for the transition from Wenzel to Cassie Baxter wetting dependent on surface features and the fraction of liquid-air [23]. The graphs seen in B, C, and D, represent the curves for Wenzel and Cassie-Baxter wetting (equations 1 and 3) for G415, G303, and G140 surfaces respectively. Wetting starts in the Wenzel regime and transitions to Cassie-Baxter as contact angle increases. (Values of 0.5 for f_{SL} and 1.48, 1.63, and 1.79 for R_f for G415, G303, and G140 surfaces respectively were used, see Materials and Methods.)

with nanochannels. The first generation of these substrates utilized a low molecular weight PMMA additive (Figure 3.2). Increasing the molecular weight was beneficial.

In addition, these films were susceptible to cracking when sterilized in 70/30% (v/v) ethanol to water prior to biological experimentation. Thus, sterilization was changed to an additional UV exposure of 10 minutes. Also helpful was limiting and preventing water vapor exposure to APMDS during coating of the glass slides. Finally, the precursor PMMA/MMA/initiator solution was used for only up to an 8 hour period, down from up to a 48 hour period. All of these changes lead to improvements in the film stability. The second generation of nanoPMMA films was much less susceptible to cracking and delamination.

After quantitatively confirming the features molded on the second generation nanoPMMA films, we investigated the wettability and calculated surface free energies from contact angle measurements. The anisotropy of the surface features was reflected in the contact angle measurements and the surface free energy calculations. The standard definition of hydrophilicity regards surfaces with contact angles of less than 90° as hydrophilic. Surfaces with contact angles greater than 90 ° are deemed hydrophobic. Our results suggest that smooth PMMA surfaces are hydrophilic. When Wenzel wetting occurs on a hydrophilic surface, as we observed, hydrophiliciy increases on surfaces with high R_f [23].(It should be noted that the smooth PMMA films have an inherent roughness and are not atomistically smooth. The roughness (R_a or R_q)is lower than that of the controlled roughness of the imparted gratings.) Hence, the G140 surfaces should be the most hydrophilic of the nanoPMMA. When considering contact angle anistropy, nanoPMMA films are slightly hydrophilic (parallel) and

slightly hydrophobic (perpendicular) dependent on groove direction. Our calculated surface energies for smooth PMMA were similar to values reported by Owens and Wendt and our nanoPMMA SFE values were similar to those in a previous report [24,25]. These findings also agree with recent simulations as discussed in detail below.

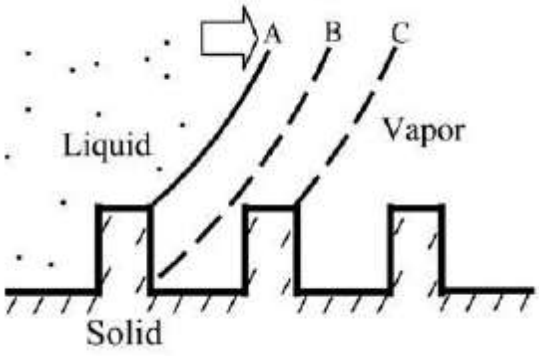

Figure 3.6 Liquid motion perpendicular to the gratings is impeded. The schematic illustrates discrete stages of liquid motion perpendicular to the grating direction. The gratings present an energy barrier[23].

Approaches to understand wetting and surface free energy on the nanoscale are still limited, yet one recent report estimated the influence of feature shape and size on the energy barrier for droplet motion (see schematic in Figure 3.7)[27]. In particular, the droplet motion is impeded when parallel nanogrooves are present but only in the direction perpendicular to the grooves. This impediment leads to the droplet shape anisotropy, similar to what we observed on nanoPMMA. As the feature height increases the barrier energy also increases (Figure 3.7). This energy barrier does not exist in the direction parallel to the grooves[27], hence, the droplet can expand

unimpeded parallel to the grooves. The barrier results from the work required to extend the liquid-air interface and the liquid-solid interface[37]. (These predictions were validated by another study that showed discrete jumps in droplet motion perpendicular to the groove direction (Figure 3.6). Motion parallel to the gratings was continuous. Retraction of the droplet proceeds, initially, with preferential withdrawal parallel to the grooves, then switches directions when the drop shape distortion is so great that the energetics favors perpendicular retraction[33].) Though the geometry of these predictions is not identical to our gratings these predictions are corroborated by what we observed experimentally: G415 surfaces have the greatest depth (200 nm), thus, had the greatest anisotropy in the contact angles (as observed in the difference between and measurements), and had the greatest anisotropy in observed SFE. This suggests that the G415 had the greatest energy barrier for droplet motion perpendicular to the gratings. This makes the gratings 'more wettable' in the parallel direction and 'less wettable' transverse to the gratings. We reemphasize that these recent reports have not suggested new or refined methods for calculating SFE that differ from the method proposed by Owens and Wendt.

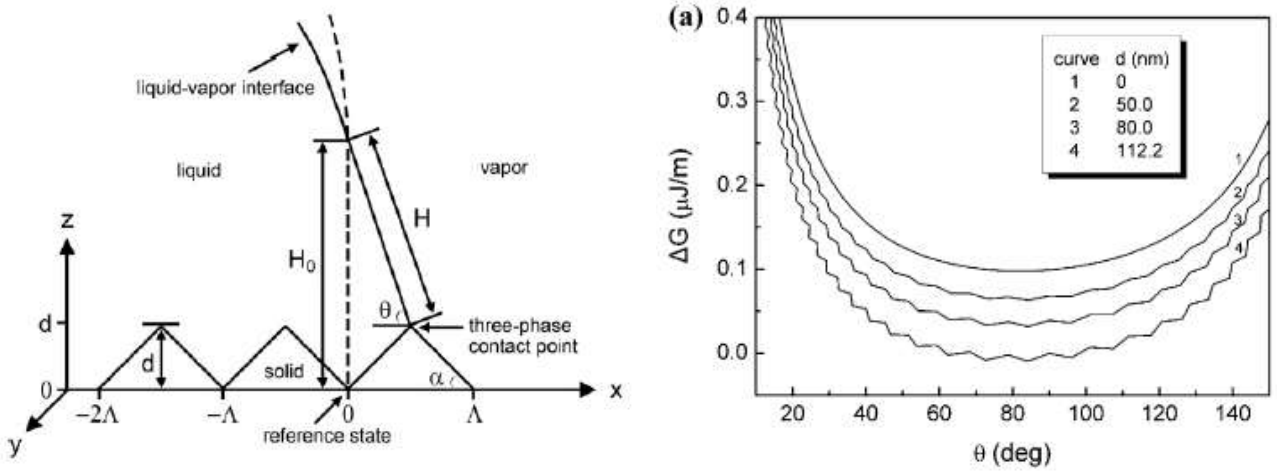

Figure 3.7 Modelling the droplet motion energy barrier shows that feature size height is important. Schematic illustrating the surface geometry and three-phase contact line used to predict the energy barrier for droplet motion perpendicular to the grooves. The graph shows the free energy change as a function of the instantaneous contact angle perpendicular to the grooves. As groove height increases the free energy change increases, indicating a larger barrier for motion[27].

The question that remains: does this altered wettability significantly alter how a protein adsorbs? Overall, it would be beneficial to understand how these surface free energy differences will influence protein adsorption. However, there is currently no accepted framework of nanoscale structure-property relationships that relates interfacial energy to the degree and specificity of protein adsorption. [38] Part of the reason for this is because the wide range of elements that comprise proteins makes even simple hypotheses regarding adsorption difficult[39]. Proteins are usually only a few nanometers in size, meaning that the interaction area of an individual protein with a surface such as our nanoPMMA will be relatively small. In our case, the nanoscale gratings on PMMA films increase the available surface area (G415- 48% greater

surface area, G303- 63%, and G140- 79%) compared to smooth PMMA films, thus there is the potential for greater protein interaction on nanoPMMA. Increased protein adsorption, however, has been shown to both hinder and promote cell adhesion[40-42]. More important than protein amount is the conformation of the adsorbed protein. Thus, in the discussion below, we try to discern if changes in surface free energy can predict changes in protein conformation giving rise to potential downstream changes in cell behavior.

It is widely accepted that most proteins undergo conformational changes when adsorbed onto a solid surface. The conformational changes result because a protein's free energy minimum in solution is rarely the minimum when in contact with a surface[39]. Comparing the total energy changes of nanoPMMA to approximate changes in protein conformation is necessary to attempt to predict the influence of topography on cell behavior. One way to estimate the effect of the changes in SFE energy on proteins is to compare it to the energy needed to unfold ECM proteins. A report suggests that as little as 5 pN of force can be exerted by a single motor protein[43]. This force can unfold ECM proteins (when sustained for 1 minute; 170 pN can do the same in 0.001 second). We can use this information to estimate the energy per area required to unfold an ECM molecule like fibronectin. Fibronectin has a hydrodynamic radius of 9 nm and has a hydrodynamic radius of 22 nm when elongated. We can use this information to estimate 25 nm as the approximate distance of unfolding, along with a 5 pN force, and an area of πr^2 (r= 9 nm) to calculate an energy of unfolding to

be ~0.50 mJ/m^2 per fibronectin molecule. If we want to know the total energetic requirement for fibronectin in soltution, we start with its serum concentration which is reported to be 300 μg/mL in serum[44]. We typically use 20% FBS (v/v) in cell media formulations, hence the concentration of FN is ~60 μg/mL. Thus, through simple calculations converting to total moles and total molecules etc. we can see that the total energy required for all fibronectin unfolding is ~4 x 10^{13} mJ/m^2. At the single molecule level, there is sufficient additional SFE in the direction parallel to the nanogratings to unfold ~10 fibronectin molecules. Clearly this is a minute number relative to the total number of fibronectin and other ECM molecules present in FBS. Even if this estimate is off by 2 or 3 orders of magnitude the number of proteins significantly modulated by the surface is a small percentage of the whole. Additionally, there are protein-protein interactions, competitive adsorption, and other factors which will alter the conformational landscape. Hence, these estimates suggest that unless a low concentration of serum proteins is used, the proteins will likely not be significantly altered to expose cryptic binding sites[43] that may promote osteogenesis compared to smooth surfaces.

We showed that we can create nanotopographic films of PMMA that mimic the scale and architecture of bone. Contact angle measurements and wetting calculations revealed that Wenzel wetting occurs on nanoPMMA. Additionally, the surface features induce anistropy in wettability, causing surface orientation dependent changes in SFE. We estimated how these SFE changes may influence protein

unfolding and from these estimates predicted that protein changes would not be sufficient to enhance osteogenesis in MSCs.

3.5 References

1 Prodanov, L. *et al.* The effect of nanometric surface texture on bone contact to titanium implants in rabbit tibia. *Biomaterials* **34**, 2920-2927, doi:DOI 10.1016/j.biomaterials.2013.01.027 (2013).

2 Kim, J. *et al.* Synergistic effects of nanotopography and co-culture with endothelial cells on osteogenesis of mesenchymal stem cells. *Biomaterials* **34**, 7257-7268, doi:DOI 10.1016/j.biomaterials.2013.06.029 (2013).

3 Watari, S. *et al.* Modulation of osteogenic differentiation in hMSCs cells by submicron topographically-patterned ridges and grooves. *Biomaterials* **33**, 128-136, doi:DOI 10.1016/j.biomaterials.2011.09.058 (2012).

4 Guilak, F. *et al.* Control of Stem Cell Fate by Physical Interactions with the Extracellular Matrix. *Cell Stem Cell* **5**, 17-26, doi:DOI 10.1016/j.stem.2009.06.016 (2009).

5 Huebsch, N. & Mooney, D. J. A Role for Integrin-ECM Bonds as Mechanotransducers that Modulate Adult Stem Cell Fate. *Mechanobiology of Cell-Cell and Cell-Matrix Interactions*, 23-46, doi:Doi 10.1007/978-1-4419-8083-0_3 (2011).

6 Biggs, M. J. P. *et al.* The use of nanoscale topography to modulate the dynamics of adhesion formation in primary osteoblasts and ERK/MAPK signalling in STRO-1+enriched skeletal stem cells. *Biomaterials* **30**, 5094-5103, doi:DOI 10.1016/j.biomaterials.2009.05.049 (2009).

7 Khatiwala, C. B., Kim, P. D., Peyton, S. R. & Putnam, A. J. ECM Compliance Regulates Osteogenesis by Influencing MAPK Signaling Downstream of RhoA and ROCK. *J Bone Miner Res* **24**, 886-898, doi:Doi 10.1359/Jbmr.081240 (2009).

8 Khatiwala, C. B., Peyton, S. R., Metzke, M. & Putnam, A. J. The regulation of osteogenesis by ECM rigidity in MC3T3-E1 cells requires MAPK activation. *J Cell Physiol* **211**, 661-672, doi:Doi 10.1002/Jcp.20974 (2007).

9 Engler, A. J., Sen, S., Sweeney, H. L. & Discher, D. E. Matrix elasticity directs stem cell lineage specification. *Cell* **126**, 677-689, doi:DOI 10.1016/j.cell.2006.06.044 (2006).

10 Dalby, M. J. *et al.* The control of human mesenchymal cell differentiation using nanoscale symmetry and disorder. *Nat Mater* **6**, 997-1003, doi:Doi 10.1038/Nmat2013 (2007).

11 Khang, D. *et al.* Role of subnano-, nano- and submicron-surface features on osteoblast differentiation of bone marrow mesenchymal stem cells. *Biomaterials* **33**, 5997-6007, doi:DOI 10.1016/j.biomaterials.2012.05.005 (2012).

12 Kilian, K. A., Bugarija, B., Lahn, B. T. & Mrksich, M. Geometric cues for directing the differentiation of mesenchymal stem cells. *P Natl Acad Sci USA* **107**, 4872-4877, doi:DOI 10.1073/pnas.0903269107 (2010).

13 Kulangara, K., Yang, Y., Yang, J. & Leong, K. W. Nanotopography as modulator of human mesenchymal stem cell function. *Biomaterials* **33**, 4998-5003, doi:DOI 10.1016/j.biomaterials.2012.03.053 (2012).

14 McBeath, R., Pirone, D. M., Nelson, C. M., Bhadriraju, K. & Chen, C. S. Cell shape, cytoskeletal tension, and RhoA regulate stem cell lineage commitment. *Dev Cell* **6**, 483-495, doi:Doi 10.1016/S1534-5807(04)00075-9 (2004).

15 Prodanov, L. *et al.* The interaction between nanoscale surface features and mechanical loading and its effect on osteoblast-like cells behavior. *Biomaterials* **31**, 7758-7765, doi:DOI 10.1016/j.biomaterials.2010.06.050 (2010).

16 Wood, J. A. *et al.* The modulation of canine mesenchymal stem cells by nano-topographic cues. *Exp Cell Res* **318**, 2438-2445, doi:DOI 10.1016/j.yexcr.2012.06.022 (2012).

17 Yim, E. K. F., Darling, E. M., Kulangara, K., Guilak, F. & Leong, K. W. Nanotopography-induced changes in focal adhesions, cytoskeletal organization, and mechanical properties of human mesenchymal stem cells. *Biomaterials* **31**, 1299-1306, doi:DOI 10.1016/j.biomaterials.2009.10.037 (2010).

18 Weiner, S. & Wagner, H. D. The material bone: Structure mechanical function relations. *Annual Review of Materials Science* **28**, 271-298, doi:DOI 10.1146/annurev.matsci.28.1.271 (1998).

19 Allori, A. C., Sailon, A. M. & Warren, S. M. Biological basis of bone formation, remodeling, and repair - Part II: Extracellular matrix. *Tissue Eng Part B-Re* **14**, 275-283, doi:DOI 10.1089/ten.teb.2008.0083 (2008).

20 Kerschnitzki, M. *et al.* The organization of the osteocyte network mirrors the extracellular matrix orientation in bone. *J Struct Biol* **173**, 303-311, doi:DOI 10.1016/j.jsb.2010.11.014 (2011).

21 Lewis, G. Viscoelastic properties of injectable bone cements for orthopaedic applications: State-of-the-art review. *J Biomed Mater Res B* **98B**, 171-191, doi:Doi 10.1002/Jbm.B.31835 (2011).

22 Jaberi, J., Gambrell, K., Tiwana, P., Madden, C. & Finn, R. Long-Term Clinical Outcome Analysis of Poly-Methyl-Methacrylate Cranioplasty for Large Skull Defects. *J Oral Maxil Surg* **71**, E81-E88, doi:DOI 10.1016/j.joms.2012.09.023 (2013).

23 Nosonovsky, M. & Bhushan, B. Multiscale Dissipative Mechanisms and Hierarchical Surfaces: Friction, Superhydrophobicity, and Biomimetics. *Nanosci Technol*, 1-277 (2008).

24 Owens, D. K. & Wendt, R. C. Estimation of Surface Free Energy of Polymers. *J Appl Polym Sci* **13**, 1741-&, doi:DOI 10.1002/app.1969.070130815 (1969).

25 Liu, Y. J. *et al.* Nanoimprinted ultrafine line and space nanogratings for liquid crystal alignment. *Nanotechnology* **23**, doi:Artn 465302 Doi 10.1088/0957-4484/23/46/465302 (2012).

26 Yong, X. & Zhang, L. T. Nanoscale Wetting on Groove-Patterned Surfaces. *Langmuir* **25**, 5045-5053, doi:Doi 10.1021/La804025h (2009).

27 Zhao, Y., Lu, Q. H., Li, M. & Li, X. Anisotropic wetting characteristics on submicrometer-scale periodic grooved surface. *Langmuir* **23**, 6212-6217, doi:Doi 10.1021/La0702077 (2007).

28 Chung, J. Y., Youngblood, J. P. & Stafford, C. M. Anisotropic wetting on tunable micro-wrinkled surfaces. *Soft Matter* **3**, 1163-1169, doi:Doi 10.1039/B705112c (2007).

29 Li, W., Fang, G. P., Lij, Y. F. & Qiao, G. J. Anisotropic wetting behavior arising from superhydrophobic surfaces: Parallel grooved structure. *J Phys Chem B* **112**, 7234-7243, doi:Doi 10.1021/Jp712019y (2008).

30 Leroy, F. & Muller-Plathe, F. Can Continuum Thermodynamics Characterize Wenzel Wetting States of Water at the Nanometer Scale? *J Chem Theory Comput* **8**, 3724-3732, doi:Doi 10.1021/Ct300089j (2012).

31 Hirvi, J. T. & Pakkanen, T. A. Wetting of nanogrooved polymer surfaces. *Langmuir* **23**, 7724-7729, doi:Doi 10.1021/La700558v (2007).

32 Gao, L. C. & McCarthy, T. J. An Attempt to Correct the Faulty Intuition Perpetuated by the Wenzel and Cassie "Laws". *Langmuir* **25**, 7249-7255, doi:Doi 10.1021/La901416m (2009).

33 Kusumaatmaja, H., Vrancken, R. J., Bastiaansen, C. W. M. & Yeomans, J. M. Anisotropic drop morphologies on corrugated surfaces. *Langmuir* **24**, 7299-7308, doi:Doi 10.1021/La800649a (2008).

34 Landis, W. J., Song, M. J., Leith, A., Mcewen, L. & Mcewen, B. F. Mineral and Organic Matrix Interaction in Normally Calcifying Tendon Visualized in 3 Dimensions by High-Voltage Electron-Microscopic Tomography and Graphic Image-Reconstruction. *J Struct Biol* **110**, 39-54, doi:DOI 10.1006/jsbi.1993.1003 (1993).

35 Nudelman, F. *et al.* The role of collagen in bone apatite formation in the presence of hydroxyapatite nucleation inhibitors. *Nat Mater* **9**, 1004-1009, doi:Doi 10.1038/Nmat2875 (2010).

36 Tas, N. R., Haneveld, J., Jansen, H. V., Elwenspoek, M. & van den Berg, A. Capillary filling speed of water in nanochannels. *Appl Phys Lett* **85**, 3274-3276, doi:Doi 10.1063/1.1804602 (2004).

37 Johnson, R. E. & Dettre, R. H. Contact Angle Hysteresis .3. Study of an Idealized Heterogeneous Surface. *J Phys Chem-Us* **68**, 1744-&, doi:Doi 10.1021/J100789a012 (1964).

38 Hung, A. *et al.* Ordering Surfaces on the Nanoscale: Implications for Protein Adsorption. *J Am Chem Soc* **133**, 1438-1450, doi:Doi 10.1021/Ja108285u (2011).

39 Rabe, M., Verdes, D. & Seeger, S. Understanding protein adsorption phenomena at solid surfaces. *Adv Colloid Interfac* **162**, 87-106, doi:DOI 10.1016/j.cis.2010.12.007 (2011).

40 Szott, L. M. & Horbett, T. A. Protein interactions with surfaces: cellular responses, complement activation, and newer methods. *Curr Opin Chem Biol* **15**, 677-682, doi:DOI 10.1016/j.cbpa.2011.04.021 (2011).

41 Koh, L. B., Rodriguez, I. & Venkatraman, S. S. The effect of topography of polymer surfaces on platelet adhesion. *Biomaterials* **31**, 1533-1545, doi:DOI 10.1016/j.biomaterials.2009.11.022 (2010).

42 Koh, L. B., Rodriguez, I. & Venkatraman, S. S. Conformational behavior of fibrinogen on topographically modified polymer surfaces. *Phys Chem Chem Phys* **12**, 10301-10308, doi:Doi 10.1039/C001747g (2010).

43 Vogel, V. & Sheetz, M. Local force and geometry sensing regulate cell functions. *Nat Rev Mol Cell Bio* **7**, 265-275, doi:Doi 10.1038/Nrm1890 (2006).

44 Underwood, P. A. & Bennett, F. A. A Comparison of the Biological-Activities of the Cell-Adhesive Proteins Vitronectin and Fibronectin. *J Cell Sci* **93**, 641-649 (1989).

CHAPTER 4

The Influence of PMMA Nanotopography on the Osteogenic Phenotype of Mesenchymal Stem Cells

4.1 Introduction

Chapter 3 discussed a method to produce surfaces which have similar size and alignment of collagen fibrils that are found in native bone. As has been discussed in previous chapters, the clinical need to improve current orthopedic implants is twofold: 1. to reduce the economic impact, and most importantly, 2.) to improve the quality of life of thousands of people. Thus, strategies which add to our current knowledge of bone formation or enhance current clinical practices are desirable. Improvements will likely prolong implant lifetime, reduce the need for revision surgery, drive down the economic impact, and improve quality of life.

To achieve these goals, stem cells, specifically, adult mesenchymal stem cells have been targeted for bone regeneration strategies. Mesenchymal stem cells (MSCs) are self-renewing marrow derived cells that are multipotent[1]. Because of the relative ease of isolation and high degree of plasticity, MSCs have been explored for tissue engineering and regenerative medicine applications[2-5]. MSCs' plasticity includes the

ability to differentiate into chondrogenic, adipogenic and osteogenic phenotypes. Promoting an osteogenic lineage may be useful for bone tissue engineering strategies when combined with scaffolds to enhance osteogenesis for various orthopedic therapies[6].

A cell's environment is crucial to its function and behavior, and an important feature of the cellular microenvironment is the ECM (as discussed in previous chapters). Cells recognize and respond to chemical and physical ECM cues, including adhesive ligands, mechanical properties, and topography [5,7]. Cells adhere to the ECM's various binding motifs through transmembrane integrin receptors. Integrin receptors are capable of transducing adhesive signals into biochemical signals and physically connect the ECM to the cytoskeleton. ECM proteins (e.g. collagen I, vitronectin, fibronectin) contain different ligands that may engage different integrin receptors; specific integrins are known to regulate osteogenic differentiation[8]. Matrix mechanical properties have also been shown to influence osteogenic differentiation, with more rigid substrates driving osteogenic differentiation in 2D cell cultures[9-11]. Other studies have shown micro- and nanotopography of varied surface chemistries to influence osteogenic differentiation as well[1,6,8,12-19].

Producing *in vivo* mineral in an *in vitro* environment may be enhanced by mimicking the structure of native bone. Many studies have reported on the influence of micro- and nano-topographies on the proliferation, genotype, and protein levels of osteoprogenitor cells, but rarely have they quantitatively assessed the deposited

mineral. Hence, it is unclear whether topography drives a phenotype capable of producing mineral *in vitro* or *in vivo* similar to physiologically relevant bone. Being able to control or promote osteogenic differentiation via topography may be useful for bone and orthopedic implant applications if mineral production can be enhanced and the mineral produced is chemically similar to native bone.

As discussed in Chapter 3, we created an approximate replica of the nanotopographic structure of bone using an idealized surface of poly(methyl methacrylate) (PMMA) to investigate the role of surface nanotopography in driving the osteogenic differentiation of MSCs. PMMA is used clinically as a bone cement in orthopedic applications [20,21]. Thus, motivated by the potential to enhance osteointegration and bone healing via imprinted nanotopographic cues on an FDA-approved orthopedic material, we focused specifically on mineralization as a functional metric of the mature bone phenotype. We hypothesized that our nanoPMMA surfaces with (controlled) feature sizes and alignment similar to collagen fibrils would enhance mineral quantity. After characterizion with atomic force microscopy (AFM) and scanning electron microscopy (SEM) as discussed in Chapter 3, MSCs were subsequently seeded and cultured on the nanofilms for up to 21 days. Focal adhesion size, cell proliferation, cell alignment, ALP levels, calcium and phosphate deposition, and Ca:P ratios were assessed at various time points to investigate the role of PMMA nanotopography on osteogenic differentiation in MSCs.

4.2 Materials and Methods

4.2.1 Cell culture

Human bone marrow-derived MSCs were obtained from a commercial source (Lonza, Walkersville, MD) at passage 2. As part of the manufacturer's quality control, MSCs were tested for purity by flow cytometry and for their ability to differentiate into osteogenic, chondrogenic and adipogenic lineages and are positive for the cell surface markers CD105, CD166, CD29 (integrin β1), and CD44, and negative for CD14, CD34 and CD45. MSCs were maintained in high glucose (4.5 g/L) Dulbecco's modified Eagle medium (DMEM, Invitrogen, Carlsbad, CA) supplemented with 10% fetal bovine serum (FBS, Invitrogen). All cultures were incubated at 37°C and 5% CO_2. Media were changed every 2-3 days. MSCs were routinely expanded in 2D cultures and harvested with 0.05% Trypsin-EDTA (Invitrogen). Cells were used between passage 6 and 10.

4.2.2 Initial cell adhesion and proliferation

PMMA substrates were cut to approximately 1 cm x 1 cm and sterilized under UV light for ten minutes. After UV sterilization, the substrates were rinsed twice with sterile Dulbecco's phosphate buffered saline (PBS) (Invitrogen) pH 7.4, and then placed in 24 well plates prior to cell seeding. To determine if nanoPMMA influenced the number of adherent MSCs, cells were seeded at 5000 cells/cm^2 and allowed to adhere for four hours in osteogenic growth media (OGM), consisting of alpha-

minimum essential media (αMEM, Invitrogen), 20% FBS, 2 mM L-glutamine (CellGro, Manassas, VA), 1% penticillin/streptomycin (CellGro), and 5 mg/mL gentamicin (Invitrogen). After 4 hours, cells were rinsed with PBS, and then fixed with 4% paraformaldehyde in PBS, stained and imaged as described below. At least 5 different images (10X images) were observed on three separate surfaces. Values were normalized to the average number of cells observed on smooth PMMA surfaces. To determine the influence of nanoPMMA on proliferation, MSCs were seeded at an initial density of 2000 cells/cm^2 and allowed to proliferate in OGM. At day 4, 7, and 14, cells were rinsed with PBS, and then fixed with 4% paraformaldehyde in PBS. Cells were then rinsed with PBS three times. Cells were stained with 4',6-diamidino-2-phenylindole dihydrochloride (DAPI) in PBS (1:5000) for 10 minutes to identify their nuclei. After staining, MSCs were rinsed with PBS and then imaged on an Olympus IX81 microscope equipped with a 100W high-pressure mercury burner (Olympus America, Center Valley, PA), a Hamamatsu Orca II CCD camera (Hamamatsu Photonoics, K.K., Hamamatsu City, Japan), and Metamorph Premier software (Molecular Devices, Sunnyvale, CA). Cells that stained positive for DAPI were manually counted using Image J (NIH, Bethesda, MD). At least six (10X) images were analyzed for each condition. The number of cells per field was converted to cells per area, and then normalized to the initial number of cells seeded (2000 cells/cm^2). Three independent measurements were made and averaged.

4.2.3 Visualization of actin and vinculin using fluorescence microscopy

Cells were seeded at 2000 cells/cm^2 on PMMA films (sterilized as previously described) and grown in osteogenic base media (OBM), consisting of OGM, 10 mM β-glycerol phosphate, and 50 μg/mL L-ascorbic acid (Fisher Scientific). At day 1, 4, and 7, cells were washed with PBS, permeabilized with 10 mM N-2-hydroxyethylpiperazine-N'-2-ethanesulfonic acid (HEPES) pH 6.9, 50 mM NaCl, 3mM $MgCl_2$, 300 mM sucrose, and 1 mM ethylene glycol tetraacetic acid (EGTA) with 0.5% Triton X-100 for one minute, washed, and then permeabilized again for 30 seconds in the same buffer before fixation. Cells were then fixed with 4% paraformaldehyde in PBS. These short permeabilization steps prior to fixation remove cytosolic vinculin as previously described [22]. Cells were washed with Tris-buffered saline (250 mM Tris, 27 mM KCl, 1.37 M NaCl pH 7.4; TBS, Fisher Scientific) + 0.1% Triton X-100 (TBS-T) prior to blocking. Cells were then blocked with Abdil (2% bovine serum albumin in TBS-T) for 20 minutes and washed again with TBS-T. Cells were then incubated with Oregon Green 488 Phalloidin (Invitrogen) to stain F-actin (1:40) and mouse anti-human vinculin (1:250) to label focal adhesions in Abdil for 45 minutes. Following incubation, a TBS-T wash was used to remove unbound antibodies. Cells were then incubated for 45 minute with goat anti-mouse Alexa Fluor 594 (Invitrogen) in Abdil (1:450). Cells were then washed in TBS-T at least three times. Stained MSCs on PMMA substrates were imaged on the Olympus IX81 microscope equipped as described above.

4.2.4 Measurement of Cell Alignment

To determine the alignment of MSCs with respect to their underlying topography measurements were made using Image J at day 1, 4 and 7. First, the angle of the gratings was determined relative to the horizontal using the measure angle feature in Image J. Next, the long axis (with respect to the horizontal) of a minimum of 36 cells on each substrate was measured. The orientation angle was then computed. An angle of 0° represents perfect alignment with the underlying topography, 45° represents random orientation, and 90° represents a cell that is perpendicular to the topography.

4.2.5 Focal Adhesion size

Images were taken on the Olympus IX81 as described above, converted to grey scale and processed with a high-band pass filter using Metamorph Premier (v 7.7.2.0, Molecular Devices, Sunnyvale, CA) to sharpen and enhance the focal adhesions. Focal adhesion size was determined by tracing a line along the length of the adhesion of interest and measured using the 'Measure' feature in Image J similar to the procedure described previously[23]. A minimum of 90 adhesions were analyzed per condition.

4.2.6 Osteogenic differentiation

PMMA films were prepared and sterilized as described above. For osteogenic differentiation, MSCs were seeded at 5,000 cells/cm^2 in a 24-well plate for functional assays. Cells were cultured in OBM as described above and as previously reported[24,25].

4.2.7 Alkaline phosphatase assays

Cellular alkaline phosphatase (ALP) activity was measured at 1, 7, and 14 days, as previously described[10]. Briefly, cells were rinsed with PBS and lysed using passive lysis buffer (Promega, Madision, WI). 10mM Tris-HCl (pH 7.4) was added to the lysates; they were then briefly vortexed and centrifuged at 10,000 rpm for 10 minutes. ALP activity was assayed at 37°C in a buffer containing 100 mM glycine (Biorad, Hercules, CA) and 1 mM $MgCl_2$ (Fisher Scientific) (pH 10.5) for 20 minutes using *p*-nitrophenol phosphate (pNPP; Fisher Scientific) (50 mM) as a substrate. The reaction was terminated using 0.1 N NaOH (Fisher Scientific). The amount of pNPP liberated was determined spectrophotometrically using a Genova MK3 (Jenway, Staffordshire, United Kingdom) spectrophotometer at 405 nm. ALP activity (units/mL) was normalized by total protein levels for each specimen. A minimum of three samples were assayed for each condition.

Cells were also stained to visualize ALP activity. After an initial PBS rinse, cells were fixed with 4% paraformaldehyde in PBS for one minute and rinsed with ultrapure water twice. Cells were then rinsed in TBS-T and stained with a 0.08 M Tris buffer (pH 8.2) with 0.8 mg/mL of Fast Blue RR salt and 67.2 μg/mL napthol AS-

MX phosphate powder for 10 minutes while protected from light, similar to procedures described elsewhere [15,26]. After staining, cells were rinsed in DD water for one minute and then rinsed with TBS-T prior to imaging. Images were taken on an Olympus IX81 with a DP25 color camera.

4.2.8 Von Kossa staining

Cells were rinsed 2X in PBS and then fixed in 4% paraformaldehyde in PBS at 4°C for 30 minutes after 14 and 21 days in OM. After fixation, cells were rinsed in ultrapure water 3X and then immersed in 5% $AgNO_3$ and subjected to UV light (~365 nm) for 40 minutes. After UV exposure cells were rinsed 3X in DD water. The cells were then rinsed in sodium thiosulfate for 3 minutes and rinsed in DD water 3X. Images were taken on an Olympus IX81 with a DP25 color camera.

4.2.9 Calcium quantification

Calcium content in osteogenic cultures was quantified using the ortho-cresolphthalein complexone (OCPC) method, as previously described[27,28]. Cells were initially seeded at 5000 cells/cm^2 on sterile PMMA films as described above. To account for any differences in cell number, MSCs were counted by quantifying DAPI-stained nuclei as described above; the total numbers of cells after 14 and 21 days of culture on each substrate were used to normalize the total calcium levels. After cell number determination, cells were washed in PBS before incubation in 1 mL of 1 N

acetic acid overnight. The OCPC solution was prepared by adding OCPC to DD water with 1 N KOH (Acros) and 1 N acetic acid (Fisher Scientific). The dissolved solutions (10 μL per replicate) were then mixed with a working solution (300 μL per replicate) of OCPC solution and ethanolamine/boric acid/8-hydroxyquinoline buffer. Absorbance values were recorded using a Thermo Scientific Multiskan Spectrum spectrophotometer at 570 nm. Calcium values were quantified via a standard curve from 0 to 150 μg/mL. Specimens and standards were assayed in triplicate. Three samples of each condition were analyzed. Values were normalized to account for potential differences in cell number and substrate surface area, and then by the average calcium level observed after 14 days on smooth PMMA.

4.2.10 Scanning electron microscopy (SEM)

At day 21, cells were washed in PBS and subsequently fixed for 20 minutes in 4% PFA in PBS. After fixation, cells were washed twice in ddH2O and allowed to air dry overnight. The specimens were sputter-coated with gold and examined with a Phillips XL30FEG SEM equipped with an EDAX Phoenix X-ray energy dispersive spectrometer (XEDS). A working distance of 10 mm and an accelerating voltage of 15 kV were used for XEDS mineral chemical micro-analysis. A minimum of three areas from three distinct fields of view were scanned for 60 seconds to determine Ca:P ratios. Hydroxyapatite (HA) and mouse femur were used as controls. Briefly, hydroxyapatite powder was embedded in a viscous polymer resin and allowed to dry

overnight at 40 °C. The femur section was harvested from an 8-week old mouse and fixed in 4% paraformaldehyde in PBS for 2 days. The tissue was dehydrated in graded solutions of ethanol over 5 days, and then embedded in methyl methacrylate (MMA) using benzoyl peroxide, nonylphenyl polyethylene glycol acetate, and N,N-dimethyl-p-toluidine. After embedding, the tissue was sectioned into ~100 μm thick slices. Both HA and femur controls were sputter-coated with gold.

4.2.11 Statistical Analysis

Statistical analyses were carried out using GraphPad Prism software. All data were assessed for normality (where appropriate) using the D'Agostino-Pearson normality test. When appropriate, one-way ANOVA or the Kruskal-Wallis analysis with the respective post-hoc (Tukey or Dunn's) test was performed. Data are reported as means ± standard deviations. Significance was set at $p < 0.05$.

4.3 Results

4.3.1 MSCs cultured on controlled nanotopography show altered alignment and proliferation.

Initial cell attachment was not significantly altered on controlled nanotopography (Figure 4.1A) (for simplicity 'controlled will be dropped from this point forward). Cells did start to elongate after 4 hours on nanotopography (Figure 4.1B). MSCs preferentially oriented parallel to the alignment of the nanotopography (Figure 4.1C, D). At day 1, cells cultured on G415 and G303 surfaces were

significantly more aligned compared to those cultured on smooth and G140 PMMA. On G415, G303, and G140 PMMA films, MSCs had an elongated shape and were predominately aligned parallel to the underlying topography (Figure 4.1D). Cells grown on smooth PMMA (uncontrolled topography) were spread but showed no preferential alignment (Figure 4.1D). Quantitatively, nanotopographic substrates of all feature sizes significantly influenced cell alignment on both day 4 and day 7 compared to smooth PMMA controls (Figure 4.1C). Cell proliferation was assessed by counting DAPI-stained cell nuclei on days 4, 7, and 14. Increases in cell nuclei were not significantly altered on PMMA nanotopography compared to smooth controls at day 4 and day 7 (Figure 4.1E). By day 14, total cell number was significantly higher on all topographies compared to smooth controls. These data suggest that topography can be influential on cell proliferation after two weeks but does not significantly impact proliferation at earlier time points (day 4 and 7).

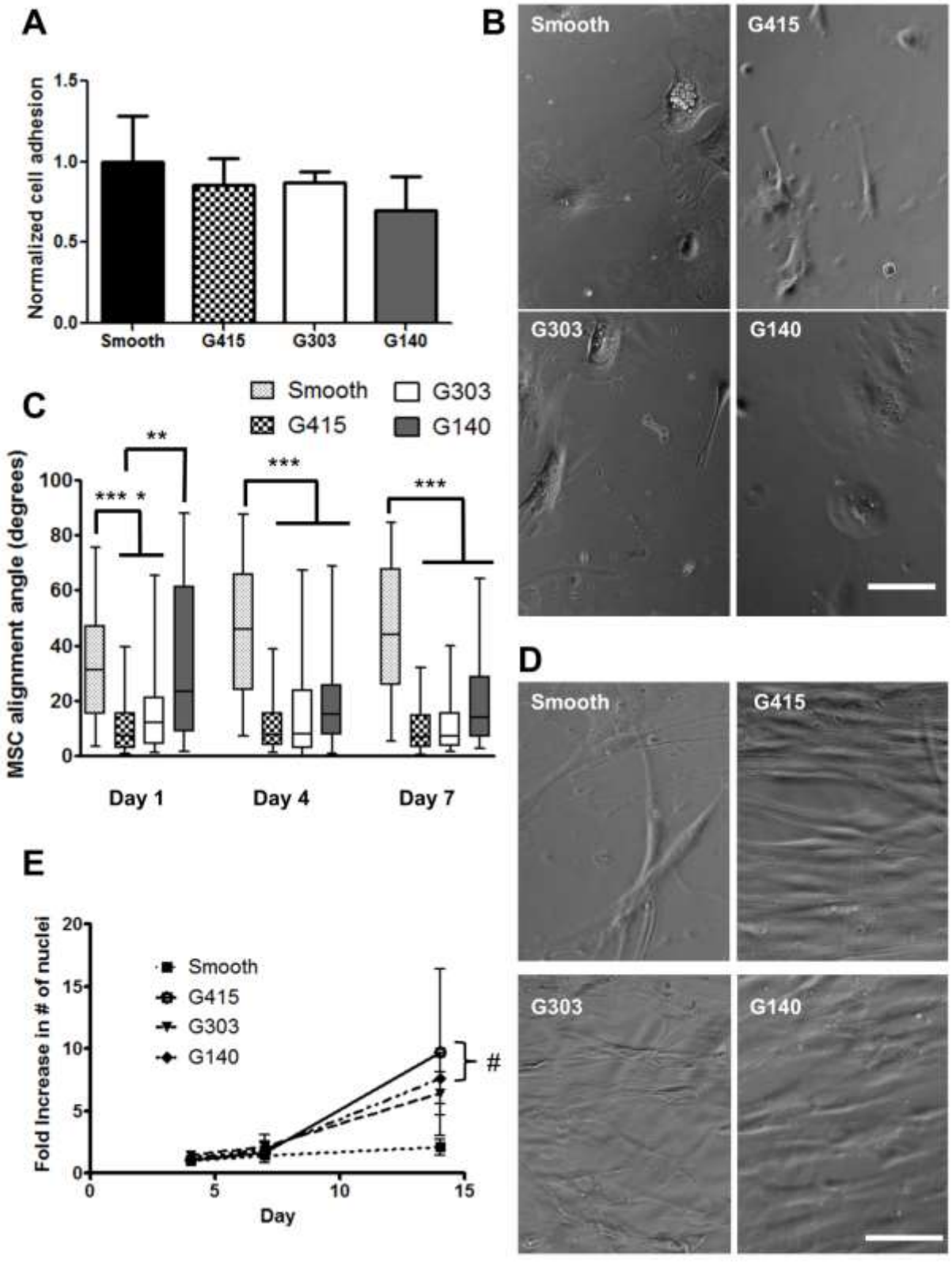

Figure 4.1. Nanotopography modulated MSC alignment and proliferation but did not modulate initial adhesion.

(Figure 4.1 cont.) (A) Similar numbers of MSCs adhered to all PMMA surfaces after four hours as quantified by DAPI stained cells. (B) Phase contrast images illustrate that cell adhesion was similar on all PMMA surfaces after four hours. Scale bar represents 100 μm. (C) Quantification of MSC alignment revealed significantly more MSC alignment (denoted by alignment angles closer to 0°, parallel to the underlying topography) on G415 and G303 substrates relative to smooth PMMA at all times points. Significant differences in alignment were also observed on G140 substrates (relative to smooth PMMA) at day 4 and 7. Data are plotted in a box and whiskers format, with the horizontal bars representing the medians, the boxes denoting the 25th and 75th confidence intervals of the data, and the whiskers denoting the boundaries of the 5th and 95th intervals. A minimum of 36 cells were analyzed for each of the conditions at each time point (nearly all the data sets were non-normally distributed, hence Kruskal-Wallis analysis was used, see Materials and Methods). (D) MSCs cultured on patterned PMMA aligned parallel to the direction of the nanotopography, as shown in these representative images following 14 days of culture. Scale bar represents 100 μm. (E) MSCs grown on G415 ($p<0.005$) and G140 ($p<0.05$) substrates proliferated at statistically greater rates compared to smooth PMMA after 14 days. Error bars represent standard deviation, n=3 for day 4, 7 and n=5 for day 14 (* $p<0.05$, ** $p < 0.01$, *** $p<0.005$).

4.3.2 MSCs cultured on nanotopography exhibit altered cytoskeletal structures and focal adhesions.

F-actin in cells grown on nanotopography was organized parallel to the underlying surface topography, while cells cultured on smooth surfaces exhibited F-actin arranged randomly (Figure 4.2A). Vinculin, a key structural component of focal adhesions[29,30], also showed altered expression patterns on substrates containing nanotopography. Vinculin staining from day 7 cultures revealed elongated focal adhesions that were aligned parallel to the underlying topography (Figure 4.2B). Focal adhesions in cells grown on smooth films were randomly arranged around the cell periphery and were not as elongated. Quantification of focal adhesion size using Image J revealed that they were not significantly elongated at day 1 and day 4 on G415, G303, and G140 films compared to smooth PMMA (Figure 4.2C). After 7 days, focal adhesions were significantly longer on G415 and G303 films compared to G140 and smooth PMMA surfaces (Figure 4.2B, C). Histograms of the focal adhesion

size distributions at day 7 not only revealed the differences in focal adhesion lengths between smooth PMMA and nanotopographic films, but also showed that the larger adhesions are present more frequently in cells cultured on the G415 and G303 films (Figure 4.2D).

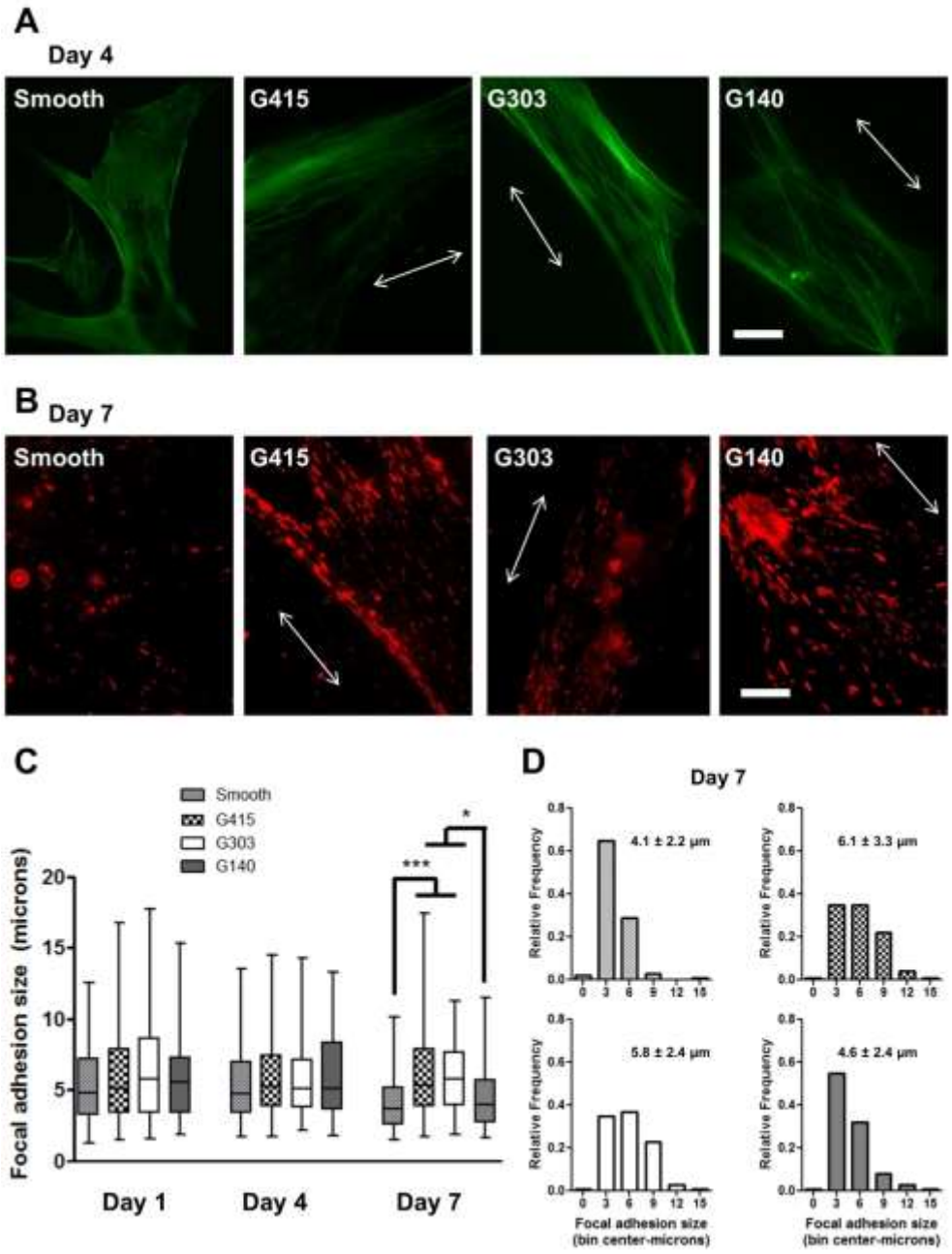

Figure 4.2. MSCs grown on nanotopography exhibit aligned actin cytoskeletons and more elongated focal adhesions.

(Figure 4.2 cont.) (A) Representative fluorescent photomicrographs of MSCs cultured on PMMA substrates for 4 days revealed the aligned orientation of the actin cytoskeleton in cells cultured on patterned substrates. Arrows indicate the orientation of the underlying topography (in A and B). Scale bar represents 25 μm. (B) Representative fluorescent photomicrographs (contrast enhanced to show differences) of MSCs cultured on PMMA substrates for 7 days following permeabilization, fixation, and staining of vinculin revealed qualitatively more elongated focal adhesions on substrates with larger topographic features (G415). Scale bar represents 25 μm. (C) Quantification of (unenhanced images of) focal adhesion size using Image J from cells cultured for 1, 4, and 7 days on PMMA substrates revealed no significant increases in focal adhesion size on the nanoPMMA substrates relative to smooth controls on Day 1 and Day 4. On Day 7, focal adhesions were significantly longer on G415 and G303 films compared to G140 and smooth PMMA surfaces. Data are plotted in a box and whiskers format, with the horizontal bars representing the medians, the boxes denoting the 25th and 75th confidence intervals of the data, and the whiskers denoting the boundaries of the 5th and 95th intervals. A minimum of 90 adhesions was assessed per condition (nearly all the data sets were non-normally distributed, hence Kruskal-Wallis analysis was used, see Materials and Methods, * p <0.05, *** p<0.005). (D) Histograms of the focal adhesion size distributions at day 7 showed that larger adhesions are present more frequently in cells cultured on the G415 and G303 films. The numbers on each graph represent the mean (+/- S.D.) adhesion size (in μm) for MSCs cultured on the PMMA substrates.

4.3.3 Nanotopography did not enhance ALP activity in MSCs.

ALP, a marker of the early stages of osteogenic differentiation [31], was assessed using the Fast Blue RR stain at day 1, 7, and 14, (Figure 4.3A), illustrating that ALP activities of the MSCs was similar on all substrates on day 7. To verify these qualitative observations, ALP activities were also quantified using the colorimetric pNpp assay. Results from this assay revealed that ALP activities increased with culture time on all substrates, but confirmed that nanotopography induced no significant changes (relative to smooth controls) after 1, 7, or 14 days (Figure 4.3B).

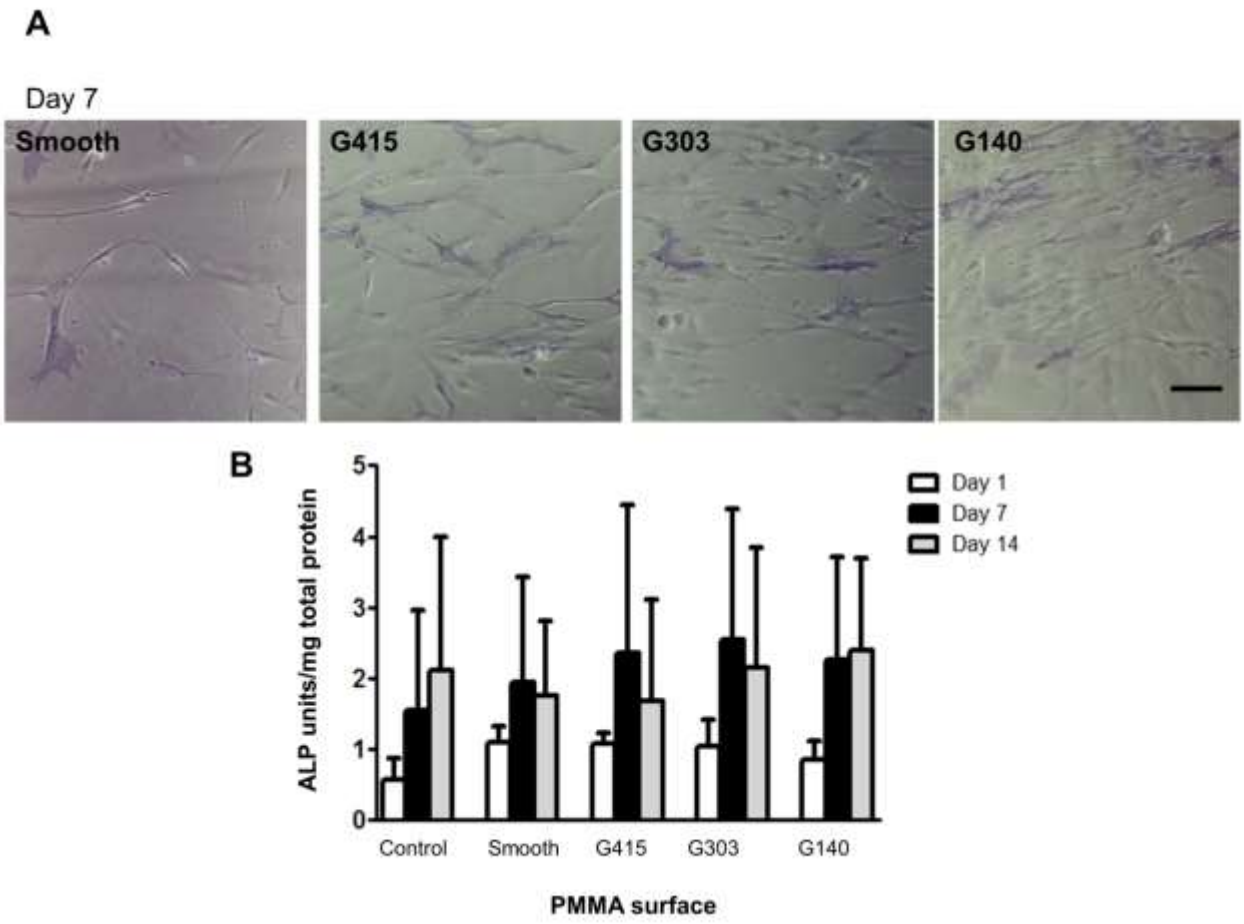

Figure 4.3. Alkaline phosphatase activities were not altered by culturing MSCs on nanotopography. (A) Micrographs of MSCs stained for active ALP after 7 days in osteogenic media (OBM) revealed no qualitative differences on PMMA nanotopgraphy. Scale bar represents 100 μm. (B) Quantification also revealed no significant differences in ALP activity for MSCs grown on nanotopography versus smooth PMMA substrates. The control group represents MSCs grown on smooth PMMA in osteogenic growth media (OGM).Data represent mean +/- standard deviation (n= 3 for day 1 and n = 5 for day 7, 14).

4.3.4 Calcium levels are minimally enhanced on nanotopography at day 14.

To assess the influence of nanotopography on the ability of MSCs to produce a mineralized matrix, the amount of deposited calcium was quantified after 14 and 21 days of culture using the OCPC assay (Figure 4.4A, B). To ensure that differences in cell proliferation on the PMMA films had no impact on the levels of calcium

observed, the results were normalized by cell number (see Materials and Methods for details). Increases in calcium deposition on nanotopography (G303 and G140 films) were observed relative to smooth PMMA after 14 days (Figure 4.4B). No significant differences were observed after 21 days in culture when comparing nanotopography to smooth PMMA, though calcium levels were approximately 2 to 3 times higher on G303 and G140 surfaces. Significant increases in calcium deposition occurred when comparing G415 at day 21 versus day 14 (with similar results for G303 and G140 films); a statistically insignificant increase was observed on smooth PMMA.

4.3.5. Mineral Ca:P ratios are influenced by nanotopography.

To assess composition, mineral deposits were stained via the Von Kossa method to visualize the presence of phosphates[32]. Topographic and smooth surfaces stained positive for phosphates (data not shown). Additionally, deposited mineral was observed using SEM (Figure 4.5A). To determine the presence of calcium and phosphorous, XEDS was used. Analysis showed that there were significant differences in the Ca:P ratio (Figure 4.5B). Mineral deposited on G415 films was the most similar to bone (Ca:P ratio 1.39 and 1.32 respectively) For reference, we observed the Ca:P ratio in hydroxyapatite to be 1.65 (theoretical ratio 1.67). Ca:P ratios in mouse femur were significantly higher than on G140, and smooth PMMA films and mineral on G415 films Ca:P ratios were significantly higher than on G303, G140, and smooth PMMA films.

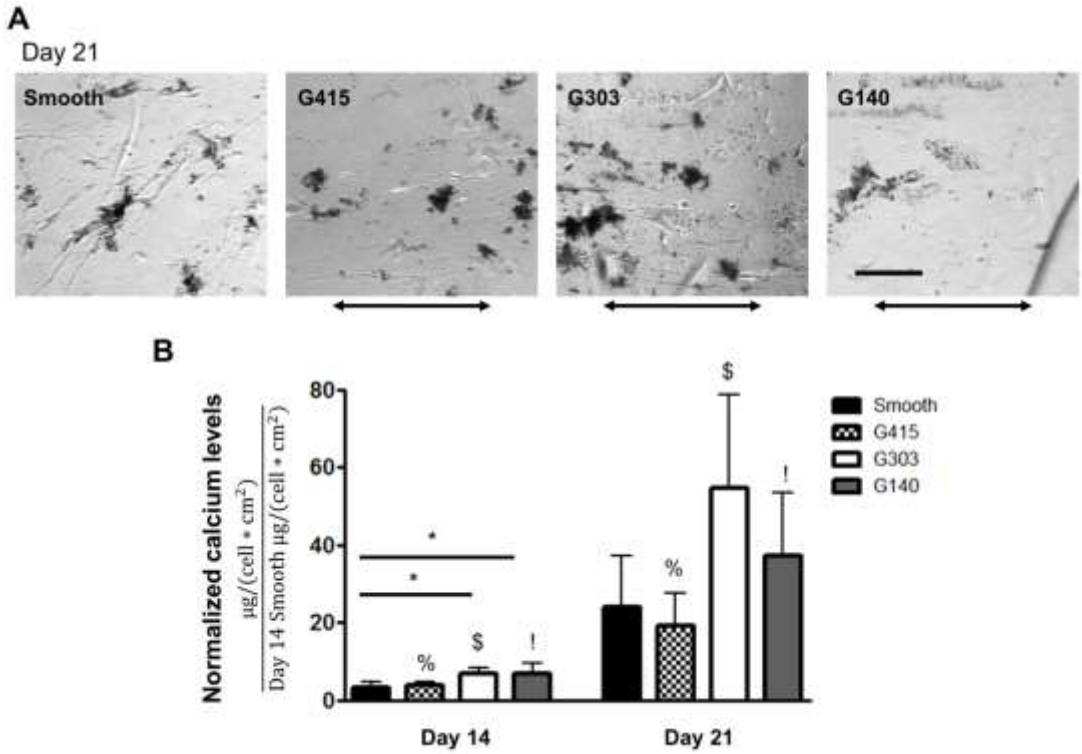

Figure 4.4. Calcium deposition was minimally influenced on nanotopography. (A) Representative phase microscopy images illustrating mineral formed on PMMA films after MSCs were grown for 21 days in osteogenic mineralization media (OBM). Arrows indicate the direction of the underlying topography. Scale represents 200 µm. (B) Quantification of total calcium levels showed that G303 and G140 PMMA nanotopographic substrates supported slightly higher levels of calcium deposition on day 14 (* p <0.05). However, there were no significant differences after 21 days (n = 3). Symbols %, $ and ! all indicate significant differences (* p <0.05) between day 14 and day 21 time points for the respective conditions.

4.4 Discussion

The ECM is a multifaceted instructive material that plays an important role in both normal and pathologic development, and is central in many regenerative strategies. Over the past 10-15 years, an increasing number of studies emphasizing the ECM's physical features, including its mechanical rigidity and its topography, have shown that cells sense and respond to ECM cues beyond just the adhesive ligands known to bind integrin receptors. In this study, we created PMMA substrates with

nanoscale gratings via capillary assisted UV lithography and used them to assess the potential functional influence of ECM topography on the osteogenic phenotype of MSCs. Cell alignment and proliferation were both influenced by topography, consistent with numerous prior studies. However, assessments of calcium quantity and composition showed that PMMA films with controlled nanotopography, at least of the feature sizes studied here, was not in fact a strong driver of an osteogenic phenotype *in vitro* compared to an control containing and uncontrolled 'smooth' topography.

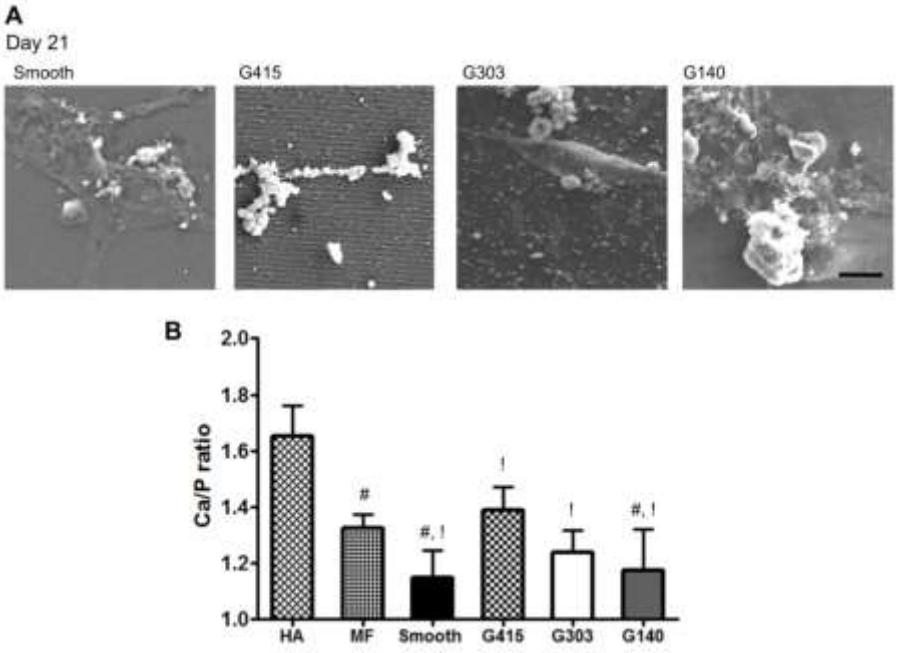

Figure 4.5. Ca:P ratios of mineral deposited on G415 substrates were similar to those found in mouse bone. (A) SEM micrographs revealed the presence of mineral after MSCs were cultured for 21 days in osteogenic media (OBM) on both smooth and nanotopographic PMMA films. Alignment of mineral was observed on the G415 substrate. Scale represents 10 μm. (B) Quantification of Ca:P ratios via XEDS revealed no significant differences between the G303, G140, and smooth PMMA substrates. The G415 films supported mineral with significantly higher Ca:P ratios compared to the other PMMA films, with values similar to those of native bone from mouse femur (MF). The Ca/P ratio of purified hydroxyapatite (HA) was quantified as a positive control. Symbols # and ! indicate that Ca:P ratios observed in MF and on G415 substrates were significantly higher (p <0.05, some comparisons showed greater significance) than other PMMA surfaces that share the same symbol, n ≥6.

To assess the impact of the nanoPMMA surfaces we first characterized their features. We discussed the synthesis, characterization, and surface energy of our nanoPMMA surfaces in detail in Chapter 3. The anisotropy of the surface features was not only reflected in the contact angle measurements and the surface free energy calculations but also in cell behavior. Specifically, we investigated the influence of nanotopography on the shape, alignment, proliferation, and initial adhesion of MSCs on PMMA gratings. Our results confirm that topography did alter cell shape, alignment at day 1, 4, and 7, and proliferation at day 14, but did not influence the number of MSCs that initially attached to the surface. Numerous other studies have reported that nanoscale gratings induce similar changes in the alignment of a wide range of cell types, including smooth muscle cells[33], fibroblasts[34], rat osteoblasts[35], cardiac myocytes[36], and even MSCs[19,37,38]. Prior studies have suggested that cell orientation (of macrophages and fibroblasts) may also be dependent on groove depth[39,40]. Protein pattering on grating surfaces may occur as well, leading to increased cell alignment[41]. Our results showed greater alignment on nanopatterns with greater depth (G415-depth 200 nm; see Table 3-1); however, in our study, grating width also varied. Thus, the increased alignment we observed cannot solely be attributed to increased grating depth. Furthermore, nanoscale gratings on PMMA films increase the available surface area (up to 79% greater surface area) compared to smooth (uncontrolled topography) PMMA films. This increase in surface area

combined with the increased cell alignment may increase the available space for cell growth, providing a possible explanation for the increased proliferation observed on PMMA substrates with nanotopography.

Because we observed changes in shape, alignment, and (to a lesser degree) proliferation of MSCs cultured on nanotopography, we next examined the actin cytoskeleton and focal adhesions. Focal adhesions have been suggested to be critically important to cell response to nanotopography[42]. Fluorescent images of the actin network revealed that the cytoskeleton was oriented parallel to the underlying topography when MSCs were cultured on patterned substrates. The focal adhesions also exhibit some degree of aligned orientation parallel to the topography, but the effect was less pronounced on the G140 substrates (those with the smallest gratings, and closest in topography to the smooth substrates). Quantification of the focal adhesion sizes showed that the G415 and G303 substrates not only supported more elongated, fibrillar adhesions than the G140 or smooth substrates, but also that these larger adhesions were present in MSCs at higher frequencies. A prior study also investigated focal adhesion size of human osteoprogenitor cells grown on PMMA surfaces with nanopits or microgratings, and reported a decrease in focal adhesion number and size on topographic surfaces compared to planar PMMA[8]. Similar findings were reported on polycarbonate[43]. Another study reported a decrease in the levels of zyxin, a molecular marker of mature focal adhesions, in hMSCs grown on 350 nm gratings of polydimethylsiloxane, suggesting that topography may disrupt

focal adhesion maturation[1]. In our case, certain topographic sizes (G415 and G303) actually supported larger adhesions than smooth substrates, suggesting that the correlation between adhesion size and nanotopography is likely a strong function of the size, shape, and chemistry of the nanoscale feature.

To characterize the influence of PMMA nanotopography on the osteogenic phenotype of MSCs, we focused on ALP activity and mineral deposition. ALP effectively increases the relative concentration of extracellular phosphate leading to more favorable conditions for hydroxyapatite formation[44]. Our results showed that MSCs expressed ALP to similar levels and activities on all PMMA substrates investigated, regardless of topography. Characterization of mineral deposition via qualitative von Kossa (phosphate) staining and a quantitative calcium assay revealed no significant increase in mineralization on topography after 21 days of culture in the presence of osteoinductive supplements. However, our data do suggest that topography may alter mineral quality by modulating the Ca:P ratio, as MSCs grown on G415 substrates produced mineral with a similar ratio as mouse bone. Other surfaces produced a highly calcium deficient mineral. *In vivo* bone is inherently calcium deficient, especially when newly formed, with reported calcium phosphate ratios of approximately 1.5 to 1.6 in rat and bovine specimens[45,46]. Low *in vivo* Ca:P ratios are often associated with osteogenesis imperfecta, which may be related to non-ideal collagen fibril sizes[47]. G415 surfaces may potentially accelerate the maturity of newly

formed HA minerals due to a collagen matrix more representative of that found in bone. Additional investigation is needed to address this possibility.

Many prior studies have investigated the influence of substrate nanotopography on the osteogenic phenotype of MSCs, but there are substantial discrepancies that remain to be resolved. Several reports claim that nanoscale features can control the osteogenic differentiation of MSCs[12,48], but the topography utilized in those studies was composed of nanoscale pits rather than the gratings used here. Likewise, numerous other studies have reported that nanoscale cues can induce the expression of osteogenic genes in MSCs[12,48-50], but did not characterize mineral quantity and quality as we did here. One study that characterized mineral deposited by rat osteoblast-like cells cultured on nanotopography showed that the mineral contained calcium and phosphorous and aligned parallel to the underlying topography[35]. However, neither the amount of calcium nor the Ca:P ratio were assessed. Another study showed that rat MSCs grown on polystyrene nanogratings had lower ALP levels than did those grown on flat substrates, but there were no significant differences in calcium deposition on topography relative to flat controls[38]. Most similar to our study, human MSCs (hMSC) grown in osteogenic media on polyurethane gratings of 200 nm width and 300 nm depth showed increased deposition of calcium compared to smooth films at day 7, but not at day 14 or 21 (Figure 4.6)[19]. Other sizes (700 nm and 2000 nm width) did not increase calcium deposition.

Besides differences in characterization methods and functional assessments of phenotype, there are many other possible reasons for the disparate observations regarding nanotopograhpy and MSC osteogenic differentiation in the literature. Amongst the most obvious are differences in material chemistry and topographic feature size. Besides differences in characterization methods and functional

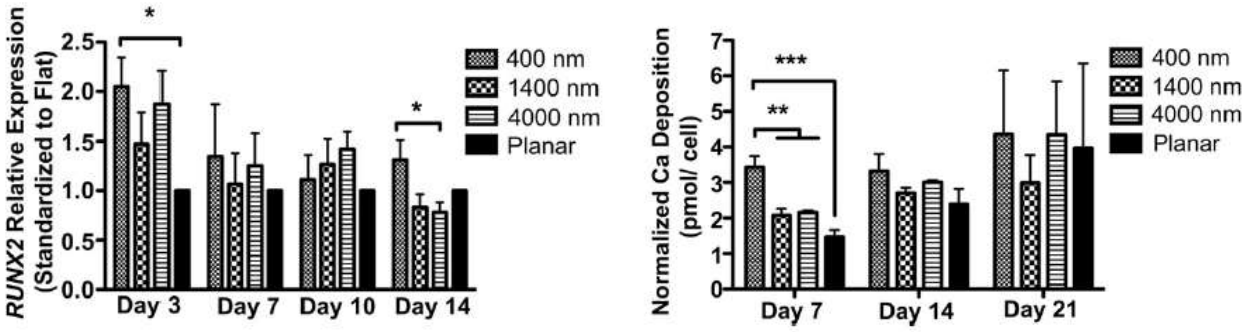

Figure 4.6. hMSC gene expression and calcium deposition on polyurethane nanogratings is not increased compared to smooth surfaces at late time points. Other reports in literature have shown similar findings to what we found on nanoPMMA- only slight enhancement due to nanotopography at early time points as illustrated in these graphs of RUNX2 expression, a marker of osteogenic differentiation, and calcium deposition, critical to mineral formation[19].

assessments of phenotype, there are many other possible reasons for the disparate observations regarding nanotopograhpy and MSC osteogenic differentiation in the literature. Amongst the most obvious are differences in material chemistry and topographic feature size. A wide variety of materials have been imprinted with topographic cues of a variety of shapes and sizes. In the case of nanotopographic gratings like those we have used here, there are studies that have used polystyrene[35,38], polyurethane[19], and PDMS[18,37], among others. Differences in material surfaces (due to

different material chemistries, treatments, or topographies) are likely to influence the SFE[51] and thus the wettability[52], perhaps leading to changes in identity and conformation of adsorbed proteins[41,53,54]. Changes in protein conformation have been linked to differences in topography[54] and result in altered cell behavior[55-57]. Surface features that change the SFE landscape, therefore, may be at least partially responsible for the observed changes in cell behavior.

Our results suggest that the slight differences in calculated SFE had little influence on the osteogenic phenotype of MSCs. This finding indicates that either SFE differences observed here were not sufficient to alter the protein landscape or the competitive adsorption from FBS mitigated any changes in ECM identity, spatial presentation, or conformation that could have potentially enhanced the osteogenic potential of MSCs on nanoPMMA. Since ECM ligand identity[58,59] and spatial presentation[60] are already known to be strong determinants of the osteogenic fate of MSCs, it may very well turn out that specific surface chemistries and nanotopographic features may indirectly alter ligand identity and spatial presentation to impact cell fate, perhaps in much the same way (and via the same mechanisms) as matrix elasticity. However, with the wide range of materials and topographies available for study, attaining consensus regarding the instructive role of topography on differentiation remains a significant challenge.

A number of previous studies combine physical topography with a single type of ECM protein (via coating, stamping etc.)[14,15,36,55]. The single adhesion cue coupled

with topography could be a strong driver of the various cell behaviors observed. In contrast, we investigated the influence of topography and uncontrolled protein adsorption from FBS on MSC osteogenic behavior in an attempt to replicate *in vivo* implant-protein environments[61]. Multiple ECM proteins in FBS are known to adsorb to surfaces, hence the osteogenic influence of one protein type may be masked by the presence of other proteins due to the abundance of multiple and varied adhesion epitopes. Disparate ligand identity has shown to play a varied role on MSC's osteogenic differentiation[59,62], thus competition for a number of ECM adhesion epitopes likely hinders activation of an osteogenic phenotype, preventing any topographic differentiation enhancement from being evident.

In this study, we focused on PMMA because of its application as a bone cement in orthopedic applications[20,21], motivated by the possibility that simply imprinting nanotopographic cues on an FDA-approved orthopedic material might enhance osteointegration and bone healing. Ultimately, whether or not nanotopography can be used to enhance bone formation and implant integration will depend on studies demonstrating its utility *in vivo*. A recent study created nanotopography on titanium implants. They found increased bone to implant contact area on most nanograting surfaces compared to the control at 4 and 8 weeks[63]. Mechanical stability of the implants was not assessed. Implants capable of promoting tissue integration and lamellar bone could reduce recovery time and reduce patient discomfort. Thus, topography may turn out to be important clinically, but further

investigations are needed. (Imparting these features on orthopedic implants is also a current challenge[42].)

We showed that MSC alignment, focal adhesion and cytoskeleton assembly, and proliferation are all influenced by nanotopographic gratings of PMMA in the 140-415 nm size range. However, using both qualitative and quantitative assessments of mineralization, we conclude that PMMA nanotopography is a poor driver of the osteogenic differentiation of MSCs *in vitro*.

4.5 References

1 Kulangara, K., Yang, Y., Yang, J. & Leong, K. W. Nanotopography as modulator of human mesenchymal stem cell function. *Biomaterials* **33**, 4998-5003, doi:DOI 10.1016/j.biomaterials.2012.03.053 (2012).

2 Rao, M. S. & Mattson, M. P. Stem cells and aging: expanding the possibilities. *Mech Ageing Dev* **122**, 713-734, doi:Doi 10.1016/S0047-6374(01)00224-X (2001).

3 De Coppi, P. *et al.* Isolation of amniotic stem cell lines with potential for therapy. *Nat Biotechnol* **25**, 100-106, doi:Doi 10.1038/Nbt1274 (2007).

4 Yen, M. L. *et al.* Efficient Derivation and Concise Gene Expression Profiling of Human Embryonic Stem Cell-Derived Mesenchymal Progenitors (EMPs). *Cell Transplant* **20**, 1529-1545, doi:Doi 10.3727/096368910x564067 (2011).

5 Guilak, F. *et al.* Control of Stem Cell Fate by Physical Interactions with the Extracellular Matrix. *Cell Stem Cell* **5**, 17-26, doi:DOI 10.1016/j.stem.2009.06.016 (2009).

6 Kim, J. *et al.* Synergistic effects of nanotopography and co-culture with endothelial cells on osteogenesis of mesenchymal stem cells. *Biomaterials* **34**, 7257-7268, doi:DOI 10.1016/j.biomaterials.2013.06.029 (2013).

7 Huebsch, N. & Mooney, D. J. A Role for Integrin-ECM Bonds as Mechanotransducers that Modulate Adult Stem Cell Fate. *Mechanobiology of Cell-Cell and Cell-Matrix Interactions*, 23-46, doi:Doi 10.1007/978-1-4419-8083-0_3 (2011).

8 Biggs, M. J. P. *et al.* The use of nanoscale topography to modulate the dynamics of adhesion formation in primary osteoblasts and ERK/MAPK signalling in STRO-1+enriched skeletal stem cells. *Biomaterials* **30**, 5094-5103, doi:DOI 10.1016/j.biomaterials.2009.05.049 (2009).

9 Khatiwala, C. B., Kim, P. D., Peyton, S. R. & Putnam, A. J. ECM Compliance Regulates Osteogenesis by Influencing MAPK Signaling Downstream of RhoA and ROCK. *J Bone Miner Res* **24**, 886-898, doi:Doi 10.1359/Jbmr.081240 (2009).

10 Khatiwala, C. B., Peyton, S. R., Metzke, M. & Putnam, A. J. The regulation of osteogenesis by ECM rigidity in MC3T3-E1 cells requires MAPK activation. *J Cell Physiol* **211**, 661-672, doi:Doi 10.1002/Jcp.20974 (2007).

11 Engler, A. J., Sen, S., Sweeney, H. L. & Discher, D. E. Matrix elasticity directs stem cell lineage specification. *Cell* **126**, 677-689, doi:DOI 10.1016/j.cell.2006.06.044 (2006).

12 Dalby, M. J. *et al.* The control of human mesenchymal cell differentiation using nanoscale symmetry and disorder. *Nat Mater* **6**, 997-1003, doi:Doi 10.1038/Nmat2013 (2007).

13 Khang, D. *et al.* Role of subnano-, nano- and submicron-surface features on osteoblast differentiation of bone marrow mesenchymal stem cells. *Biomaterials* **33**, 5997-6007, doi:DOI 10.1016/j.biomaterials.2012.05.005 (2012).

14 Kilian, K. A., Bugarija, B., Lahn, B. T. & Mrksich, M. Geometric cues for directing the differentiation of mesenchymal stem cells. *P Natl Acad Sci USA* **107**, 4872-4877, doi:DOI 10.1073/pnas.0903269107 (2010).

15 McBeath, R., Pirone, D. M., Nelson, C. M., Bhadriraju, K. & Chen, C. S. Cell shape, cytoskeletal tension, and RhoA regulate stem cell lineage commitment. *Dev Cell* **6**, 483-495, doi:Doi 10.1016/S1534-5807(04)00075-9 (2004).

16 Prodanov, L. *et al.* The interaction between nanoscale surface features and mechanical loading and its effect on osteoblast-like cells behavior. *Biomaterials* **31**, 7758-7765, doi:DOI 10.1016/j.biomaterials.2010.06.050 (2010).

17 Wood, J. A. *et al.* The modulation of canine mesenchymal stem cells by nano-topographic cues. *Exp Cell Res* **318**, 2438-2445, doi:DOI 10.1016/j.yexcr.2012.06.022 (2012).

18 Yim, E. K. F., Darling, E. M., Kulangara, K., Guilak, F. & Leong, K. W. Nanotopography-induced changes in focal adhesions, cytoskeletal organization, and mechanical properties of human mesenchymal stem cells. *Biomaterials* **31**, 1299-1306, doi:DOI 10.1016/j.biomaterials.2009.10.037 (2010).

19 Watari, S. *et al.* Modulation of osteogenic differentiation in hMSCs cells by submicron topographically-patterned ridges and grooves. *Biomaterials* **33**, 128-136, doi:DOI 10.1016/j.biomaterials.2011.09.058 (2012).

20 Lewis, G. Viscoelastic properties of injectable bone cements for orthopaedic applications: State-of-the-art review. *J Biomed Mater Res B* **98B**, 171-191, doi:Doi 10.1002/Jbm.B.31835 (2011).

21 Jaberi, J., Gambrell, K., Tiwana, P., Madden, C. & Finn, R. Long-Term Clinical Outcome Analysis of Poly-Methyl-Methacrylate Cranioplasty for Large Skull Defects. *J Oral Maxil Surg* **71**, E81-E88, doi:DOI 10.1016/j.joms.2012.09.023 (2013).

22 Cunningham, J. J., Linderman, J. J. & Mooney, D. J. Externally applied cyclic strain regulates localization of focal contact components in cultured smooth muscle cells. *Ann Biomed Eng* **30**, 927-935, doi:Doi 10.1114/1.1500408 (2002).

23 Peyton, S. R., Raub, C. B., Keschrumrus, V. P. & Putnam, A. J. The use of poly(ethylene glycol) hydrogels to investigate the impact of ECM chemistry and mechanics on smooth muscle cells. *Biomaterials* **27**, 4881-4893, doi:DOI 10.1016/j.biomaterials.2006.05.012 (2006).

24 Krause, U., Seckinger, A. & Gregory, C. A. Assays of Osteogenic Differentiation by Cultured Human Mesenchymal Stem Cells. *Methods Mol Biol* **698**, 215-230, doi:Doi 10.1007/978-1-60761-999-4_17 (2011).

25 D.J.P Prockop, G. D., B. Bunnell *Mesenchymal Stem Cells: Methods and Protocols*. (Humana Press, 2008).

26 Burstone, M. S. Histochemical demonstration of acid phosphatases with napthol AS-phosphates. *Journal of the National Cancer Institute* **21**, 523-539 (1958).

27 Ter Brugge, P. J. & Jansen, J. A. In vitro osteogenic differentiation of rat bone marrow cells subcultured with and without dexamethasone. *Tissue Eng* **8**, 321-331, doi:Doi 10.1089/107632702753725076 (2002).

28 Rao, R. R., Jiao, A., Kohn, D. H. & Stegemann, J. P. Exogenous mineralization of cell-seeded and unseeded collagen-chitosan hydrogels using modified culture medium. *Acta Biomater* **8**, 1560-1565, doi:DOI 10.1016/j.actbio.2012.01.001 (2012).

29 Wozniak, M. A., Modzelewska, K., Kwong, L. & Keely, P. J. Focal adhesion regulation of cell behavior. *Biochimica et biophysica acta* **1692**, 103-119, doi:10.1016/j.bbamcr.2004.04.007 (2004).

30 Coyer, S. R. *et al.* Nanopatterning reveals an ECM area threshold for focal adhesion assembly and force transmission that is regulated by integrin activation and cytoskeleton tension. *J Cell Sci* **125**, 5110-5123, doi:Doi 10.1242/Jcs.108035 (2012).

31 Farley, J. R. & Baylink, D. J. Skeletal Alkaline-Phosphatase Activity as a Bone-Formation Index Invitro. *Metabolism* **35**, 563-571, doi:Doi 10.1016/0026-0495(86)90016-8 (1986).

32 Bonewald, L. F. *et al.* Von Kossa staining alone is not sufficient to confirm that mineralization in vitro represents bone formation. *Calcified Tissue Int* **72**, 537-547, doi:DOI 10.1007/s00223-002-1057-y (2003).

33 Yim, E. K. F. *et al.* Nanopattern-induced changes in morphology and motility of smooth muscle cells. *Biomaterials* **26**, 5405-5413, doi:DOI 10.1016/j.biomaterials.2005.01.058 (2005).

34 Kim, D. H. *et al.* Mechanosensitivity of fibroblast cell shape and movement to anisotropic substratum topography gradients. *Biomaterials* **30**, 5433-5444, doi:10.1016/j.biomaterials.2009.06.042 (2009).

35 Lamers, E. *et al.* The influence of nanoscale grooved substrates on osteoblast behavior and extracellular matrix deposition. *Biomaterials* **31**, 3307-3316, doi:DOI 10.1016/j.biomaterials.2010.01.034 (2010).

36 Kim, D. H. *et al.* Nanoscale cues regulate the structure and function of macroscopic cardiac tissue constructs. *P Natl Acad Sci USA* **107**, 565-570, doi:DOI 10.1073/pnas.0906504107 (2010).

37 Teo, B. K. *et al.* Nanotopography modulates mechanotransduction of stem cells and induces differentiation through focal adhesion kinase. *Acs Nano* **7**, 4785-4798, doi:10.1021/nn304966z (2013).

38 Wang, P. Y., Li, W. T., Yu, J. S. & Tsai, W. B. Modulation of osteogenic, adipogenic and myogenic differentiation of mesenchymal stem cells by submicron grooved topography. *J Mater Sci-Mater M* **23**, 3015-3028, doi:DOI 10.1007/s10856-012-4748-6 (2012).

39 WojciakStothard, B., Curtis, A., Monaghan, W., Macdonald, K. & Wilkinson, C. Guidance and activation of murine macrophages by nanometric scale topography. *Exp Cell Res* **223**, 426-435, doi:DOI 10.1006/excr.1996.0098 (1996).

40 Walboomers, X. F., Monaghan, W., Curtis, A. S. G. & Jansen, J. A. Attachment of fibroblasts on smooth and microgrooved polystyrene. *J Biomed Mater Res* **46**, 212-220, doi:Doi 10.1002/(Sici)1097-4636(199908)46:2<212::Aid-Jbm10>3.0.Co;2-Y (1999).

41 Lord, M. S., Foss, M. & Besenbacher, F. Influence of nanoscale surface topography on protein adsorption and cellular response. *Nano Today* **5**, 66-78, doi:DOI 10.1016/j.nantod.2010.01.001 (2010).

42 McNamara, L. E. *et al.* Nanotopographical Control of Stem Cell Differentiation. *Journal of Tissue Engineering* **1**, 120623-120623, doi:10.4061/2010/120623 (2010).

43 Biggs, M. J. P., Richards, R. G., Gadegaard, N., Wilkinson, C. D. W. & Dalby, M. J. Regulation of implant surface cell adhesion: Characterization and quantification of S-phase primary osteoblast adhesions on biomimetic nanoscale substrates. *J Orthop Res* **25**, 273-282, doi:Doi 10.1002/Jor.20319 (2007).

44 Allori, A. C., Sailon, A. M. & Warren, S. M. Biological basis of bone formation, remodeling, and repair - Part II: Extracellular matrix. *Tissue Eng Part B-Re* **14**, 275-283, doi:DOI 10.1089/ten.teb.2008.0083 (2008).

45 Kuhn, L. T. *et al.* A comparison of the physical and chemical differences between cancellous and cortical bovine bone mineral at two ages. *Calcified Tissue Int* **83**, 146-154, doi:DOI 10.1007/s00223-008-9164-z (2008).

46 Bigi, A. *et al.* Chemical and structural characterization of the mineral phase from cortical and trabecular bone. *J Inorg Biochem* **68**, 45-51, doi:Doi 10.1016/S0162-0134(97)00007-X (1997).

47 Cassella, J. P. & Ali, S. Y. Abnormal Collagen and Mineral Formation in Osteogenesis Imperfecta. *Bone Miner* **17**, 123-128, doi:Doi 10.1016/0169-6009(92)90722-P (1992).

48 McMurray, R. J. *et al.* Nanoscale surfaces for the long-term maintenance of mesenchymal stem cell phenotype and multipotency. *Nat Mater* **10**, 637-644, doi:Doi 10.1038/Nmat3058 (2011).

49 You, M. H. *et al.* Synergistically Enhanced Osteogenic Differentiation of Human Mesenchymal Stem Cells by Culture on Nanostructured Surfaces with Induction Media. *Biomacromolecules* **11**, 1856-1862, doi:Doi 10.1021/Bm100374n (2010).

50 Teo. in *Methods in Cell Biology* Vol. 98 Ch. 11, (2010).

51 Hermitte, L., Thomas, F., Bougaran, R. & Martelet, C. Contribution of the comonomers to the bulk and surface properties of methacrylate copolymers. *J Colloid Interf Sci* **272**, 82-89, doi:DOI 10.1016/j.jcis.2003.08.055 (2004).

52 Gao, L. C. & McCarthy, T. J. How Wenzel and Cassie were wrong. *Langmuir* **23**, 3762-3765, doi:Doi 10.1021/La062634a (2007).

53 Lim, J. Y. *et al.* Surface energy effects on osteoblast spatial growth and mineralization. *Biomaterials* **29**, 1776-1784, doi:DOI 10.1016/j.biomaterials.2007.12.026 (2008).

54 Koh, L. B., Rodriguez, I. & Venkatraman, S. S. Conformational behavior of fibrinogen on topographically modified polymer surfaces. *Phys Chem Chem Phys* **12**, 10301-10308, doi:Doi 10.1039/C001747g (2010).

55 Denis, F. A., Pallandre, A., Nysten, B., Jonas, A. M. & Dupont-Gillain, C. C. Alignment and assembly of adsorbed collagen molecules induced by

anisotropic chemical nanopatterns. *Small* **1**, 984-991, doi:DOI 10.1002/smll.200500116 (2005).

56 Koh, L. B., Rodriguez, I. & Venkatraman, S. S. The effect of topography of polymer surfaces on platelet adhesion. *Biomaterials* **31**, 1533-1545, doi:DOI 10.1016/j.biomaterials.2009.11.022 (2010).

57 Li, D. & Chen, H. Regulation of Protein/Surface Interactions by Surface Chemical Modification and Topographic Design. *Acs Sym Ser* **1120**, 301-319 (2012).

58 Salasznyk, R. M., Williams, W. A., Boskey, A., Batorsky, A. & Plopper, G. E. Adhesion to Vitronectin and Collagen I Promotes Osteogenic Differentiation of Human Mesenchymal Stem Cells. *J Biomed Biotechnol* **2004**, 24-34 (2004).

59 Kundu, A. K. & Putnam, A. J. Vitronectin and collagen I differentially regulate osteogenesis in mesenchymal stem cells. *Biochem Biophys Res Commun* **347**, 347-357 (2006).

60 Trappmann, B. *et al.* Extracellular-matrix tethering regulates stem-cell fate. *Nat Mater* **11**, 642-649, doi:10.1038/nmat3339 (2012).

61 Rabe, M., Verdes, D. & Seeger, S. Understanding protein adsorption phenomena at solid surfaces. *Adv Colloid Interfac* **162**, 87-106, doi:DOI 10.1016/j.cis.2010.12.007 (2011).

62 Salasznyk, R. M., Klees, R. F., Boskey, A. & Plopper, G. E. Activation of FAK is necessary for the osteogenic differentiation of human mesenchymal stem cells on laminin-5. *J Cell Biochem* **100**, 499-514, doi:Doi 10.1002/Jcb.21074 (2007).

63 Prodanov, L. *et al.* The effect of nanometric surface texture on bone contact to titanium implants in rabbit tibia. *Biomaterials* **34**, 2920-2927, doi:DOI 10.1016/j.biomaterials.2013.01.027 (2013).

CHAPTER 5

Investigating Mesenchymal Stem Cell Osteogenic Differentiation via Modulated Matrix Elasticity and Nanotopography

5.1 Introduction

As has been discussed extensively in Chapter 1, 2, and 4, the extracellular matrix plays a critical role in driving cell behavior. Cell behavior is strongly influenced by cell adhesion. The availability of matrix adhesion sites is important to cell adhesion, illustrating that the ECM functions as an anchorage site[1,2]. ECM proteins like collagen, fibronectin, laminin etc., allow for anchorage via integrins to specific ligands[3] and convey information across the cell membrane. This information regulates ECM production and assembly, cell proliferation, differentiation, and apoptosis.[4] Additionally, integrins are critical to connecting the actin cytoskeleton to the ECM and to sensation of materials properties of protein coated substrates[4,5].

In addition to its biochemical information content, the ECM possesses certain physical characteristics that are sensed by a cell's integrins including matrix elasticity and (as discussed in Chapter 4) topography. Cells sense elastic cues through

modulation of the composition of focal adhesions that result from myosin dependent effects on the actin cytoskeleton[4,6,7]. The modulation of various proteins, like vinculin at focal adhesion leads to structural changes.[6] These structural changes can initiate or modulate cell signaling events that often involve RhoA, a critical mechanosensitive switch[8]. Similarly, mechanosensitive signaling pathways have been suggested to be involved in sensing topography[9-11]. Recent evidence suggests that cells on topographic environments employ filopodia to orient and spread, in contrast to those spreading on smooth surfaces which transition from a filopodia-rich to a lamellipodia-dominated regime[12]. Ultimately, essential to sensing matrix elasticity or topography is the availability of ligand binding sites. Cells respond to these cues (sometimes in similar ways) as it has been well established that matrix elasticity, ligand identity, and topography influence cell behavior[7,9,13-20].

Because ECM properties influence cell behaviors it is vital to understand the role each property plays both individually and in combination. Understanding how these cues activate the cellular response would be helpful in developing therapies that attempt to drive specific cell behaviors such as bone regeneration[21]. Matrix elasticity, ligand identity[22,23], and (in some instances) topography[10,24] drive an osteogenic response. Hence combining these material inputs could further enhance the osteogenic response. To the best of our knowledge, attempts to study matrix elasticity, ligand identity, and nanotopography together are limited[25] and their

combined impact on osteogenesis, therefore, remains incompletely understood. Thus, coupling matrix elasticity, ligand identity, and topography in a tailored and controlled way will enhance our understanding and may lead to new or improved strategies in orthopedic and other clinical settings. Here we couple these inputs through the use of 'imprinted' elastically tunable UV polymerizable hydrogels to assess and test the hypothesis that coupling nanotopography, matrix elasticity, and Col I will have a synergistic impact on osteogenesis.

5.2 Methods and Materials

5.2.1. Manufacturing of urethane vinyl acrylate molds

Molds were made using a precursor solution consisting of a urethane diacrylate pre-polymer- Ebecryl 280 (Allnex, Brussels, Belgium), a low viscosity acrylated monomer- trimethylolpropane(-ethoxylate)6-triacrylate (M3160) at 30 wt. % of the Ebecryl 280, two photoiniatiators- Irgacure 184 (1-hydroxy-cyclohexyl-phenyl-ketone) and Darocur 1173 (2-hydro-2-methyl-1-phenyl-1-propane) (BASF, Florham Park, NJ) at 1.5 wt. % of the Ebecryl and M3160 precursor, and a releasing agent- Rad 2200N (TEGO-Evonik, Hopewell, VA) at 1 wt. % of the Ebecryl and M3160 precursor (all chemicals were graciously donated). The poly(urethane) acrylate (PUA) precursor solution was mixed and stored at 4 °C overnight (and was stable for weeks under those storage conditions) to allow dissipation of trapped air bubbles. The

polymerization technique was similar to that previously reported[26]. Briefly, the precursor solution was deposited on (heptadecafluoro-1,2,2,2-tetrahydrodecyl) trichlorosilane (FTDS) (Gelest, Morrisville, PA) coated silicon molds (LightSmyth Technologies, Eugene OR). The silicon (Si) molds were patterned with square wave gratings of different depths and widths in order to create the molds with varied nanotopography with features described in Chapter 2. The pre-cursor solution was placed on top of the silicon molds and glass slides were placed on-top of the pre-cursor solution and subjected to UV-light ~365 nm (~3 mW/cm^2) for 20 seconds (Figure 5.1). After polymerization, the PUA molds were removed from the glass and Si molds. Molds were then placed nanograting side up and exposed to UV-light ~365 nm (~3 mW/cm^2) for 24 hours to eliminate any unreacted initiators. Smooth PUA molds absent of topography were also manufactured in a similar fashion using No. 1 coverglass (VWR) slides in place of the Si master. Molds will be designated by the following names for simplicity and clarity (as described in Chapter 2): smooth, G415, G303, and G140.

5.2.2 AFM and SEM of PUA molds

To assess the topographic surface features of nanoPUA molds, a Dimension Icon scanning probe microscope (Bruker, Camarillo, CA) was used for imaging. Specifically, NCH-10 silicon probes (NanoAndMore USA, Lady's Island, SC) were used to scan the molds. A sampling rate of 384 lines and a scan rate of 0.5 Hz were

used. The PUA was also sputter-coated with gold and examined with a Phillips XL30FEG SEM at a working distance of 7 mm, an accelerating voltage of 3 kV, and a spot size of 4.

5.2.3 Polymerization of polyethylene glycol diacrylate gels

Poly (ethylene glycol diacrylate) (PEGDA) was obtained from Sigma (M_w: 700 g/mol) or made in-house (M_w: 3,400 g/mol) as described elsewhere[27]. Stock solutions were made by varying the weight percentage of PEGDA per volume of PBS as follows (labels identify the final wt. % of PEGDA). The initiator solution, consisting of a fresh stock of 600 mg/mL 2,2-dimethoxy-2-phenylacetophenone (DMPA) (Acros Organics) in N-vinyl pyrrolidone (NVP), was vortexed with the stock solution of PEGDA. After mixing, the solution was briefly centrifuged and the solution was filtered with a PVDF 13mm syringe filter (0.22 μm, Fisher). Various volumes of the filtered precursor solution were used to make either cylinders for rheology (see below) or thin films for cell culture experimentation (aseptically). For cell culture, precursor solution was placed on an acrylated glass slides and covered with a PUA mold and polymerized with UV light (~365nm, 3 mW/cm^2) for 10 minutes. Following removal of the PUA mold, the imprinted PEGDA gels immobilized on glass substrates were then placed in PBS in a 12-well plate and allowed to equilibrate at 37 °C for at least 24 hours prior to protein conjugation.

Acrylated glass slides were prepared as follows. Glass slides were submerged in piranha acid for 5 minutes and then rinsed in water. After the water rinse, the slides were rinsed in ethanol and dried in dry N_2 gas. The slides were then placed in a solution of (3-acryloxy propyl) methyl dichlorosilane (APMDS) and n-heptane (100μL/100mL) for 15 minutes under vacuum. They were then baked at 60 °C for 20 minutes. After baking, acrylated slides were stored under vacuum for up to 3 weeks. (Note: PEGDA gels are very adherent to the acrylated slides, especially if the acrylated slides are 'fresh' as PEGDA gels have remained stable and adherent for at least 2 months at 37 °C in PBS. When the acrylated slides are 'aged', or approximately 3 to 4 weeks old, the gels detach after less than 4 weeks or less at 37 °C in PBS.)

5.2.4 AFM of PEGDA gels

To assess the topographic surface features of PEGDA gels, a Dimension Icon scanning probe microscope (Bruker, Camarillo, CA) was used for imaging. Specifically, NCH-10 silicon probes (NanoAndMore USA, Lady's Island, SC) were used to scan the molds. A sampling rate of 384 lines and a scan rate of 0.5 Hz were used. Gels were imaged dry. Prior to imaging, gels were dried in a graded series of ethanol and water rinses starting with 70/30 % ethanol/water for at least 5 minutes. That was followed by 80/20, 90/10 ethanol/water and 100% water rinses for at least 5 minutes each. Gels were then allowed to dry overnight.

5.2.5 Shear rheological measurements

For bulk mechanical testing 350 μL of precursor solution was aseptically cast into ~8mm diameter cylinders in a Teflon mold by exposure to UV light at ~365 nm, ~3mW/cm^2 for 10 minutes. Hydrogels were transferred to a 12-well plate and incubated at 37 °C in PBS for up to 21 days. Gels were allowed to equilibrate for 24 hours in PBS prior to rheological measurements. Rheological measurements were performed similarly to previously reported methods[27] on a TA Instruments (New Castle, DE) rheometer. Briefly, measurements were taken with an 8 mm parallel plate geometry, in which both surfaces were coated with P800 wet sandpaper (3M, St. Paul, MN) to prevent slip. Gaps were adjusted to accommodate the height of the hydrogels and were set to achieve ~5% compression to prevent slip. The storage (G') and loss moduli (G") were averaged from mechanical spectra using a strain rate of 1 rad/s and 0.1% strain for n=4 samples. To determine changes in storage moduli over time, samples were allowed to aseptically equilibrate at 37 °C in PBS for 2 ('new', Figure 5.4) or 21 days. Gels were tested in shear as described above.

5.2.6 Assessment of PEGDA swelling

To assess PEGDA hydrogel swelling, a procedure similar to previous reports was followed[25,27]. Briefly, cylindrical plugs of 5 and 20% 700 g/mol PEGDA were polymerized as previously described, and weighed 'wet' after polymerization. They were then immersed in either ultra-pure filtered water or PBS for 72 hours. Each gel

was weighed again to determine its 'swollen' weight. Gels in PBS were then rinsed with water 4 times over 30 minutes to ensure elution of any salt. All gels were lyophilized for 48 hours and ('dry') weighed a final time. These weights were used to calculate Q_r, the relaxed swelling ratio using 1.1192 and 0.9982 g/mL for the density of PEGDA and water respectively at 20 °C. A sample size of n=3 was used for all conditions.

5.2.7 Attachment of collagen I to nanoPEGDA

ECM proteins were conjugated to the PEGDA substrates using Sulfo-SANPAH (*N*-Sulfosuccinimidyl-6-(4'-azido-2'-nitrophenylamino) hexanoate; ThermoFisher) as previously described[28]. For each conjugation the ratio of 10 μL stock Sulfo-SANPAH solution per 4 mL of MES buffer was used to make a working solution. MES buffer consists of 0.1 M MES (2-(N-morpholino)ethanesulfonic acid) and 0.5 M NaCl, pH 6.0. Each gel was rinsed with MES buffer after aspirating the PBS from each well. Following the MES rinse, the working solution was added (~200 μL/well) and exposed to UV-light ~365 nm, ~2mW/cm^2 for 15 minutes. Every 5 minutes each plate was gently agitated. Each well was then rinsed with MES buffer solution and the process of adding the working solution and subsequent UV exposure was repeated. After the final 15 minutes, the substrates were rinsed three times in MES buffer. Finally, the substrates were rinsed in PBS before rat tail collagen I (Advanced BioMatrix, San Diego, CA) was added at 5 or 50 μg/mL (effectively ~1.25

and 12.5 μg/cm^2 respectively) in PBS (final concentration) to each well. Each plate was then placed on a rocker for 2 hours. After, rocking substrates were rinsed once in PBS and stored at 4 °C (for up to 1 week) until cell seeding.

5.2.8 Cell culture

Human bone marrow-derived MSCs were obtained from a commercial source (Lonza, Walkersville, MD) at passage 2. As part of the manufacturer's quality control, MSCs were tested for purity by flow cytometry and for their ability to differentiate into osteogenic, chondrogenic and adipogenic lineages and are positive for the cell surface markers CD105, CD166, CD29 (integrin β1), and CD44, and negative for CD14, CD34 and CD45. MSCs were maintained in high glucose (4.5 g/L) Dulbecco's modified Eagle medium (DMEM, Invitrogen, Carlsbad, CA) supplemented with 10% fetal bovine serum (FBS, Invitrogen). All cultures were incubated at 37°C and 5% CO_2. Media were changed every 2-3 days. MSCs were routinely expanded in 2D cultures and harvested with 0.05% Trypsin-EDTA (Invitrogen). Cells were used between passage 6 and 11.

5.2.9 Cell adhesion and proliferation

To determine the influence of nanoPMMA on proliferation, MSCs were seeded at an initial density of 2000 cells/cm^2 and allowed to proliferate in osteogenic growth media (OGM), consisting of alpha-minimum essential media (αMEM, Invitrogen),

20% FBS, 2 mM L-glutamine (CellGro, Manassas, VA), 1% penticillin/streptomycin (CellGro), and 5 mg/mL gentamicin (Invitrogen). At day 4, 7, and 14, cells were rinsed with PBS, and then fixed with 4% paraformaldehyde in PBS. Cells were then rinsed with PBS three times. Cells were stained with 4',6-diamidino-2-phenylindole dihydrochloride (DAPI) in PBS (1:5000) for 10 minutes to identify their nuclei. After staining, MSCs were rinsed with PBS and then imaged on an Olympus IX81 microscope equipped with a 100W high-pressure mercury burner (Olympus America, Center Valley, PA), a Hamamatsu Orca II CCD camera (Hamamatsu Photonoics, K.K., Hamamatsu City, Japan), and Metamorph Premier software (Molecular Devices, Sunnyvale, CA). Cells that stained positive for DAPI were manually counted using Image J (NIH, Bethesda, MD). At least six (10X) images were analyzed for each condition. The number of cells per field was converted to cells per area, and then normalized to the initial number of cells seeded (2000 cells/cm^2). Two independent measurements were made and averaged.

5.2.10 Visualization of actin and vinculin using fluorescence microscopy

Cells were seeded at 2000 cells/cm^2 on sterile PEGDA gels and grown in OGM. At day 4 cells were washed with PBS, then fixed with 4% paraformaldehyde in PBS. Cells were washed with Tris-buffered saline (250 mM Tris, 27 mM KCl, 1.37 M NaCl pH 7.4; TBS, Fisher Scientific) + 0.1% Triton X-100 (TBS-T) prior to blocking. Cells were then blocked with Abdil (2% bovine serum albumin in TBS-T) for 20

minutes and washed again with TBS-T. Cells were then incubated with Oregon Green 488 Phalloidin (Invitrogen) to stain F-actin (1:40) and mouse anti-human vinculin (1:250) to label focal adhesions in Abdil for 45 minutes. Following incubation, a TBS-T wash was used to remove unbound antibodies. Cells were then incubated for 45 minute with goat anti-mouse Alexa Fluor 594 (Invitrogen) in Abdil (1:450). Cells were then washed in TBS-T at least three times. Stained MSCs on PEGDA gels were imaged on the Olympus IX81 microscope equipped as described above.

5.2.11 Osteogenic differentiation

NanoPEGDA gels were prepared and sterilized as described above. For osteogenic differentiation, MSCs were seeded at 5,000 cells/cm^2 in a 12-well plate for functional assays. Cells were cultured in osteogenic base media (OBM), consisting of OGM, 10 mM β-glycerol phosphate, and 50 μg/mL L-ascorbic acid (Fisher Scientific) as previously reported [20,29,30].

5.2.12 Von Kossa staining

Cells were rinsed 2X in PBS and then fixed in 4% paraformaldehyde in PBS at 4°C for 30 minutes after up to 21 days in OM. After fixation, cells were rinsed in ultrapure water 3X. Glass slides containing the nanoPEGDA gels were transferred to new 12-well plates for further analysis (see below). The remaining cell layer (on TCPS) was then immersed in 5% $AgNO_3$ and subjected to UV light (~365 nm) for 40

minutes. After UV exposure cells were rinsed 3X in Millipore water. The cells were then rinsed in sodium thiosulfate for 3 minutes and rinsed in Millipore water 3X. Images were taken on an Olympus IX81 with a DP25 color camera.

5.2.13 Calcium quantification

Calcium content in osteogenic cultures on nanoPEGDA was quantified using the ortho-cresolphthalein complexone (OCPC) method, as previously described [31,32]. Cells were initially seeded at 5000 cells/cm^2 on sterile PEGDA substrates as described above and cultured for up to 21 days in OBM. As described above, cells were rinsed in PBS, then fixed in 4% paraformaldehyde for 20 minutes, and subsequently washed in PBS followed by ultrapure water before incubation in 1 mL of 1 N acetic acid overnight. The OCPC solution was prepared by adding OCPC to ultrapure water with 1 N KOH (Acros) and 1 N acetic acid (Fisher Scientific). The dissolved solutions (10 μL per replicate) were then mixed with a working solution (300 μL per replicate) of OCPC solution and ethanolamine/boric acid/8-hydroxyquinoline buffer. Absorbance values were recorded using a Thermo Scientific Multiskan Spectrum spectrophotometer at 570 nm. Calcium values were quantified via a standard curve from 0 to 150 μg/mL. Specimens and standards were assayed in triplicate. Three samples of each condition were analyzed. Values were normalized to account for potential differences in substrate surface area (apparent surface area was used, not actual surface area).

5.2.14 Scanning electron microscopy (SEM)

At day 21, cells were washed in PBS and subsequently fixed for 20 minutes in 4% PFA in PBS. After fixation, cells were washed twice in ddH_2O and subjected to a graded series of ethanol and water rinses and then allowed to air dry overnight (as described above for AFM imaging). Specimens were removed from their glass backing and attached to a double-sided piece of Scotch tape (3M, St. Paul, MN) that was then placed on a glass slide. The specimens were then sputter-coated with gold and examined with a Phillips XL30FEG SEM equipped with an EDAX Phoenix X-ray energy dispersive spectrometer (XEDS). A working distance of 10 mm and an accelerating voltage of 15 kV were used for XEDS mineral chemical micro-analysis. A minimum of six distinct areas from multiple fields of view were scanned for 60 seconds to determine Ca:P ratios. Hydroxyapatite (HA) was used as a control. Briefly, hydroxyapatite powder was embedded in a viscous polymer resin and allowed to dry at 40 °C. The HA control was also sputter-coated with gold.

5. 2.15 Statistical Analysis

Statistical analyses were carried out using GraphPad Prism software. All data were assessed for normality (where appropriate) using the D'Agostino-Pearson normality test. When appropriate, one-way ANOVA or the Kruskal-Wallis analysis

with the respective post-hoc (Tukey or Dunn's) test was performed. Data are reported as means ± standard deviations. Significance was set at $p < 0.05$.

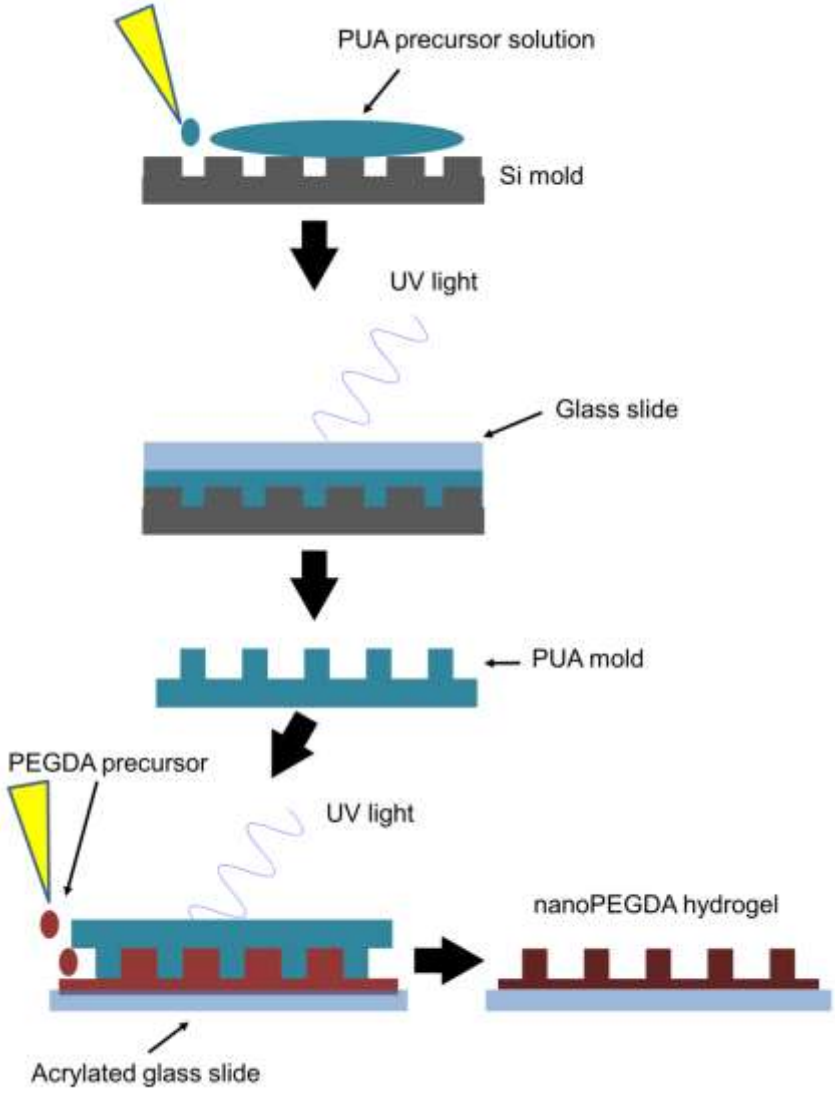

Figure 5.1 Capillary assisted UV lithography polymerization method was used to produce PEGDA films with nanotopography and tunable elasticity. A precursor solution of poly urethane acrylate (PUA) was placed on a Si mold containing nanoscale gratings. A glass slide was placed on top of the precursor solution, which was then exposed to UV light for 20 seconds. After polymerization the PUA mold was used to make nanoPEGDA hydrogels of varied size and elasticity. See Methods and Materials for a detailed description. This process was modified from previous reports.[26, 33]

5.3 Results

5.3.1 Nanotopography on PUA molds was confirmed by SEM and AFM.

PUA molds with nanotopographic features were fabricated using UV-assisted capillary force lithography (Figure 5.1). The topographic dimensions of the films were confirmed using SEM (Figure 5.2) and AFM. As expected, the PUA molds had similar dimensions to the Si master molds that were used as a template for polymerization.

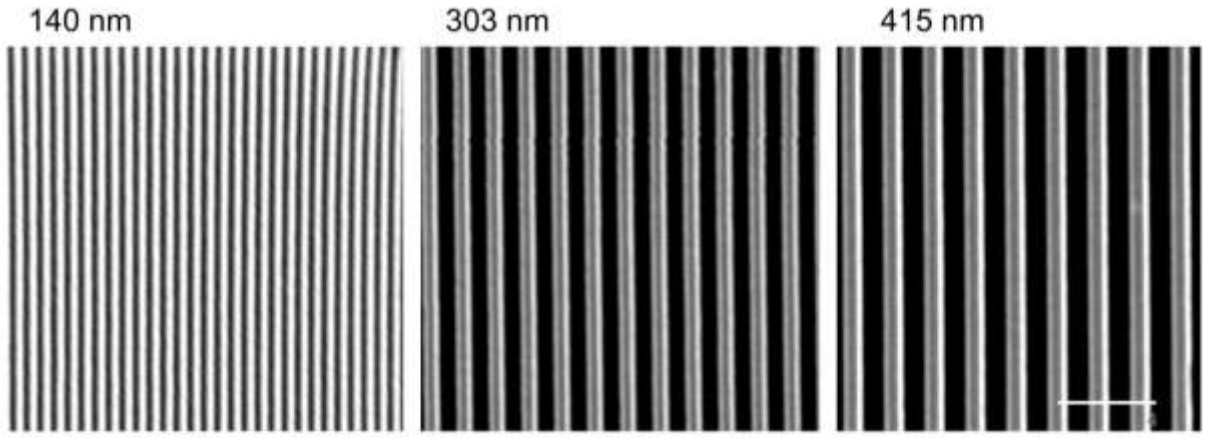

Figure 5.2 SEM confirms PUA nanofeatures. SEM micrographs depict the nanoscale of the PUA molds. AFM was also performed (data not shown) that corroborated these images. (Scale = 200 μm.)

5.3.2 Nanotopography on PEGDA gels is confirmed by AFM.

PEGDA films with nanotopographic features were fabricated using a UV cross-linkable system (see Materials and Methods) (Figure 5.1). The presence of controlled nanotopographic features was confirmed using AFM (Figure 5.3). The nanoPEGDA films were designated G415, G303, and G140 (the same nomenclature used for nanoPMMA). Smooth films had uncontrolled topography in the range of

tens of nanometers compared to hundreds of nanometers for controlled nanotopographic surfaces (G415, G303, G140).

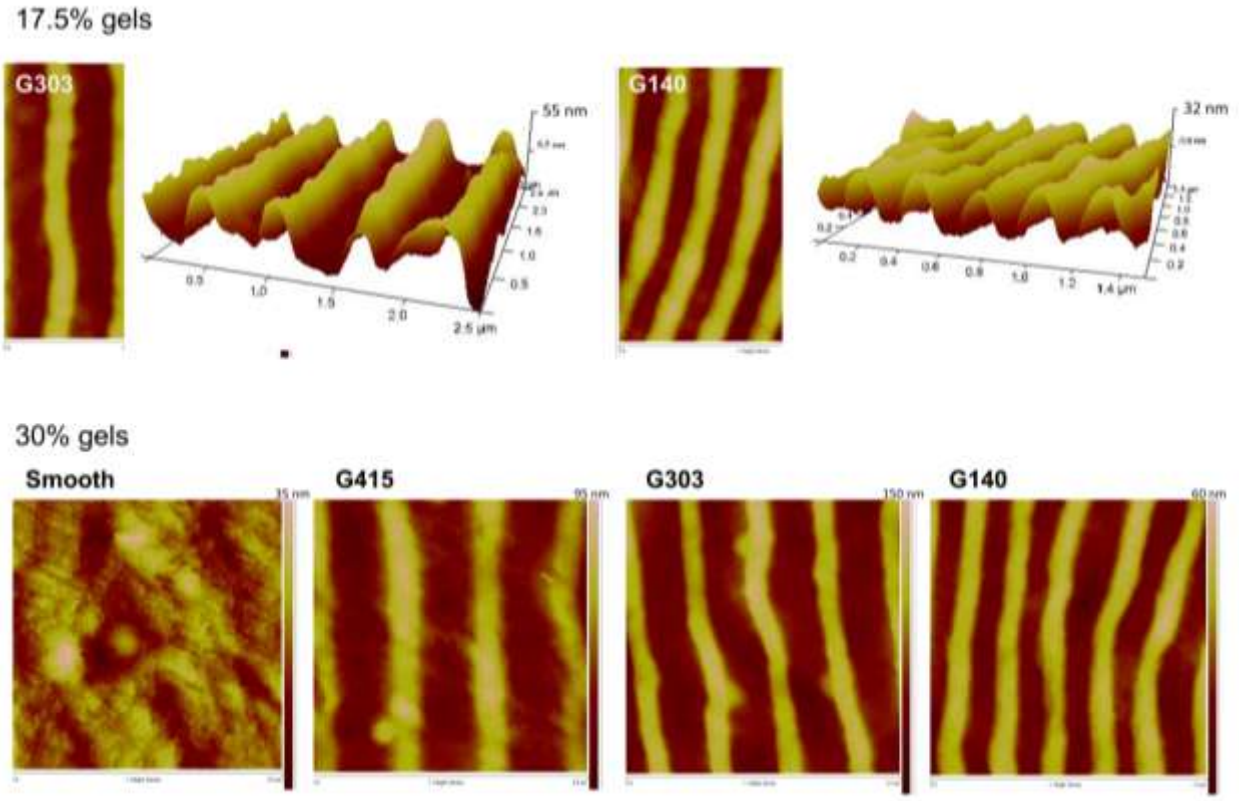

Figure 5.3 AFM of PEG gels illustrates nanotopgraphic features. PEGDA hydrogels were polymerized as previously described using a 3400 g/mol precursor. After dehydration films of 17.5 and 30 wt. % were assessed with AFM which revealed nanoscale gratings. As expected because of the loss of water, the scale of the gratings is reduced in comparison to the PUA mold.

5.3.3 PEGDA gels have tunable elasticity as determined by shear rheology.

The elasticity of PEGDA hydrogels is tunable through variations in PEGDA concentration, PEGDA chain length, or cross-linker/initiator concentration. Here, we modulated elasticity by using two different chain lengths and by altering the initial PEGDA precursor concentration. To determine the influence of these parameters on

PEGDA gels we performed rheological measurements to estimate the shear storage moduli (G') of these materials. Gels exhibited increased G' values occurred as PEGDA % increased and as the initial chain length decreased, as expected (Figure 5.4). Because PEGDA gels are hydrolytically labile, we performed rheology measurements after 21 days to determine changes in G'. In all instances, G' values decreased from their initial levels, but the decrease observed in 15% 700 g/mol gels was statistically significant (Figure 5.4 top left graph) where all others were not. This suggests that degradation of mechanical properties may have some impact on cell behavior, though degradation should occur on all smooth and nanoPEGDA surfaces so the net effect is likely negligible.

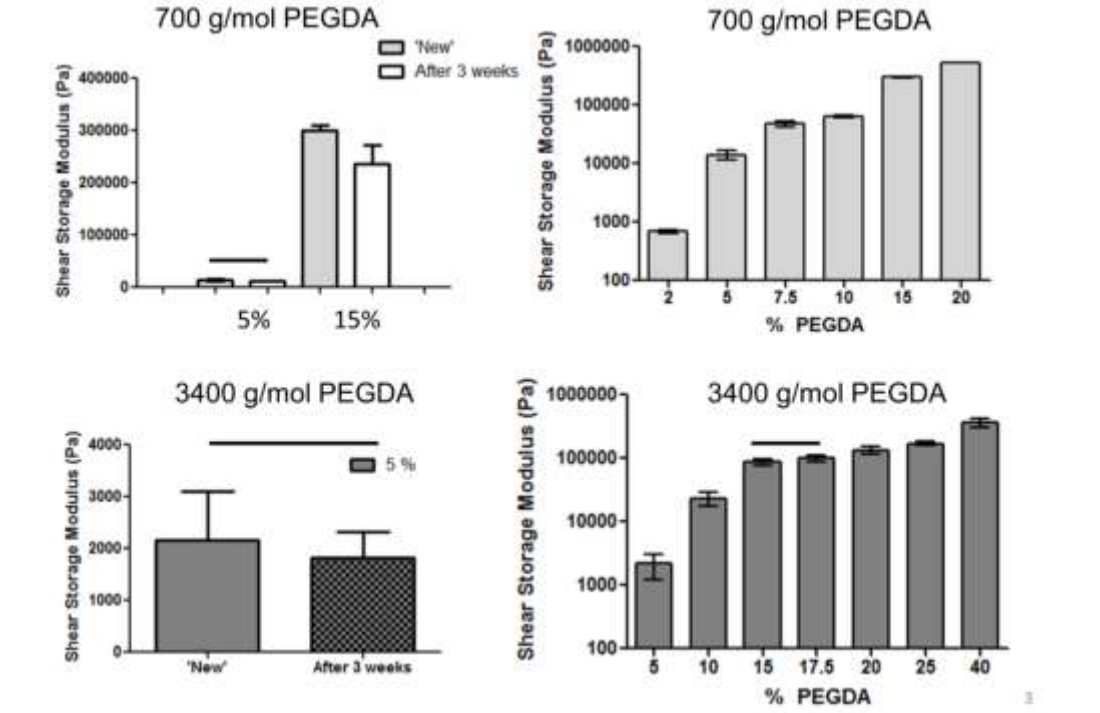

Figure 5.4 PEGDA hydrogels have tunable elasticity. Two different molecular weight PEGDAs (700 and 3,400 g/mol) were polymerized and sheared using a rheometer to obtain shear storage moduli data (see Materials and Methods). The smaller PEGDA chain gels were stiffer at comparable weight percentage of polymer. After 3 weeks in PBS at 37 °C mechanical properties were susceptible to degradation in 700 g/mol 15% gels. (Data connected by a bar is not statistically signficiant; all others are $p<0.05$, $n\geq3$.)

5.3.4 Polymerized PEGDA gels do not swell and contact angle measurements are not practical.

The swelling of PEGDA gels is minimal as indicated by the relaxed swelling ratio, Q_r, of approximately 1 for both 5 and 20% gels immersed in water and PBS (Figure 5.5). These data are supported by data from Nealey et al. as seen in Figure 5.5A.[25] Nealey et al. utilized higher molecular weight gels that did swell appreciably. Because gels of M_w 700 g/mol do not swell significantly, the shape and size of these gels can be preserved *in vitro* (and potentially *in vivo*) if their dimensions are greater than 100 nm. [34] Thus, because retaining feature size and shape is important to

determine effects of elastically tunable nanoPEGDA hydrogels, subsequent cell experiments were performed on 700 g/mol gels.

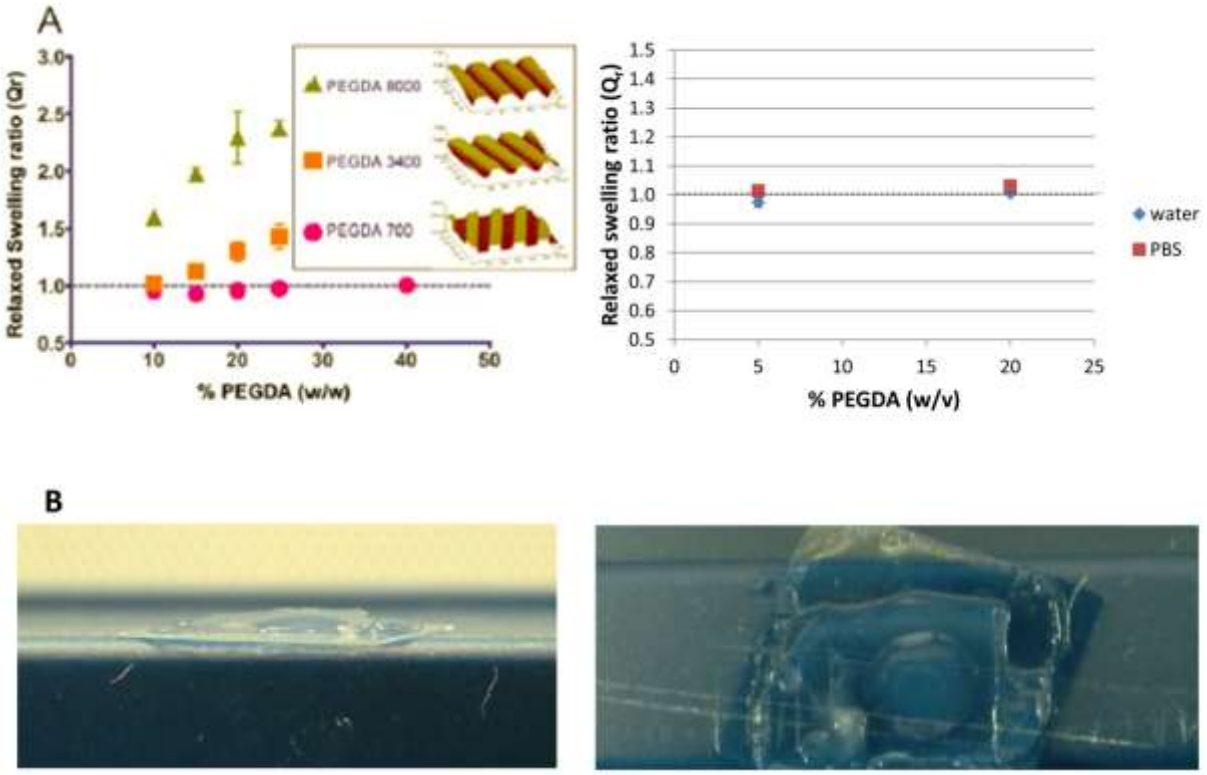

Figure 5.5 PEGDA gels do not appreciably swell from their initial gelled state and contact angles measurements are not practical. A.)Hydrogels of 700 g/mol PEGDA (5 and 20%) did not significantly swell in PBS or water after polymerization (right panel). This agrees with a previous report (left panel) that tested similar gels[25]. B.) Contact angle measurements were attempted but determined not feasible as, in most instances, water completely spread on gels; when a drop did form (Smooth, 20 wt.% ,700 g/mol) (left panel; right panel: top view) the contact angle was < 20°. (See more information in Results and Discussion for full explanation.)

Contact angle measurements were attempted on smooth and nanoPEGDA gels. A 5 μL drop of water was gently placed on PEGDA films. The droplet immediately spread over the surface. In an attempt to overcome this limitation, water was wicked off the surface with a Kim-Wipe tissue prior to adding the droplet. Again,

the water spread over the entire surface. On one occasion, as seen in Figure 5.5B, the droplet remained stable (on a smooth gel, 20 wt.% ,700 g/mol). The estimated contact angle was ~19.7°. The repeated spreading of water on these surfaces along with discussion with the laboratory housing the goniometer determined that measuring contact angles on PEGDA (of 10-20° when possible) is erratic and impractical. Another possible approach to measure contact angles is through use of the captive-bubble technique[35], however, the laboratory housing the goniometer (mentioned in Chapter 3) does not have the apparatus/set-up to perform these experiments. It is unknown if this equipment is available elsewhere on campus or if this technique would work with nanoPEGDA films.

5.3.5 Cells adhere to Col I conjugated PEGDA hydrogels-alignment, cytoskeletal features, and proliferation do not appear to be modulated.

As seen in Figure 5.6, cells adhered to PEGDA films. Cells did not consistently align with the underlying topography on nanoPEGDA surfaces, as suggested by the random orientation and lack of distinct directional elongation of cells seeded on grating surfaces. Cytoskeletal staining for actin and vinculin also showed no qualitative differences. Semi-quantitative assessment of proliferation determined no major differences on surfaces conjugated with 5 μg/mL col I (Figure 5.7) both when comparing changes in elasticity or comparing smooth to nanograting surfaces. Cell proliferation seemed to be unchanged.

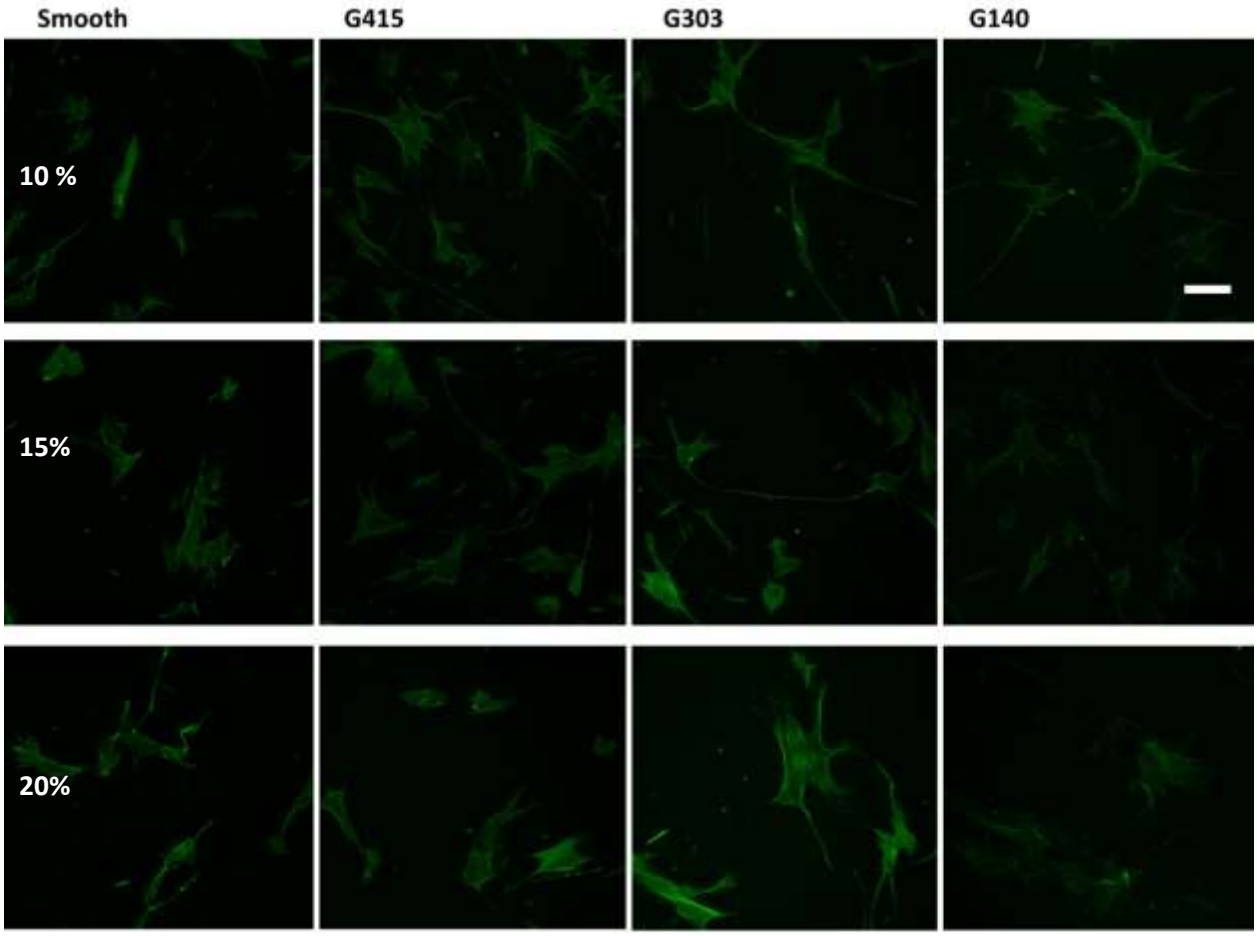
Smooth
G415
G303
G140
10 %
15%
20%

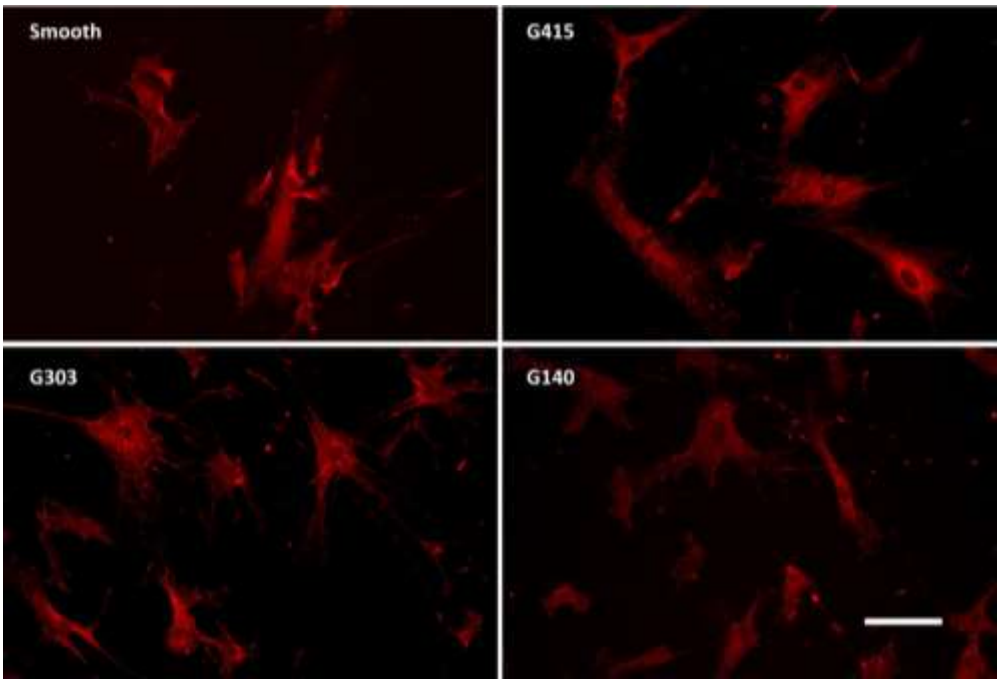
Smooth
G415
G303
G140

Figure 5.6 Cells on PEGDA gels show similar cytoskeletal characteristics on smooth and nanoPEGDA. Fluorescent images in the top panel (green) depict actin filaments after 4 days on PEGDA films conjugated with 5 μg/mL Col I. (See Materials and Methods for exact description of staining procedures). The bottom panel (red) shows staining of vinculin after 4 days on 5 μg/mL Col I 15% PEGDA gels, typically localized at focal adhesions. (Scale = 100 microns.)

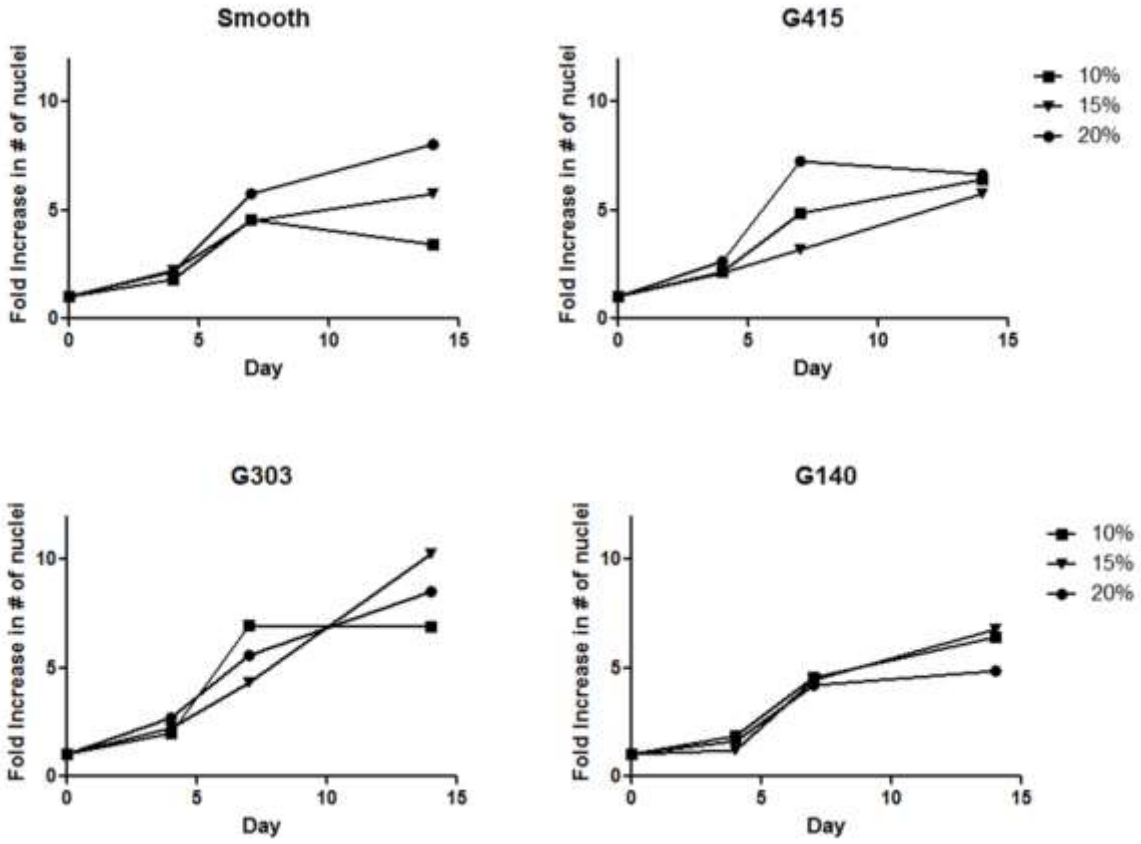

Figure 5.7 Cell proliferation is minimally influenced by nanotopography.
Semi-quantitative data (n=2) suggests that there are only minimal differences in cell numbers over two weeks on surfaces of varied topography and elasticity. Gels were conjugated with 5 μg/mL col I (as described in Materials and Methods).

5.3.6 nanoPEGDA has minimal impact on calcium deposited by MSCs.

To assess the influence of elasticity and nanotopography on the ability of MSCs to produce a mineralized matrix the amount of total calcium was quantified after 21 days of culture on PEGDA surfaces using the OCPC assay (Figure 5.8). Values were

normalized by the apparent surface area to correct for any differences in film size. Overall, calcium levels were minimally impacted by nanotopographic features. Only 10 wt. % G303 (5 μg/mL) gels had significantly higher calcium deposition than smooth surfaces (of the same wt. %). Ligand density shifted calcium averages higher, with 5 μg/mL Col I surfaces driving slightly increased calcium levels. Only 15 wt. % gels with Col I conjugated at 5 μg/mL showed stastitically higher calcium levels than 50 μg/mL gels. An (non-statistical) increase in calcium levels correlated with increasing elasticity for smooth gels conjugated with 5 μg/mL Col I.

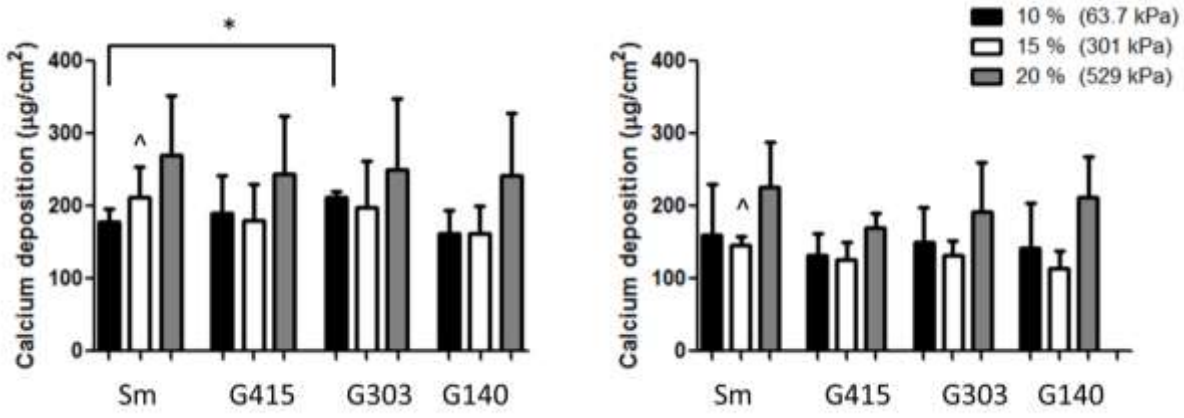

Figure 5.8 Calcium deposition on PEGDA was minimally influenced by nanotopography. The graph on the left is quantification of gels conjugated with 5 μg/mL collagen I at day 21; at right is quantification of gels conjugated with 50 μg/mL Col I. Quantification of total calcium levels showed that only 10 wt. % G303 (5 μg/mL) gels had significantly higher calcium deposition than smooth surfaces (of the same wt. %). 5 μg/mL Col I PEGDA gels had elevated total calcium levels compared to similar 50 μg/mL Col I gels (of the same wt.%) but only the 15% smooth gel showed significantly higher calcium levels when conjugated with 5 μg/mL col I (^ * p <0.05)(n = 3).

5.3.7 nanoPEGDA has minimal impact on Ca/P ratios in MSC deposited mineral.

To assess composition, mineral deposits of the culture area surrounding the nanoPEGDA gel were stained via the Von Kossa method to visualize the presence of

phosphates [36]. (PEGDA films were removed and placed in another 12 well plate after fixation, the original well was then stained for phosphates). These stains were positive (data not shown).Topographic and smooth surfaces showed the presence of mineral deposition via bright field imaging (data not shown). Additionally, deposited mineral was observed using SEM (Figure 5.8). To determine the presence of calcium and phosphorous, XEDS was used. Analysis showed that there were no significant differences in the Ca:P ratio on nanoPEGDA compared to smooth surfaces. Mineral deposited on PEGDA films had Ca:P ratios ranging from 1.30 (G303) to 1.39 (G415 and G140) and 1.30 (G303 and G140) to 1.37 (G415) on 5 and 50 μg/mL Col I conjugated PEGDA gels. For reference, we observed the Ca:P ratio in hydroxyapatite to be 1.65 (theoretical ratio 1.67).

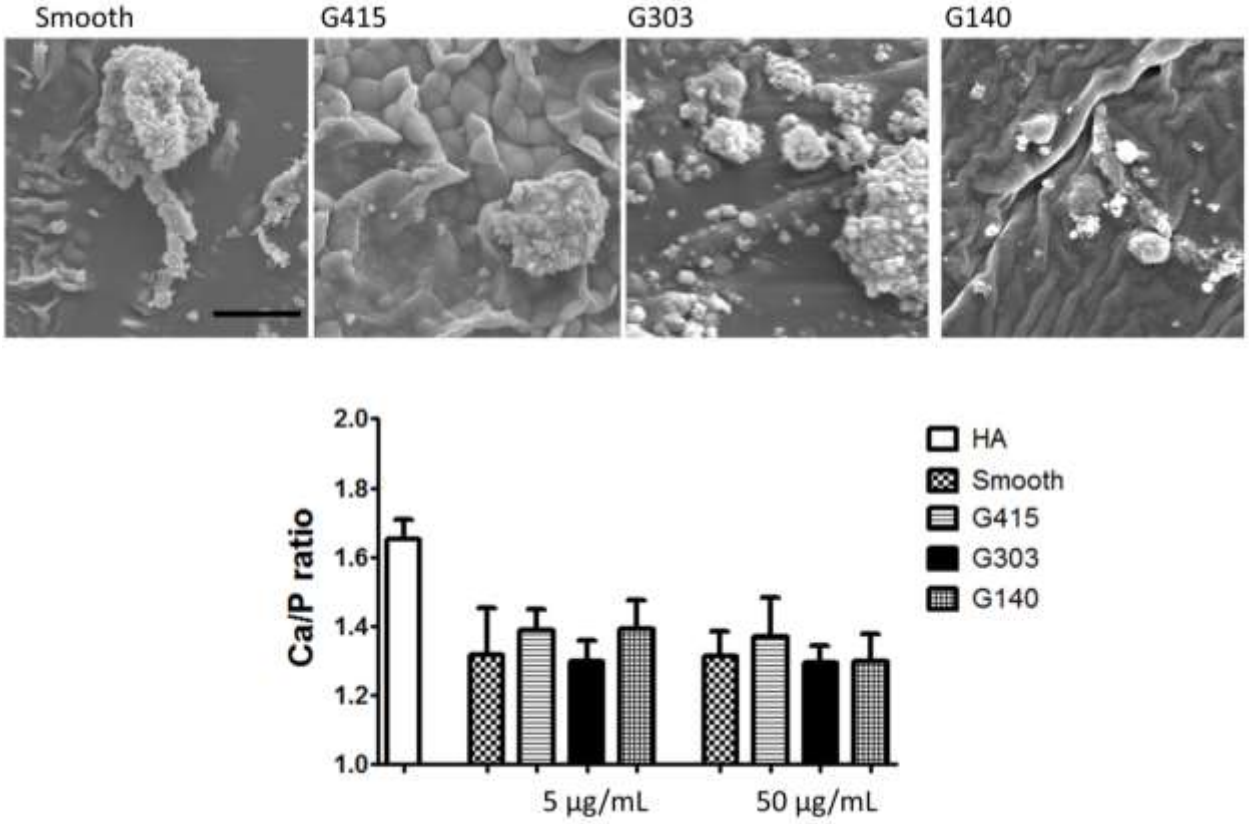

Figure 5.9 Ca:P ratio on nanoPEGDA is not altered. Ca/P ratios are similar for all conditions of 10 wt.% PEGDA gels (~64kPa G') after 21 days conjugated with different densities of collagen I (5 and 50 µg/mL). Micrographs show mineral on each respective surface. All groups were significantly lower than the HA control ($p < 0.05$). (Scale = 200 microns.)

5.4 Discussion

The ECM is a diverse and instructional material that is critical to cell behavior and tissue function. Of late, literature reports suggest that cells sense and respond to ECM elasticity and topography in addition to their adhesive cues. Most previous investigations have looked at these three factors in pairs, either coupling topography with ligand concentration (or identity) or coupling matrix elasticity with ligand concentration (or identity). Dependent on the parameters investigated, the outcome sometimes showed an enhanced osteogenic response. In this study, we created

tunable elastic surfaces imparted with controlled nanotopographic features conjugated with Col I to, at least to the best of our knowledge, be the first to investigate the role of all three factors in driving an hMSC osteogenic phenotype. We varied the mechanical properties to try replicate the elastic properties of a collagenous network[7]. The controlled nanofeatures were used to replicate the scale and architecture of collagen fibrils in native bone[37,38]. We found that, through assessments of calcium quantity and composition, topography coupled with tunable PEGDA matrices of varied ligand concentration, did not have a synergistic impact and were not a strong driver of an osteogenic phenotype, at least with the features and mechanical properties studied here. Substrate elasticity did drive an enhanced osteogenic phenotype though the influence was not statistically significant.

After quantitatively assessing the shear storage modulus of two different chain lengths (700; 3,400 g/mol) and varied polymer concentrations (up to 40%), we quantitatively assessed the swelling ratio of PEGDA gels of M_w: 700 g/mol in PBS and water. We found that gels do not swell appreciably after polymerization, similar to a previous report.[25] (Note: if hydrogels are dehydrated they will shrink. Upon rehydration they will swell and achieve approximately the same volume as when first polymerized; these measurements were performed to assess if additional swelling occurred after polymerization.) Because the gels do not swell, we can reasonably expect that the nanofeatures will not be distorted, at least not because of swelling. We confirmed the presence of nanofeatures using AFM. Next we investigated the

adhesion and proliferation of MSCs to the gels. We did not see any (semi-qualitative) differences in cell proliferation due to nanotopography or changes in elasticity.

Likewise, when investigating the actin cytoskeleton, focal adhesions, and cell shape we did not see any notable qualitative differences in fluorescent images. Cells had similar shape on all surfaces regardless of the presence of nanotopography. A previous report showed alignment of cardiomyocytes with the underlying topography on similar nanoPEGDA surfaces[33]. Another report using epithelial cells showed mixed results on nano and microPEGDA: alignment was dependent on media formulation and RGD presence[25]. Cells usually behaved similarly to cells on smooth surfaces (random alignment, minimal elongation) on the 400 nm width topographic surfaces. Depending on conditions, cells would align parallel and even perpendicular to their underlying surfaces. Our result is most similar to the behavior of the epithelial cells. Clearly, differences in cell type, ligand identity, cell density, substrate elasticity (our surfaces are approximately two to four orders of magnitude softer)[33], or other factors may contribute to the varied alignment response. In addition, other reports of cell alignment are associated with high modulus materials[39-41].

To characterize the influence of nanotopography, elasticity, and ligand concentration on osteogenic phenotype in MSCs we focused on mineral deposition. Our results showed that, through quantitative measurements of calcium levels after 21 days, nanotopography did not enhance the osteogenic phenotype of MSCs compared to those grown on smooth PEGDA. The exception was on 10% (63.7 kPA) 5μg/mL

Col I conjugated G303 nanoPEGDA surfaces as levels were statistically higher than on smooth surfaces (with the same elasticity and ligand concentration). Overall, ligand concentration was influential on elevating calcium levels on surfaces with 5μg/mL compared to 50 μg/mL Col I, though these levels were not statistically significant (except with 15% smooth gels). To further assess the influence of nanotopography, elasticity, and ligand concentration on the osteogenic phenotype of MSCs we assessed the mineral composition using SEM-XEDS to determine Ca:P ratios. No significant differences were seen on nanotopographic surfaces compared to smooth surfaces or on surfaces of different ligand concentration on 10 wt. % gels. Ca:P ratios were slightly higher on gels with 5μg/mL compared to 50 μg/mL Col I, though these differences were not statistically significant. (Ca:P ratios on 5 μg/mL Col I gels of 15 wt% did not have enhanced values relative to smooth (uncontrolled topographic) surfaces; data not shown) Taken together these data suggest that nanotopography coupled with tunable substrates of varied ligand density minimally enhance an osteogenic phenotype. With these data, it seems the best option would be to use a surface conjugated with 5 μg/mL Col I and a feature size of 415 nm because it couples the highest Ca:P ratio with similar calcium levels to smooth surfaces, at least for 10 wt. % (63.7 kPa) gels. Further investigation is needed into mineral Ca:P ratios on higher modulus substrates. Both *in vitro* and *in vivo* physiological mineral formation (and the respective calcium and phosphate content) is contingent on collagen, both

the production and structure[37,38,42-46] as osteogenesis imperfect is associated with non-ideal collagen fibril size[47].

In addition to collagen's role in the structure and function of bone is its role as an anchorage site for cells. Cells respond differently to native and partially denatured collagen[13]. Key to this response is the availability of integrin binding sites. Activation of various integrins is known to drive osteogenesis.[22,23,48] Specifically, the $\alpha_2\beta_1$ integrin is associated with collagen mediated osteogenesis[49]. This integrin and others are known to activate intercellular signaling pathways for osteogenesis to varying degrees.[22] Because of these findings we choose to tether collagen I to our PEGDA gels. We varied the concentration of Col I as varied ligand concentration has been associated with altered cell response[19]. We did not see marked differences due to changes in ligand density, though this may be because we looked at functional assessments of mineral by quantifying calcium levels and Ca:P ratios rather than gene and protein expression levels. In addition, the mechanics of the underlying substrate and the cell type were different[19,28], thus it is difficult to make appropriate comparisons. What those previous studies clearly showed, however, is that intercellular signaling was influenced by ligand identity and matrix elasticity.

The intracellular signaling pathway that was influenced through modulation of matrix elasticity involves MAPK. Sensation of matrix elasticity depends on cell anchorage sites. Signaling molecules at focal adhesions (FAs) and downstream of FAs

are involved in mechanosensing[19]. RhoA was found to have a crucial role in modulating ERK expression on substrates of increasing stiffness, implicating its importance to sensation of mechanical cues. Additionally, RhoA was found to be associated with MSC osteogenic differentiation[10]. These findings suggest that RhoA activation in response to matrix elasticity is crucial to MSC differentiation. Our results suggest that when assessing mineral deposition on PEGDA hydrogels conjugated with Col I (5 μg/mL) increased matrix elasticity does enhance calcium levels on smooth surfaces though the results were not statistically significant. This same trend was not seen on nanotopography. This suggests that RhoA activation might be different when the two cues are coupled, though this needs to be assessed (as many factors could be contributing to this result: cell type, differences in elasticities between studies etc.). A recent study suggests that matrix ligand conjugation and the subsequent cellular response is highly dependent on matrix structure[14,50]; this could also play a role in the observed results. Recent evidence suggests that cells use similar machinery and intercellular signaling to sense matrix elasticity and topography[12]. This may explain why some reports suggest increased expression of pFAK and other osteogenic markers on topographic surfaces[17,39,51].

In this study, we focused on PEG hydrogels because they can be tuned mechanically, imparted with nano- and micro-topography, copolymerized with biodegradable polymers, or conjugated with ECM proteins via a variety of published techniques[25] to investigate the cellular response to these inputs, specifically MSC

differentiation. Thus, all or some of these inputs (in addition to others) can be fine-tuned to drive a desired cell behavior. Here we assessed slight turns of the 'knobs' for elasticity, topography, and ligand concentration on osteoegenic (functional) phenotype. The parameters we tested did not produce a synergistic enhancement of MSC osteogenic phenotype, but softer or stiffer gels, different feature sizes or shapes, and different ligands may produce a different response. Further investigations are necessary to determine if further fine tuning of these knobs can drive, potentially synergistically, osteogenesis in MSCs. Additional investigations are also necessary to determine how to modulate the presentation of adhesion ligands as this seems to be the likely cause (or, at least, a contributing factor) for driving altered cell behaviors on surfaces with varied topography and elasticity.

5.5 References

1 Pompe, T. *et al.* Dissecting the Impact of Matrix Anchorage and Elasticity in Cell Adhesion. *Biophys J* **97**, 2154-2163, doi:DOI 10.1016/j.bpj.2009.07.047 (2009).

2 Gonzalez-Garcia, C., Sousa, S. R., Moratal, D., Rico, P. & Salmeron-Sanchez, M. Effect of nanoscale topography on fibronectin adsorption, focal adhesion size and matrix organisation. *Colloid Surface B* **77**, 181-190, doi:DOI 10.1016/j.colsurfb.2010.01.021 (2010).

3 Mauney, J. & Volloch, V. Collagen I matrix contributes to determination of adult human stem cell lineage via differential, structural conformation-specific elicitation of cellular stress response. *Matrix Biol* **28**, 251-262, doi:DOI 10.1016/j.matbio.2009.04.002 (2009).

4 Schoen, I., Pruitt, B. L. & Vogel, V. The Yin-Yang of Rigidity Sensing: How Forces and Mechanical Properties Regulate the Cellular Response to Materials.

Annual Review of Materials Research **43**, 589-618, doi:10.1146/annurev-matsci-062910-100407 (2013).

5 Prodanov, L. *et al.* The interaction between nanoscale surface features and mechanical loading and its effect on osteoblast-like cells behavior. *Biomaterials* **31**, 7758-7765, doi:DOI 10.1016/j.biomaterials.2010.06.050 (2010).

6 Schwarz, U. S. & Gardel, M. L. United we stand - integrating the actin cytoskeleton and cell-matrix adhesions in cellular mechanotransduction. *J Cell Sci* **125**, 3051-3060, doi:Doi 10.1242/Jcs.093716 (2012).

7 Engler, A. J., Sen, S., Sweeney, H. L. & Discher, D. E. Matrix elasticity directs stem cell lineage specification. *Cell* **126**, 677-689, doi:DOI 10.1016/j.cell.2006.06.044 (2006).

8 Peyton, S. R. & Putnam, A. J. Extracellular matrix rigidity governs smooth muscle cell motility in a biphasic fashion. *J Cell Physiol* **204**, 198-209, doi:Doi 10.1002/Jcp.20274 (2005).

9 Kilian, K. A., Bugarija, B., Lahn, B. T. & Mrksich, M. Geometric cues for directing the differentiation of mesenchymal stem cells. *P Natl Acad Sci USA* **107**, 4872-4877, doi:DOI 10.1073/pnas.0903269107 (2010).

10 McBeath, R., Pirone, D. M., Nelson, C. M., Bhadriraju, K. & Chen, C. S. Cell shape, cytoskeletal tension, and RhoA regulate stem cell lineage commitment. *Dev Cell* **6**, 483-495, doi:Doi 10.1016/S1534-5807(04)00075-9 (2004).

11 Biggs, M. J. P. *et al.* The use of nanoscale topography to modulate the dynamics of adhesion formation in primary osteoblasts and ERK/MAPK signalling in STRO-1+enriched skeletal stem cells. *Biomaterials* **30**, 5094-5103, doi:DOI 10.1016/j.biomaterials.2009.05.049 (2009).

12 Albuschies, J. & Vogel, V. The role of filopodia in the recognition of nanotopographies. *Sci Rep-Uk* **3**, doi:Artn 1658 Doi 10.1038/Srep01658 (2013).

13 Denis, F. A., Pallandre, A., Nysten, B., Jonas, A. M. & Dupont-Gillain, C. C. Alignment and assembly of adsorbed collagen molecules induced by anisotropic chemical nanopatterns. *Small* **1**, 984-991, doi:DOI 10.1002/smll.200500116 (2005).

14 Li, B. J., Moshfegh, C., Lin, Z., Albuschies, J. & Vogel, V. Mesenchymal Stem Cells Exploit Extracellular Matrix as Mechanotransducer. *Sci Rep-Uk* **3**, doi:Artn 2425 Doi 10.1038/Srep02425 (2013).

15 Zhang, D. & Kilian, K. A. The effect of mesenchymal stem cell shape on the maintenance of multipotency. *Biomaterials* **34**, 3962-3969, doi:DOI 10.1016/j.biomaterials.2013.02.029 (2013).

16 Dalby, M. J. *et al.* The control of human mesenchymal cell differentiation using nanoscale symmetry and disorder. *Nat Mater* **6**, 997-1003, doi:Doi 10.1038/Nmat2013 (2007).

17 Yim, E. K. F., Darling, E. M., Kulangara, K., Guilak, F. & Leong, K. W. Nanotopography-induced changes in focal adhesions, cytoskeletal organization, and mechanical properties of human mesenchymal stem cells. *Biomaterials* **31**, 1299-1306, doi:DOI 10.1016/j.biomaterials.2009.10.037 (2010).

18 Tay, C. Y. *et al.* Micropatterned matrix directs differentiation of human mesenchymal stem cells towards myocardial lineage. *Exp Cell Res* **316**, 1159-1168, doi:DOI 10.1016/j.yexcr.2010.02.010 (2010).

19 Khatiwala, C. B., Kim, P. D., Peyton, S. R. & Putnam, A. J. ECM Compliance Regulates Osteogenesis by Influencing MAPK Signaling Downstream of RhoA and ROCK. *J Bone Miner Res* **24**, 886-898, doi:Doi 10.1359/Jbmr.081240 (2009).

20 Janson, I. A., Kong, Y. P. & Putnam, A. J. Nanotopographic Substrates of Poly (Methyl Methacrylate) Do Not Strongly Influence the Osteogenic Phenotype of Mesenchymal Stem Cells In Vitro. *Plos One* **9**, e90719, doi:10.1371/journal.pone.0090719 (2014).

21 Mauney, J. R. *et al.* Matrix-mediated retention of in vitro osteogenic differentiation potential and in vivo bone-forming capacity by human adult bone marrow-derived mesenchymal stem cells during ex vivo expansion. *J Biomed Mater Res A* **79A**, 464-475, doi:Doi 10.1002/Jbm.A.30876 (2006).

22 Kundu, A. K. & Putnam, A. J. Vitronectin and collagen I differentially regulate osteogenesis in mesenchymal stem cells. *Biochem Bioph Res Co* **347**, 347-357, doi:DOI 10.1016/j.bbrc.2006.06.110 (2006).

23 Salasznyk, R. M., Klees, R. F., Boskey, A. & Plopper, G. E. Activation of FAK is necessary for the osteogenic differentiation of human mesenchymal stem

cells on laminin-5. *J Cell Biochem* **100**, 499-514, doi:Doi 10.1002/Jcb.21074 (2007).

24 McMurray, R. J. *et al.* Nanoscale surfaces for the long-term maintenance of mesenchymal stem cell phenotype and multipotency. *Nat Mater* **10**, 637-644, doi:Doi 10.1038/Nmat3058 (2011).

25 Yanez-Soto, B., Liliensiek, S. J., Murphy, C. J. & Nealey, P. F. Biochemically and topographically engineered poly(ethylene glycol) diacrylate hydrogels with biomimetic characteristics as substrates for human corneal epithelial cells. *J Biomed Mater Res A* **101A**, 1184-1194, doi:Doi 10.1002/Jbm.A.34412 (2013).

26 Choi, S. J., Yoo, P. J., Baek, S. J., Kim, T. W. & Lee, H. H. An ultraviolet-curable mold for sub-100-nm lithography. *J Am Chem Soc* **126**, 7744-7745, doi:Doi 10.1021/Ja048972k (2004).

27 Singh, R. K., Seliktar, D. & Putnam, A. J. Capillary morphogenesis in PEG-collagen hydrogels. *Biomaterials* **34**, 9331-9340, doi:DOI 10.1016/j.biomaterials.2013.08.016 (2013).

28 Khatiwala, C. B., Peyton, S. R. & Putnam, A. J. Intrinsic mechanical properties of the extracellular matrix affect the behavior of pre-osteoblastic MC3T3-E1 cells. *Am J Physiol-Cell Ph* **290**, C1640-C1650, doi:DOI 10.1152/ajpcell.00455.2005 (2006).

29 Krause, U., Seckinger, A. & Gregory, C. A. Assays of Osteogenic Differentiation by Cultured Human Mesenchymal Stem Cells. *Methods Mol Biol* **698**, 215-230, doi:Doi 10.1007/978-1-60761-999-4_17 (2011).

30 D.J.P Prockop, G. D., B. Bunnell *Mesenchymal Stem Cells: Methods and Protocols*. (Humana Press, 2008).

31 Ter Brugge, P. J. & Jansen, J. A. In vitro osteogenic differentiation of rat bone marrow cells subcultured with and without dexamethasone. *Tissue Eng* **8**, 321-331, doi:Doi 10.1089/107632702753725076 (2002).

32 Rao, R. R., Jiao, A., Kohn, D. H. & Stegemann, J. P. Exogenous mineralization of cell-seeded and unseeded collagen-chitosan hydrogels using modified culture medium. *Acta Biomater* **8**, 1560-1565, doi:DOI 10.1016/j.actbio.2012.01.001 (2012).

33 Kim, D. H. *et al.* Nanoscale cues regulate the structure and function of macroscopic cardiac tissue constructs. *P Natl Acad Sci USA* **107**, 565-570, doi:DOI 10.1073/pnas.0906504107 (2010).

34 Caldorera-Moore, M. *et al.* Swelling behavior of nanoscale, shape- and size-specific, hydrogel particles fabricated using imprint lithography. *Soft Matter* **7**, 2879-2887, doi:Doi 10.1039/C0sm01185a (2011).

35 Cheng, L., Muller, S. J. & Radke, C. J. Wettability of silicone-hydrogel contact lenses in the presence of tear-film components. *Curr Eye Res* **28**, 93-108, doi:DOI 10.1076/ceyr.28.2.93.26231 (2004).

36 Bonewald, L. F. *et al.* Von Kossa staining alone is not sufficient to confirm that mineralization in vitro represents bone formation. *Calcified Tissue Int* **72**, 537-547, doi:DOI 10.1007/s00223-002-1057-y (2003).

37 Weiner, S. & Wagner, H. D. The material bone: Structure mechanical function relations. *Annual Review of Materials Science* **28**, 271-298, doi:DOI 10.1146/annurev.matsci.28.1.271 (1998).

38 Landis, W. J., Song, M. J., Leith, A., Mcewen, L. & Mcewen, B. F. Mineral and Organic Matrix Interaction in Normally Calcifying Tendon Visualized in 3 Dimensions by High-Voltage Electron-Microscopic Tomography and Graphic Image-Reconstruction. *J Struct Biol* **110**, 39-54, doi:DOI 10.1006/jsbi.1993.1003 (1993).

39 Watari, S. *et al.* Modulation of osteogenic differentiation in hMSCs cells by submicron topographically-patterned ridges and grooves. *Biomaterials* **33**, 128-136, doi:DOI 10.1016/j.biomaterials.2011.09.058 (2012).

40 Wood, J. A. *et al.* The modulation of canine mesenchymal stem cells by nano-topographic cues. *Exp Cell Res* **318**, 2438-2445, doi:DOI 10.1016/j.yexcr.2012.06.022 (2012).

41 Teixeira, A. I., Abrams, G. A., Bertics, P. J., Murphy, C. J. & Nealey, P. F. Epithelial contact guidance on well-defined micro- and nanostructured substrates. *J Cell Sci* **116**, 1881-1892, doi:Doi 10.1242/Jcs.00383 (2003).

42 Silver, F. H. & Landis, W. J. Deposition of apatite in mineralizing vertebrate extracellular matrices: A model of possible nucleation sites on type I collagen. *Connect Tissue Res* **52**, 242-254, doi:Doi 10.3109/03008207.2010.551567 (2011).

43 Kerschnitzki, M. *et al.* The organization of the osteocyte network mirrors the extracellular matrix orientation in bone. *J Struct Biol* **173**, 303-311, doi:DOI 10.1016/j.jsb.2010.11.014 (2011).

44 Allori, A. C., Sailon, A. M. & Warren, S. M. Biological basis of bone formation, remodeling, and repair - Part II: Extracellular matrix. *Tissue Eng Part B-Re* **14**, 275-283, doi:DOI 10.1089/ten.teb.2008.0083 (2008).

45 Nudelman, F. *et al.* The role of collagen in bone apatite formation in the presence of hydroxyapatite nucleation inhibitors. *Nat Mater* **9**, 1004-1009, doi:Doi 10.1038/Nmat2875 (2010).

46 Marsh, M. E., Munne, A. M., Vogel, J. J., Cui, Y. Q. & Franceschi, R. T. Mineralization of Bone-Like Extracellular-Matrix in the Absence of Functional Osteoblasts. *J Bone Miner Res* **10**, 1635-1643 (1995).

47 Cassella, J. P. & Ali, S. Y. Abnormal Collagen and Mineral Formation in Osteogenesis Imperfecta. *Bone Miner* **17**, 123-128, doi:Doi 10.1016/0169-6009(92)90722-P (1992).

48 Klees, R. F., Salasznyk, R. M., Vandenberg, S., Bennett, K. & Plopper, G. E. Laminin-5 activates extracellular matrix production and osteogenic gene focusing in human mesenchymal stem cells. *Matrix Biol* **26**, 106-114, doi:DOI 10.1016/j.matbio.2006.10.001 (2007).

49 Kundu, A. K., Khatiwala, C. B. & Putnam, A. J. Extracellular Matrix Remodeling, Integrin Expression, and Downstream Signaling Pathways Influence the Osteogenic Differentiation of Mesenchymal Stem Cells on Poly(Lactide-Co-Glycolide) Substrates. *Tissue Eng Pt A* **15**, 273-283, doi:DOI 10.1089/ten.tea.2008.0055 (2009).

50 Trappmann, B. *et al.* Extracellular-matrix tethering regulates stem-cell fate. *Nat Mater* **11**, 642-649, doi:Doi 10.1038/Nmat3339 (2012).

51 Lim, J. Y. *et al.* The regulation of integrin-mediated osteoblast focal adhesion and focal adhesion kinase expression by nanoscale topography. *Biomaterials* **28**, 1787-1797, doi:DOI 10.1016/j.biomaterials.2006.12.020 (2007).

CHAPTER 6

Conclusions and Future Directions

6.1 Contributions of this Dissertation

This work has demonstrated that nanotopographic features that mimic the architecture of bone do not enhance calcium levels in mineral deposited by hMSCs though in some cases surfaces promote a more mature mineral. In addition, this work demonstrated that nanotopography coupled with varied matrix elasticity and ligand concentration does not strongly drive an osteogenic phenotype in hMSCs. Three specific aims were addressed to formulate these conclusions.

Specific Aim 1

Develop and characterize model nanotopographic surfaces that mimic the native architecture of bone.

Specific Aim 2

Assess the impact of topographical cues on MSC osteogenic differentiation.

Specific Aim 3

Investigate if nanotopography and matrix stiffness synergistically enhances osteogenic differentiation.

Two material platforms for cell culture were created to support the completion of these aims. The first platform was created using a photopolymerization technique to produce films of PMMA, a material commonly used in orthopedic applications, with nanotopographic features. It was demonstrated that MSCs aligned parallel to the underlying topography yet these changes in cell shape (relative to smooth surfaces) did not translate to an enhanced osteogenic phenotype as determined through assessments of calcium levels and Ca:P ratios. The second platform, a photopolymerizable polymer PEGDA, has an extensive history as a tissue engineering platform. PEGDA can be tunable and 'imprintable' to modulate the mechanical properties and impart nanofeatures. It was demonstrated, similar to PMMA, that when combining critical ECM cues, topography, elasticity, and ligand concentration, no synergistic enhancement of hMSC osteogenesis was observed.

6.2 Conclusions

Fulfillment of Specific Aim 1 required the development of a material that replicated the nanoscale architecture of the mineralized collagen fibril of bone.(The nanoscale gaps between fibrils are important for the aggregation and growth of calcium phosphate particles into lamellar sheets[1].) We developed a technique utilizing the capillarity effect of small channels[2] to create UV-polymerized PMMA nanofilms. We validated the nanoscale dimensions of these films using scanning probe microscopy (AFM) and scanning electron microscopy. The film features ranged from 140 to 415 nm and 110 to 200 nm in width and height respectively. We then measured contact angles on these surfaces to determine changes in the surface free energy. Contact angles on nanoPMMA were altered compared to smooth controls as anisotropy, similar to the underlying surface, was observed. This effect suggests that full wetting, known as Wenzel wetting, occurred. Smooth PMMA was slightly hydrophilic thus Wenzel wetting should be expected on nanograting PMMA surfaces. To confirm our expectations and our observations, we calculated the transition between Wenzel and Cassie-Baxter wetting[3] on our nanoPMMA surfaces. These calculations confirmed that our expectations and observations were correct. The height of the nanogratings presents an energy barrier to liquid droplet motion perpendicular to the gratings. As a result, the droplet elongates parallel to the direction of the gratings. We measured the contact angle perpendicular and parallel to the gratings and used an approximation developed specifically for polymers[4] to estimate the surface free energy. We observed increases in SFE parallel to gratings and

decreases perpendicular to gratings. To understand the role of changes in SFE on protein adsorption we estimated the energy required to promote unfolding. We found the energy change was not sufficient to promote significant unfolding. This suggested and was confirmed in our cellular assays that the changes in SFE are insufficient to promote significant changes in protein adsorption that enhances osteogenesis.

Fulfilment of specific Aim 2 required the use of our nanoPMMA films developed in Aim 1. Using these films to replicate bone architecture, we showed that MSC alignment, focal adhesion and cytoskeleton assembly, and proliferation are all influenced by nanotopographic gratings of PMMA in the 140-415 nm size range (width, depths 100 to 200 nm). Initial adhesion (after 4 hours) to nanoPMMA surfaces was similar to smooth controls suggesting that subsequent differences in observed behavior are not due to differences in initial cell number on each respective surface. We investigated ALP levels, as ALP is intimately involved in mineral formation[5] and is a known marker of osteogenesis[6], and found no significant enhancement on nanoPMMA (compared to smooth controls). We used both qualitative and quantitative assessments of mineralization, to conclude that PMMA nanotopgraphy is a poor driver of the ostegenic differentiation of MSCs *in vitro*. Differences in Ca:P ratios present in deposited mineral were influenced by topographic surfaces with specific feature sizes, suggesting that certain feature sizes (specifically 415 nm width, 200 nm height) might enhance maturation of deposited mineral. Matrix maturation and correct collagen fibril spacing is clinically relevant

because health maladies such as osteogenesis imperfecta result because of abnormal collagen-mineral structure[7]. Finally, our results agree with *in vivo* work using nanogratings showing that nanotopography does not enhance bone formation after 8 weeks in rabbits[8](Figure 6.2).

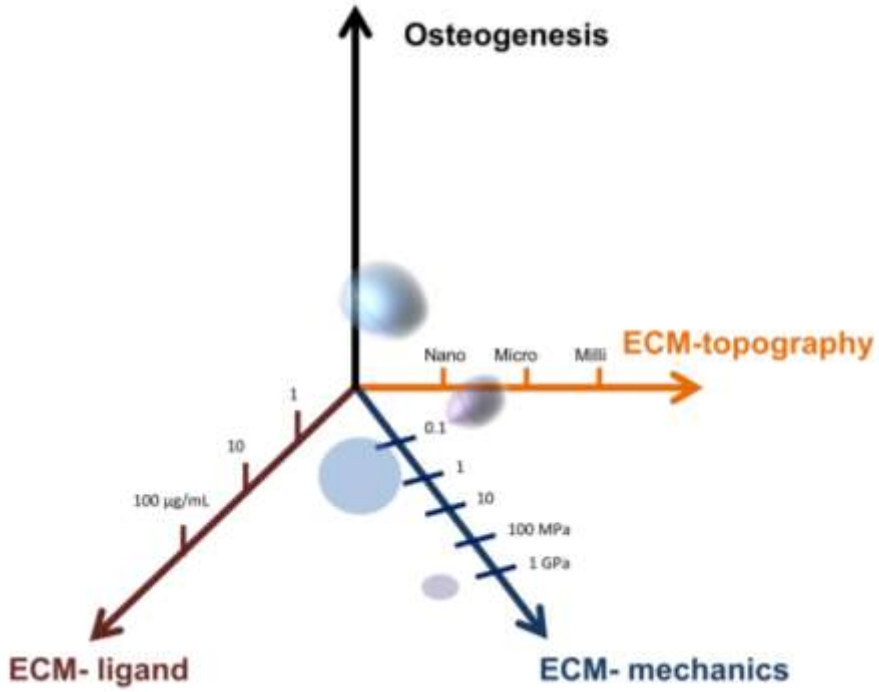

Figure 6.1 A 4-D map illustrating the regions assessed for enhanced osteogenesis. Nanotopography, ligand concentration, and matrix mechanics were modulated using either platforms of PMMA or PEGDA. The regions assessed did not show enhancement of osteogenesis in MSCs as determined mainly by quantitative assessment of mineral deposition. Collagen I was the ligand used with PEGDA, other ECM proteins could also be investigated.

Fulfilment of specific Aim 3 required development of a material platform that allowed for the modulation of substrate elasticity and 'imprinting' of nanofeatures onto the substrate surface. PEGDA was used to develop films with both tunable elasticity and nanofeatures that mimic the size and architecture of collagen fibrils (similar to Aim1). Using these films to replicate bone architecture, we showed that we

could manufacture substrates with elasticities that spanned several orders of magnitude and contained nanoscale gratings. Mechanical properties were chosen to replicate the approximate elasticity of *in vivo* collagenous matrices[9]. We also showed that MSC alignment is not influenced by the underlying topography. Similarly, the focal adhesions did not appear to be altered on nanoPEGDA compared to smooth controls. We used both qualitative and quantitative assessments of mineralization to show minimal enhancement of calcium levels on nanoPEGDA compared to controls. Ca:P ratios showed a slight dependence when coupling ligand concentration and topography in comparison to smooth controls. These findings lead us to conclude that PEGDA nanotopography coupled with tunable elasticity does not produce a synergistic enhancement of osteogenic differentiation of MSCs *in vitro*.

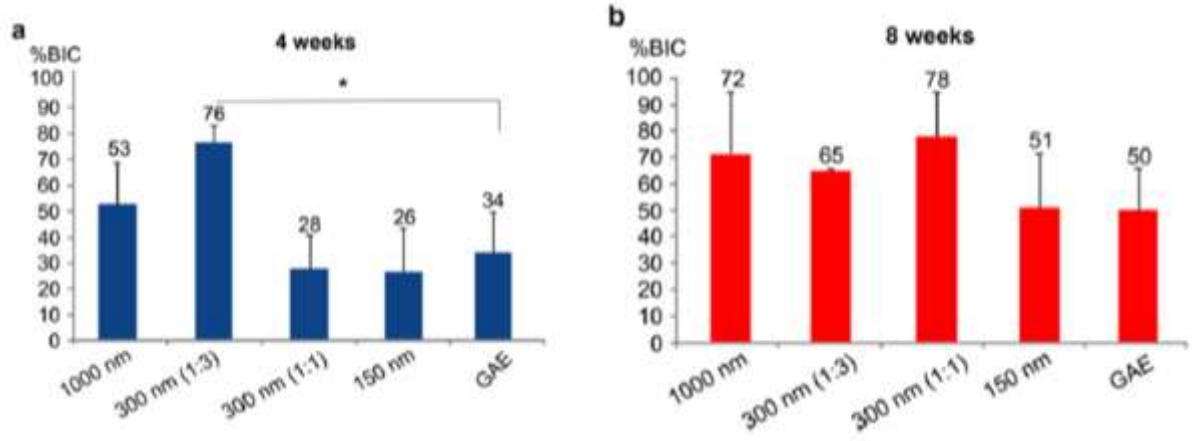

Figure 6.2 *In vivo* data suggesting that nanotopgraphy does not enhance long term increases in bone in contact (BIC) with the implant. Nanotopography on titanium disk implants in a rabbit model did not show improved results compared to a smooth control (SAE)[8].

Collectively, these findings on nanoPMMA and nanoPEGDA suggest that topography is not a strong driver of MSC osteogenesis, at least in the confines of the parameters we investigated (Figure 6.1). 3-D nanofibrous poly (L-lactic acid) scaffolds were shown to enhance protein adsorption and various osteogenic markers compared to flat controls in embryonic stem cells, suggesting that other shapes, sizes, and topographic arrangements may enhance osteogenesis[10]. Though, as highlighted in Chapter 2, factors like cell type, surface chemistry, fiber arrangement, and the 3D environment could be important factors in these findings. Thus, comparing our findings and conclusions of MSC behavior on PMMA and nanoPEGDA may not be translated nor easily compared to other material systems. Hence, because of the number of variables involved in these systems, quantitatively mapping similar 4-D spaces may provide vital information for parameters that improve osteogenesis over flat controls. The 3-D scaffolds may present solutions for bone tissue engineering. The quasi-3D topographic features we assessed have greater application for current orthopedic implants. Though our findings, coupled with the *in vivo* report by Prodanov et al.[8], suggests that nanotopography on implants may not be worth the manufacturing effort and economic cost.

Looking globally, our findings may hint at the role of topography in embryo and tissue development. Early tissue development and formation involves a wide number of cues and is a combination of ECM organization and cell proliferation and differentiation. Yet, in order for the ECM to become organized cells in the tissue

space must first deposit ECM proteins and then modify and organize those proteins to perform the appropriate functions. Therefore, it is possible that intrinsic topography and ECM alignment seen in bone and cardiac tissue result primarily to perform the appropriate function of the local environment and tissue space rather than to promote cell differentiation; differentiation may be a secondary role for topography.

6.3 Limitations

As mentioned previously, there are processing complications when making films with nanofeatures. This highlights the difficulty in making these surfaces for cell culture investigations and the need to explore some additional considerations.

In producing nanoPEGDA it was difficult to verify the presence of nanofeatures (especially in comparison to nanoPMMA which can be done optically depending on the feature size). The presence of nanofeatures is critical to being able to assess differences in cell behavior compared to smooth surfaces. Our AFM scans showed the presence of topography, yet at low weight percent (<10 % gels of the 3400 g/mol PEGDA) nanofeatures were not detected. As the percentage of PEGDA decreases the material available to polymerize in the nanochannels of the PUA mold becomes limited, likely limiting the robustness of surface features. Other reports using nanoPEGDA have used ≥10 % PEGDA precursor solutions[11,12] suggesting that nanotopographic features may be absent at lower concentrations. Thus, it is important

to develop a method to easily detect the presence of nanofeatures even if it is only semi-quantitative to ensure that batch to batch processing of nanoPEGDA (of all wt. %) is consistently imparted with nanofeatures.

One limitation in this study has to do with protein presentation and cell adhesion modulation. As previously discussed in Chapter 2, cell adhesion is critical to cell behavior. To understand why, we have to understand seemingly unrelated reports. One report suggests that collagenous matrices have elasticity of ~100 kPa[9]. Elasticity in this range is potentially only the case in early tissue development as analysis of noncalcified collagen matrices and calcified cartilage and bone (from human patella) have shown that the modulus of these tissues ranged many orders of magnitude higher (~1-20 GPa)[13]. This suggests that in adult tissue the influence of modulus may be less important than previously suggested and the gels of tunable mechanical properties tested here and elsewhere[9,14,15] are not of a physiological relevant regime of adult bone tissue. Furthermore, the work by Trappmann et al. suggests that matrix mechanics matters when the ligand is tethered in such a way that a cell can generate forces to pull on it[15]. This finding is further validated by reports that the ability to generate force at adhesion sites (and develop mature focal adhesions) depends on the availability and size of adhesion regions[16,17]. Collectively, these findings suggest that matrix mechanical or topographical modulation of cell behavior and osteogenesis (compared to control surfaces) depends on promoting adhesions that allow for higher force generation. Currently, predicting what conditions (the size and shape of

topography and how ECM proteins are adsorbed or tethered to a surface) drive protein changes that modulate adhesion forces and cell behavior is limited[18].

Another limitation is related to manufacturing nanosurfaces either for orthopedic implants or that are large enough to develop patterned tissue. The current techniques are not easily scalable much beyond ten to a hundred square centimeters. Recent implants in rabbits used nanotitanium surfaces on flat disks[8] a few square centimeters in size; this reinforces the limitations of scalable nanosurfaces. Creating similar topography on surfaces with curvature, as is the case with orthopedic implants, is, as of yet, not possible on the scale and shapes necessary to be tested clinically. Thus, advances in manufacturing technologies and techniques are needed before conclusions can be made regarding nanotopography and increased implant life time.

6.4 Future Directions

The results from the aims fulfilled for this study provide a better understanding of the role that topography and coupling matrix topography and elasticity have in driving osteogenesis in MSCs (or lack thereof). This study has implications for a few areas that could be further explored.

We have shown that uncontrolled protein adsorption from FBS on nanoPMMA does not promote enhanced osteogenesis in MSCs. Other reports have utilized single ECM proteins on nano-[19-21] and microsurfaces[22] and often report an enhanced osteogenic response. These studies often fail to perform assessments of

mineral quantity and composition. Thus, stamping proteins onto nanoPMMA would allow for a more thorough understanding of the role of topography and single ECM proteins on osteogenic phenotype in MSCs. Specifically it would test the hypothesis that initial adhesion drives cell commitment and differentiation. Additionally, this technique would allow for better assessment of the amount and composition of deposited mineral. This process is illustrated in Figure 6.3. The flexible PUA molds developed in Aim 3 could be used to transfer FBS or ECM proteins onto nanoPMMA. Varying the amount and identity of the stamped ECM protein would allow for a systematic assessment of this method. Stamping the proteins in a direction perpendicular to the grating direction would assess the influence of ligand cues vs. topographic cues, similar to a report using microtopography[22].

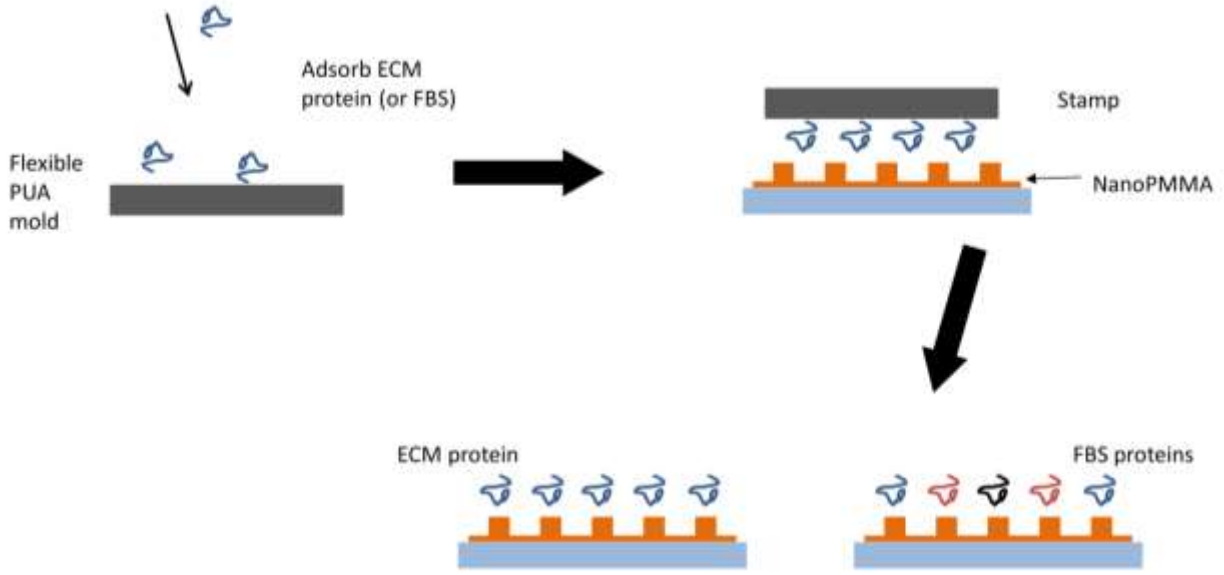

Figure 6.3 Proposed method for stamping ECM proteins on nanoPMMA (or other material) surfaces. The method would help investigate the importance of initial adhesion on cell differentiation.

An additional aspect that could also be investigated on both nanoPMMA and nanoPEGDA systems is the influence of mixed surfaces of nanotopography and smooth regions. The motivation for this is that a recent report suggested that cells have different preferences for topography over time[23]. Specifically, cell division events were observed occurring centered over nanowire islands. Cell contact with smooth surface during division was minimized. It is unclear if this is specific to cell type, feature size and shape, or surface chemistry. However, if this is found to be robust for a number of cell types and surface features, surfaces could be manufactured to investigate if cells prefer smooth regions over topographic regions. Multiple cell types could be investigated on the same surface. Potentially, certain topographic/smooth/ cell combinations could promote stem cell differentiation or stemness. There is some precedent for this, at least in regard to co-culture, as co-culture of ECs and MSCs on topographic surfaces showed enhanced osteogenesis compared to smooth controls[24].

We showed that collagen tethered to nanoPEGDA gels did not enhance osteogenesis compared to smooth controls. There are two additional aspects that could be investigated regarding this finding. The first involves changing the ligand identity. Ligand identity is influential on cell differentiation[25-28] and though collagen I is typically considered to be the best choice to promote osteogenesis it is possible that the partially denatured collagen used in our studies promoted a more stem-like state. This may be the case as a report suggested that partially denatured collagen maintained MSC stemness while promoted osteogenic differentiation in pre-

osteoblasts[29]. Thus, changing the conjugated ligand may promote osteogenic differentiation. The other aspect to investigate is whether or not FAK and other molecules implicated in the MAPK cascade are unregulated on nanoPEGDA surfaces of tunable elasticity. Our data suggests that these signaling molecules are not enhanced, though this needs to be investigated to determine if this is true. Reports have shown that modulating elasticity drives changes in the MAPK cascade and osteogenic differentiation[9,14,30,31]. If coupling nanotopography and elasticity were to cause downregulation of these pathways it would turn alter our understanding of these cues and these pathways.

Matrix mechanical cues *in vitro* have been shown to drive osteogenesis as previously discussed. In addition, cells *in vivo* are known to respond to dynamic loading conditions; cells manufacture new mineral and matrix and resorb damaged matrix as the need arises[1,5,30]. Thus, adding a dynamic load to cells on nanotopography may help us better understand the interplay between these factors. Our lab has previously studied angiogenesis under dynamic stretch[32] therefore the equipment is available to impart dynamic mechanical stresses on MSCs under osteogenic conditions. The PUA molds that were made for Aim 3 could be modified for use as a cell culture platform[24,33]. Because PUA is similar to PDMS in that is highly elastic[34], it could also be used for stretching purposes. The elasticity of PUA substrates is also modifiable (though PUA would not be as soft nor have the range of elastic properties

as PEGDA does). This set-up would be a better approximation of *in vivo* conditions than the *in vitro* conditions currently used.

Finally, one finding that seemed to be consistent regardless of surface chemistry or ligand concentration was that G415 surfaces consistently promoted 'elevated' Ca:P ratios. As mentioned previously, collagen fibril spacing is a key to normal mineral formation[35-37]. Abnormal fibril spacing is known to play a role in osteogenesis imperfecta[7] thus it is critical to investigate the collagen structure of the mineral produced on the nanotopographic surfaces, especially on G415 surfaces, to determine if these surfaces promote a normal healthy physiologic collagen matrix . The methods necessary to investigate mineral collagen gap size would likely require additional techniques. Specifically, cryoTEM (transmission electron microscopy) and low dose selected area electron diffraction (LDSAED) would be helpful to investigate collagen fibril spacing and mineralization.

We have shown that nanotopography *in vitro* alone and coupled with substrate elasticity were not strong drivers of osteogenesis in MSCs. This groundwork opens up additional avenues to explore which will aid our understanding of the roles that ECM properties of topography, elasticity, and ligand identity have in osteogenic differentiation. Hopefully this knowledge will lead to new techniques and therapies which can be implemented in the clinic to improve people's lives.

6.5 References

1 Weiner, S. & Wagner, H. D. The material bone: Structure mechanical function relations. *Annual Review of Materials Science* **28**, 271-298, doi:DOI 10.1146/annurev.matsci.28.1.271 (1998).

2 Tas, N. R., Haneveld, J., Jansen, H. V., Elwenspoek, M. & van den Berg, A. Capillary filling speed of water in nanochannels. *Appl Phys Lett* **85**, 3274-3276, doi:Doi 10.1063/1.1804602 (2004).

3 Nosonovsky, M. & Bhushan, B. Multiscale Dissipative Mechanisms and Hierarchical Surfaces: Friction, Superhydrophobicity, and Biomimetics. *Nanosci Technol*, 1-277 (2008).

4 Owens, D. K. & Wendt, R. C. Estimation of Surface Free Energy of Polymers. *J Appl Polym Sci* **13**, 1741-&, doi:DOI 10.1002/app.1969.070130815 (1969).

5 Allori, A. C., Sailon, A. M. & Warren, S. M. Biological basis of bone formation, remodeling, and repair - Part II: Extracellular matrix. *Tissue Eng Part B-Re* **14**, 275-283, doi:DOI 10.1089/ten.teb.2008.0083 (2008).

6 Farley, J. R. & Baylink, D. J. Skeletal Alkaline-Phosphatase Activity as a Bone-Formation Index Invitro. *Metabolism* **35**, 563-571, doi:Doi 10.1016/0026-0495(86)90016-8 (1986).

7 Cassella, J. P. & Ali, S. Y. Abnormal Collagen and Mineral Formation in Osteogenesis Imperfecta. *Bone Miner* **17**, 123-128, doi:Doi 10.1016/0169-6009(92)90722-P (1992).

8 Prodanov, L. *et al.* The effect of nanometric surface texture on bone contact to titanium implants in rabbit tibia. *Biomaterials* **34**, 2920-2927, doi:DOI 10.1016/j.biomaterials.2013.01.027 (2013).

9 Engler, A. J., Sen, S., Sweeney, H. L. & Discher, D. E. Matrix elasticity directs stem cell lineage specification. *Cell* **126**, 677-689, doi:DOI 10.1016/j.cell.2006.06.044 (2006).

10 Smith, L. A., Liu, X. H., Hu, J. A. & Ma, P. X. The Enhancement of human embryonic stem cell osteogenic differentiation with nano-fibrous scaffolding. *Biomaterials* **31**, 5526-5535, doi:DOI 10.1016/j.biomaterials.2010.03.065 (2010).

11 Yanez-Soto, B., Liliensiek, S. J., Murphy, C. J. & Nealey, P. F. Biochemically and topographically engineered poly(ethylene glycol) diacrylate hydrogels with biomimetic characteristics as substrates for human corneal epithelial cells. *J Biomed Mater Res A* **101A**, 1184-1194, doi:Doi 10.1002/Jbm.A.34412 (2013).

12 Kim, D. H. *et al.* Nanoscale cues regulate the structure and function of macroscopic cardiac tissue constructs. *P Natl Acad Sci USA* **107**, 565-570, doi:DOI 10.1073/pnas.0906504107 (2010).

13 Gupta, H. S. *et al.* Two different correlations between nanoindentation modulus and mineral content in the bone-cartilage interface. *J Struct Biol* **149**, 138-148, doi:DOI 10.1016/j.jsb.2004.10.010 (2005).

14 Khatiwala, C. B., Kim, P. D., Peyton, S. R. & Putnam, A. J. ECM Compliance Regulates Osteogenesis by Influencing MAPK Signaling Downstream of RhoA and ROCK. *J Bone Miner Res* **24**, 886-898, doi:Doi 10.1359/Jbmr.081240 (2009).

15 Trappmann, B. *et al.* Extracellular-matrix tethering regulates stem-cell fate. *Nat Mater* **11**, 642-649, doi:Doi 10.1038/Nmat3339 (2012).

16 Gonzalez-Garcia, C., Sousa, S. R., Moratal, D., Rico, P. & Salmeron-Sanchez, M. Effect of nanoscale topography on fibronectin adsorption, focal adhesion size and matrix organisation. *Colloid Surface B* **77**, 181-190, doi:DOI 10.1016/j.colsurfb.2010.01.021 (2010).

17 Coyer, S. R. *et al.* Nanopatterning reveals an ECM area threshold for focal adhesion assembly and force transmission that is regulated by integrin activation and cytoskeleton tension. *J Cell Sci* **125**, 5110-5123, doi:Doi 10.1242/Jcs.108035 (2012).

18 Lord, M. S., Foss, M. & Besenbacher, F. Influence of nanoscale surface topography on protein adsorption and cellular response. *Nano Today* **5**, 66-78, doi:DOI 10.1016/j.nantod.2010.01.001 (2010).

19 Lim, J. Y. *et al.* The regulation of integrin-mediated osteoblast focal adhesion and focal adhesion kinase expression by nanoscale topography. *Biomaterials* **28**, 1787-1797, doi:DOI 10.1016/j.biomaterials.2006.12.020 (2007).

20 Yim, E. K. F., Darling, E. M., Kulangara, K., Guilak, F. & Leong, K. W. Nanotopography-induced changes in focal adhesions, cytoskeletal organization,

and mechanical properties of human mesenchymal stem cells. *Biomaterials* **31**, 1299-1306, doi:DOI 10.1016/j.biomaterials.2009.10.037 (2010).

21 Biggs, M. J. P. *et al.* The use of nanoscale topography to modulate the dynamics of adhesion formation in primary osteoblasts and ERK/MAPK signalling in STRO-1+enriched skeletal stem cells. *Biomaterials* **30**, 5094-5103, doi:DOI 10.1016/j.biomaterials.2009.05.049 (2009).

22 Charest, J. L., Eliason, M. T., Garcia, A. J. & King, W. P. Combined microscale mechanical topography and chemical patterns on polymer cell culture substrates. *Biomaterials* **27**, 2487-2494, doi:DOI 10.1016/j.biomaterials.2005.11.022 (2006).

23 Albuschies, J. & Vogel, V. The role of filopodia in the recognition of nanotopographies. *Sci Rep-Uk* **3**, doi:Artn 1658 Doi 10.1038/Srep01658 (2013).

24 Kim, J. *et al.* Synergistic effects of nanotopography and co-culture with endothelial cells on osteogenesis of mesenchymal stem cells. *Biomaterials* **34**, 7257-7268, doi:DOI 10.1016/j.biomaterials.2013.06.029 (2013).

25 Salasznyk, R. M., Klees, R. F., Boskey, A. & Plopper, G. E. Activation of FAK is necessary for the osteogenic differentiation of human mesenchymal stem cells on laminin-5. *J Cell Biochem* **100**, 499-514, doi:Doi 10.1002/Jcb.21074 (2007).

26 Klees, R. F., Salasznyk, R. M., Vandenberg, S., Bennett, K. & Plopper, G. E. Laminin-5 activates extracellular matrix production and osteogenic gene focusing in human mesenchymal stem cells. *Matrix Biol* **26**, 106-114, doi:DOI 10.1016/j.matbio.2006.10.001 (2007).

27 Kundu, A. K. & Putnam, A. J. Vitronectin and collagen I differentially regulate osteogenesis in mesenchymal stem cells. *Biochem Bioph Res Co* **347**, 347-357, doi:DOI 10.1016/j.bbrc.2006.06.110 (2006).

28 Kundu, A. K., Khatiwala, C. B. & Putnam, A. J. Extracellular Matrix Remodeling, Integrin Expression, and Downstream Signaling Pathways Influence the Osteogenic Differentiation of Mesenchymal Stem Cells on Poly(Lactide-Co-Glycolide) Substrates. *Tissue Eng Pt A* **15**, 273-283, doi:DOI 10.1089/ten.tea.2008.0055 (2009).

29 Taubenberger, A. V., Woodruff, M. A., Bai, H. F., Muller, D. J. & Hutmacher, D. W. The effect of unlocking RGD-motifs in collagen I on pre-osteoblast adhesion and differentiation. *Biomaterials* **31**, 2827-2835, doi:DOI 10.1016/j.biomaterials.2009.12.051 (2010).

30 Khatiwala, C. B., Peyton, S. R. & Putnam, A. J. Intrinsic mechanical properties of the extracellular matrix affect the behavior of pre-osteoblastic MC3T3-E1 cells. *Am J Physiol-Cell Ph* **290**, C1640-C1650, doi:DOI 10.1152/ajpcell.00455.2005 (2006).

31 Khatiwala, C. B., Peyton, S. R., Metzke, M. & Putnam, A. J. The regulation of osteogenesis by ECM rigidity in MC3T3-E1 cells requires MAPK activation. *J Cell Physiol* **211**, 661-672, doi:Doi 10.1002/Jcp.20974 (2007).

32 Ceccarelli, J., Cheng, A. & Putnam, A. J. Mechanical Strain Controls Endothelial Patterning During Angiogenic Sprouting. *Cell Mol Bioeng* **5**, 463-473, doi:DOI 10.1007/s12195-012-0242-y (2012).

33 You, M. H. *et al.* Synergistically Enhanced Osteogenic Differentiation of Human Mesenchymal Stem Cells by Culture on Nanostructured Surfaces with Induction Media. *Biomacromolecules* **11**, 1856-1862, doi:Doi 10.1021/Bm100374n (2010).

34 Choi, S. J., Yoo, P. J., Baek, S. J., Kim, T. W. & Lee, H. H. An ultraviolet-curable mold for sub-100-nm lithography. *J Am Chem Soc* **126**, 7744-7745, doi:Doi 10.1021/Ja048972k (2004).

35 Silver, F. H. & Landis, W. J. Deposition of apatite in mineralizing vertebrate extracellular matrices: A model of possible nucleation sites on type I collagen. *Connect Tissue Res* **52**, 242-254, doi:Doi 10.3109/03008207.2010.551567 (2011).

36 Landis, W. J., Song, M. J., Leith, A., Mcewen, L. & Mcewen, B. F. Mineral and Organic Matrix Interaction in Normally Calcifying Tendon Visualized in 3 Dimensions by High-Voltage Electron-Microscopic Tomography and Graphic Image-Reconstruction. *J Struct Biol* **110**, 39-54, doi:DOI 10.1006/jsbi.1993.1003 (1993).

37 Nudelman, F. *et al.* The role of collagen in bone apatite formation in the presence of hydroxyapatite nucleation inhibitors. *Nat Mater* **9**, 1004-1009, doi:Doi 10.1038/Nmat2875 (2010).

Appendix 1: A Safe and Efficient Method to Retrieve Mesenchymal Stem Cells from Three-Dimensional Fibrin Gels

Bita Carrion Ph.D.*, Isaac A. Janson*, Yen Peng Kong Ph.D., and Andrew J. Putnam Ph.D. (*co-first author) Tissue Engineering C 2014

A1.1 Introduction

Bone marrow stromal cells, commonly referred to as mesenchymal stem cells (MSCs), are non-hematopoietic cells found in the adult bone marrow that possess multipotent characteristics. MSCs have the ability to differentiate into multiple lineages, including osteogenic, adipogenic, and chondrogenic phenotypes. Due to their high degree of plasticity and relative ease of isolation from many tissues[1-5], MSCs have been explored in numerous clinical trials for tissue engineering and regenerative medicine applications. Despite the apparent therapeutic potential of MSCs, most likely through trophic factor secretion[6] current understanding of the intrinsic and extrinsic components of the microenvironment that regulate their activity *in vivo* remains incomplete. Fundamental knowledge regarding these components is

desirable, not only to better understand MSC biology, but also to improve the translational potential of these cells.

The current dogma is that developing physiologically relevant artificial models capable of instructing stem cells will require a more accurate recapitulation of their native niche[7,8]. In an attempt to reconstruct the stem cell microenvironment that more closely mimics *in vivo* conditions, many investigators are exploring the use of three-dimensional (3D) culture systems. Recent studies suggest that MSCs maintained in two-dimensional (2D) culture systems gradually lose their proliferative potential, colony forming efficiency, and differentiation capacity with time[9-11]. While the evidence that 3D culture methods provide a cellular environment more consistent with that *in vivo* is persuasive[12-17], there is still a need for optimized culture models for large-scale, long term expansion of stem cells with uniform properties that are capable of differentiating into selected mature cell types with high efficiency and purity[18]. Furthermore, the development of efficient methods to safely extract these cells from 3D tissue culture is important, both to meet the high cell volumes required for therapeutic applications and to characterize how cells grown in 3D models are regulated by various components of an artificial niche.

We focused on MSC encapsulation within fibrin, in part because fibrin is a widely-used material[19], that has been shown to promote cell survival and proliferation both *in vitro* and *in vivo*[20-23]. There is compelling evidence that fibrin supports delivery of stem cells, such as bone marrow mononuclear cells (BMMNC)[24,25], human MSCs[20,26,27], and stimulates MSC differentiation toward osteogenic and chondrogenic differentiation[27-29]. We have used fibrin extensively as an ECM analog capable of

supporting capillary morphogenesis *in vitro*[30-33], and neovascularization *in vivo*[31,34]. We have also shown that co-cultures of MSCs and endothelial cells in 3D fibrin hydrogels readily form pericyte-invested capillary networks[32,35,36], which has prompted our efforts to better understand how the perivascular location of MSCs may influence their phenotype[35]. However, our efforts were limited in part by the lack of a simple yet effective method to safely recover and characterize MSCs residing within the fibrin hydrogels.

Recovery of cells from collagen hydrogels and collagen-based tissues can be readily achieved using collagenase, but no comparably simple method to retrieve viable cells from 3D fibrin culture models exists, to the best of our knowledge. In most cases, commonly used proteolytic enzymes, including trypsin and collagenase, have been used for primary cell isolation from a variety of tissue types[37-40]. However, when used to dissolve fibrin for *in vitro* models, these enzymes do not yield a single cell suspension effectively. Furthermore, longer incubation times with these enzymes required for dissolving the gels may damage the cells harvested for subcultivation or other studies. Previous studies have used 3D fibrin gels as biomimetic substrates for isolation of stem cells residing in various tissues[41,42]. Using urokinase, cells outgrown from these tissues were isolated by selective degradation of the 3D fibrin gels. In this paper, we used nattokinase, a Bacillus-derived serine protease that is known for its potent fibrinolytic activity[43-45], to recover encapsulated MSCs from 3D fibrin gels. Compared with other fibrinolytic enzymes like urokinase and plasmin, nattokinase is

reportedly more efficient in degrading fibrin gels[44]. We demonstrated that nattokinase yields significantly higher MSC recovery as compared with other proteolytic enzymes, including trypsin and TrypLE. Additionally, we found that this enzyme-mediated recovery is not harmful, as assessed by cellular proliferation and viability in 3D culture. Finally, using our extraction protocol, we showed that cells recovered from 3D hydrogels were capable of differentiating into osteogenic and adipogenic lineages. This extraction method is an effective system that could potentially be used to safely and efficiently harvest a variety of cell types from 3D fibrin cultures for subsequent use in numerous applications, including expansion, bioassays, and *in vivo* implantation.

A1.2 Materials and Methods

A1.2.1 Cell culture

Human bone marrow-derived MSCs were obtained from a commercial source (Lonza, Walkersville, MD) at passage 2. As part of the manufacturer's quality control, these MSCs were tested for purity by flow cytometry and for their ability to differentiate into osteogenic, chondrogenic and adipogenic lineages. Cells are positive for the cell surface markers CD105, CD166, CD29 (integrin β1), and CD44, and negative for CD14, CD34 and CD45. MSCs were maintained in high glucose (4.5 g/L) Dulbecco's modified Eagle medium (DMEM, Invitrogen, Carlsbad, CA) supplemented with 10% fetal bovine serum (FBS, Invitrogen). All cultures were

incubated at 37°C and 5% CO_2. Media were changed every 2 days. MSCs were routinely expanded in 2D cultures and harvested with 0.05% Trypsin-EDTA (Invitrogen). Cells were used prior to passage 8 for differentiation experiments and prior to passage 11 for viability and cell extraction experiments. For 2D controls to the 3D experiments described below, MSCs were cultured for 1, 7, or 14 days. We identify these times as 'pre-culture', indicating the culture time prior to harvesting and subsequent analysis.

A1.2.2 Construction of the 3D culture model

MSCs were encapsulated within 3D fibrin gels via methods similar to those used previously to create a 3D co-culture model of capillary morphogenesis[32]. In brief, $5x10^4$ MSCs were mixed within a 2.5, 5, or 10 mg/mL fibrinogen solution (Sigma-Aldrich, St. Louis, MO; Lot# 069K7636v, 65-85% protein). Five hundred microliters of this solution containing MSCs was combined with 10 μL of thrombin (50 U/mL; Sigma) in a single well of a 12-well plate to make one gel construct. This process was repeated until the desired number of gels was constructed. Constructs were left undisturbed for 5 minutes to allow partial gelation before incubating for an additional 25 minutes at 37°C and 5% CO_2. Gels were then cultured in DMEM supplemented with 10% FBS. Media were changed every 2 days. Cells were retrieved from 3D fibrin gels on days 1, 7, and 14 post-assembly. We identify the time of culture in 3D fibrin

gels as 'pre-culture', indicating the culture time prior to retrieval and subsequent analysis.

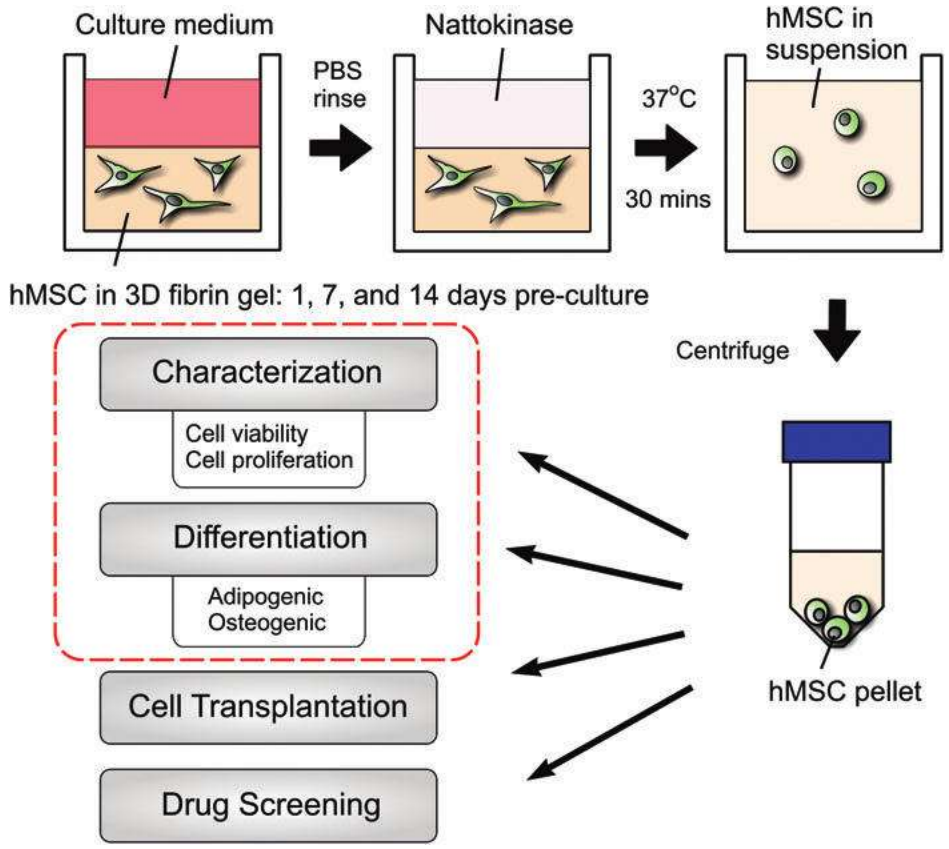

Figure A1.1. **Illustration depicting the method by which MSCs were extracted from 3D fibrin gels.** We developed a simple new method for efficiently retrieving MSCs encapsulated within 3D fibrin hydrogels. Cells were cultured within the fibrin gels for 1, 7, or 14 days prior to retrieval. The key component of the extraction process is a fibrinolytic enzyme, nattokinase. Treatment of the cell-seeded hydrogels with nattokinase for 30 minutes (longer incubations required for more concentrated gels) results in a single cell suspension, which can be collected and concentrated via centrifugation, and then subsequently used in additional assays or for different applications.

A1.2.3 Retrieving viable cells from 3D fibrin gel constructs

MSCs embedded in 3D fibrin gels were recovered using one of three methods: our novel recovery technique (Fig. A1.1) involving the fibrinolytic enzyme nattokinase, or methods involving 0.05% tryspin-EDTA (Gibco, Grand Island, NY) or 100% TrypLE (Invitrogen). In our new method, a fibrinolytic solution was prepared by dissolving 50 FU/mL (fibrin degradation units) of nattokinase (NSK-SD, Japan Bio Science Laboratory Co., Ltd, Osaka, Japan), in phosphate buffered saline (PBS) containing 1 mM EDTA (Fisher Scientific). Gels were washed with PBS before dislodging them from the well siding using a small spatula. Gels were subsequently dissolved by adding 500 μl of the fibrinolytic solution and incubating at 37°C for 30 minutes (for the 2.5 mg/mL fibrin gels) or 60 minutes (for the 5 and 10 mg/mL fibrin gels). These incubation times were determined empirically based on observations of gel dissolution. Upon dissolution, the contents of each well were collected and centrifuged. Cells were then washed with cold PBS before subsequent procedures. The same dissolution conditions, as described above, were implemented in methods involving trypsin-EDTA or TrypLE.

A1.2.4 Quantitative polymerase chain reaction (qPCR)

The multilineage potential of MSCs recovered following fibrinolysis was determined in part via qPCR to assess the expression of genes associated with osteogenic and adipogenic differentiation. In brief, MSCs cultured for up to 14 days were retrieved from either 3D fibrin gels using our novel nattokinase-based recovery

method, or collected from 2D cultures via standard trypsinization. Harvested cells were then subjected to standard adipogenic or osteogenic induction protocols (described below) in 2D culture for 7 and 21 days, respectively[46-50]. Total RNA was isolated from cells using the SV Total RNA Isolation System (Promega, Madison, WI). The RNA concentration and purity of each sample were determined by A260/A280 absorptions using a Nanodrop ND-1000 (Thermo Scientific, Rochester, NY) spectrometer. Equal amounts of total RNA from each sample were used to create first strand cDNA using the ImProm-II Reverse Transcription System (Promega). The PCR amplification was performed with the KAPA SYBR® Fast Universal Master Mix (Kapa Biosystems, Woburn, MA) on a 7500 Fast Real-Time PCR System (Applied Biosystems) in a final volume of 20 μl using cycling parameters (3 min 95°C; 3 sec, 95°C; 20 sec, 60°C with the latter two steps repeated for 40 times). Each reaction was performed in triplicate and the $\Delta\Delta C_T$ method was used for the gene expression analysis[51]. The gene encoding for peptidylprolyl isomerase (PPIA) was used as the housekeeping gene as it has been shown to have the most stable expression levels of a variety of housekeeping gene candidates under different conditions[52]. The primer sequences of the genes for qPCR are provided in Table A1.1.

Table A1.1. Primer sequences designed via Primer-Blast and used for qPCR.

Gene	*Sense primer*	*Antisense primer*
BGLAP	5′-AGGCACCCTTCTTTCCTCTTC-3′	5′-TTCCTCTTCTGGAGTTTATTTGGGA-3′
CEBPA	5′-ATGCAAACTCACCGCTCCAAT-3′	5′-GAGGCAGGAAACCTCCAAATAAA-3′
PPARG	5′-ATTACGAAGACATTCCATTCACAAG-3′	5′-CTCAGAATAATAAGGTGGAGATGC-3′
PPIA	5′-GTCTTGTGTGTTGTCTGGTTA-3′	5′-ATGTTTGATGTTTATTTCCACCTTG-3′
RUNX2	5′-CAGAAGGGAGGAGATGTGTGTA-3′	5′-TTGCTAATGCTTCGTGTTTCCA-3′

A1.2.5 Quantification of cell viability via fluorescent activated cell sorting (FACS)

To assess viability, cells were retrieved from 3D cultures 6 hours after initial cell seeding by incubating the gels in the nattokinase fibrinolytic solution described above. For these assays, the 3D fibrin gels were incubated in the fibrinolytic solution for 90 minutes. Cells were then resuspended in ice cold PBS, pelleted by centrifugation at 2000 rpm at 4°C for 5 minutes, and then incubated with a 3 μM solution of propidium iodide (PI, Invitrogen) in PBS pH 7.2, for 15 minutes at room temperature. Samples were then washed twice and resuspended in 2% FBS in PBS for flow cytometry analysis. Unstained cell suspensions were prepared in parallel as control samples.

A1.2.6 Multilineage differentiation protocols

After pre-culture on 2D substrates or in 3D fibrin gels, MSCs were tested for their differentiation capacity. For adipogenic differentiation, MSCs retrieved from 2D cultures or extracted from a 3D fibrin gel were reseeded at 20,000 cells/cm^2 in a 24-well plate for functional assays, or in a 6-well plate for gene expression assays via

qPCR. Cells were maintained in either adipogenic growth media (AGM, a control), consisting of αMEM (Gibco), 10% FBS, 1% penticillin/streptomycin (CellGro, Manassas, VA), and 5 mg/mL gentamicin (Gibco), or adipogenic induction media (AIM), consisting of AGM, 1 μM dexamethasone (Sigma-Aldrich, St. Louis, MO), 0.5 mM 3-isobutyl-1-methylxanthine (IBMX) (Acros Organics, Geel, Belgium), 10 μg/mL insulin (Gibco), 0.2 mM indomethacin (Sigma-Aldrich)[48,53].

For osteogenic differentiation, MSCs pre-cultured on 2D substrates or in 3D fibrin gels for up to 14 days were retrieved and subsequently reseeded at 5,000 cells/cm^2 in a 24-well plate for functional assays, or in a 6-well plate for qPCR. Cells were maintained in osteogenic growth media (OGM), consisting of αMEM (Gibco), 20% FBS, 2 mM L-glutamine (CellGro), 1% penticillin/streptomycin, and 5mg/mL gentamicin, or osteogenic base media (OBM), consisting of OGM, 10 mM β-glycerol phosphate (Sigma-Aldrich), and 50 μg/mL L-ascorbic acid (Fisher Scientific). After 14 days in OBM, cells were cultured in osteogenic mineralization media (OMM, containing OBM + 100 nM dexamethasone (Sigma-Aldrich)) as previously reported[48,53]. For simplicity OBM and OMM will be referred to as osteogenic induction media (OIM).

A1.2.7 Oil Red O staining, imaging, and quantification

Adipogenic differentiation was assessed in part by staining cultures with Oil Red O and quantifying as previously described[48,54]. Briefly, a 12.2 mM stock solution

of Oil Red O dye (Sigma) was dissolved in isopropanol. Cells were fixed in 4% paraformaldehyde at 4°C for 30 minutes after 7 and 14 days of culture in AIM. Cells were then rinsed in PBS at least twice. Stock Oil Red O solution was added to PBS at a ratio of 3:2 to create the working solution. The working solution was filtered with a 0.22 micron filter (Millipore, Billerica, MA) prior to use. Each well was immersed in the Oil Red O working solution for 20 minutes. After staining, each well was quickly rinsed 3X in a 60/40 isopropanol/PBS solution to remove excess Oil Red O. The wells were then rinsed 2X in PBS and imaged on an Olympus microscope IX51 equipped with a DP25 color camera. After imaging, 4% IGEPAL-CA630 (Sigma) in isopropanol was added to each well and protected from light for 15 minutes. Each well was then analyzed with a Thermo Scientific Multiskan Spectrum spectrophotometer at 520 nm to determine the absorbance of each well. The absorbance of Oil Red O was normalized to the total cell number in each well as determined by nuclei counting using DAPI staining[55]. Three images per condition were analyzed to determine the number of cells per well. Four wells per condition were used to quantify the levels of Oil Red O.

A1.2.8 Von Kossa staining

Cells were rinsed in PBS 2X and then fixed in 4% paraformaldehyde at 4°C for 30 minutes after 14 and 21 days in OIM. After fixation, cells were rinsed in double distilled (DD) water 3X and then immersed in 5% $AgNO_3$ (Sigma) and subjected to

UV light (~365 nm) for 40 minutes. After UV exposure cells were rinsed 3X in DD water. The cells were then rinsed in sodium thiosulfate (Sigma) for 3 minutes and rinsed in DD water 3X. Images were taken on an Olympus IX51 with a DP25 color camera.

A1.2.9 Calcium quantification

Calcium content in osteogenic cultures was quantified using the ortho-cresolphthalein complexone (OCPC) method, as previously described[49,50]. Cells were washed in PBS twice before incubation in 1 mL of 1 N acetic acid overnight. The OCPC solution was prepared by adding OCPC to DD water with 1 N KOH and 1 N acetic acid. The dissolved solutions (10 μL per replicate) were then mixed with a working solution (300 μL per replicate) of OCPC solution and ethanolamine/boric acid/8-hydroxyquinoline buffer (all from Sigma, except KOH (Acros)). Absorbance values were recorded using a Thermo Scientific Multiskan Spectrum spectrophotometer at 570 nm. Calcium values were quantified via a standard curve from 0 to 150 μg/mL. Samples and standards were assayed in triplicate.

A.1.2.10 Statistical Analysis

Statistical analyses were carried out using GraphPad Prism software. Data are reported as means ± standard deviations. All statistical comparisons were made by performing a one-way analysis of variance (ANOVA), followed by Tukey's multiple

comparison tests to judge significance between two data sets at a time. *P* values less than 0.05 were considered statistically significant. Statistics for qPCR were performed on $\Delta\Delta C_T$ values.

A1.3 Results

A1.3.1 Nattokinase efficiently degrades 3D fibrin gels without damaging cells.

We developed and applied a new method (Fig. A1.1) to recover cells encapsulated within 3D fibrin hydrogels based on nattokinase, a powerful fibrinolytic enzyme that is mostly known for its blood thinning effects. To validate the method, we first quantified the percentage of cells extracted from 3D fibrin gels (Fig. A1.2A). Six hours after initial cell encapsulation, fibrin gels were degraded using trypsin, TrypLE, or our nattokinase solution. A 30-minute incubation in the nattokinase solution enabled nearly 100% recovery of the cells entrapped in 2.5 mg/mL fibrin gels. By comparison, a significantly lower percentage of the encapsulated MSCs were retrieved from the gels using either trypsin or TrypLE. A 60-minute incubation with nattokinase was optimal for the more concentrated 5 and 10 mg/mL fibrin gels, resulting in an efficient cell retrieval comparable to that attained with nattokinase in lower concentration gels and significantly better than that attained with 60-minute incubations with TrypLE (Fig. A1.2A). Furthermore, quantification of propidium iodide staining via flow cytometry revealed similar levels of viability when comparing

cells recovered from 2.5 mg/mL 3D fibrin gels (cultured for 14 days) digested using nattokinase to those recovered from 2D cultures (Fig. A1.2B). The viability of the cells was maintained even when the cell-seeded gels were incubated in the nattokinase solution for 90 minutes (Fig. A1.2B), but anecdotally we observed no changes in viability after incubation times up to 2 hours (data not shown). In addition, we also cultured the MSCs within 2.5 mg/mL 3D fibrin gels for up to 14 days, and quantified the number of cells retrieved via nattokinase to assess their proliferation rates. Data showed that MSCs proliferated at comparable rates in both 2D and 3D (Fig. A1.2C). Looking across time points, these data also suggest that our nattokinase-based method is effective for recovering cells encapsulated within 3D fibrin gels across a range of cell densities.

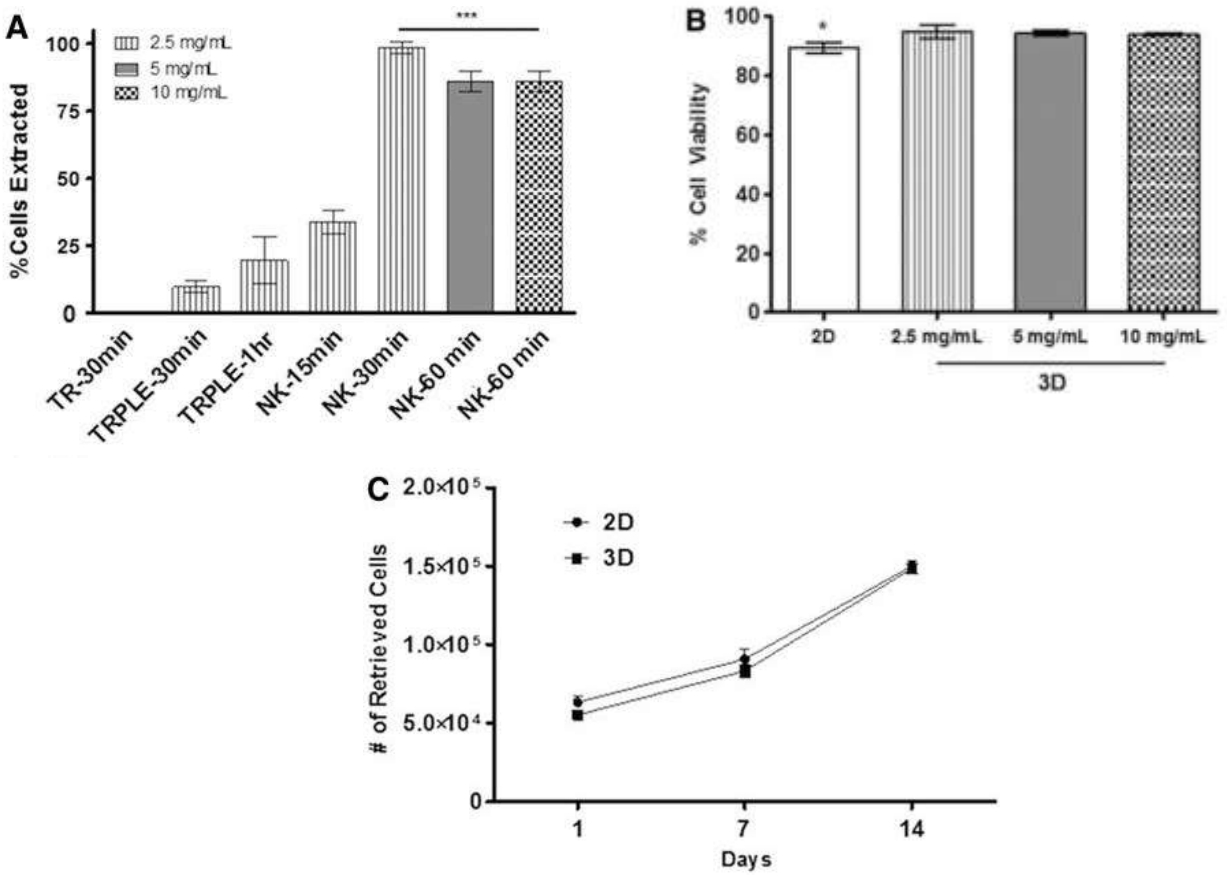

Figure A1.2. Enzyme-assisted extraction of MSCs from 2D and 3D cultures. (A) Nattokinase (NK) yielded a significantly higher percentage of MSCs extracted from 3D fibrin gels relative to the other proteolytic enzymes [trypsin (TR) and TrypLE (TRPLE)]. To quantify the percentage of cells recovered, MSC-seeded fibrin gels were dissolved 6 hours after initial cell seeding (50K cells/gel). For 2.5 mg/mL fibrin gels, cells were efficiently retrieved after a 30-minute incubation in the nattokinase-based fibrinolytic solution; 5 and 10 mg/mL gels were incubated for 60 minutes Retrieved cells were pooled together from a total of 3 gels for each technical sample. *** indicates that all of the groups under the line are significantly different from those groups not under the line ($p \leq 0.001$). (B) After 14 days of pre-culture in 3D fibrin gels, nearly 100% of the MSCs extracted from via nattokinase were viable, as quantified via PI staining and flow cytometry. (C) After 1, 7, or 14 days of pre-culture, MSCs were retrieved from 3D fibrin gels (using nattokinase) or harvested from 2D cultures (using trypsin). The number of cells retrieved from the cultures was comparable at all time points for both culture conditions.

A.1.3.2 MSCs retrieved from 3D fibrin gels maintain their adipogenic potential.

To assess the adipogenic differentiation potential of MSCs pre-cultured for 1, 7, or 14 days in fibrin gels and subsequently retrieved via nattokinase, harvested cells

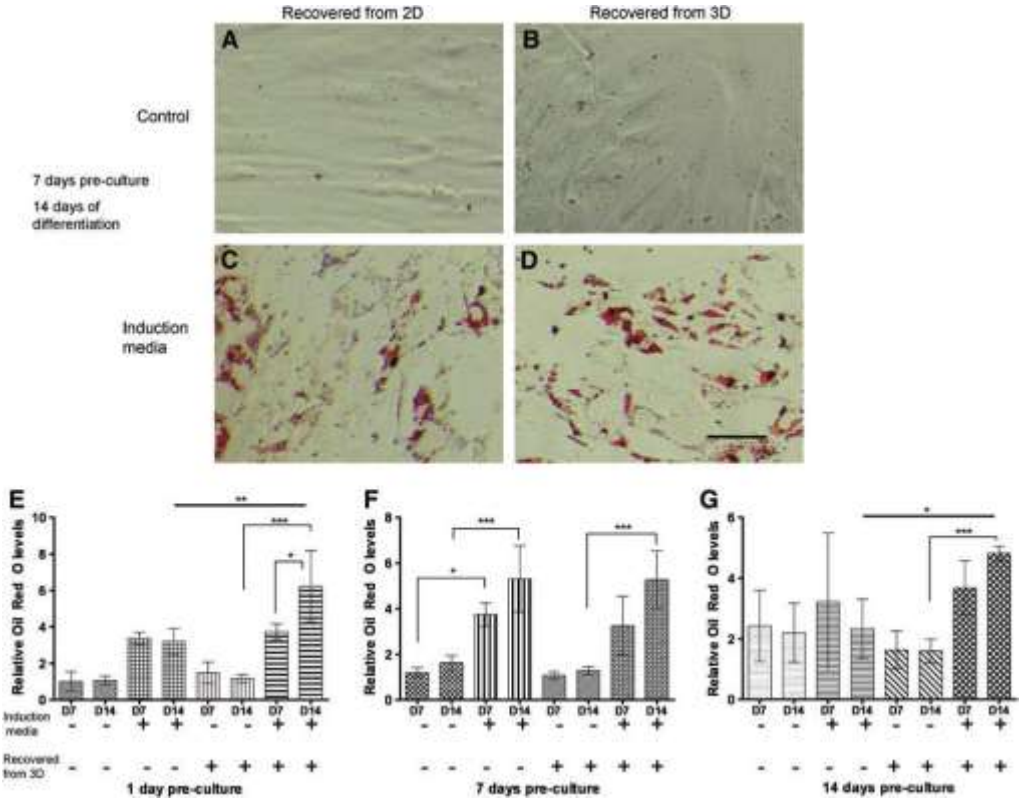

Figure A1.3. MSCs maintain the potential to become adipogenic after extraction from 3D fibrin gels. Micrographs from MSCs grown on 2D TCPS (A, C) or in 3D fibrin gels (B, D) for 7 days of pre-culture and then extracted and maintained in growth media (A, B) or differentiated in adipogenic media (C, D) for 14 additional days in 2D culture. Cells were stained using the Oil Red O method. Scale bar represents 200 μm. (E, F, G) MSCs were grown for periods of 1 (E), 7 (F), or 14 days (G) in either 2D or 3D environments, extracted via trypsin (2D) or nattokinase (3D) and subsequently re-plated in 2D cultures. These cultures were then subjected to either growth media or adipogenic induction media for up to 14 days. Relative Oil Red O levels were generated by dividing the measured values first by the numbers of cells in each well and then normalized to the baseline levels expressed by MSCs cultured in 2D growth media after 1 day of pre-culture (i.e., the first data point on the bar graph in E). These data show that the presence of soluble adipogenic supplements and prolonged culture times in these supplements generally enhance adipogenic differentiation of the MSCs, as expected. They also show that MSCs retrieved from 3D fibrin gels via nattokinase have no apparent deficits in adipogenesis. * refers to $p \leq 0.05$, ** refers to $p \leq 0.01$ *** refers to $p \leq 0.001$ for statistical significance.

were grown in media with various factors known to induce adipogenic differentiation followed by staining for the presence of lipid deposits with Oil Red O. Lipid deposits were detected 7 and 14 days after induction (Fig. A1.3C, D). Quantitative assessment of Oil Red O levels (Fig. A1.3E, F, G) showed that MSCs retrieved from 3D fibrin gels via nattokinase were readily induced to form lipid droplets in the presence of soluble adipogenic supplements, with levels of Oil Red O comparable to those in cells cultured exclusively in 2D. These data suggest that nattokinase extraction of MSCs from fibrin does not diminish their ability to differentiate into adipocytes.

A.1.3.3 MSCs retrieved from 3D fibrin gels maintain their osteogenic potential.

To assess the osteogenic differentiation potential of MSCs pre-cultured for up to 14 days in fibrin gels and subsequently extracted via nattokinase, harvested cells were cultured in OIM, and compared to those grown exclusively on tissue culture polystyrene (TCPS) as a control. Mineral deposition was visualized via the common Von Kossa phosphate staining protocol. MSCs differentiated in OIM after growth on 2D TCPS or recovered from 3D fibrin gels stained positive for phosphates after 14 and 21 days (Fig. A1.4C, D). In parallel, the amounts of calcium deposited by the MSCs were quantified via the OCPC method. Cells cultured in OIM showed elevated calcium levels (compared to non-induced controls), regardless of whether or not they were grown exclusively in 2D or were first extracted from 3D fibrin gels via nattokinase (Fig. A1.4E, F, G). Specifically, cells pre-cultured for 14 days in 3D fibrin

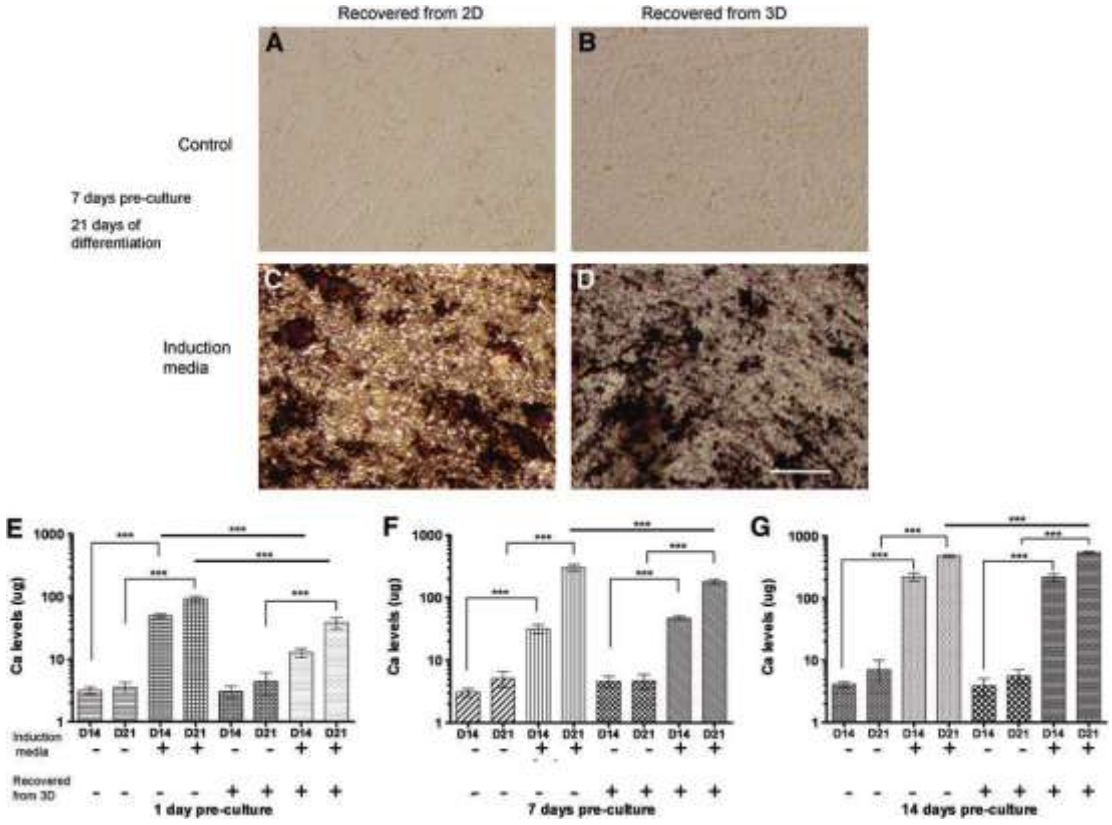

Figure A1.4. MSCs maintain the potential to become osteogenic after extraction from 3D fibrin gels. Micrographs from MSCs grown on 2D TCPS (A, C) or in 3D fibrin gels (B, D) for 7 days of pre-culture and then extracted and maintained in growth media (A, B) or differentiated in osteogenic media (C, D) for 21 additional days in 2D culture. Cells were stained using the von Kossa method. Scale bar represents 200 μm. (E, F, G) MSCs were grown for periods of 1 (E), 7 (F), or 14 days (G) in either 2D or 3D environments, extracted via trypsin (2D) or nattokinase (3D) and subsequently re-plated in 2D cultures. These cultures were then subjected to either growth media or osteogenic induction media for up to 21 days. Total calcium levels were then quantified as an indication of osteogenic differentiation as described in the Materials and Methods. These data show that the presence of soluble osteogenic supplements and prolonged culture times in these supplements generally enhance osteogenic differentiation of the MSCs, as expected. They also show that MSCs retrieved from 3D fibrin gels via nattokinase have no apparent deficits in osteogenesis. *** refers to $p \leq 0.001$ for statistical significance.

gels, recovered with nattokinase, and then differentiated for 14 additional days showed equivalent calcium levels compared to cells grown on a 2D surface [approximately 220 μg]. Collectively, these data qualitatively and quantitatively suggest

that nattokinase extraction of MSCs from fibrin does not reduce their osteogenic differentiation potential.

A.1.3.4 MSCs retrieved from 3D fibrin gels express genes associated with osteogenic and adipogenic lineages.

Finally, we quantified the expression of several genes associated with adipogenic and osteogenic differentiation to further assess how well MSCs pre-cultured for 1, 7, and 14 days and subsequently extracted from 3D fibrin gels via nattokinase sustain their multipotency. Specifically, for Oil Red O, Von Kossa, and calcium assays described above, MSCs were first grown on 2D TCPS or within 3D fibrin gels for up to 14 days, recovered, and subjected to the appropriate induction media favorable for differentiation. Gene expression analysis was performed on cells after 7 and 21 days in adipogenic and osteogenic-specific culture conditions, respectively. Similar levels of *PPARγ* and *CEBPα* were detected in cells cultured in adipogenic media for 7 days (Fig. A1.5A, B), regardless of whether they had first been cultured in 3D fibrin gels and recovered with nattokinase or cultured exclusively on 2D TCPS. However, control cultures grown in baseline medium did not show adipogenic differentiation. Likewise, qPCR analysis confirmed that MSCs retrieved from 3D fibrin gels via nattokinase were also able to upregulate the gene expression levels of *Runx2* and *BGLAP* in response to osteogenic inductive media (Fig. A1.5C, D). These findings collectively suggest that nattokinase extraction of MSCs from 3D

fibrin gels does not negatively impact their ability to express key genes associated with adipogenic and osteogenic differentiation.

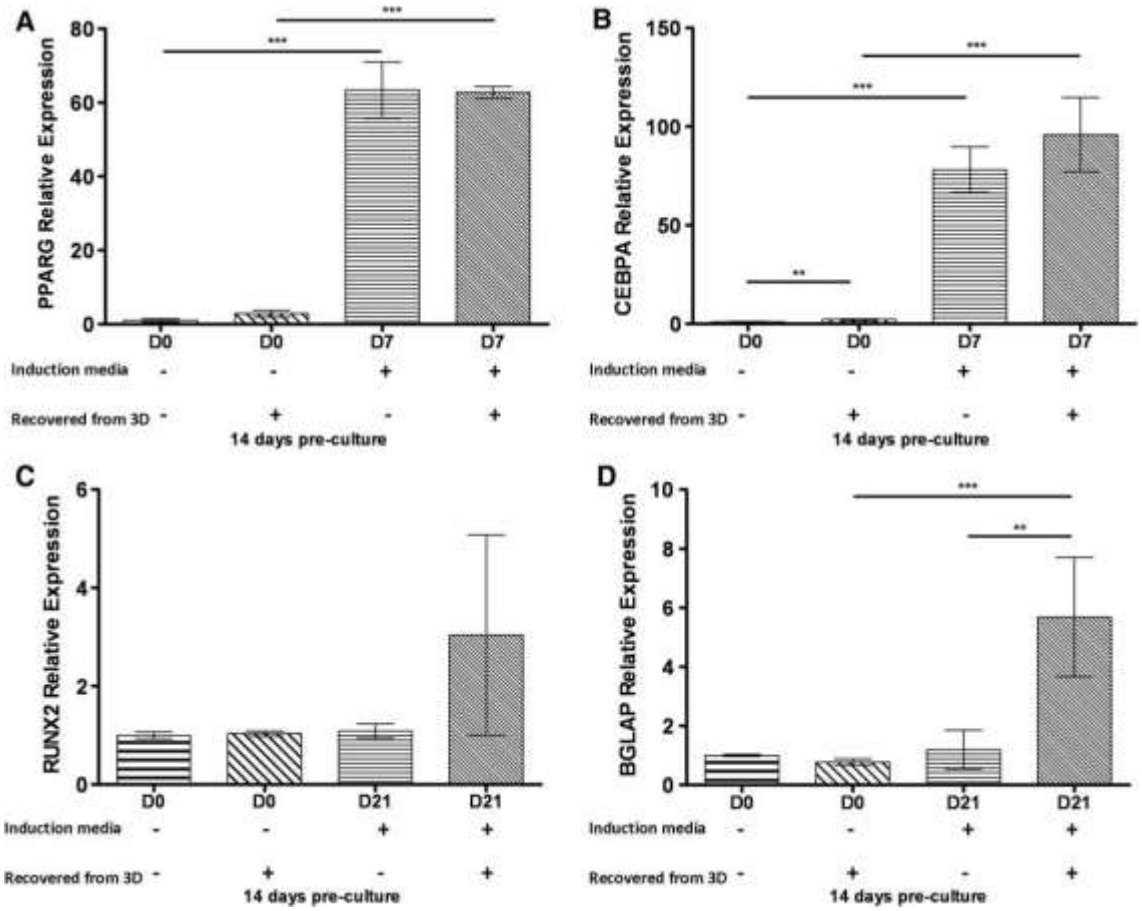

Figure A1.5. qPCR analysis of adipogenic and osteogenic marker gene expression levels in MSCs retrieved from culture conditions. MSCs were recovered from 2D (via trypsin) and 3D cultures (via nattokinase) after 14 days of pre-culture, and then subjected to either adipogenic or osteogenic induction media for either an additional 7 or 21 days, respectively. Total RNA was extracted from the cells and subjected to qPCR analysis to assess expression levels of (A) PPARG, (B) CEBPA, (C) RUNX2, and (D) BGLAP. Statistics were performed on $\Delta\Delta C_T$ values and are indicated as shown (** refers to $p \leq 0.01$, *** refers to $p \leq 0.001$. Collectively, these data showed that MSCs pre-cultured in 3D fibrin gels and subjected to nattokinase extraction were capable of subsequently expressing genes consistent with osteogenic and adipogenic differentiation potential.

A1.4 Discussion

In an effort to recapitulate the structural and functional characteristics of *in vivo* microenvironments, significant emphasis in the tissue engineering and biomaterials

communities has been placed on the development of 3D cell culture systems[56]. However, analytical assays and tools commonly used to assess cell phenotypes in 2D cultures are typically more complicated in 3D, and generally require that cells first be retrieved from the 3D environment. Recovery of viable cells from 3D cultures has been limited by the lack of suitable methods to retrieve encapsulated cells. In our own previous work, we have extensively used fibrin to investigate capillary morphogenesis *in vitro* and neovascularization *in vivo*[32,35,57]. However, despite our experience with fibrin, we lacked a simple yet effective method to recover cells encapsulated within fibrin hydrogels for further characterization. Here we have presented a safe and efficient protocol for the isolation of cells from 3D fibrin gels based on the strong fibrinolytic enzyme nattokinase, a serine protease of the subtilisin family that has strong fibrinolytic activity.

To validate this method, we first assessed the efficiency of nattokinase for retrieving cells from fibrin gels compared to other commonly used proteolytic enzymes, trypsin (another serine protease)[58] and TrypLE™ (a recombinant fungal trypsin-like protease)[59,60]. Using MSCs as a model cell type, we showed that nattokinase was > 4X more efficient than TrypLE™ for cell extraction (Fig. A1.2A). The number and viability of MSCs extracted from fibrin via nattokinase were also nearly equivalent to cells harvested from 2D tissue culture plastic via trypsin (Fig. A1.2B, C), suggesting that MSCs proliferate to a comparable extent in 3D fibrin as

they do on 2D polystyrene and that nattokinase does not compromise their plasma membranes.

We next investigated the effects of cell extraction via nattokinase on the multilineage potential of MSCs harvested from 3D fibrin gels. Traditional adipogenic and osteogenic differentiation assays were performed in 2D cultures using MSCs that were first propagated within and retrieved from 3D fibrin gels, and compared to cells that were grown and then differentiated entirely in 2D. Analysis of Oil Red O levels, an indicator of lipid formation, showed that MSCs extracted from 3D fibrin gels via nattokinase extraction were equally capable of adipogenic differentiation as controls from 2D cultures (Fig. A1.3). Furthermore, q-PCR analyses of the genes encoding for PPARγ, a key regulator of adipogenesis, and CEBPα, a positive feedback loop regulator of PPARγ expression[46,61,62], suggested that nattokinase extraction after 14 days of pre-culture in 3D fibrin gels followed by 7 days of exposure to adipogenic differentiation media did not alter the adipogenic potential of MSCs (Fig. A1.5A, B). Similarly, von Kossa staining and quantification of calcium levels revealed qualitatively and quantitatively that nattokinase did not alter the ability of MSCs to synthesize a matrix capable of mineralization (Fig. A1.4). Quantitative PCR analysis confirmed that cells extracted from fibrin via nattokinase were capable of osteogenic gene expression. The expression of BGLAP (the gene encoding for osteocalcin) in cells extracted from 3D was elevated with respect to cells grown on 2D surfaces (Fig. A1.5D), suggesting

that priming the cells for a period of time in 3D fibrin gels prior to induction may in fact enhance the osteogenic phenotype. Differences in RUNX2 gene expression, an early marker of osteogenic differentiation[63], showed similar trends (Fig. A1.5C), but were not significantly different in MSCs induced down an osteogenic lineage for 21 days preceded by 14 days of growth in 3D fibrin gels relative to cells cultured exclusively in 2D. Collectively, these data illustrate that nattokinase extraction does not diminish the potential of MSCs recovered via nattokinase to undergo subsequent adipogenesis or osteogenesis, or to express genes characteristic of these two phenotypes.

In the human body, fibrinolysis is achieved mainly by the serine protease plasmin[64], but can also be achieved by matrix metalloproteinases (MMPs) in certain circumstances[65,66]. Plasmin is generated by enzymatic cleavage of plasminogen, either via urokinase plasminogen activator (uPA) or tissue plasminogen activator (tPA). Activation via uPA requires initial binding of uPA to the cell membrane-anchored uPA receptor (uPAR), thereby sequestering plasmin activation and proteolysis to the immediate vicinity of the cell surface. Conversely, activation by tPA does not require prior binding to a cell surface receptor, and results in a global activation of plasmin. Given these mechanisms, a reasonable enzyme to extract cells from 3D fibrin gels would be plasmin, or the activators of plasmin uPA or tPA. In fact, prior studies have used purified urokinase to isolate stromal cells from 3D fibrin gel cultures[41,42]. In those studies, the authors dissolved their fibrin gels in a solution consisting of

medium containing serum (the source of the plasminogen) and 5000 units of urokinase. However, we did not compare these enzymes side-by-side in this study primarily due to their high cost relative to nattokinase. Achieving comparable levels of fibrinolytic activity via purified urokinase would be approximately 300x more expensive than nattokinase, while plasmin would cost nearly 42,000x more. Other possible enzymes were also considered, including proteinase K, collagenase, and Accutase; however, since none of these are specific for fibrin[67-69], we reasoned that they would not be as efficient.

Trypsin is commonly used to passage cells during 2D cell culture, but our data show that retrieving cells from 3D fibrin gels using trypsin is very inefficient, even when the gels are exposed to the enzyme for 30 minutes. As prolonged exposure to trypsin causes an upregulation in proteins that regulate apoptosis[70], we concluded that incubation times longer than 30 minutes would be undesirable. We speculate that the increased efficiency of cell retrieval and the high degree of cell viability achieved with 30 minutes of nattokinase is likely due to its high affinity and fibrinolytic specificity to cross-linked fibrin[43-45]. Although we are unaware of direct comparisons of the relative affinities of nattokinase and trypsin to fibrin, trypsin has markedly lower affinity to fibrin compared to plasmin[71]. Furthermore, a previous report suggested that nattokinase has higher affinity to cross-linked fibrin than plasmin[72]. Thus, it is reasonable to infer that nattokinase also has a higher affinity to fibrin compared to trypsin.

MSCs from bone marrow and a variety of other adult tissues are already the focus of numerous human clinical trials[73,74], and have shown enormous promise in preclinical studies to facilitate bone regeneration[75], promote tissue neovascularization[76-78], and reduce inflammation[79]. Much of their therapeutic benefit seems to be related to their trophic effects, i.e. through the secretion of numerous growth factors[79]. In the case of bone marrow, MSCs are relatively rare cells (approximately 0.01% of the nucleated cells from a low-density Percoll gradient[80]), and are typically isolated based on their adherent properties[80]. Significantly larger numbers of cells (~10^7) are needed for therapeutic applications, in part because the number of cells that actually engraft within target tissues may be quite low[81]. As a result, MSCs are typically expanded via standard 2D cell cultures. However, it has previously been shown that culturing MSCs on 2D surfaces, over time, diminishes the expression levels of surface markers commonly associated with MSCs (e.g. VCAM-1, ICAM-1, and CD157)[82], and adversely effects their proliferation and telomere length[9,10]. A quasi-3D fibrin culture where cells were grown on fibrin gels retained multipotentiality of MSCs[83], but it is unclear if a protocol consisting entirely of 3D culture would be even better in terms of maintaining MSCs' multipotency. With the simple enzymatic method to digest fibrin without harming the cells that we have described here, the possibility now exists that MSCs can be cultured exclusively in 3D from the time of harvest (or perhaps the first passage, to exploit their adherent properties to isolate them from other cell types) to the time of therapeutic application.

Furthermore, cultures of multiple cell types could now theoretically be grown in 3D fibrin gels, extracted via nattokinase, and subsequently sorted via FACS for subsequent analyses or applications. In our own work, we expect this methodology will enable our efforts to better understand cross-talk between MSCs and endothelial cells in the perivascular niche[35].

A1.5 Conclusion

Retrieving viable cells with high efficiency from 3D environments is non-trivial. We described here a simple yet effective method to harvest MSCs encapsulated within 3D fibrin gels using a powerful fibrinolytic enzyme, nattokinase. Our data show that MSCs recovered from 3D fibrin gels using nattokinase are not only viable, but also retain their proliferative and multilineage potential. Demonstrated for MSCs, this method will likely be useful to also retrieve other cell types from 3D fibrin gels for subsequent applications, including expansion, bioassays, and *in vivo* injection.

A.1.6 References

1 Rao, M. S. & Mattson, M. P. Stem cells and aging: expanding the possibilities. *Mech Ageing Dev* **122**, 713-734, doi:S0047-6374(01)00224-X (2001).

2 Sarugaser, R., Ennis, J., Stanford, W. L. & Davies, J. E. Isolation, propagation, and characterization of human umbilical cord perivascular cells (HUCPVCs). *Methods Mol Biol* **482**, 269-279, doi:10.1007/978-1-59745-060-7_17 (2009).

3 De Coppi, P. *et al.* Isolation of amniotic stem cell lines with potential for therapy. *Nat Biotechnol* **25**, 100-106, doi:10.1038/nbt1274 (2007).

4 Yen, B. L. *et al.* Brief report--human embryonic stem cell-derived mesenchymal progenitors possess strong immunosuppressive effects toward natural killer cells as well as T lymphocytes. *Stem Cells* **27**, 451-456, doi:10.1634/stemcells.2008-0390 (2009).

5 Yen, M. L. *et al.* Efficient Derivation & Concise Gene Expression Profiling of Human Embryonic Stem Cell-Derived Mesenchymal Progenitors (EMPs). *Cell Transplant*, doi:10.3727/096368910X564067ct0107yenetalpdf (2011).

6 Caplan, A. I. & Correa, D. The MSC: an injury drugstore. *Cell Stem Cell* **9**, 11-15, doi:10.1016/j.stem.2011.06.008 (2011).

7 Lutolf, M. P. & Blau, H. M. Artificial stem cell niches. *Adv Mater* **21**, 3255-3268, doi:10.1002/adma.200802582 (2009).

8 Gilbert, P. M. & Blau, H. M. Engineering a stem cell house into a home. *Stem Cell Res Ther* **2**, 3, doi:10.1186/scrt44 (2011).

9 Banfi, A. *et al.* Proliferation kinetics and differentiation potential of ex vivo expanded human bone marrow stromal cells: Implications for their use in cell therapy. *Exp Hematol* **28**, 707-715, doi:S0301-472X(00)00160-0 (2000).

10 Baxter, M. A. *et al.* Study of telomere length reveals rapid aging of human marrow stromal cells following in vitro expansion. *Stem Cells* **22**, 675-682, doi:10.1634/stemcells.22-5-675 (2004).

11 Reiser, J. *et al.* Potential of mesenchymal stem cells in gene therapy approaches for inherited and acquired diseases. *Expert Opin Biol Ther* **5**, 1571-1584, doi:10.1517/14712598.5.12.1571 (2005).

12 Mendez-Ferrer, S. *et al.* Mesenchymal and haematopoietic stem cells form a unique bone marrow niche. *Nature* **466**, 829-834, doi:10.1038/nature09262 (2010).

13 Markway, B. D. *et al.* Enhanced chondrogenic differentiation of human bone marrow-derived mesenchymal stem cells in low oxygen environment micropellet cultures. *Cell Transplant* **19**, 29-42, doi:10.3727/096368909X478560 (2010).

14 Wang, W. *et al.* 3D spheroid culture system on micropatterned substrates for improved differentiation efficiency of multipotent mesenchymal stem cells. *Biomaterials* **30**, 2705-2715, doi:10.1016/j.biomaterials.2009.01.030 (2009).

15 Jahn, K., Richards, R. G., Archer, C. W. & Stoddart, M. J. Pellet culture model for human primary osteoblasts. *Eur Cell Mater* **20**, 149-161, doi:vol020a13 (2010).

16 Ungrin, M. D., Joshi, C., Nica, A., Bauwens, C. & Zandstra, P. W. Reproducible, ultra high-throughput formation of multicellular organization from single cell suspension-derived human embryonic stem cell aggregates. *PLoS One* **3**, e1565, doi:10.1371/journal.pone.0001565 (2008).

17 Cook, M. M. *et al.* Micromarrows--three-dimensional coculture of hematopoietic stem cells and mesenchymal stromal cells. *Tissue Eng Part C Methods* **18**, 319-328, doi:10.1089/ten.TEC.2011.0159 (2012).

18 King, J. A. & Miller, W. M. Bioreactor development for stem cell expansion and controlled differentiation. *Curr Opin Chem Biol* **11**, 394-398, doi:10.1016/j.cbpa.2007.05.034 (2007).

19 Breen, A., O'Brien, T. & Pandit, A. Fibrin as a delivery system for therapeutic drugs and biomolecules. *Tissue Eng Part B Rev* **15**, 201-214, doi:10.1089/ten.TEB.2008.0527 (2009).

20 Ho, W., Tawil, B., Dunn, J. C. & Wu, B. M. The behavior of human mesenchymal stem cells in 3D fibrin clots: dependence on fibrinogen concentration and clot structure. *Tissue Eng* **12**, 1587-1595, doi:10.1089/ten.2006.12.1587 (2006).

21 Christman, K. L. *et al.* Injectable fibrin scaffold improves cell transplant survival, reduces infarct expansion, and induces neovasculature formation in ischemic myocardium. *J Am Coll Cardiol* **44**, 654-660, doi:10.1016/j.jacc.2004.04.040 (2004).

22 Syedain, Z. H., Bjork, J., Sando, L. & Tranquillo, R. T. Controlled compaction with ruthenium-catalyzed photochemical cross-linking of fibrin-based engineered connective tissue. *Biomaterials* **30**, 6695-6701, doi:10.1016/j.biomaterials.2009.08.039 (2009).

23 Huang, N. F. *et al.* Bone marrow-derived mesenchymal stem cells in fibrin augment angiogenesis in the chronically infarcted myocardium. *Regen Med* **4**, 527-538, doi:10.2217/rme.09.32 (2009).

24 Ryu, J. H. *et al.* Implantation of bone marrow mononuclear cells using injectable fibrin matrix enhances neovascularization in infarcted myocardium. *Biomaterials* **26**, 319-326, doi:10.1016/j.biomaterials.2004.02.058 (2005).

25 Ruger, B. M. *et al.* Vascular morphogenesis by adult bone marrow progenitor cells in three-dimensional fibrin matrices. *Differentiation* **76**, 772-783, doi:10.1111/j.1432-0436.2007.00259.x (2008).

26 Bensaid, W. *et al.* A biodegradable fibrin scaffold for mesenchymal stem cell transplantation. *Biomaterials* **24**, 2497-2502, doi:S014296120200618X (2003).

27 Catelas, I. *et al.* Human mesenchymal stem cell proliferation and osteogenic differentiation in fibrin gels in vitro. *Tissue Eng* **12**, 2385-2396, doi:10.1089/ten.2006.12.2385 (2006).

28 Dickhut, A., Gottwald, E., Steck, E., Heisel, C. & Richter, W. Chondrogenesis of mesenchymal stem cells in gel-like biomaterials in vitro and in vivo. *Front Biosci* **13**, 4517-4528, doi:3020 (2008).

29 Baumgartner, L., Arnhold, S., Brixius, K., Addicks, K. & Bloch, W. Human mesenchymal stem cells: Influence of oxygen pressure on proliferation and chondrogenic differentiation in fibrin glue in vitro. *J Biomed Mater Res A* **93**, 930-940, doi:10.1002/jbm.a.32577 (2010).

30 Ghajar, C. M., Blevins, K. S., Hughes, C. C., George, S. C. & Putnam, A. J. Mesenchymal Stem Cells Enhance Angiogenesis in Mechanically Viable Prevascularized Tissues via Early Matrix Metalloproteinase Upregulation. *Tissue Eng* **12**, 2875-2888 (2006).

31 Ghajar, C. M. *et al.* The effect of matrix density on the regulation of 3-D capillary morphogenesis. *Biophys J* **94**, 1930-1941, doi:10.1529/biophysj.107.120774 (2008).

32 Ghajar, C. M. *et al.* Mesenchymal cells stimulate capillary morphogenesis via distinct proteolytic mechanisms. *Exp Cell Res* **316**, 813-825, doi:10.1016/j.yexcr.2010.01.013 (2010).

33 Kachgal, S. & Putnam, A. J. Mesenchymal stem cells from adipose and bone marrow promote angiogenesis via distinct cytokine and protease expression mechanisms. *Angiogenesis* **14**, 47-59, doi:10.1007/s10456-010-9194-9 (2011).

34 Kniazeva, E., Kachgal, S. & Putnam, A. J. Effects of extracellular matrix density and mesenchymal stem cells on neovascularization in vivo. *Tissue engineering. Part A* **17**, 905-914, doi:10.1089/ten.TEA.2010.0275 (2011).

35 Carrion, B. *et al.* Recreating the perivascular niche ex vivo using a microfluidic approach. *Biotechnol Bioeng* **107**, 1020-1028, doi:10.1002/bit.22891 (2010).

36 Kachgal, S., Carrion, B., Janson, I. A. & Putnam, A. J. Bone marrow stromal cells stimulate an angiogenic program that requires endothelial MT1-MMP. *J Cell Physiol* **227**, 3546-3555, doi:10.1002/jcp.24056 (2012).

37 Kossack, N. *et al.* Isolation and characterization of pluripotent human spermatogonial stem cell-derived cells. *Stem Cells* **27**, 138-149, doi:10.1634/stemcells.2008-0439 (2009).

38 Sun, N. *et al.* Feeder-free derivation of induced pluripotent stem cells from adult human adipose stem cells. *Proc Natl Acad Sci U S A* **106**, 15720-15725, doi:10.1073/pnas.0908450106 (2009).

39 Huang, G. T. *et al.* Stem/progenitor cell-mediated de novo regeneration of dental pulp with newly deposited continuous layer of dentin in an in vivo model. *Tissue Eng Part A* **16**, 605-615, doi:10.1089/ten.TEA.2009.0518 (2010).

40 Farias, V. A. *et al.* Human umbilical cord stromal stem cell express CD10 and exert contractile properties. *Placenta* **32**, 86-95, doi:10.1016/j.placenta.2010.11.003 (2011).

41 Yang, Y. I. *et al.* Fibrin matrix-supported three-dimensional organ culture of adipose tissue for selective outgrowth, expansion, and isolation of adipose-derived stem cells. *Acta Biomater* **7**, 4109-4119, doi:10.1016/j.actbio.2011.07.027 (2011).

42 Choi, M. Y. *et al.* The isolation and in situ identification of MSCs residing in loose connective tissues using a niche-preserving organ culture system. *Biomaterials* **33**, 4469-4479, doi:10.1016/j.biomaterials.2012.03.009 (2012).

43 Urano, T. *et al.* The profibrinolytic enzyme subtilisin NAT purified from Bacillus subtilis Cleaves and inactivates plasminogen activator inhibitor type 1. *J Biol Chem* **276**, 24690-24696, doi:10.1074/jbc.M101751200 (2001).

44 Sumi, H., Hamada, H., Tsushima, H., Mihara, H. & Muraki, H. A novel fibrinolytic enzyme (nattokinase) in the vegetable cheese Natto; a typical and popular soybean food in the Japanese diet. *Experientia* **43**, 1110-1111 (1987).

45 Fujita, M. *et al.* Purification and characterization of a strong fibrinolytic enzyme (nattokinase) in the vegetable cheese natto, a popular soybean fermented food in Japan. *Biochem Biophys Res Commun* **197**, 1340-1347, doi:10.1006/bbrc.1993.2624 (1993).

46 McBeath, R., Pirone, D. M., Nelson, C. M., Bhadriraju, K. & Chen, C. S. Cell shape, cytoskeletal tension, and RhoA regulate stem cell lineage commitment. *Dev Cell* **6**, 483-495, doi:S1534580704000759 (2004).

47 Pittenger, M. F. *et al.* Multilineage potential of adult human mesenchymal stem cells. *Science* **284**, 143-147 (1999).

48 Prockop, D. J. P., Donald G.; Bunnell, Bruce A. in *Methods in molecular biology v. 449* (Humana Press, Totowa, N.J., 2008).

49 Rao, R. R., Jiao, A., Kohn, D. H. & Stegemann, J. P. Exogenous mineralization of cell-seeded and unseeded collagen-chitosan hydrogels using modified culture medium (vol 8, pg 1560, 2012). *Acta Biomaterialia* **8**, 2417-2417, doi:DOI 10.1016/j.actbio.2012.03.037 (2012).

50 Ter Brugge, P. J. & Jansen, J. A. In vitro osteogenic differentiation of rat bone marrow cells subcultured with and without dexamethasone. *Tissue Eng* **8**, 321-331, doi:10.1089/107632702753725076 (2002).

51 Schmittgen, T. D. & Livak, K. J. Analyzing real-time PCR data by the comparative C(T) method. *Nat Protoc* **3**, 1101-1108 (2008).

52 Fink, T. *et al.* Instability of standard PCR reference genes in adipose-derived stem cells during propagation, differentiation and hypoxic exposure. *BMC Mol Biol* **9**, 98, doi:10.1186/1471-2199-9-98 (2008).

53 Krause, U., Seckinger, A. & Gregory, C. A. Assays of Osteogenic Differentiation by Cultured Human Mesenchymal Stem Cells. *Mesenchymal Stem Cell Assays and Applications* **698**, 215-230, doi:Doi 10.1007/978-1-60761-999-4_17 (2011).

54 Stacey, D. H., Hanson, S. E., Lahvis, G., Gutowski, K. A. & Masters, K. S. In vitro Adipogenic Differentiation of Preadipocytes Varies with Differentiation Stimulus, Culture Dimensionality, and Scaffold Composition. *Tissue Eng Pt A* **15**, 3389-3399, doi:DOI 10.1089/ten.tea.2008.0293 (2009).

55 Tarnowski, B. I. *et al.* Automatic Quantitation of Cell-Growth and Determination of Mitotic Index Using Dapi Nuclear Staining. *Pediatr Pathol* **13**, 249-265 (1993).

56 Lutolf, M. P., Gilbert, P. M. & Blau, H. M. Designing materials to direct stem-cell fate. *Nature* **462**, 433-441, doi:10.1038/nature08602 (2009).

57 Grainger, S. J. & Putnam, A. J. Assessing the permeability of engineered capillary networks in a 3D culture. *PLoS One* **6**, e22086, doi:10.1371/journal.pone.0022086 (2011).

58 Kocholaty, W., Ellis, W. W. & Jensen, H. Activation of Plasminogen by Trypsin and Plasmin. *Blood* **7**, 882-890 (1952).

59 T'Joen, V., Declercq, H. & Cornelissen, M. Expansion of human embryonic stem cells: a comparative study. *Cell Proliferat* **44**, 462-476, doi:DOI 10.1111/j.1365-2184.2011.00773.x (2011).

60 Marley, M. S. D. *et al.* Efficacy of a recombinant trypsin product against bovine herpesvirus I associated with in vivo- and in vitro-derived bovine embryos. *Theriogenology* **69**, 746-757, doi:DOI 10.1016/j.thefiogenology.2007.10.026 (2008).

61 Kanematsu, D. *et al.* Isolation and cellular properties of mesenchymal cells derived from the decidua of human term placenta. *Differentiation* **82**, 77-88, doi:DOI 10.1016/j.diff.2011.05.010 (2011).

62 Kim, W. K., Meliton, V., Amantea, C. M., Hahn, T. J. & Parhami, F. 20(S)-Hydroxycholesterol inhibits PPAR gamma expression and adipogenic differentiation of bone marrow stromal cells through a hedgehog-dependent mechanism. *J Bone Miner Res* **22**, 1711-1719, doi:Doi 10.1359/Jbmr.070710 (2007).

63 Psaltis, P. J. *et al.* Enrichment for STRO-1 Expression Enhances the Cardiovascular Paracrine Activity of Human Bone Marrow-Derived Mesenchymal Cell Populations. *J Cell Physiol* **223**, 530-540, doi:Doi 10.1002/Jcp.22081 (2010).

64 Lijnen, H. R. Elements of the fibrinolytic system. *Ann N Y Acad Sci* **936**, 226-236 (2001).

65 Hiraoka, N., Allen, E., Apel, I. J., Gyetko, M. R. & Weiss, S. J. Matrix metalloproteinases regulate neovascularization by acting as pericellular fibrinolysins. *Cell* **95**, 365-377 (1998).

66 Hotary, K. B. *et al.* Matrix metalloproteinases (MMPs) regulate fibrin-invasive activity via MT1-MMP-dependent and -independent processes. *J Exp Med* **195**, 295-308 (2002).

67 Brendlerschwaab, S. Y. *et al.* Cells of Different Tissues for in-Vitro and in-Vivo Studies in Toxicology - Compilation of Isolation Methods. *Toxicol in Vitro* **8**, 1285-1302 (1994).

68 MacCoss, M. J., Wu, C. C. & Yates, J. R. Probability-based validation of protein identifications using a modified SEQUEST algorithm. *Anal Chem* **74**, 5593-5599, doi:Doi 10.1021/Ac025826t (2002).

69 Shao, L. J. *et al.* Generation of iPS cells using defined factors linked via the self-cleaving 2A sequences in a single open reading frame. *Cell Res* **19**, 296-306, doi:Doi 10.1038/Cr.2009.20 (2009).

70 Huang, H. L. *et al.* Trypsin-induced proteome alteration during cell subculture in mammalian cells. *J Biomed Sci* **17**, Doi 10.1186/1423-0127-17-36 (2010).

71 Kolev, K., Tenekedjiev, K., Komorowicz, E. & Machovich, R. Functional evaluation of the structural features of proteases and their substrate in fibrin surface degradation. *Journal of Biological Chemistry* **272**, 13666-13675 (1997).

72 Fujita, M., Ito, Y., Hong, K. & Nishimuro, S. Characterization of Nattokinase-Degraded Products from Human Fibrinogen or Cross-Linked Fibrin. *Fibrinolysis* **9**, 157-164 (1995).

73 Giordano, A., Galderisi, U. & Marino, I. R. From the laboratory bench to the patient's bedside: an update on clinical trials with mesenchymal stem cells. *Journal of cellular physiology* **211**, 27-35, doi:10.1002/jcp.20959 (2007).

74 Wagner, J., Kean, T., Young, R., Dennis, J. E. & Caplan, A. I. Optimizing mesenchymal stem cell-based therapeutics. *Curr Opin Biotechnol* **20**, 531-536, doi:10.1016/j.copbio.2009.08.009 (2009).

75 Simmons, C. A., Alsberg, E., Hsiong, S., Kim, W. J. & Mooney, D. J. Dual growth factor delivery and controlled scaffold degradation enhance in vivo bone formation by transplanted bone marrow stromal cells. *Bone* **35**, 562-569 (2004).

76 Nagaya, N. *et al.* Transplantation of mesenchymal stem cells improves cardiac function in a rat model of dilated cardiomyopathy. *Circulation* **112**, 1128-1135 (2005).

77 Silva, G. V. *et al.* Mesenchymal stem cells differentiate into an endothelial phenotype, enhance vascular density, and improve heart function in a canine chronic ischemia model. *Circulation* **111**, 150-156 (2005).

78 Kinnaird, T. *et al.* Local delivery of marrow-derived stromal cells augments collateral perfusion through paracrine mechanisms. *Circulation* **109**, 1543-1549 (2004).

79 Caplan, A. I. Adult mesenchymal stem cells for tissue engineering versus regenerative medicine. *J Cell Physiol* (2007).

80 Bruder, S. P., Jaiswal, N. & Haynesworth, S. E. Growth kinetics, self-renewal, and the osteogenic potential of purified human mesenchymal stem cells during extensive subcultivation and following cryopreservation. *Journal of cellular biochemistry* **64**, 278-294 (1997).

81 Parekkadan, B. & Milwid, J. M. Mesenchymal Stem Cells as Therapeutics. *Annu Rev Biomed Eng* **12**, 87-117, doi:DOI 10.1146/annurev-bioeng-070909-105309 (2010).

82 Honczarenko, M. *et al.* Human bone marrow stromal cells express a distinct set of biologically functional chemokine receptors. *Stem Cells* **24**, 1030-1041, doi:DOI 10.1634/stemcells.2005-0319 (2006).

83 Colley, H., McArthur, S. L., Stolzing, A. & Scutt, A. Culture on fibrin matrices maintains the colony-forming capacity and osteoblastic differentiation of mesenchymal stem cells. *Biomed Mater* **7**, Doi 10.1088/1748-6041/7/4/045015 (2012).

Appendix 2: An alternate method for producing nanoPMMA topographic surfaces—and the cellular response of mouse pre-osteoblasts

A2.1 Introduction

As mentioned throughout this thesis, there is a strong need to help overcome issues that arise because of an aging population, continued prevalence of bone defects, and revision surgeries[1,2]. Here in the United States that economic cost is soon to top $20 billion annually[3]. Strategies which enhance our knowledge of bone formation and regeneration, or enhance current clinical practices are needed. Enhancements will prolong implant lifetime, reduce the need for revisions, and drive down the economic impact, while improving a patient's quality of life.

As previously described, bone is a hierarchical structure with a great deal of order and alignment on the nanoscale. Replicating this structure may promote cell deposited mineral to form lamellar-like bone more quickly or efficiently. Thus, an alternate strategy to the capillary assisted UV-lithographic technique outlined in Chapter 3 is to use nanoimprint lithography to produce nanofeatures that mimic the nanoscale environment observed in bone.

We developed an approximate replica of the nanotopographic structure of bone using an idealized surface of poly(methyl methacrylate) (PMMA) to investigate the role of surface nanotopography in driving the osteogenic differentiation of mouse calvarial pre-osteoblasts (MC3T3-E1). Clinically, PMMA is used as a bone cement in orthopedic surgery [4,5]. We were motivated by the potential to enhance osteointegration and bone healing via imprinted nanotopographic cues. We hypothesized, similar to Chapter 3, that our nanoPMMA surfaces with aligned features on the order of collagen fibrils would mimic the structure of native bone would enhance mineral quantity. To test this hypothesis, we characterized our nanoimprint PMMA films using atomic force microscopy (AFM) and scanning electron microscopy (SEM) to validate their submicron dimensions. In addition, we measured contact angles via the sessile drop method to determine differences in wettability. Cell proliferation, ALP expression, and cytoskeletal markers were also investigated.

A2.2 Materials and Methods

2.2.1 Manufacturing of PMMA films

Glass No. 1 coverslips (Fisher/VWR) were cleaned in a piranha acid solution for 30 minutes, rinsed in distilled water and then dried in nitrogen. A layer of MOPTS (silane, Gelest) was deposited using chemical vapor deposition to improve the

adherence of PMMA. PMMA (MW 15,000 g/mol, Sigma) was dissolved with toluene to create a 6% (wt./v) solution. The solution was filtered with a 0.22 micron filter to remove any impurities and large particles. The solution was spin coated onto the MOPTS coated glass slides and baked for ~10 minutes at 120 °C. After spin coating, the smooth PMMA films were nanoimprinted on a hydraulic press situated in a Class 1000 clean room and subject to heating above T_g (~105 °C) and a mechanical load using a silicon master mold (Lightsmyth) to impart the mold features. The substrates were cooled before being separated from the Si mold. The Si masters were treated with a surfactant, 1H, 1H, 2H, 2H-pefluorodecyl-tricholosilane (FTDS) to promote polymer release[6]. Two mold sizes were used: 139 nm wide (110 nm deep) and 416 nm wide (200 nm deep) (LightSmyth, Eugene, OR). Smooth PMMA films absent of topography were also manufactured. PMMA films will be designated by the following names for simplicity and clarity: smooth, G415, and G140.

Table A2.1 Nomenclature and AFM measurements of PMMA films with nanotopographic features.

		Height (nm)	Width (nm)	Base (nm)	Gap width (nm)
G415	Average	258	354	599	467
	Std. Dev.	11	41	34	24
G140	Average	146	128	207	162
	Std. Dev.	4	14	14	12

A2.2.2 Characterization of PMMA films with atomic force microscopy

AFM tips were obtained from Pacific Nanotechnology and used on an Integrated Dynamics Engineering AFM. All images were taken in tapping mode. Three or more scans were taken on each substrate and 3 areas from each scan were analyzed to determine the measurements of the nanotopographic substrates. The measurements were taken using the cross section surface profiles. The measurements obtained were the grating width, grating height, width between gratings (gap width), and the width of each grating at the bottom of each well (base width) as displayed in Table A2.1.

A2.2.3 Characterization of PMMA films with scanning electron microscopy

To use a complementary method to assess nanofeatures, imprinted PMMA films were imaged with and SEM. A Carl Zeiss Ultra field emission scanning electron microscope (FESEM) was used to obtain images with nanoscale resolution of the PMMA substrates. The samples were coated with a thin layer of gold to prevent charging. A working distance of 7 mm and an accelerating voltage of 5 kV was used.

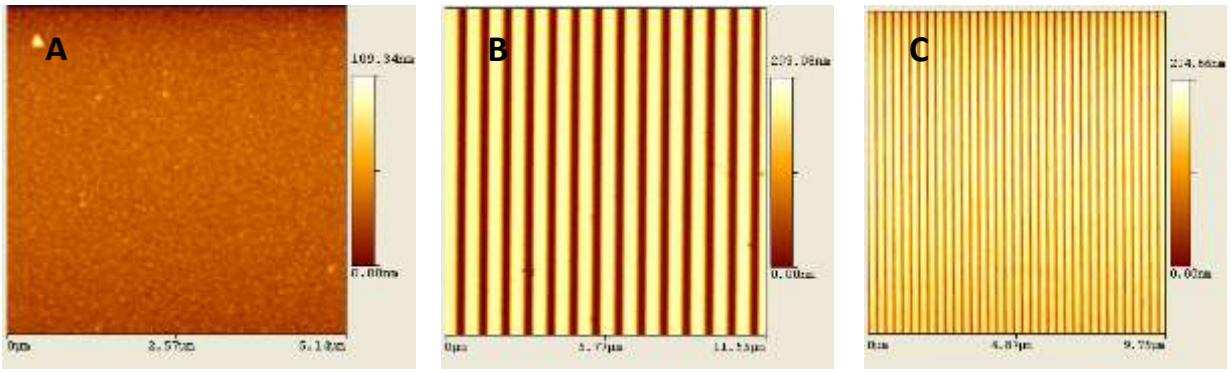

Figure A2.1. AFM scans illustrate the effectiveness of nanoimprint lithography to produce PMMA films with nanotopography. A. Smooth PMMA film. B. G415 film (416 nm wide grating, 200 nm height). C. G140 film (139 nm wide, 110 nm height).

A2.2.4 Determination of contact angles

Distilled water and phosphate buffered saline (PBS) were used to determine wettability of nanosubstrates. An ~10 μL droplet of each solution was placed on the surface of the topography of interest. An image was taken with a Nikon D90 SLR camera. For drops on nanotopography, anisotropy of the contact angle was observed, thus images were taken perpendicular and parallel to the grating direction ('transverse' means the image plane was perpendicular to the long-axis direction of the underlying topography). A minimum of three measurements per substrate were imaged, using nitrogen gas to dry the substrate as needed. Images were quantified using 'DropSnake', a Java plug-in that is part of the ImageJ imaging software.

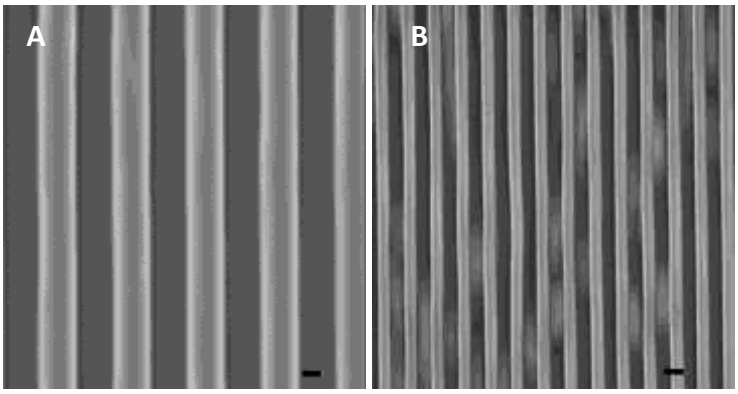

Figure A2.2. SEM images confirm nanofeatures. Nanoimprint lithographic films size A. G415 and B. G140 (scale bar 200 nm).

A2.2.5 Cell culture conditions

MC3T3-E1 pre-osteoblasts (ATCC) were cultured in alpha-MEM growth media [GM] (Invitrogen) supplemented with 10% fetal bovine serum (ATCC), 5% penicillin/streptomycin (Mediatech) and 0.5% gentamicin (Invitrogen). For osteogenic assays cells were supplemented with 10 mM β-glycerol phosphate, 50 μg/mL ascorbic acid, and 100 nM dexamethasone (all from Sigma Aldrich). Cells were grown at confluence (100,000/cm^2) for osteogenic assays. Cells used were between passages 3 and 9.

A.2.2.6 Proliferation assay

To assess the effects of topography on proliferation, MC3T3-E1 cells were cultured in GM at a density of 10,000/cm^2. Media was changed every 2 to 3 days. At days 2, 5, and 9, cells were fixed with paraformaldehyde. Cell nuclei were stained with DAPI (1:5000). At least nine images were manually counted per condition.

A2.2.7 Mineralization-Von Kossa

To assess phosphate formation in deposited mineral a Von Kossa stain kit was obtained from American Mastertech Scientific. After 14 days, cells were first rinsed with PBS then fixed with 4% paraformaldehyde for 30 minutes. After rinsing with distilled water three or more times, 5% silver nitrate was added to each well. Fixed cells were exposed to UV light for 40 minutes and then rinsed with distilled water. Sodium thiosulfate was then added for ~3 minutes to remove any excess silver. Wells were then rinsed with distilled water and imaged using optical microscopy.

A2.2.8 Alkaline phosphatase expression

We measured cellular alkaline phosphatase (ALP) activity, at days 7, 14, and 21. Cells were washed with cold PBS and lysed using passive lysis buffer (Promega). Lysates were homogenized, sonicated, and centrifuged in 10 mM Tris-HCl (pH 7.4; Sigma). ALP activity in the lysates was assayed at 37°C in a buffer containing 100 mM glycine and 1 mM MgCl2 (pH 10.5), for 20 min using p-nitrophenol phosphate (pNPP) (50 mM; all from Sigma) as a substrate. The amount of pNPP was determined spectrophotometrically after the enzymatic reaction was terminated using 0.1 N NaOH. ALP activity (units/mL) was normalized with total protein measurements for each sample.

A2.2.9 Immunofluorescent staining

Cells were imaged using an Olympus IX51 fluorescence microscope equipped with a 100 W high-pressure mercury burner (Olympus America), a QImaging QICAM 12-bit Color Fast 1394 camera (QImaging) and acquired with QCapture Pro. Future images will be taken with an Olympus IX81 spinning disk confocal microscope with a 100 W high-pressure mercury burner (Olympus America), Himatsu camera, and acquired with Metamorph Premier (Molecular Devices). A minimum of three areas per substrate will be taken and any quantification data will be averaged with measurements from three other substrates.

A2.2.10 F-Actin staining

Oregon Green 488 phalloidin (Invitrogen) was used to identify F-actin filaments at day 15. Briefly, cells were washed in PBS then fixed in 4% paraformaldehyde. They cells were then washed with tris-buffered saline with 0.1% Triton-X (TBS-T). TBS + 0.5% Triton-X was used to permeabilize the cell membrane. Cells were incubated with Oregon Green 488 for 45 minutes after being blocked with Abdil (antibody diluting solution) for 20 minutes.

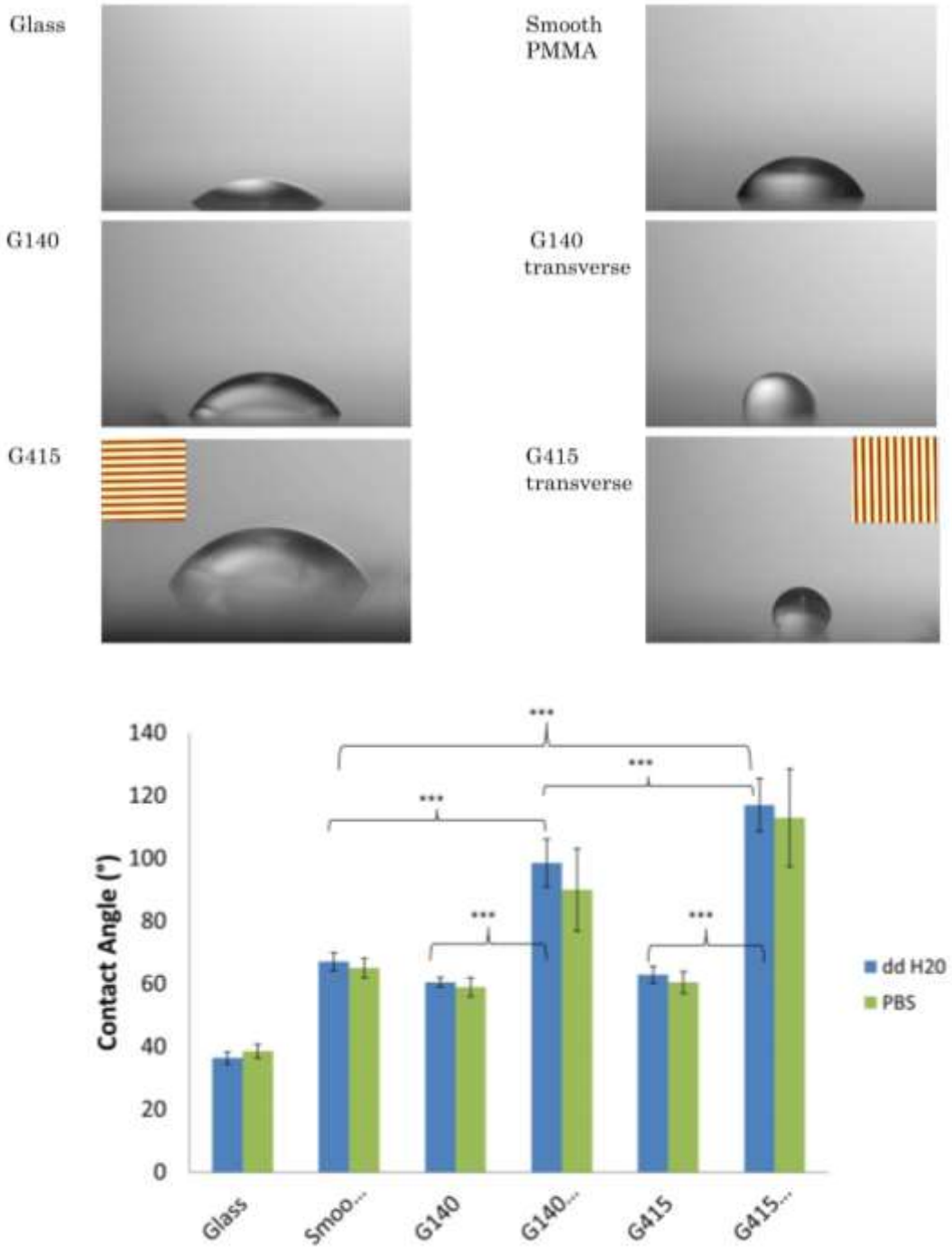

Figure A2.3. Contact angle measurements show anisotropy on nanoPMMA films. Images illustrating wettability of water on glass and smooth, G415, and G140 PMMA films. Insets on G415 images show the direction of the underlying topography. Measurements were also taken using PBS as seen in the graph. 'G140…' and 'G415…' refer to measurements in the direction perpendicular (transverse) to the gratings.

A2.2.11 Statistical Analysis

Statistical analyses were carried out using GraphPad Prism software. One-way ANOVA with the respective post-hoc (Tukey) test was performed. Data are reported as means ± standard deviations. Significance was set at $p < 0.05$.

A2.3 Results

A2.3.1 Nanotopography on PMMA films is confirmed by AFM and SEM.

PMMA films with nanotopographic features were fabricated using nanoimprint lithography. The topographic dimensions of the films were confirmed using AFM (Figure A2.1, A2.2; Table A2.1). As expected, the films had similar dimensions to the Si master molds that were used for polymerization, and the substrates were designated G415, G303, and G140 based on these dimensions (Table A2.1).

A2.3.2 Contact angle measurements illustrate anisotropic wettability.

The contact angle of distilled water and PBS showed anisotropy when measured on nanotopography (Figure A2.3). No anisotropy was observed on smooth surfaces. Significant differences were observed between smooth and 'transverse' nanosubstrate measurements and between G415 transverse and G140 tranverse measurements. These data, illustrated in Figure A2.5, indicate that substrates with 415 nm lines are more hydrophobic than the smaller 140 nm substrates as well as the

smooth substrates. Greater hydrophobicity has been associated with stronger protein-substrate interactions. [7]

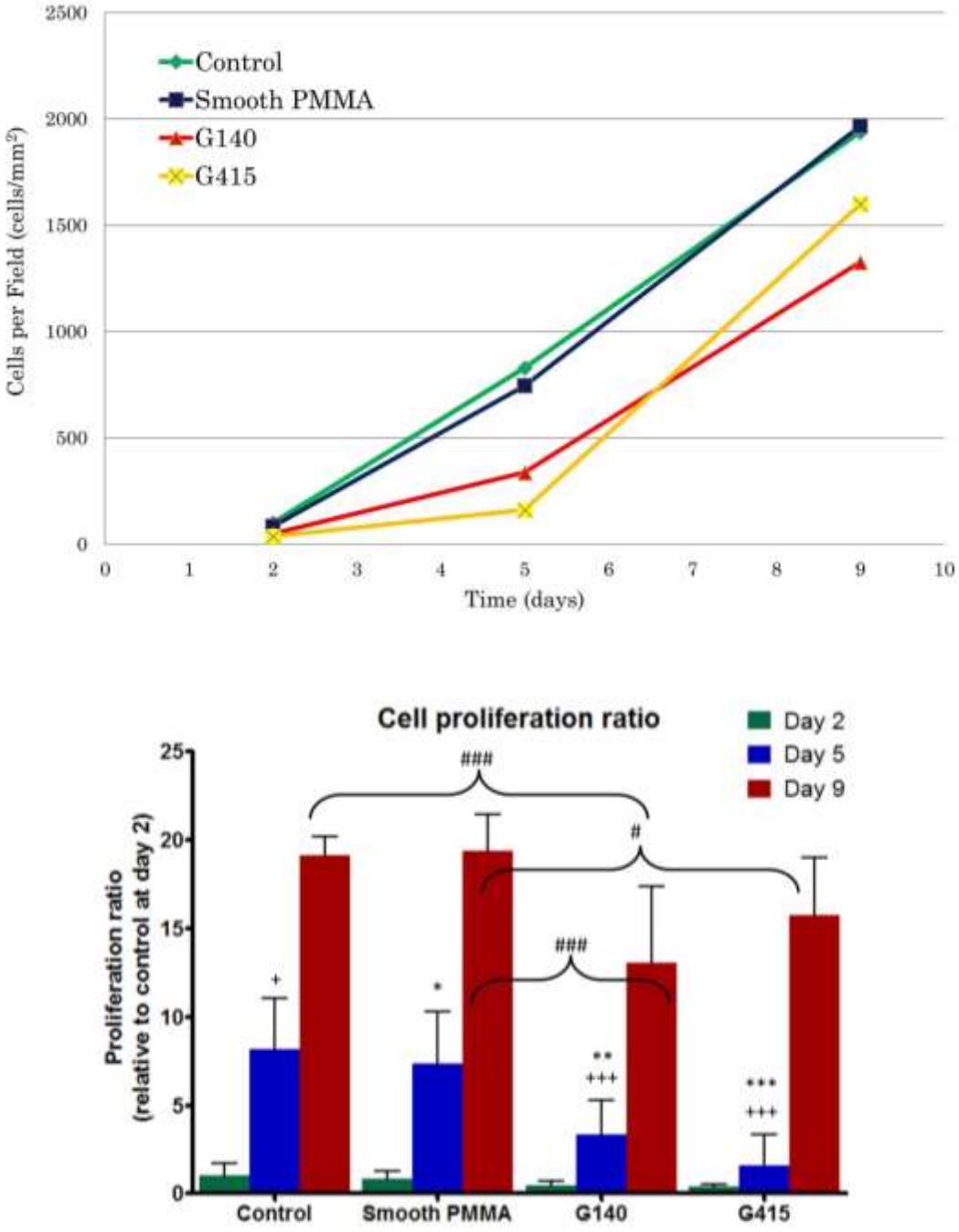

Figure A2.4. Cell proliferation is attenuated on nanoimprinted PMMA films. Top graph shows raw cell proliferation values. The bottom growth is relative proliferation compared to control (tissue culture plastic) at day 2.

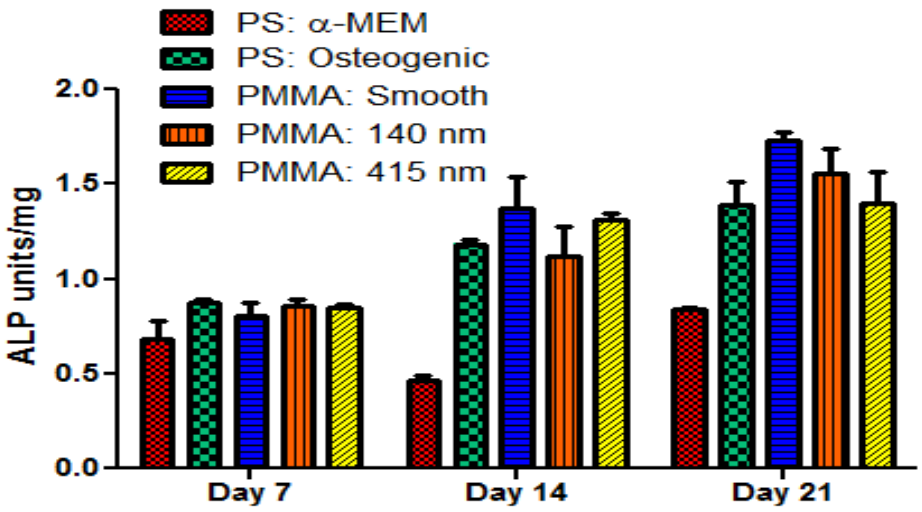

Figure A2.5. ALP expression on nanoPMMA is not enhanced. ALP expression of MC3T3-E1 cells was assessed at days 7, 14, and 21. (Red- cells grown in GM on tissue culture polystyrene (PS), green- cells grown on PS in GM, blue-cells grown on PMMA, orange-140 nm gratings, yellow-415 nm gratings; blue, orange, yellow grown in OM.)

A2.3.3 Cell proliferation is altered by nanotopography.

Cell proliferation was influenced by nanotopgraphy. A significantly lower number of cells were observed on nanosubstrates in comparison to smooth TCP or PMMA as depicted in Figure A2.4. Significant differences were observed between Smooth PMMA and G415 and G140 at days 5 and 9. These data suggest that topography modulates adhesion in a way that down regulates proliferation signals. The exact mechanism imparted by the topography is unclear.

A2.3.4 ALP levels are unchanged on nanotopography.

Alkaline phosphatase levels were assessed at day 7, day 14, and day 21. Alkaline phosphatase is a tissue non-specific differentiation marker observed in bone cells and

elsewhere[8]. Typically levels peak at early time points and then fall off at later time points. We observed a slight rise in ALP levels over time on cells grown in osteogenic media on smooth and nanotopography surfaces as shown in Figure A2.5. No significant differences have been observed.

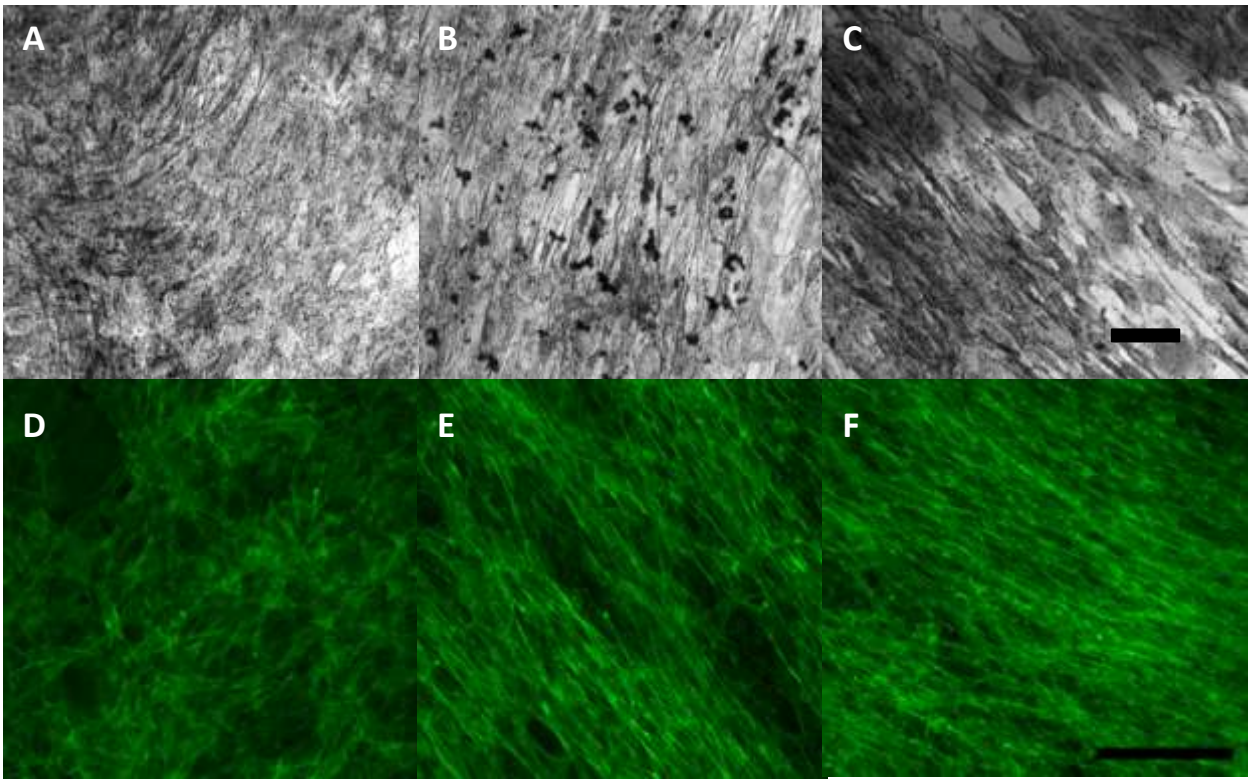

Figure 2.6. Nanotopograpy qualitatively alters phosphate deposition and actin alignment compared to smooth surfaces. Von Kossa and actin immunofluorescent micrographs of MC3T3-E1 cells on PMMA films. Top row is Von Kossa staining (14 days), from left to right Smooth (A, D), G415 (B, E), and G140 (C, F) substrates. The bottom row: actin filament staining (after 15 days, scale bar: 100 microns).

.

A.2.3.6 Qualitative differences in mineralization observed on nanotopography

Figure A2.6 illustrates differences observed after 14 days of culture in osteogenic media. Qualitatively, cells grown on nanotopography produced more

mineral than those grown on smooth surfaces. At this time only qualitative data is available.

A.2.3.7 Qualitative differences in f-actin of cells seeded on nanotopography

F-Actin images taken at day 15, in Figure A2.6, illustrate that cells aligned to a great degree in the same direction as their underlying topography. Cells cultured on smooth surfaces showed an equiaxed morphology, whereas cells grown on topography displayed an elongated and stretched anisotropic morphology.

A2.4 Discussion

In an attempt to mimic the size and alignment of native bone we used nanoimprint lithography to create PMMA films with nanogratings. We confirmed the size and structure of these surfaces with AFM and SEM. We then looked at their wettability and found distinct differences between smooth surfaces. Much of the behavior observed was similar to what we observed with nanoPMMA films made using capillary assisted UV lithography (UV nanoPMMA) (as described in detail in Chapter 3). It should be noted that creating these nanoimprint films requires special facilities and equipment. Clean room conditions and a nanoimprinter are both necessary to reliably produce films according to this method. For these reasons we

switched to the UV lithographic method (as discussed in Chapter 3) for future experiments.

We then wanted to assess the behavior of pre-osteoblasts on these nanoimprinted films. To assess cell behavior, we investigated cell proliferation, ALP expression, phosphate formation in mineral, and actin alignment. Much of the observations were similar to the behavior we observed in hMSCs on UV nanoPMMA. One difference was that cell proliferation was attenuated by nanoimprinted PMMA at day 9. Only qualitative mineral assessments were performed so it was unclear if the qualitative observation translated to quantitative differences. In addition, this observation was only observed once. Cells were not producing mineral to significant levels in order to reproduce and confirm these results. Lack of mineralization and the process of mineralization will be discussed in greater detail in Appendix 3.

A2.5 Conclusions

The method described here produced similar nanosize films as described in Chapter 3, indicating that multiple processing routes can be used to produce surfaces that mimic native bone. Topography does influence the behavior of pre-osteoblasts but there is insufficient data to conclude if nanoimprinted PMMA gratings promote an osteogenic phenotype compared to a smooth surface. Comparing results with pre-osteoblasts and hMSCs in Chapter 3 is difficult because of the insufficient amount of data, though because the two processing methods produced similar feature sizes and

similar wetting behavior any differences observed in cell behaviors can likely be attributed, in large part, to the different cell types.

A2.6 References

1 Prodanov, L. *et al.* The effect of nanometric surface texture on bone contact to titanium implants in rabbit tibia. *Biomaterials* 34, 2920-2927, doi:DOI 10.1016/j.biomaterials.2013.01.027 (2013).

2 Kim, J. *et al.* Synergistic effects of nanotopography and co-culture with endothelial cells on osteogenesis of mesenchymal stem cells. *Biomaterials* 34, 7257-7268, doi:10.1016/j.biomaterials.2013.06.029 (2013).

3 Watari, S. *et al.* Modulation of osteogenic differentiation in hMSCs cells by submicron topographically-patterned ridges and grooves. *Biomaterials* 33, 128-136, doi:DOI 10.1016/j.biomaterials.2011.09.058 (2012).

4 Lewis, G. Viscoelastic properties of injectable bone cements for orthopaedic applications: State-of-the-art review. *J Biomed Mater Res B* 98B, 171-191, doi:Doi 10.1002/Jbm.B.31835 (2011).

5 Jaberi, J., Gambrell, K., Tiwana, P., Madden, C. & Finn, R. Long-Term Clinical Outcome Analysis of Poly-Methyl-Methacrylate Cranioplasty for Large Skull Defects. *J Oral Maxil Surg* 71, E81-E88, doi:DOI 10.1016/j.joms.2012.09.023 (2013).

6 Pang, S. W. *et al.* Reversal imprinting by transferring polymer from mold to substrate. *J Vac Sci Technol B* 20, 2872-2876, doi:10.1116/1.1523404 (2002).

7 Brash, J. L., Horbett, T. A. *Proteins at interfaces: physiochemical and biochemical studies*. (American Chemical Society, 1987).

8 Warren, S. M., Allori, A. C. & Sailon, A. M. Biological basis of bone formation, remodeling, and repair - Part II: Extracellular matrix. *Tissue Eng Part B-Re* 14, 275-283, doi:10.1089/ten.teb.2008.0083 (2008).

Appendix 3: Mineralization in MSCs and MC3T3-E1s

A3.1 Introduction

As has been discussed throughout this thesis, there is a great need to extend orthopedic implant life whether that be through strategies that utilize current materials like titanium, PMMA, poly(lactic-co- glycolic acid), alumina etc. or to develop entirely new strategies that replace current practices. Essential to both sets of strategies is the formation of bone. We explored, in brief, some of the background regarding bone composition, structure, function, and mineralization in Chapter 1. We did not thoroughly explore the concept of mineralization, however, and we will attempt to do that here.

An additional motivator for this discussion involves the data from Appendix 2. To summarize, the pre-osteoblast cells stopped producing mineral to the same level as was initially observed. A number of experiments were performed to determine the cause as will be discussed below. Ultimately, these cells seemed to become divergent. This has been reported elsewhere.[1] Thus, the process of mineralization was intimately explored while troubleshooting this issue.

A3.2 Materials and Methods

A3.2.1 Cell culture

Human bone marrow-derived MSCs were obtained from a commercial source (Lonza, Walkersville, MD) at passage 2. As part of the manufacturer's quality control, these MSCs were tested for purity by flow cytometry and for their ability to differentiate into osteogenic, chondrogenic and adipogenic lineages. Cells are positive for the cell surface markers CD105, CD166, CD29 (integrin β1), and CD44, and negative for CD14, CD34 and CD45. MSCs were maintained in high glucose (4.5 g/L) Dulbecco's modified Eagle medium (DMEM, Invitrogen, Carlsbad, CA) supplemented with 10% fetal bovine serum (FBS, Invitrogen). All cultures were incubated at 37°C and 5% CO_2. Media were changed every 2 days. MSCs were routinely expanded in 2D cultures and harvested with 0.05% Trypsin-EDTA (Invitrogen). Cells were used prior to passage 8 for differentiation experiments and prior to passage 11 for viability and cell extraction experiments. For 2D controls to the 3D experiments described below, MSCs were cultured for 1, 7, or 14 days. We identify these times as 'pre-culture', indicating the culture time prior to harvesting and subsequent analysis.

For osteogenic differentiation, MSCs were seeded at 5,000 cells/cm^2 in a 24-well plate for functional assays on UV nanoPMMA. Cells were maintained in osteogenic growth media (OGM), consisting of αMEM (Gibco), 20% FBS, 2 mM L-

glutamine (CellGro), 1% penticillin/streptomycin, and 5mg/mL gentamicin, or osteogenic base media (OBM), consisting of OGM, 10 mM β-glycerol phosphate (Sigma-Aldrich), and 50 μg/mL L-ascorbic acid (Fisher Scientific) similar to conditions previously reported.[2,3]).

MC3T3-E1 pre-osteoblasts (ATCC) were cultured in alpha-MEM growth media [GM] (Invitrogen) supplemented with 10% fetal bovine serum (ATCC), 5% penicillin/streptomycin (Mediatech) and 0.5% gentamicin (Invitrogen). For osteogenic assays cells were supplemented with 10 mM β-glycerol phosphate, 50 μg/mL ascorbic acid, and 100 nM dexamethasone (all from Sigma Aldrich). Cells were grown at confluence (100,000/cm^2) for osteogenic assays. Cells used were between passages 3 and 9. Most of the troubleshooting experiments were performed on tissue culture polystyrene, though nanoimprinted PMMA was also used.

A3.2.2 FTIR spectroscopy

A Jasco FTIR 4100 (Easton, MD) was used to analyze HA and cell deposited mineral samples. The samples were scanned using the attenuated total reflectance (ATR) attachment in ambient air (making sure to collect a background scan prior to scanning each sample).

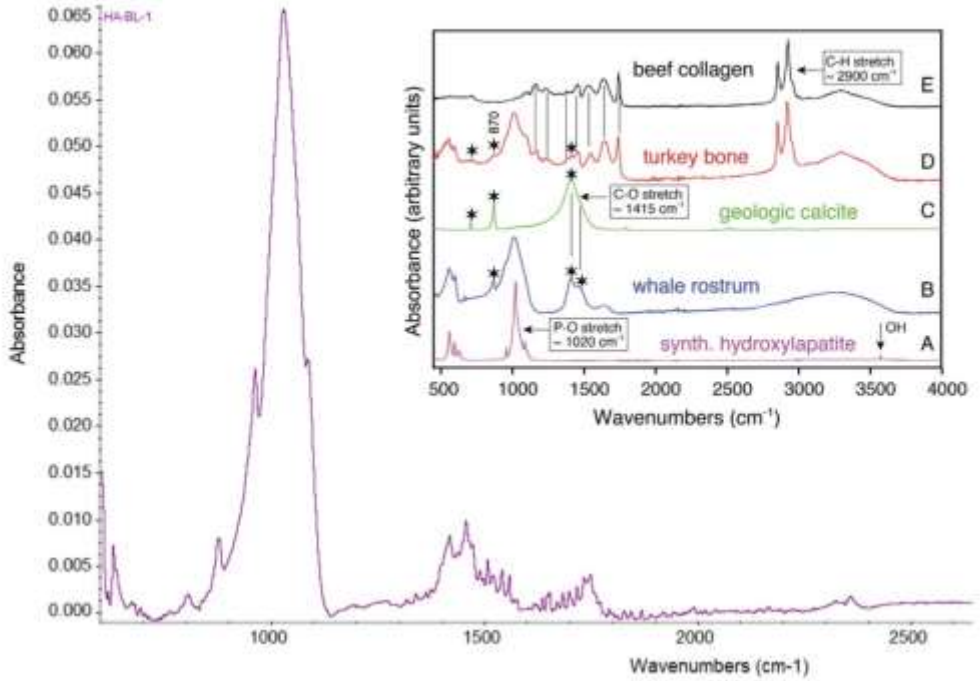

Figure A3.1. FTIR can be used to detect mineralization. An HA standard was analyzed using an FTIR (see Materials and Methods) using an ATR attachment. This spectra, when compared to the inset[4], indicates that FTIR can be used to detect HA and its analogues.

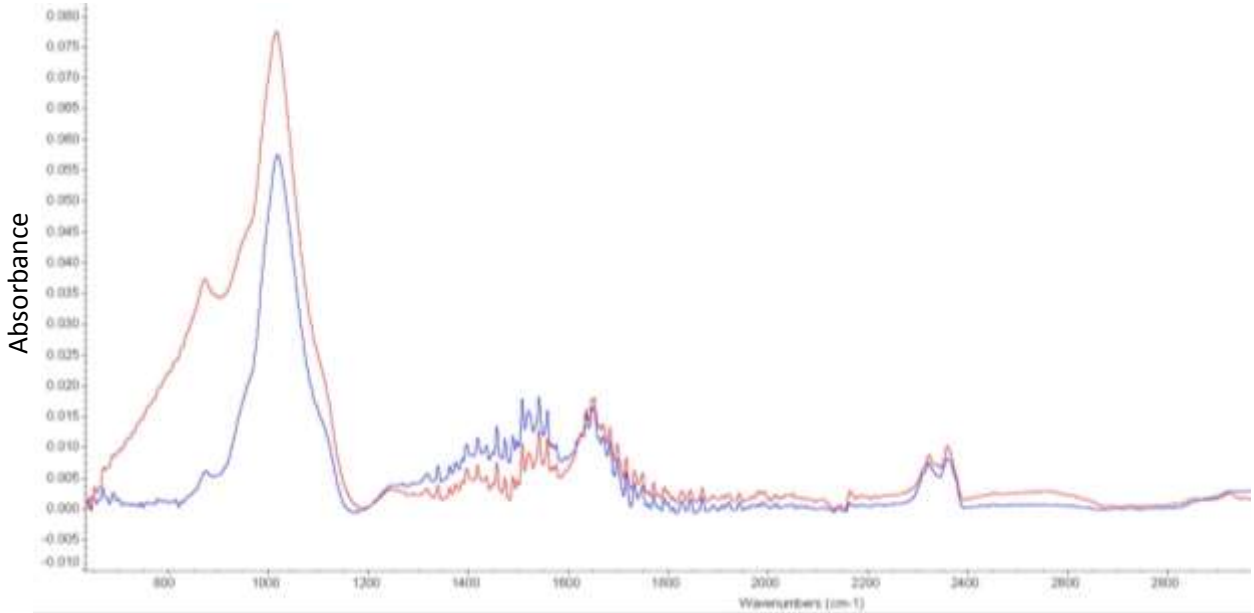

Figure A3.2. FTIR does detect cell mineral deposits similar to HA The above spectrum from MSC deposited mineral and ECM on a G415 PMMA (red) and G140 (blue) substrate illustrates the similarity to HA (see Figure A3.1). Peaks are not as sharp compared to HA; that is likely due to the presence of Col I and other ECM components.

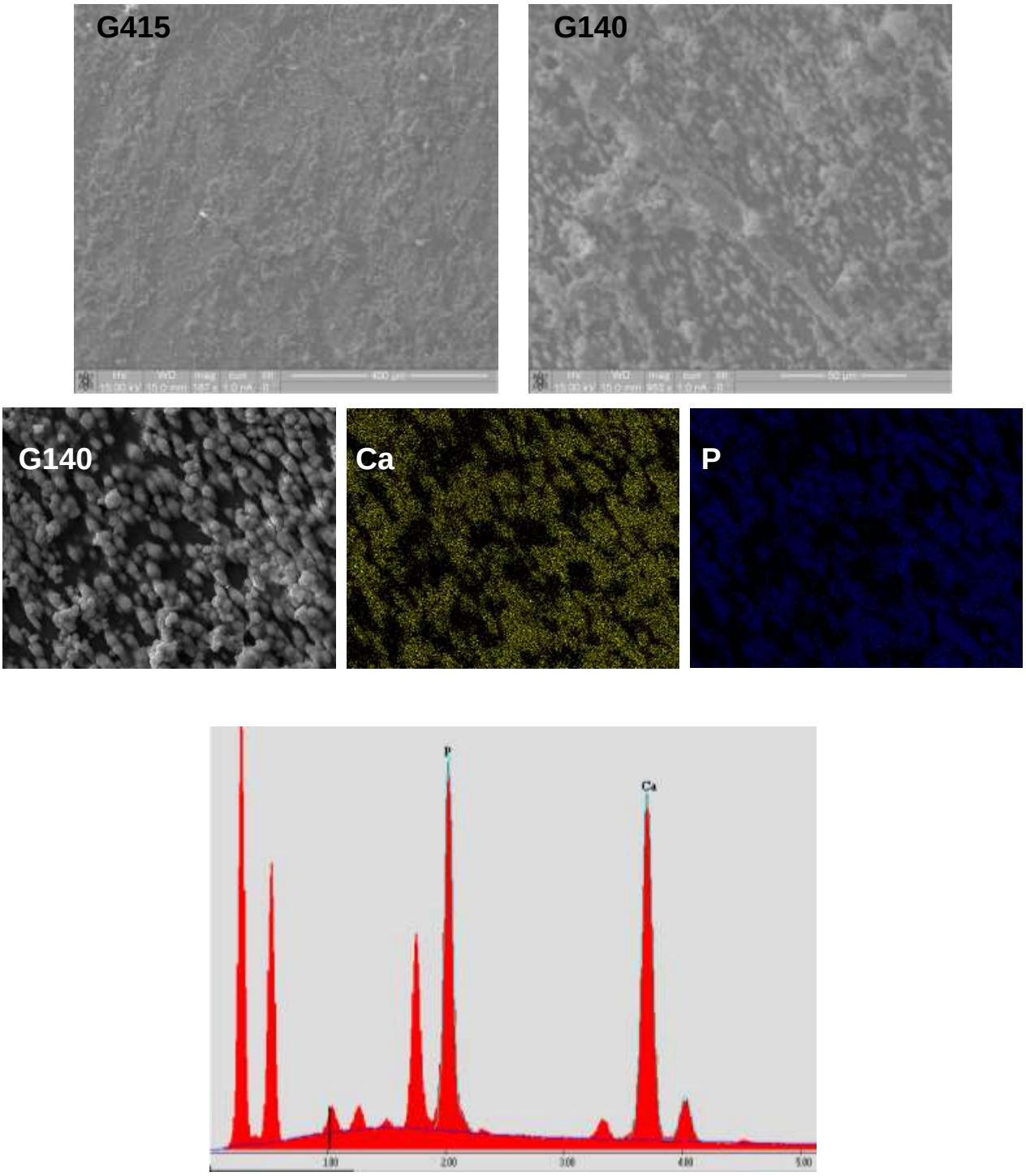

Figure A3.3. Mineralization analysis. SEM-EDS micrographs of mineral deposited by hMSC on G415 and G140 nanoPMMA analyzed to reveal spectroscopic maps of Ca and P. Elemental analysis was done (bottom) to determine Ca/P ratios. (See Chapter 4).

A3.2.3 Von Kossa staining

Cells were rinsed in PBS 2X and then fixed in 4% paraformaldehyde at 4°C for 30 minutes after 14 and 21 days in OIM. After fixation, cells were rinsed in double distilled (DD) water 3X and then immersed in 5% $AgNO_3$ (Sigma) and subjected to UV light (~365 nm) for 40 minutes. After UV exposure cells were rinsed 3X in DD water. The cells were then rinsed in sodium thiosulfate (Sigma) for 3 minutes and rinsed in DD water 3X. Images were taken on an Olympus IX51 with a DP25 color camera.

A3.2.4 Scanning electron microscopy (SEM)

At day 21, cells were washed in PBS and subsequently fixed for 20 minutes in 4% PFA in PBS. After fixation, cells were washed twice in ddH2O and allowed to air dry overnight. The specimens were sputter-coated with gold and examined with a Phillips XL30FEG SEM equipped with an EDAX Phoenix X-ray energy dispersive spectrometer (XEDS). A working distance of 10 mm and an accelerating voltage of 15 kV were used for XEDS mineral chemical micro-analysis. A minimum of three areas from three distinct fields of view were scanned for 60 seconds to determine Ca:P ratios. Hydroxyapatite (HA) (Sigma) was used as a control. Briefly, hydroxyapatite powder was embedded in a viscous polymer resin and allowed to dry overnight at 40 °C. All samples were sputter-coated with gold.

A3.3 Results

A3.3.1 Von Kossa assessments revealed lack of mineral formation.

MC3T3-E1 cells mineral deposition declined over time. It was unclear why. This was first determined via visual inspection and also with Von Kossa staining. As Von Kossa stains for phosphates[5] it was unclear if calcium rich deposits were present as OCPC (Chapter 4 and 5) assays for calcium were not performed. Cell media formulations were altered to ensure the absence of ascorbic acid in growth media (most alpha-MEM contains ascorbic acid) as ascorbic acid is a known driver of collagen I production[6], a key component for a mineralized matrix. Ascorbic acid type was changed as different forms have different stability in solution[7,8]. Dexamethasone administration was changed to be added at later time points (day 7 or day 14). Cell density was altered from 50k/cm^2 to 200k/cm^2. Collagen (rat tail type I) was deposited on the surface of TCPS as well as on nanoPMMA (nanoimprint) films. None of these, either independently or in combination, seemed to return mineral deposition to a near normal level. Because of these findings, the pre-osteoblasts were deemed divergent.

A.3.3.2 MSC mineral was assessed via FTIR, XEDS.

Because pre-osteoblasts diverged and were poor producers of a mineralized matrix, we switched to hMSCs. hMSCs, as has been highlighted throughout this

thesis, have the potential to differentiate into a multitude of cell types including osteoblasts. We showed that hMSCs could produce mineral that was both phosphate and calcium rich through Von Kossa staining and the calcium assay respectively (Chapter 4, Appendix 1). We used a few other methods to assess mineralization. FTIR spectra for HA, as seen in Figure A3.1, illustrates the utility of FTIR to identity bone-like mineral. We then assessed the mineral deposited by cells on our nanoPMMA surfaces as seen in Figure A3.2. Because of the addition of organic content (cells, ECM etc.) the peaks lose some of their sharpness, but the characteristic peaks of HA are still present. Figure A3.3 shows SEM micrographs of mineral deposited on nanoPMMA as well as chemical maps of Ca and P. These results combined with the FTIR results suggest that the mineral deposited has characteristics similar to HA, though it may be calcium deficient as discussed in Chapter 4, but it is likely physiologic mineral because much of the mineral is associated with the cell and surrounding matrix.[5]

A3.4 Discussion

We observed a lack of mineral formation when culturing mouse pre-osteoblasts. In contrast, we observed an HA-like mineral when culturing hMSCs. The cell culture conditions were not identical, though they were similar, so that may have played a role in the differences observed. Additionally, cell density was also different for each cell type. MSCs have been shown to become osteogenic when seeded at low

cell density[9], and thusly MSCs were cultured at 5000k/cm^2. Pre-osteoblasts were cultured at higher densities to try to eliminate the effects of different cell proliferation rates across conditions. These may explain some of the different observations. The divergent nature of the preosteoblasts is likely the main reason for the observations as cell culture conditions were modulated and changed to further promote mineral formation and none were successful

The process of mineralization requires many components including cells[10], matrix components[11], and soluble ions and proteins[12]. Cells are needed to either modify and remove existing cartilaginous ECM or deposit new ECM capable of promoting mineralization.[10] Mineralization is physiologic when it is associated with cells and the surrounding matrix.[5] Dystrophic mineral can result from high concentrations of phosphate and the soluble calcium found in cell culture media[10]. These findings highlight the importance of the matrix and soluble components. Both calcium and phosphate are necessary for mineral formation but phosphates have been identified as the limiting component[11].

As mentioned, the matrix is essential to mineralization. Interestingly, if a mature matrix is present it can mineralize in the absence of cells[13]. The mature matrix was a cellular byproduct thus it highlights the importance of the cells in producing a template capable of mineralizing. The template for mineralization is composed mostly of collagen I (as mentioned in Chapter 1 and 4)[14]. The hexagonal packing[15] and the gaps between collagen fibrils, specifically at the C-terminal region, are believed to be

the site of HA aggregation and growth[16]. These gap sites are associated with charged amino acids that have the lowest electrostatic potential energy promoting a favorable area for association with negatively charged amorphous calcium phosphate-polyaspartic acid complexes.[16] Fetuin and other non-collagenous proteins (NCP) can also nucleate amorphous calcium phosphates (ACP). Though, collagen I alone is capable of inducing mineral growth (and as suggested by the capability of mineralization in mature matrices). The role of the NCPs seems to be for stabilization of ACP for entry into the collagen matrix.[16] The NCPs prevent further growth of amorphous clusters[17], potential serving to stabilize but also restrict growth to the gap regions of the collagen matrix. These findings suggest that collagen I is essential for physiological mineral formation.

A3.5 Conclusion

Because a matrix comprised of collagen I is essential for nucleation and growth of physiologic mineral it suggests that hMSCs were depositing Col I in sufficient quantity and with the appropriate structural arrangement to promote mineral formation. In contrast, the near absence of mineral in MC3T3-E1 cells cultures suggests they were: 1. not producing Col I at all, 2. not producing Col I in sufficient quantity to support mineral formation, 3. the structure and alignment of the deposited Col I was not conducive to mineral aggregation and growth, or 4. a combination of 2

and 3. Thus, with the understanding of the necessary components for physiologic mineral, the findings further support the conclusion that MC3T3-E1s became divergent.

A3.6 References

1 Wang, D. *et al.* Isolation and characterization of MC3T3-E1 preosteoblast subclones with distinct in vitro and in vivo differentiation mineralization potential. *J Bone Miner Res* **14**, 893-903, doi:DOI 10.1359/jbmr.1999.14.6.893 (1999).

2 Krause, U., Seckinger, A. & Gregory, C. A. Assays of Osteogenic Differentiation by Cultured Human Mesenchymal Stem Cells. *Mesenchymal Stem Cell Assays and Applications* **698**, 215-230, doi:Doi 10.1007/978-1-60761-999-4_17 (2011).

3 Prockop, D. J. P., Donald G.; Bunnell, Bruce A. in *Methods in molecular biology v. 449* (Humana Press, Totowa, N.J., 2008).

4 Pasteris, J. D., Wopenka, B. & Valsami-Jones, E. Bone and tooth mineralization: Why apatite? *Elements* **4**, 97-104, doi:Doi 10.2113/Gselements.4.2.97 (2008).

5 Boyan, B. D. *et al.* Osteoblast-mediated mineral deposition in culture is dependent on surface microtopography. *Calcified Tissue Int* **71**, 519-529, doi:DOI 10.1002/s00223-001-1114-y (2002).

6 Peterkof.B. Effect of Ascorbic-Acid on Collagen Polypeptide Synthesis and Proline Hydroxylation during Growth of Cultured Fibroblasts. *Arch Biochem Biophys* **152**, 318-&, doi:Doi 10.1016/0003-9861(72)90221-4 (1972).

7 Saika, S. Ascorbic-Acid and Proliferation of Cultured Rabbit Keratocytes. *Cornea* **12**, 191-198, doi:Doi 10.1097/00003226-199305000-00002 (1993).

8 Hata, R. I. & Senoo, H. L-Ascorbic-Acid 2-Phosphate Stimulates Collagen Accumulation, Cell-Proliferation, and Formation of a 3-Dimensional Tissue-Like Substance by Skin Fibroblasts. *J Cell Physiol* **138**, 8-16, doi:DOI 10.1002/jcp.1041380103 (1989).

9 McBeath, R., Pirone, D. M., Nelson, C. M., Bhadriraju, K. & Chen, C. S. Cell shape, cytoskeletal tension, and RhoA regulate stem cell lineage commitment. *Dev Cell* **6**, 483-495, doi:Doi 10.1016/S1534-5807(04)00075-9 (2004).

10 Boyan, B. D., Schwartz, Z. & Boskey, A. L. The importance of mineral in bone and mineral research. *Bone* **27**, 341-342, doi:Doi 10.1016/S8756-3282(00)00347-1 (2000).

11 Allori, A. C., Sailon, A. M. & Warren, S. M. Biological basis of bone formation, remodeling, and repair - Part II: Extracellular matrix. *Tissue Eng Part B-Re* **14**, 275-283, doi:DOI 10.1089/ten.teb.2008.0083 (2008).

12 Allori, A. C., Sailon, A. M. & Warren, S. M. Biological basis of bone formation, remodeling, and repair - Part I: Biochemical signaling molecules. *Tissue Eng Part B-Re* **14**, 259-273, doi:DOI 10.1089/ten.teb.2008.0082 (2008).

13 Marsh, M. E., Munne, A. M., Vogel, J. J., Cui, Y. Q. & Franceschi, R. T. Mineralization of Bone-Like Extracellular-Matrix in the Absence of Functional Osteoblasts. *J Bone Miner Res* **10**, 1635-1643 (1995).

14 Weiner, S. & Wagner, H. D. The material bone: Structure mechanical function relations. *Annual Review of Materials Science* **28**, 271-298, doi:DOI 10.1146/annurev.matsci.28.1.271 (1998).

15 Silver, F. H. & Landis, W. J. Deposition of apatite in mineralizing vertebrate extracellular matrices: A model of possible nucleation sites on type I collagen. *Connect Tissue Res* **52**, 242-254, doi:Doi 10.3109/03008207.2010.551567 (2011).

16 Nudelman, F. *et al.* The role of collagen in bone apatite formation in the presence of hydroxyapatite nucleation inhibitors. *Nat Mater* **9**, 1004-1009, doi:Doi 10.1038/Nmat2875 (2010).

17 Nudelman, F., Sonmezler, E., Bomans, P. H. H., de With, G. & Sommerdijk, N. A. J. M. Stabilization of amorphous calcium carbonate by controlling its particle size. *Nanoscale* **2**, 2436-2439, doi:Doi 10.1039/C0nr00432d (2010).

Appendix 4: Procedures

Alkaline Phosphatase Assay

Materials

ALP Harvest buffer: 10 mM tris-HCl, pH 7.4
2 mM PMSF (add at time of assay) (In general it is recommended to
ALP Assay buffer: 100 mM Glycine make all buffers immediately
1 mM $MgCl_2$, pH 10.5 stored at 4℃ before assaying)
PNPP substrate: 50 mM p-Nitrophenol Phosphate
Passive Lysis buffer 5X (-20°C)
Appropriate Cell Lysates (made using passive lysis buffer)
0.1 N NaOH
PBS
dd H_2O

Procedure

1. Wash cultured cells using TBS
2. Dilute 5X Passive lysis buffer in dd H_2O to final concentration of 1X
3. Lyse cells using 1X Passive Lysis Buffer (15 minute incubation)
   -use 100 µL per well (for 24 well plate)
3. Scrape cell layer and rewash well with the 1X passive lysis buffer with plastic spatula use lysis buffer in well
4. Store the lysates on ice or in -80℃ for later use
   Note: if storing for later use add PMSF- final working conc. of 1mM

For the assay: (For normalization, BSA of total protein done in parallel is necessary)

1. Add 100 µL ALP harvest buffer to lysates
2. Sonicate lysates on a continuous setting for 4 seconds
3. Centrifuge the lysates at 10000 rpm for 10 minutes at 4℃
4. Use 100 µL of sonicated sample supernatant
5. Prepare control sample (blank) with 100 µL of dd H_2O in a microcentrifuge tube
6. Add 300 µL of ALP assay buffer to samples and blank
   a. Blank1-ALP assay buffer + ddH2O + NaOH + pnPP
7. Add 100 µL of PNPP substrate to sample tubes, vortex, incubate in 37℃ water bath for 20 minutes
8. To stop reaction add 500 µL of 0.1 N NaOH to tubes, vortex

9. Read absorbance at 405 nm on spectrophotometer
10. Calculated ALP units/ mL using the following equation

UNITS ALP/mL: = [A_{405} / (18.5*incubation time in minutes*sample volume in mL)]*1000

Normalize to total protein level i.e.

$$\frac{\text{(UNITS ALP/mL)}}{\text{(Protein conc. μg/mL)}} = \text{(UNITS ALP/μg of protein)}$$

Oil Red O procedure

(adapted from Reger et al pg 98, Mesenchymal Stem Cells: Methods and Protocols by Prockop, Phinney, Bunnell Humana Press 2008)

STOCK solution:

Weigh 2.5 g oil Red O (sigma O0625), dissolve in 500 mL isopropanol. [Can scale down to 0.5 g in 100 mL]

Dissolve completely. Store in a tightly capped bottle at RT protected from light. Store for up to 3 months.

WORKING solution:

3 mL of STOCK mixed with 2 mL of PBS (scale up as needed)

Mix and wait 10 minutes before filtering with a 0.22 micron filter unit.

Wait 10 min before use.

STAINING:

Aspirate any media.

Rinse each well with PBS (x2) ~ 500 mL

Aspirate PBS.

Fix cells in 4% paraformaldehyde ~30 minutes at 4 C.

Rinse each well with PBS (x2) ~ 300 to 400 uL (for 24 well plate)

Add ~250 to 300 μL Oil Red O to each well, or as much is needed to cover cells

Incubate at RT for 20 minutes.

Aspirate Oil Red O and rinse in 60/40 isopropanol/PBS 3 times, do so very quickly.

Rinse in PBS (or ddH2O) at least 2 times or until background/PBS is clear.

Image.

Quantification:

Add ~250 uL per well of 4% IGEPAL-CA630 in isopropanol. (Make sure to have at least 2 'blank' wells that contain only the 4% solution.)

Cover with Al foil, wait 15 minutes.

Use plate reader at 520 nm to record absorbance.

Note: 60/40 isopropanol/PBS doesn't appear to remove lipids though the intensity of the lipids in cells does diminish, especially as the rinse time increases (5 seconds vs 5 minutes). 60/40 is a good solution to remove excess crystalline/aggregate Oil Red O that has not associated with lipids inside cells.

Sulfo-SANPAH procedure

Notes: Use sterile gels (if not sterile put in hood and turn on UV)

200 µl 2-3 mm thick gels are too tall for routine SS procedures, must work on thinner gels

Use approx. 200 µl (or less) sulfo-s working solution per gel

Need:
Sulfo-SANPAH (Pierce, stock is in DMSO)
Sterile PBS (warm/room temperature)
Sterile MES buffer, pH 6.0 → 0.1 M MES (2-(*N*-morpholino)ethanesulfonic acid) 10.66 g (per 500 mL)
0.5 M NaCl 14.62 g (per 500 mL)

Steps

1. Let SS stock thaw (normally at -20C)

2. Estimate total volume needed by counting number of gels

Example- 7 gels *.2 mL *2 irradiations = 2.8 mL, round up to 3mL

3. Transfer large UV lamp into hood after cleaning with ethanol (need plastic supports)

4. Aspirate PBS.

5. Rinse gels with MES buffer 1X.

6. Prepare working solution. Cover tube in aluminum foil to protect from light. (for every 12 mL of working solution need 30 µL of stock; scale as needed)

7. Add volume of working solution to each gel (try to place on top of each gel).

8. Expose to UV for 15 minutes, shake every 5 minutes or so.

9. Rinse with MES buffer 1X.

10. Repeat UV step (8) again with remaining working solution for 15 minutes.

11. Rinse with MES 3X.

12. Rinse with PBS.

13. Make collagen solution from stock. Target concentration is 50 μg/mL collagen. (Need 400 μL per gel) (Check each bottle of collagen for its concentration as it varies)

7 gels *.4 mL = 2.8 mL, round up to 3 mL

(50 μg/mL)*(3mL PBS) = (9.21x10^3 μg/mL)(?)

? = 0.0162 mL or 16.2 μL collagen in 3mL of PBS

14. Add collagen solution to each gel/well (try to place on top).

15. Put on Rocker for 2 hours after wrapping in parafilm (to keep sterile)

16. Rinse with sterile PBS 2X.

17. Use immediately or wrap in parafilm and store at 4C.

Notes: Can be stored up to one week at 4C.

Can also be used with other proteins (fibronectin, vitronectin, laminin etc)

OCPC Calcium Assay

Materials

1N acetic acid (2.862 mL glacial acetic acid in 47.138 mL water)
Plate shaker
Samples (can be stored at -80C)
KOH
$CaCl_2$
Ethanolamine
O-Cresolphthalein Complexone (OCPC)
Boric acid
Hydroxyquinoline
Ethanol

Solutions

Calcium Standard – 91.75 mg $CaCl_2$ in 25 mL ddH_2O (1 mg/mL)

Solution A 14.8 M ethanaolamine/boric acid buffer (natural pH 11)

0.5 mL ethanolamine

1 mL water

0.36 g boric acid-mix

0.5 mL ethanolamine-mix until boric acid is dissolved

8 mL ethanolamine

Solution B OCPC

166.7 µL N KOH (2.81 g KOH in 50 mL water)

25 mL water

26.7 mg OCPC

166.7 µL 1 N acetic acid

Solution C hydroxyquinoline (orange hue)

0.5 g 8-hydroxyquinoline

10 mL 95% ethanol (ethanol + water)

Working Solution 5 parts A + 5 parts B + 2 parts C + 88 parts water

Standard Curve

Name	Concentration	Vol. of Ca Standard (µL)	Vol. of 1N acetic acid (µL)
A"	150 µg/mL	150	850
A'	125 µg/mL	125	875
A	100 µg/mL	100	900
B	50 µg/mL	500 from A	500
C	25 µg/mL	500 from B	500
D	12.5 µg/mL	500 from C	500
E	6.25 µg/mL	500 from D	500
F	3.125 µg/mL	500 from E	500
G	1.5625 µg/mL	500 from F	500
H	0 µg/mL	0	1000

Directions

1. No fixation is necessary, if not, aspirate media then proceed to step 4.
2. Rinse cells with PBS. Aspirate.
3. Fix cells with 4% paraformaldehyde in PBS for 20 minutes. Rinse with water. Aspirate.

4. Add 1 mL of 1 N acetic acid to each sample.
5. Shake overnight on the shaker (~200 rpm).
6. Collect samples in microcentrifuge tube and store samples at -80C if needed.
7. Make calcium standard curve samples.
8. Add 10 µl of each sample/standard into a well of a 96 well plate (do so in triplicate).
9. Add 300 µL of working solution to each well.
10. Incubate the plate(s) for 10 minutes at room temperature, protect from light.
11. Read the plate at 565 nm using a plate reader.

Notes: Calcium standard and solutions should be stored at 4 °C for up to 2 weeks.

Typically day 21 samples are highly concentrated and need to be diluted 5X to fall on the standard curve.